Friction

(Quarterly, Started in 2013)
Volume 5 Number 3 / September 2017

ISSN 2223-7690
CN 10-1237/TH

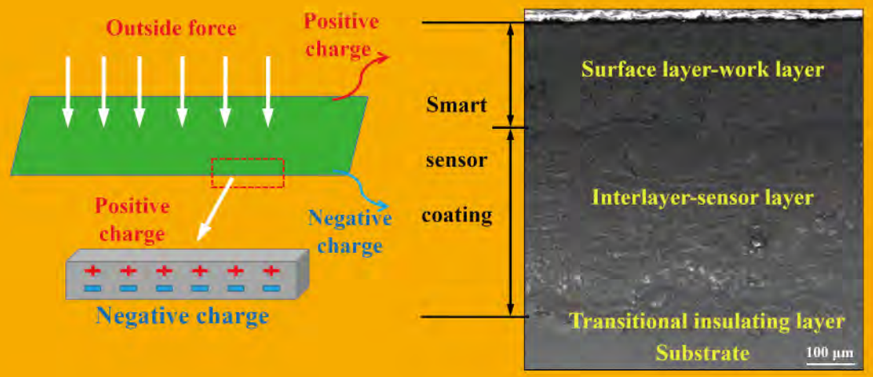

Design and application of friction pair surface modification coating for remanufacturing

摩擦（英文）（季刊，2013年创刊） 第5卷 第3期 2017年9月出版

Editor-in-Chief	Jianbin Luo	主管单位	教育部
Sponsored by	Tsinghua University	主办单位	清华大学
Supported by	Chinese Tribology Institute	学术支持	中国机械工程学会摩擦学分会
Edited by	Friction Editorial Office	主　　编	雒建斌
Published by	Tsinghua University Press	编　　辑	《摩擦》编辑部
Address	Xueyan Building, Tsinghua University, Beijing 100084, China	出版发行	清华大学出版社有限公司
		印刷单位	北京天成印务有限责任公司
Website	http://www.springer.com/40544 http://friction.tsinghuajournals.com		

Online Manuscript Submission, Review and Tracking System http://mc03.manuscriptcentral.com/friction

ISSN 2223-7690
09>
9 772223 769170

40544 Friction Volume 5 Number 3 2017 pp 231–360

ISSN 2223-7690
CN 10-1237/TH

Friction

Special Issue on 6th World Tribology Congress

Volume 5 Number 3 / September 2017

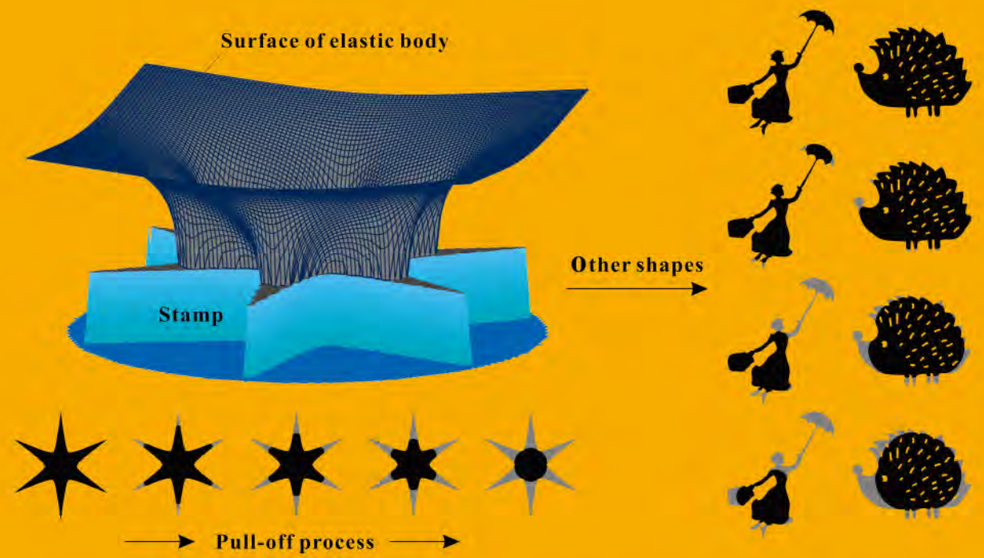

Strength of adhesive contacts: Influence of contact geometry and material gradients

TSINGHUA UNIVERSITY PRESS
Springer

Friction
ISSN 2223-7690
CN 10-1237/TH
Vol. 5, No. 3, September 2017

Contents

TSINGHUA UNIVERSITY PRESS Springer

Friction **5**(3): 231–232 (2017)
https://doi.org/10.1007/s40544-017-0187-1
ISSN 2223-7690
CN 10-1237/TH

EDITORIAL

Guest editorial: Special issue on 6th World Tribology Congress

Jianbin LUO

State Key Laboratory of Tribology, Tsinghua University, Beijing 100084, China

The 6th World Tribology Congress (WTC 2017), hosted by Chinese Tribology Institute (CTI) and organized by the State Key Laboratory of Tribology (SKLT) of Tsinghua University, will be held in Beijing, China, on September 17–22, 2017. The objective of the congress is to highlight recent important progress in tribology and to strengthen the links between academia and industry. More than 900 oral presentations and over 300 posters have been accepted in 9 tracks, 170 oral sessions and 2 poster sessions. The exhibition and networking on WTC 2017 are designed to broaden knowledge and provide a range of perspectives on tribology. A technical exhibition and some visits to SKLT of Tsinghua University are also organized.

As chairman of the Organization Committee of WTC 2017 and the Editor-in-Chief of the journal *Friction*, I have invited prominent and specialized experts in tribology to contribute their works based on their plenary and keynote reports to the special issue on WTC 2017 for celebrating the grand congress. The research progresses in this special issue bridge over the fundamentals of tribology and its applications to industrial practices. This issue contains 8 invited papers to demonstrate the breadth and the timeliness of tribology and to anticipate future developments. These papers include:

- Four review articles on discussing how tribology has been helping us to advance and to survive, the properties and development status of multilayer coating systems for tribological applications, the influence of tribology on global energy consumption, costs and emissions, and the tribological behavior of sintered iron-based self-sintered and iron-based self-lubricating composites;
- Four research papers on the influence of contact geometry and material gradients on the strength of adhesive contacts, the comparison of stick and slip contact conditions for a coated sphere compressed by a rigid flat, the combined effect of surface microgeometry and adhesion in normal and sliding contacts of elastic bodies, and the design and application of friction pair surface modification coating for remanufacturing.

The first paper, by Gwidon W. Stachowiak, reviews the contribution and the importance of tribology in industry and society. This paper provides a good overview of how tribology has been effectively applied in various industries to advance the quality of our lives, e.g., by reducing energy consumption and managing pollution or contamination of the environment. Further, the author forecasts that new challenges such as sustainability, climate change, and gradual degradation of the environment require new solutions and innovative approaches as humanity progresses.

Mahdi Khadem et al. review the properties and the development of multilayer coating systems with the aim of providing a comprehensive overview of multilayer coating for tribological applications and gaining a better understanding of their advantages and limitations. The general issues related to materials, design concepts, mechanical properties, deposition method, and friction and wear characteristics of multilayer coatings are also discussed in detail. Specifically, Ti-based and Cr-based coatings were emphasized because Ti and Cr are identified as elements used widely in many multilayer coating applications.

Kenneth Holmberg and Ali Erdemir assess the impact of friction and wear on global energy consumption, economic losses, and CO_2 emissions worldwide in the four main energy consuming sectors, namely, transportation, manufacturing, power generation and residential, by using a methodology developed by the authors in their case studies on

passenger cars, trucks and buses, paper machines, and the mining industry. They then estimate potential savings that can be gained by employing the proposed tribological solutions. This review paper provides material evidence of the significance of tribology to the general public.

Jose Daniel Biasoli de Mello et al. review the tribological behavior of sintered iron-based self-lubricating composites. The most important results obtained by an ongoing research program toward the development of innovative, low-cost, self-lubricating composites with a low friction coefficient and high mechanical strength and wear resistance are presented and discussed in detail. Special emphasis is given to uniaxial die pressing of solid lubricant particles mixed with matrix powders and to metal injection molding associated with *in situ* generation of solid lubricant particles.

Valentin L. Popov et al. present an experimental investigation and numerical simulation for contacts of rigid punches with a flat but oddly shaped face contacting a soft, adhesive counterpart. When it is carefully pulled off, they find that in contrast to circular shapes, detachment does not occur instantaneously; instead, the detachment fronts start at pointed corners and travel inward until the final configuration is reached. For elongated indenters, the final shape resembles the original one with rounded corners. Numerical simulations are performed using a new formulation of the boundary element method for simulation of adhesive contacts suggested by Pohrt and Popov. The method is extended for describing power-law gradient media. This work provides a very inspiring base for the community to extend their investigation of the influence of microcontact shapes.

A finite element analysis is used by Shai Ronen et al. to study a comparison of stick and slip contact conditions for a coated sphere compressed by a rigid flat. A comparison with the slip contact condition is presented in terms of the critical contact parameters and plasticity evolution. Empirical expressions are provided for critical interferences of the first and second yield inceptions, in the coating and on the substrate side of the interface, respectively. An expression is also provided for the dimensionless coating thickness for optimal resistance to plasticity under the stick contact condition. Additionally, the relations between different contact parameters in the elastic-plastic regime are presented.

Irina Goryacheva et al. develop an approach to investigate the combined influence of surface microgeometry and adhesion on the load–distance dependence and energy dissipation in an approach–separation cycle, as well as on the formation and rupture of adhesive bridges during friction. The energy dissipation in a cycle of approach-separation of asperities of rough surfaces is calculated. Then the adhesive component of the friction force is calculated using the energy dissipation. The Maugis-Dugdale approximation is used for modeling the adhesive interactions. A specific feature of the paper is that contrary to many other studies in the area, the mutual influence of microcontacts is taken into account by the authors.

Remanufacturing is an important method to recover the dimensional accuracy of waste parts and effective way to enhance the working performance of a workpiece. Haidou Wang et al. summarize the preparation methods and engineering application of a series of remanufacturing coatings. The operation mechanism of micro/nano multilayer composite coatings with long-term efficacy life was revealed clearly. A series of wear-resistance & anti-fatigue coatings were prepared successfully. A failure-warning intelligent coating based on piezo-effect was designed and sprayed on friction pair surface, which can monitor the state and damage of moving parts real-timely. This paper has an important referential significance for the surface modification of frication pairs and remanufacturing of worn parts.

Friction **5**(3): 233–247 (2017)
https://doi.org/10.1007/s40544-017-0173-7
ISSN 2223-7690
CN 10-1237/TH

REVIEW ARTICLE

How tribology has been helping us to advance and to survive

Gwidon W. STACHOWIAK*

Tribology Laboratory, School of Mechanical and Civil Engineering Curtin University, Bentley, Western Australia 6102, Australia

Received: 09 May 2017 / Revised: 25 May 2017 / Accepted: 07 June 2017

Abstract: Movement between contacting surfaces ranges from macro to micro scales, from the movement of continental plates and glaciers to the locomotion of animals and insects. Surface topographies, lubricant layers, contaminants, operating conditions, and others control it, i.e., this movement depends on the tribological characteristics of a system. Before the industrial revolution, friction and wear were controlled by the application of animal fat or oil. During the industrial revolution, with the introduction of trains and other machinery, the operating conditions at the contacting surfaces changed dramatically. New bearings were designed and built and simple lubrication measures were no longer satisfactory. It became critical to understand the lubrication mechanisms involved. During that period, solid theoretical foundations, leading to the development of new technologies, were laid. The field of tribology had gained a significant prominence, i.e., it became clear that without advancements in tribology the technological progress would be limited. It was no longer necessary to build oversized ship bearings hoping that they would work. The ship or automobile bearings could now be optimized and their behavior predicted. By the middle of the 20th century, lubrication mechanisms in non-conformal contacts, i.e., in gears, rolling contact bearings, cams and tappets, etc., were also finally understood.

Today, we face new challenges such as sustainability, climate change and gradual degradation of the environment. Problems of providing enough food, clean water and sufficient energy to the human population to pursue a civilized life still remain largely unsolved. These challenges require new solutions and innovative approaches. As the humanity progresses, tribology continue to make vital contributions in addressing the demands for advanced technological developments, resulting in, for example, reducing the fuel consumption and greenhouse gases emission, increasing machine durability and improving the quality of life through artificial implants, among the others.

Keywords: tribology; friction; lubrication and wear

1 Tribology as part of our lives

In our everyday life we take many things for granted. It never occurs to us to pause and think why our hands or feet provide a perfect grip on most of the surfaces. We rarely think why sharks swim so fast or why geckos can walk on glass surface even when upside down. We expect spacecraft or satellites that we send to explore our solar system and beyond to operate smoothly even after many months or years of being idle. We expect that our trains and aircraft would stop exactly at the designated places at train stations and airports. When hopping into a car we don't think twice about the material used for the car seats. We don't think often why the tectonic plates or glaciers move with apparent ease. These seemingly diverse problems, and many others, are of great interest and research focus of tribologists. Tribology has helped us to discover not only the underlying mechanisms involved but also how to utilize these findings in practical applications.

We now understand why, as the response to stress,

* Corresponding author: Gwidon W. STACHOWIAK, E-mail: Gwidon.Stachowiak@curtin.edu.au

our hands and feet sweat. The reason is to provide a perfect grip to either hold a weapon firmly or to facilitate a rapid escape. We found that a special skin texture combined with streamlined bodies allows sharks to swim very fast. We managed to duplicate this texture on artificial surfaces with potential applications ranging from swimsuits to submarines. The gecko's ability to climb vertical walls and walk on ceilings lies in the structure of their feet containing complex hierarchical arrangements of lamellae, setae, branches and spatula. These billions of spatula bond to the surface by long range van der Waals forces [1–4]. However, it seems that the electrostatic effects cannot completely be ruled out as they might be contributing to the gecko's adhesion on some surfaces [4]. Attempts to duplicate these remarkable features of the gecko's feet in manufacturing self-cleaning, re-attachable dry adhesive tapes have already been made [5].

As the humanity progressed, new technologies, devices, materials and surface treatments required novel lubricants and lubrication systems. The technological advancements, like the development of high-speed trains, aircraft, space stations, computer hard discs, artificial implants, and many other engineering and bio-medical systems, have only been possible through the advances in tribology. For example, the question of how to safely stop a 16 car (about 400 m long) high-speed train travelling at 280 km/h or more, or A380 travelling at 250 km/h on landing and weighing almost 400 tones is an important one. When brakes are applied a large proportion of the kinetic energy of the train or the plane is dissipated as heat. Traditionally used brake material would crack due to the thermal stress. Therefore carbon fiber brakes are used instead.

A new technological frontier of space also demanded urgent tribological solutions. In space the environment is extreme: temperatures are below −200 ℃, there is vacuum and radiation. The temperature gradients are very large since the metal surface can heat up to +250 ℃ when exposed to the sun. Traditionally used lubricants wouldn't work, as they would either freeze, evaporate or decompose under radiation. As there is no oxygen and water in space no friction reducing oxide layers could grow to provide some form of a lubricating solid film on the surfaces. To reduce friction and combat wear in space new surface coatings suitable for vacuum conditions have therefore been developed. These coatings consist of a thin layer of soft film, typically molybdenum disulphide, artificially deposited on the surfaces. Coatings of solid lubricant are built up atom by atom yielding a mechanically strong surface layer with a long life service and the minimum quantity of solid lubricant [6].

There is also science behind the material selection for car seats, as the material chosen must perform well with different fabrics/leathers that we wear. Neither low nor high friction materials for car seats would be popular with the users.

At the macroscale, the layers of water and fragmented rock dictate the movement of glaciers or geological plates, i.e., this movement is controlled by the tribological principles.

Friction and wear are accepted as an integral part of our lives and we often take their effects for granted. For example, we notice how crucial the effect of friction is on our walk especially when the friction dramatically drops, i.e., when the surface is slippery and we fall. When there is a problem with friction or wear then we seek a technological solution. For example, if the roads were slippery all the time, like after the first autumn rain, then we would quickly develop a technology to provide safe driving and braking under those conditions.

There is an inevitable cost related to wear and friction. Wear results in continuous renewal of our possessions and costs energy. Industries producing shoes, car tyres, slurry pumps, etc., would suffer enormously if their products did not wear. The price we pay for this is high as energy and materials are consumed to replace the worn items. Mining minerals, crude oil and gas requires energy. Further energy is needed to transform the ore into metals, crude oil into petroleum, etc. But this is not the end of it. Energy is needed to manufacture and transport the components produced across the globe and also to overcome friction in machine elements such as pistons, gears and bearings. The friction between moving machine elements in particular results in waste of an enormous amount of energy. Rapidly growing human population with a strong appetite for new products, combined

with our limited energy resources, poses a serious challenge to the researchers in tribology. Our resources and energy are in finite supply and hence the need to control wear and friction becomes increasingly urgent. In addition, the rapid spread of the lifestyle from the advanced countries to the developing countries inevitably brings extra demands and pressures on the available resources and energy. The study of friction and wear would therefore continue to provide many challenges for the researchers in tribology for many decades to come.

2 Lubrication to combat friction

Long before the initiation of any historical records, the early humans used basic tribological principles in their everyday lives. For example, the importance of friction and sliding speed was quickly recognized when rubbing two sticks together to make fire. To rotate the stick faster a bow was utilized. How the humans discovered this principle of the temperature rise in sliding contact that was then used to light the fire is unknown. Perhaps prehistoric people had noticed that hands warm up when rubbed together and then tried this with the sticks. We'll never know. The ancient history contains abundant examples of the applied study of friction and wear. For example, lubricants were used in sledges to move large stone blocks for the construction of the pyramids at Giza or to move massive monuments; a wheel with a lubricated bearing was developed for chariots and carts, etc. [7].

The effect of fat on friction reduction was probably known long before the recorded history. At the beginning, the prehistoric farmers experimented with animal fat to lubricate the axles of their carts before embarking on a more ambitious task of manufacturing first grease. The animal fat was mixed with soda. The mixture, when placed in the cart's bearing, turned into grease with the help of frictional heat. At that time the concept of a lubricant and lubrication was born. People found that to prevent the axles from overheating was to keep them lubricated. This is a basic principle behind reducing friction and wear, i.e., to make sure that a layer of lubricant is present between the sliding surfaces all the time. This phenomenon was easily observed but to put science behind it was a far more difficult task, and centuries had elapsed before solid theoretical foundations of lubrication were laid.

The pioneering study of a lubrication mechanism between two conformal sliding surfaces was conducted towards the end of the 19th century. As usually is the case, necessity dictated the rigorous scientific research into the mechanisms behind the lubrication process. During the industrial revolution railways were developed and used on regular basis in England. However, the railway axle bearings were a continuous source of problems. As rolling contact bearings were not yet commercially available, these were simple journal bearings with lubricating holes located on the top. The problem was that often, during the operation, these bearings ceased to rotate or became very hot due to excessive friction, frequently catching a fire. Stopping the wheel rotation resulted in a flat spot on its rolling surface, rendering the wheel practically useless. Wheels were costly to replace and repair.

Thus in 1896 the Institution of Mechanical Engineers commissioned one of its top engineers, Beauchamp Tower, to investigate this problem. For the first time a systematic and detailed study of the friction in journal bearings was performed. However, the problem was so unusual that after a few months of testing the issue of high friction in these bearings was still largely unresolved. As often happens in science a chance intervened with a lucky discovery. When bearings were running in the laboratory it was noticed that the lubricating holes were persistently leaking oil. Plugging leaking holes with rags and then with wooden bungs didn't help much. Tower then realized that the oil in the bearing must be under a considerable pressure. When the pressure was measured it became clear that it was high enough to support the bearing load [8] (Fig. 1). What's more, the high pressure implied that between the bearing and shaft surfaces there was a layer of a lubricant of sufficient thickness to separate them. The solution was to remove the lubrication hole and instead fit a container with oil underneath. This was a major discovery and at that point the existing knowledge of lubrication and its effects on friction and wear was transformed forever.

Tower's discovery provided strong experimental evidence supporting the hydrodynamic theory of lubrication that was being developed at the time by

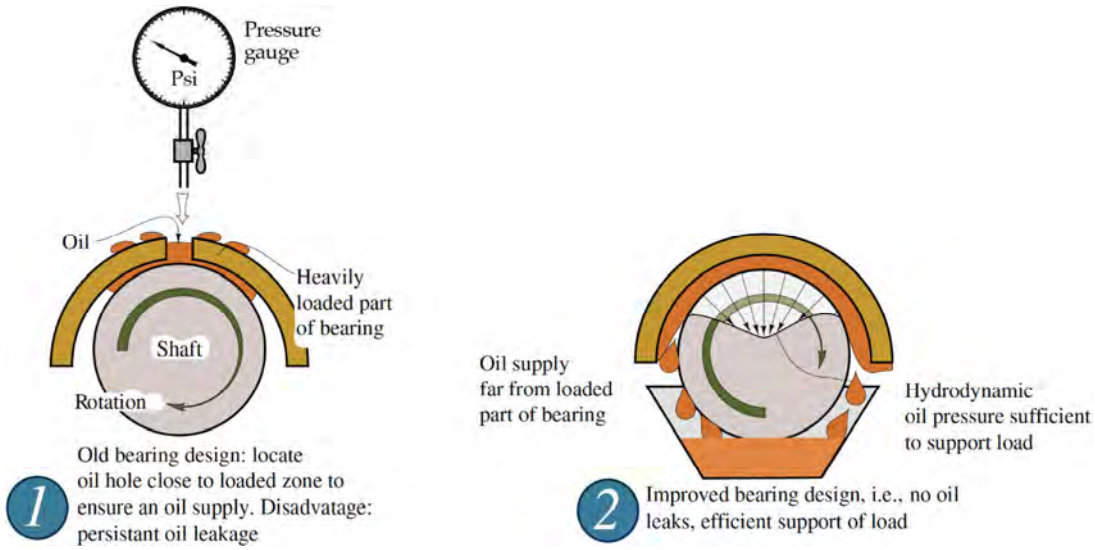

Fig. 1 Discovery of hydrodynamic lubrication in axle bearing (adapted from Ref. [9]).

Reynolds [10]. It needs to be mentioned that the concept of a film of lubricant separating two sliding surfaces was not new. It had been proposed earlier by Leupold in 1735, Leslie in 1804, Rennie in 1829, Adams in 1853 and Hirn in 1854 [7]. What was new, however, was the science, encapsulated in a set of elegant mathematical equations, neatly describing the lubrication mechanism in action. A combination of Tower's experimental results and Reynolds' mathematical analysis provided a vital tool in bearing design. It replaced numerous empirical ideas on railway axle bearing lubrication and effectively solved the problem. In this early lubrication research, Tower's measurements did not include other fundamental bearing parameters, such as operating temperature, elastic deformation of the bearing under load or inertia effects. This was done much later [11].

By the middle of the 20th century the lubrication mechanisms in conformal contacts in hydrodynamic and hydrostatic bearings had been well studied, understood and defined. However, the mechanism of lubrication operating in highly loaded non-conformal contacts remained a mystery for some time. Non-conformal contacts are commonly found in gears, rolling contact bearings, cams and tappets, etc., and the contact areas and stresses are very much different from those encountered in conformal, hydrodynamic contacts. The contact areas are very small and the resulting contact pressures are much higher, over 1 GPa. In 1880 Heinrich Hertz developed neat stress formulas for various non-conformal contact geometries [12], which are still in use today.

It was known that a very thin lubricating film existed between gear teeth. The thickness of these films, once measured, was far too low to be reliably predicted by the classical hydrodynamic theory [13]. Two Russian researchers, Ertel and Grubin, solved the mystery and provided the answer. They realized that a combination of three effects: hydrodynamics, elastic deformation of the metal surfaces and the increase in the oil's viscosity under extreme pressures found in these heavily loaded non-conformal contacts, contributed to the lubrication mechanism operating [14, 15]. Hence the mechanism was named elastohydrodynamic lubrication (EHL), which effectively means that the contacting surfaces deform elastically under the hydrodynamic pressure generated in a thin layer of the lubricating film. These lubricating films are extremely thin, in the range of 0.1 to 1 μm. However, despite their low thickness these films still manage to effectively separate the interacting surfaces, resulting in a significant reduction of wear and friction.

For many years little was known about the nature of the EHL films. Initially, the thickness of these films could only be estimated using electrical resistance or capacitance methods but the accurate confirmation was lacking for some time. In the 1960s Cameron and Gohar [16, 17] provided the answer. They devised a

simple test comprising a glass disc and a bearing ball. The glass disc was covered with the semi-reflective coating allowing for half the light to be reflected off the glass surface and half to pass through the oil film and be reflected off the steel ball. The elastohydrodynamic films observed were thin enough to provide a good interference effect with visible light. The observations showed that under large contact stresses the surface of the ball deformed elastically to produce a continuous oil entrapment in the shape of a "horseshoe" on the edges of the contact. This elastic oil entrapment effect, shown in Fig. 2, is commonly known as the "end constriction". The elastic deformation at the constriction is lower than that in the centre. Under high contact pressures the lubricant starts behaving as a "solid material", i.e., the steel surface deforms elastically around the lubricant, at the edges of the contact. With this technique EHL films in "soft" contacts with polymethylmethacrylate and polyurethane have also been measured [18].

The EHL problem was far too complex for the analytical analysis. The simultaneous solution of sets of equations describing the hydrodynamic effect due to the relative motion of the surfaces, elastic deformations and changes in the lubricant's rheology due to very high contact pressures was impossible to achieve analytically. Dowson and Higginson accomplished this task employing numerical methods. They used the Ferranti-Pegasus valve-based computer to figure out the solution. The computer contained 3,000 valves and it took Dowson and Higginson 3,000 hours to get enough results for their paper. Their efforts resulted in an elegant formula for the elastohydrodynamic film thickness, which is still used today [19].

The application of computers in solving lubrication problems was a major breakthrough with far reaching implications. After this our approach to hydrodynamic or EHL lubrication was never the same. Before, there was always a gap between what was required in the real engineering world and the solutions available. With this new computational approach it was now possible to incorporate in the analysis of bearings common features such as heat transfer from a bearing to its housing. But, numerical methods not only provided tools to solve differential equations and complex engineering problems but also helped to gain the general understanding of the physical phenomena occurring.

Over the last several decades, significant progress has been made in both the EHL film measurement methods and in our understanding of the phenomena occurring in the EHL contacts. Main limitations of the original interferometry technique are its resolution and the requirement that one of the contacting bodies must be transparent. As the measurement resolution is dictated by the wavelength of visible light, films of thickness lower that 0.1 μm could not be accurately measured.

The application of an additional solid spacer layer

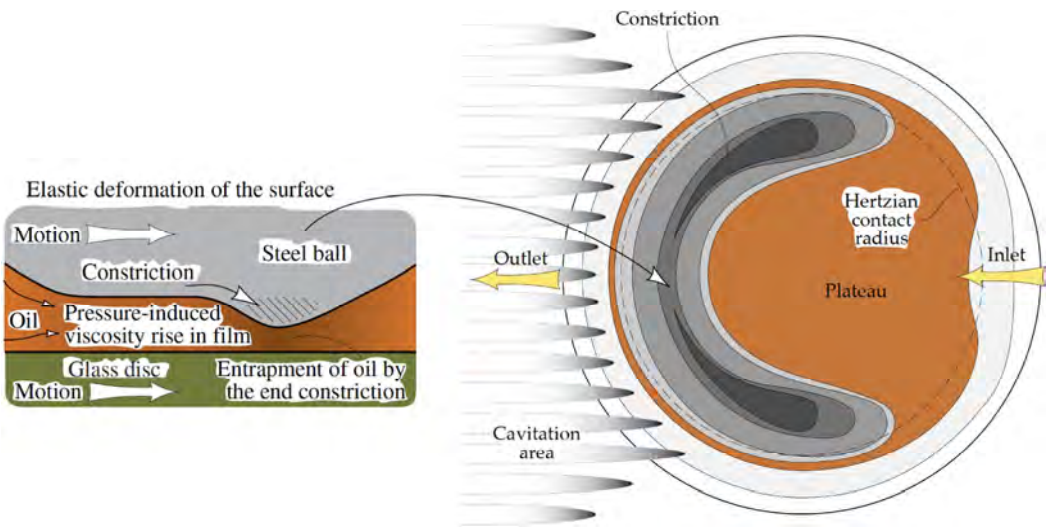

Fig. 2 Elastic oil entrapment effect in elastohydrodynamic lubrication (adapted from Refs. [9, 15]).

combined with spectrometric analysis of the light reflected from the contact provided a significant improvement and allowed for the measurement and mapping of very thin lubricant films, down to 10 nm [20, 21]. With this new technology it appeared that observations and thickness measurements of boundary films might be within the reach. However, the problem is that most of the real contacts in machine components are metal-to-metal. Thus, the transparent body requirement is a constraint for the optical interferometry and limits its use as essentially a laboratory technique. The studies of thin films and the influence of metallic surfaces on the film chemistry became possible later with the application of precise capacitance measurements using LCR meters with automatic balancing bridges [22].

A unique feature of EHL contacts is that they can provide traction. The difference between traction and friction is in the way the mechanical energy is processed. In the case of traction this energy is transmitted between the contacting bodies (i.e., one body is driving another) while with friction it is dissipated [15]. The traction is sufficiently high for the engineering applications like, for example, variable speed transmissions. The attractiveness of these transmissions lies in their ability to maintain infinitely variable output speed and almost a constant torque over the speed range. These features and low noise of these devices make them very attractive for applications in machine tools, textile industry and also in motor vehicles. The EHL traction has been studied in detail, followed by the development of traction fluids and advanced traction drives.

Recently, surface textures have been investigated, in both hydrodynamic and EHL contacts, as a means of reducing friction and wear and also improving performance. Small dimples in micrometre size are introduced into the surfaces resulting in friction and wear reduction. The topic is thoroughly investigated both experimentally and theoretically/numerically. New numerical methods simulating the dimple effects on friction and load capacity in hydrodynamic contacts are continuously being developed [23].

In many practical applications there are cases where the operating conditions are such that neither hydrodynamic nor elastohydrodynamic lubrication is effective. The question then is: how are the interacting machine components lubricated and what is the lubrication mechanism involved? The traditional name for this type of lubrication is "boundary lubrication" or more precisely "boundary and extreme-pressure lubrication". Neither of these terms describes accurately the processes at work since these concepts had been conceived long before any fundamental understanding of the mechanisms was available. Boundary and extreme-pressure lubrication is a combination of complex phenomena depending on lubricant properties, contacting body characteristics and operating contact conditions. The lubrication mechanisms involved can be classified in terms of relative load and limiting frictional temperature [15]. The lubrication mechanism is mostly controlled by the additives present in the oil. Since the cost of lubricant additives is almost negligible compared to the value of the mechanical equipment, the commercial benefits involved in this type of lubrication are large. In general, boundary and extreme-pressure lubrication involves the formation of low-friction, protective layers on the wearing surfaces. First mechanisms, i.e., the adsorption model of lubrication, were postulated by Hardy and Doubleday [24, 25] and later developed by Bowden and Tabor [26] followed by many others.

The pioneering work of Bowden and Tabor has been extended by the development of a new area in tribology called tribochemistry which focuses on the chemical reactions taking place between the lubricant and surfaces under boundary lubrication conditions [27]. Numerous researchers, notably Stephen Hsu, Nic Spencer, Keiji Nakayama, Eddy Tysoe, Jean Michel Martin, Nobuo Ohmae and others, laid the solid foundations for this new branch of tribology.

3 Wear

From the beginning of our civilization until the 19th century wear was routinely accepted as inevitable part of life which forces continuous renewal of most of our possessions. Items like shoes, ploughs, cart bearings and emerging machines were wearing out only to be replaced by new components. This process of continuous renewal has many benefits as it keeps the economy going, but it has also many disadvantages

since resources and energy are consumed to replace the worn items. Friction wastes an enormous amount of energy. From the moment petroleum emerges from the ground to when it is burnt as fuel, there are frictional losses. However, more than 100 years ago, there was one wear problem which could not be easily accepted, i.e., the problem with wear of gold coins in circulation in Great Britain.

In 1898, King George III commissioned Charles Hatchett to investigate whether this weight loss could be attributed to normal, everyday wear. To investigate the problem, in a systematic way, Hatchett built a special tribometer to evaluate the wear rate of the coins. After extensive testing Hatchett concluded that rapid coins wear due to their everyday use could not account for their rapid weight loss [7, 28]. In his experiments Hattchet demonstrated that wear can be assessed in a systematic way.

Much earlier Desaguliers hypothesized that friction and wear between clean surfaces depended on the mutual adhesion of the contacting solids [29]. This concept remained as a valid model for almost two hundred years. The experimental work of Bowden and Tabor [30] into adhesion and friction between clean metals enhanced this theory and dramatically advanced our understanding of friction and wear. Despite its initial universal acceptance, the theory linking friction to adhesive bonding between contacting surface asperities and wear has since been modified and further advanced in the light of new experimental and numerical simulations evidence conducted at the atomic level [31].

In another research, about two hundred years ago in 1804, Leslie provided the first model of the friction between contaminated surfaces where waves of deformed material were pushed across the surface by the asperities from the opposing surface [32]. This theory remained obscure until 1984. Then, the experimental confirmation of material deformation and waves formation was provided by Challen, McLean and Oxley [33, 34]. A wearing contact was modelled by a prism of hard material sliding on a block of softer material as shown in Fig. 3. When the rigid prism was forced into the softer material and driven horizontally along the surface of the soft counterface, a wedge of deformed material accumulated in front of the prism. Undeformed material from the soft counterface flowed through this wedge, which remained at constant size. The net effect on the counterface was a layer of highly strained material. This simple model, based on slip-line fields, explained well the fundamental mechanism of abrasive wear by plastic deformation.

This study confirmed earlier observations of similar highly strained layers present on the worn surfaces [35] as well as the raised humps of material similar to the wedge [36, 37]. So it was concluded that a large proportion of the frictional energy in unlubricated sliding is dissipated in driving waves of deformed material across the surface [38]. Since then our knowledge on wear has greatly advanced. We now understand most of the wear mechanisms, and how they are influenced by materials, lubricants, operating and environmental conditions. This understanding has been essential in the design of modern machines with required long life expectancy. However, we did not stop there as further research reveals wear mechanisms operating not only at macro scales but also at micro and nano scales.

4 Biotribology

Biotribology as a new area in tribology has developed as a response to the growing interest in applying

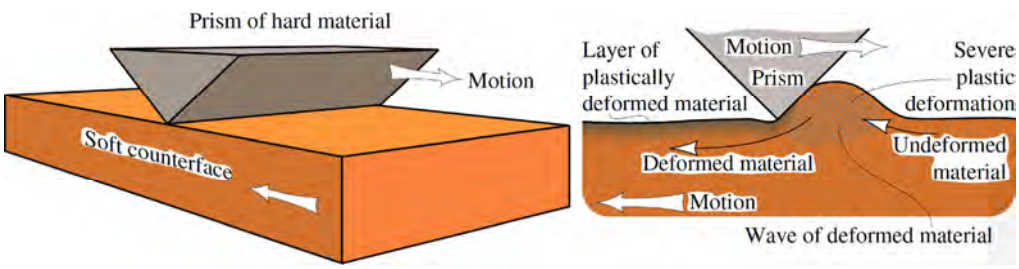

Fig. 3 Model of surface waves formation (adapted from Ref. [9]).

scientific methods to understand tribological phenomena occurring in a human body. Animal and human bodies evolved with many sliding and frictional living tissue interfaces. One of the most important examples is the interface between the external object and the skin. Oily, friction and wear-reducing substance called "sebum" is secreted by skin to improve grip by a hand or to protect feet during walking/running. Inside the body in the lungs the bronchioles can freely dilate and contract during respiration (breathing). For this to happen, an effective lubrication facilitating this function is essential. A lubricating film on the exterior of the lungs is vital to the movement of lungs within the ribcage. Similar films are essential to the movement of eyeballs. In fact, lubricating films separate most of the internal organs, e.g., liver, intestines, etc.

The human body has more than one hundred articulating joints, which act as bearings, e.g., knees, hips, feet, spine, hands, etc. These bearings facilitate walking, running, jumping, flexing of the limbs, bending, gripping by the hands, etc. The joints consist of mostly conformal cartilaginous surfaces sliding past each other. Most synovial joints exhibit very low friction coefficients and wear. The most common problem with synovial joints is arthritis, with two principal forms: osteoarthritis and rheumatoid arthritis. Osteoarthritis, characterized by the loss of articular cartilage, meniscal tears and maceration, osteophytes, and microstructural changes in the subchondral bone, is different from rheumatoid arthritis, which occurs when the body's immune system is induced to attack the synovial joints, in particular causing damage to the articular cartilage.

Osteoarthritis is a leading cause of disability among middle-aged and elderly persons. For example, in Australia alone, osteoarthritis affects more than 50% of the population over 65, at a cost of over 25 billion dollars per annum to the economy and health system [39, 40]. Despite its high cost to many societies across the world, there are no effective treatments for the disease or even symptoms relief (pain, stiffness), with the exception of weight loss and joint replacement.

Tribology has played a significant role in our understanding of osteoarthritis. Biological studies of synovial joints involve problems outside the normal range of engineering studies. However, the experimental methodologies used in studies of wear and friction of engineering materials were adapted to study wear and friction in synovial joints [41–43]. Experimental research data on wear, especially of "live" synovial joints, is notoriously difficult to obtain. Cadaver sheep joints were tested on a specially designed joint simulator in an oxygen-free sterile environment. The experiments conducted revealed that the wear particles generated in the sheep joints subjected to wear were very similar to those observed in osteoarthritic human joints. Vital conclusions about the wear mechanisms occurring in these joints were obtained. New measures were developed sensitive enough to detect minute changes occurring in knee bones and trained classifiers can now accurately predict the osteoarthritis (OA). The same principles can be used in the development of prognostic tools for, e.g., hip, hand, foot, elbow and shoulder OA and even cancers.

How is this possible? So far, "classical" surfaces have been characterized using traditional/standard surface roughness parameters, which work well with isotropic surfaces. However, many modern surfaces manufactured to suit specific performance requirements or applications often contain complex texture patterns that vary locally in roughness and directionality at different scales. There is a large variety of surface textures/patterns produced. From a viewpoint of production and application of these surfaces they need to be characterized, in the same way as the "classical" surfaces, except that different measures must be used as the standard parameters are no longer suitable. Current ASME (American Society of Mechanical Engineers) and ISO (International Organization for Standardization) surface texture standards fail to adequately describe advanced surfaces, i.e., they are either not suitable, or exhibit significant limitations. For example, how can we characterize, using traditional parameters, surfaces textures like those shown in Figs. 4 or 5? The answer might be provided by the directional fractal signature (DFS) methods, which involve the calculation of fractal dimensions in different directions and at individual scales [44]. The DFS techniques not only calculate the changes in the surface topography at different scales but also describe the surface anisotropy and show the surface dominant direction. It can be seen from

Fig. 4 that at the largest scale of 70 μm the surface changes its directionality which may affect its properties or performance, e.g., microlubrication. The DFS methods are also applicable to the characterization of surfaces which are otherwise difficult or even impossible to analyze by any other existing technique, e.g., self-structured surfaces shown in Fig. 5.

DFS methods have been adapted for use in early detection and prediction of osteoarthritis based on X-ray images of the knee or hand joints [45–51]. X-ray images of bones in knee and hand joints can be analyzed using the same DFS techniques that are used to analyze 3-D surfaces. This illustrated in Fig. 6 where the range images (with surface elevations encoded in the pixel brightness values) of a 3D surface and trabecular bone X-ray image are shown. The DFS technique can be used to accurately characterize both images.

As the osteoarthritis progresses, at some stage the joint's disease becomes untreatable by conventional means, e.g., drugs, physiotherapy, etc., and the question is: what are our options when nothing else works? The answer is in joint replacements, resurfacing and cartilage repair.

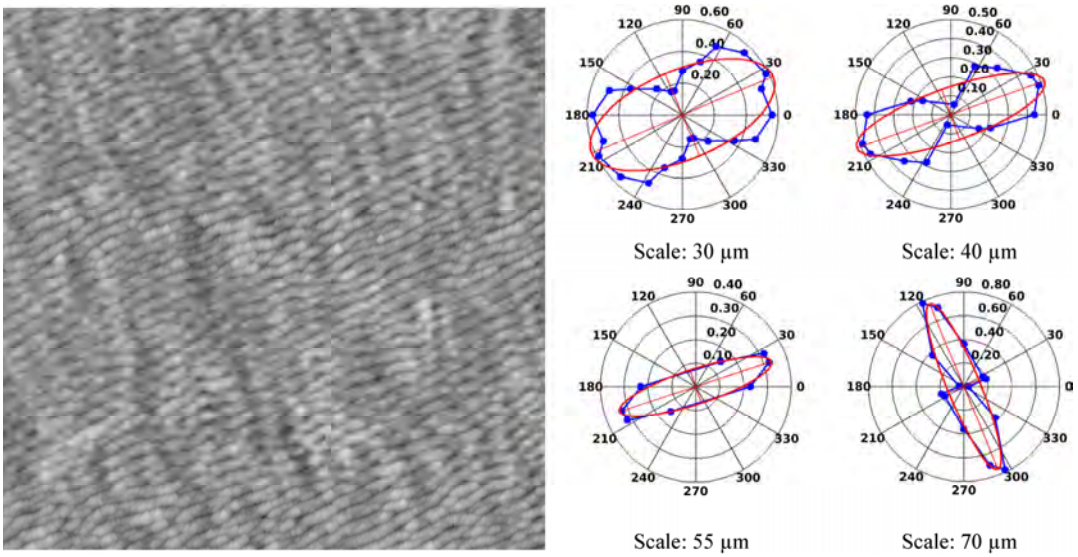

Fig. 4 Image of the textured surface together with the DFS analysis results presented as Rose plots at four scales.

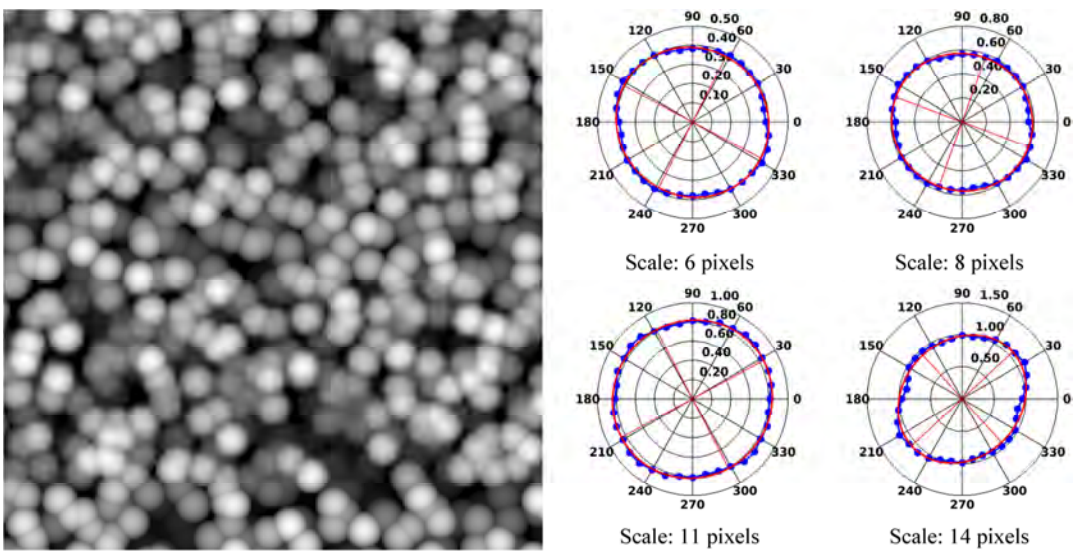

Fig. 5 Image of the self-structured surface together with the DFS analysis results using augmented blanket with rotating grid method (adapted from Ref. [48]).

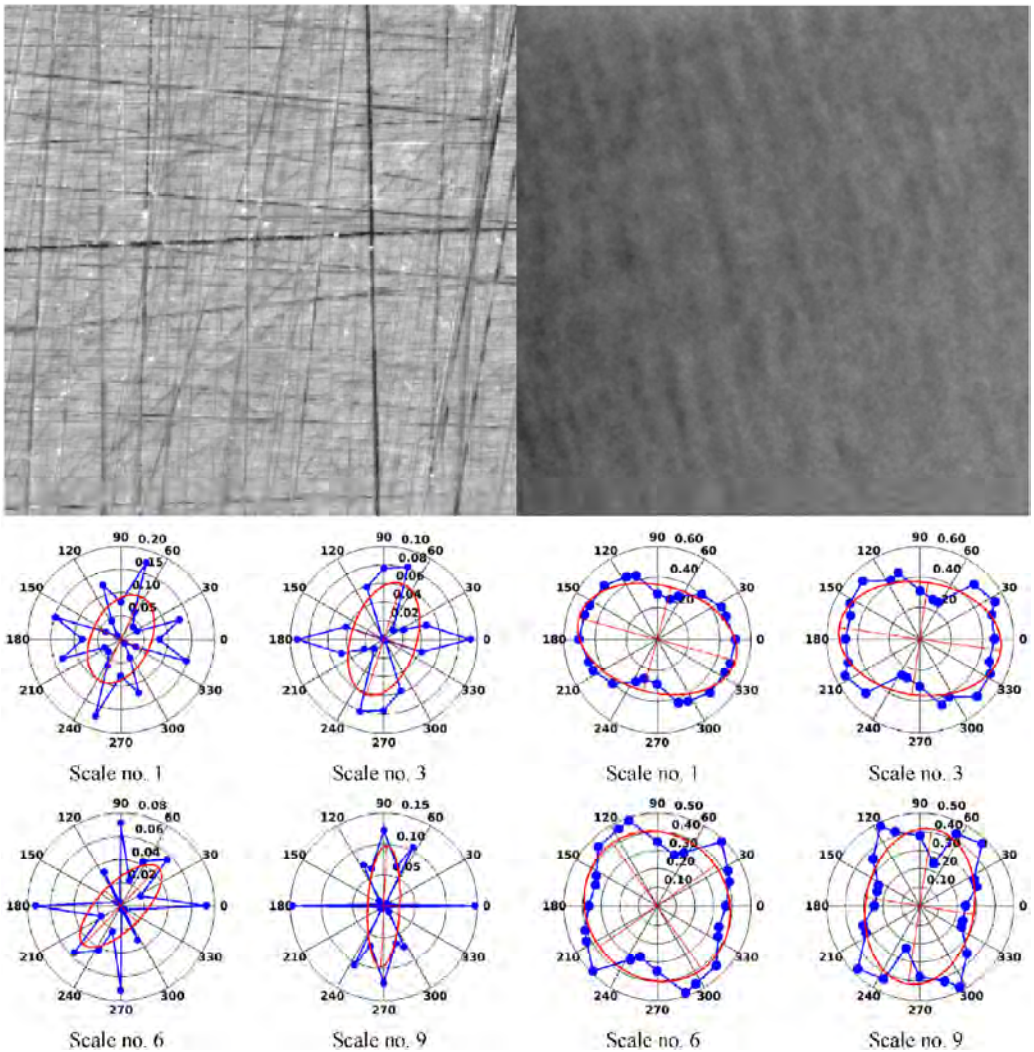

Fig. 6 Range image of the surface topography and x-ray region of interest of a normal knee together with the DFS analysis results.

Most of the tribological research has been focused on the replacements for hip and knee joints, as shown in Fig. 7. In 1881, Themistocles Glück used an ivory ball and a socket joint. Since then different materials, such as glass, steel, rubber, acrylic and materials combinations were used for hip joint replacements. It was quickly realized that the artificial joint material must not only be biocompatible, but also able to withstand the body stresses with minimum wear. The introduction of ultra-high-molecular-weight polyethylene as a bearing surface, by John Charnley in 1963, revolutionized the design of hip prostheses. It happened by pure chance. UHMWPE salesman thought that as the polyethylene was used to make gears, it should also work well in hip prostheses. Charnley initially dismissed the UHMWPE, but his laboratory technician tested it and the results were good. This discovery has led to the development of modern hip and knee joint replacements.

Early designs of knee prostheses appeared in the 1940s as simple hinges. This basic design failed to accommodate the complexities of knee movement and the failure rate was very high. Rapid loosening and infection were major problems. The introduction of UHMWPE as a bearing surface and the provision for unrestricted rotational movement solved the early failure problem and resulted in a modern knee implant. Without the input from tribology the development of knee and hip implants, which provide pain relief and improved mobility to a large number of

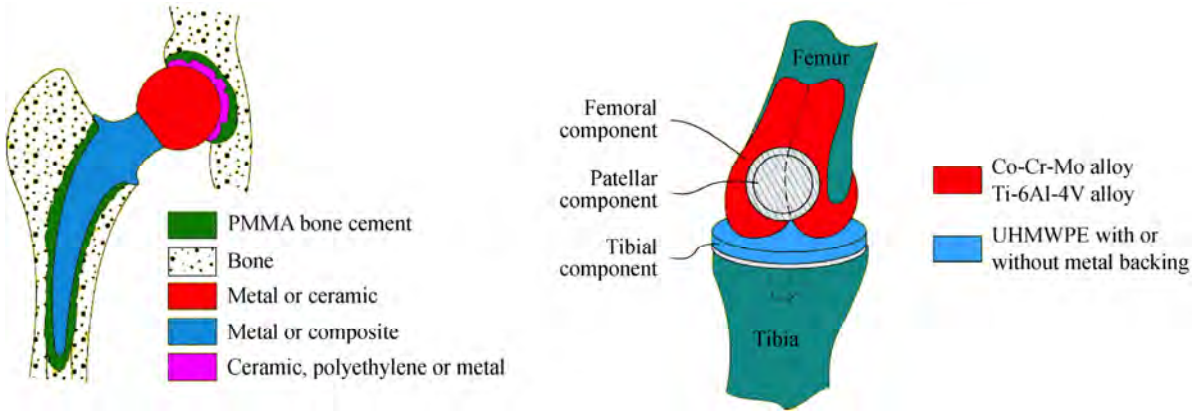

Fig. 7 Schematic diagrams of hip and knee implants (adapted from Ref. [52]).

osteoarthritis sufferers, would not be possible.

Tribology has also influenced the development of new dental restorative materials, which are fitted to an ever increasing number of patients, vascular prostheses such as artificial heart and others. Materials used for these devices notoriously suffer from wear problems.

5 Environmental tribology

Major global concerns now include rapid environmental degradation occurring across the globe, diminishing oil reserves and speedy climate change. As a response to these concerns environmental tribology has evolved with a research focus on innovative technologies, green lubricants and new materials aiming to reduce friction and wear with a bonus of reduction in energy consumption and the environmental impact.

The challenges that we face are not trivial. For example, a serious problem is the disposal of used mineral lubricating oils. These substances are often toxic and present in large volumes. To get a perspective, there are about 40 million tonnes of oils being discarded annually worldwide. Try to imagine a lake 4,000 m long, 500 m wide and 22 m deep [15]. Only a small proportion of the used oil is reprocessed and most of it is disposed back into the environment. Solution might be provided by biodegradable lubricating oils, which can be harmlessly decomposed by bacteria and fungi after use. Potential applications for biodegradable lubricants range from bulldozers and excavators which notoriously leak the hydraulic fluid during operation, to ships plagued by perennial problems of oil leakage to the sea.

Lubricants contain additives consisting of sulphur, phosphorus and many other, often toxic, compounds. Burning these additives with fuel in internal combustion engines, especially diesel, directly contributes to the acid rain and pollution in most of the cities across the globe. In some cities pollution is chronic and poses a severe health hazard. Apart from green lubricants material surfaces with artificially introduced textures are used to reduce friction and hence fuel consumption in engines.

6 Nanotribology

Device miniaturization is one of the frontier technologies of the 21st century. Introduction of micro and nanotechnologies may change the ways in which people and machines interact with the physical world. MEMS devices find applications in medicine, biotechnology, optics, electronics, aviation and many others. Mechanisms of material removal at nano/micro scale are becoming vital in the development of nano/micro grinding technologies. These technologies are needed in the production of, for example, microlenses with good surface finish for miniaturized endoscopes or cell phones.

From nanotechnology, a research field of nanotribology has emerged, which is the study of tribology in minute contacts. This is a great leap from a macro to a nano scale tribology [15, 53]. A major impact of nanotribology has been in the development of computer disk drives with high recording densities. The recording density is inversely proportional to the film thickness between the recording head and the memory

disk. The film thickness between head and disk was initially provided by aerodynamic lubrication [15]. Monomolecular films, as thin as a few nanometers, instead of the conventional 0.1 μm of air films [54], have been achieved, dramatically increasing the recording densities.

In nanotribology, it is no longer possible to apply continuum mechanics to the analysis of surface contacts; instead the contacting solids must be modelled as what they really are, a matrix of bonded atoms or ions. Atomistic (i.e., involving explicit models of atoms) molecular dynamics simulations have been used to model the sliding nano contact. Currently these studies are limited to a few nanometers of sliding distance and a few hundred of atoms, but with increased computer power such studies at a larger scale will become possible in the near future. Fundamental principles of tribology such as Amontons' law are now being analysed in detail by computational models, i.e., the forces and energy flows on each atom within a sliding contact are being computed. Initially, most of the work conducted on nanoscale has been related to friction but there is an increasing volume of studies on nanoscale wear [15]. There, the basic concepts of tribology would need to be revised. For example, how can there be wear particles when the size of the contact is much smaller than the average diameter of typical wear particles? Is plastic deformation possible in nano contacts when the contact diameter is less than the spacing between dislocations? In micro-machine, only zero or negligible wear is permissible or else the sliding components would seize [55].

As the reliable operation of minute contacts requires friction control, just like in larger contacts, nanolubrication is of importance. For nano contact, the traditional methods of lubrication are not suitable. New methods of lubrication, e.g., vapour phase, carbon molecules (bucky balls, nano-onions, etc.), non-volatile monomolecular films of lubricants (often self-assembled), are thus being developed [15].

7 Summary

Since its official introduction of the word "tribology" in the 1960s, the work of tribologists has primarily been focused on solving the immediate industrial problems of wear and friction through thorough understanding of the lubrication mechanisms and surface phenomena, and the application of better materials, novel surface technologies, improved lubricants and lubrication methods. Over the last fifty years, largely thanks to tribology, the fuel consumption in motor vehicles has almost halved with twofold power increase. This resulted in decreased pollution by an individual car unfortunately only to be counterbalanced by a dramatic increase of car users. Even though the beneficial effect was largely nullified, without tribology several cities across the world would likely reach now the pollution levels deemed unsafe for humans.

Advancements in tribology allowed for the construction of ships of monumental size, sending satellites and robots into space, development of modern data storage devices, revolution in the road and air transportation, etc. Like with any progress there is a price to pay as humanity is faced with the problems of greenhouse gas emissions, global warming and environment degradation.

Once the immediate industrial problems associated with lubrication, wear and friction have been solved, or at least attenuated, the research focus has shifted to the newly emerging areas like biotribology, environmental tribology and nanotribology. Biotribology has been developed as a result of the growing interest in applying scientific methods to understand tribological phenomena occurring in the living tissue. It seems that much of the future research will be shaped by our desire to prolong human life. As our bodies are not designed to last a hundred or more years, they would have to be augmented by the increasing numbers of components made from synthetic materials and tribology would be vital to their reliable operation.

Nanotribology is an integral part of nanotechnology. It involves studies of tribology within extremely small contacts. Atomistic molecular dynamics simulations are used to model the sliding contact to understand friction at nano scale. Environmental tribology has evolved as a response to global concerns related to the gradual environment degradation, diminishing oil reserves and rapid climate change. This has resulted in new research focused on innovative technologies, e.g., surface textures, green lubricants and advanced materials aiming to reduce friction and wear and, at

the same time, reduce energy consumption and the environmental impact.

The increasing pace of research and development yields an urgent need to predict in advance what the future directions in tribology might be. For example, as affordable oil and gas resources are gradually diminishing the major issue is how to conserve what is still left and, at the same time how to provide increasing population with adequate mobility and sufficient power. Would we still be able to live in our cities?

As in the past, tribology research would help us to solve many of the issues arising and also it would help us to survive, e.g., by reducing energy consumption, managing pollution or contamination of the environment. Will there be major advances in our fundamental knowledge of tribology in the next fifty years? Will the range of tribological applications be significantly extended? Time will show. Over the last fifty years numerous scientists have advanced our tribological knowledge by establishing solid theoretical and practical foundations but it would be up to the younger generation to write future chapters in tribology. The issues in medical engineering, nano scale, longer machine lifetime, significant reduction in fuel consumption and improved energy conservation would need to be addressed very soon and this cannot be achieved without the tribology research.

References

[1] Autumn K, Liang Y A, Hsieh S T, Zesch W, Chan W P, Kenny T W, Fearing R, Full R J. Adhesive force of a single gecko foot-hair. *Nature* **405**: 681–685 (2000)

[2] Bhushan B. Adhesion of multi-level hierarchical attachment systems in gecko feet. *Journal of Adhesion Science and Technology* **21**(12−13): 1213–1258 (2007)

[3] Cobb K. Getting a grip: How gecko toes stick. *Science News* **162**: 133 (2002)

[4] Izadi H, Stewart K M E, Penlidis A. Role of contact electrification and electrostatic interactions in gecko adhesion. *Journal of the Royal Society Interface* **11**(98): 20140371 (2014)

[5] Geim A K, Dubonos S V, Grigorieva I V, Novoselov K S, Zhukov A A, Shapoval Y S. Microfabricated adhesive mimicking gecko foot-hair. *Nature Materials* **2**: 461−463 (2003)

[6] Buckley D H. *Surface Effects in Adhesion, Friction, Wear and Lubrication*. Amsterdam: Elsevier, 1970.

[7] Dowson D. *History of Tribology, 2nd Edition*. Professional Engineering Publishing, 1998.

[8] Tower B. First report on friction experiments. In *Proc Inst Mech Eng*, 1883: 632−669.

[9] Batchelor A W, Stachowiak G W. Revealing the hidden world of wear and friction. M*echanical Engineering Transactions, Journal of the Inst. of Engineers* **20**(1): 5–13 (1995)

[10] Reynolds O. On the theory of lubrication and its application to Mr Beauchamp Tower's experiments including an experimental determination of the viscosity of olive oil. *Phil Trans Roy Soc London* **177**(Part I): 157–234 (1886)

[11] Ettles C M M, Akkok M, Cameron A. Inverse hydrodynamic methods applied to Mr Beauchamp Tower's experiments of 1885. *Transactions ASME, Journal of Lubrication Technology* **102**: 172–181 (1980)

[12] Hertz H. Uber die beruhrung fester elastischer korper. *J Reine und Angewandte Mathematik* **92**: 156–171 (1881)

[13] Martin H M. Lubrication of gear teeth. *Engineering London* **102**: 199–221 (1916)

[14] Grubin A N. Fundamentals of the hydrodynamic theory of lubrication of heavily loaded cylindrical surfaces. in *Investigation of the Contact Machine Components*. Ketova K F ed. Translation of Russian Book No. 30, Central Scientific Institute for Technology and Mechanical Engineering, Moscow, 1949.

[15] Stachowiak G W, Batchelor A W. *Engineering Tribology (Fourth Edition)*. Elsevier-Butterworth-Heinemann, 2013.

[16] Cameron A, Gohar R. Theoretical and experimental studies of the oil film in lubricated point contacts. *Proc Roy Soc London Series A* **291**: 520–536 (1966)

[17] Cameron A, Gohar R. Optical measurement of oil film thickness under elastohydrodynamic lubrication. *Nature* **200**: 458–459 (1963)

[18] Marx N, Guegan J, Spikes H A. Elastohydrodynamic film thickness of soft EHL contacts using optical interferometry. *Tribology International* **99**: 267–277 (2016)

[19] Dowson D, Higginson C. *Elastohydrodynamic Lubrication*. Oxford: Pergamon Press, 1977.

[20] Johnston G J, Wayte R, Spikes H A. The measurement and study of very thin lubricant films in concentrated contacts. *Tribol Trans* **34**(2): 187–194 (1991)

[21] Cann P M, Spikes H A. The development of a spacer layer imaging method (SLIM) for mapping elastohydrodynamic contacts. *Tribology Transactions* **39**: 915–921 (1996)

[22] Chua W-H, Stachowiak G W. The study of the dynamic thickness of organic boundary films under metallic sliding contact. *Tribology Letters* **39**: 151–161 (2010)

[23] Woloszynski T, Podsiadlo P, Stachowiak G W. Efficient solution to the cavitation problem in hydrodynamic lubrication. *Tribology Letters* **58**(1): 1–11 (2015)

[24] Hardy W B, Doubleday I. Boundary lubrication─The paraffin series. *Proc Roy Soc London Series A* **100**: 550–574 (1921)

[25] Hardy W B, Doubleday I. Boundary lubrication—The temperature coefficient. *Proc Roy Soc London Series A* **101**: 487–492 (1922)

[26] Bowden F P, Tabor D. *The Friction and Lubrication of Solids, Part 1*. Oxford: Clarendon Press, 1950.

[27] Hsu S M, Zhang J, Yin Z. The nature and origin of tribochemistry. *Tribology Letters* **13**(2): 131–139 (2002)

[28] Hatchett C. Experiments and various observations on various alloys, on the specific gravity, and on the comparative wear of gold. Being the substance of a report made to the Right Honourable the Lord of the Committee of Privy Council, appointed to take into consideration the state of the coins of the Kingdom, and the present establishment and Constitution of his Majesty's Mint. *Phil Trans R Soc London* 93: 43–194 (1868)

[29] Desaguliers J T. *A Course of Experimental Philosophy*. London: John Senex, 1734.

[30] Bowden F P, Tabor D. *The Friction and Lubrication of Solids*. Oxford: Oxford University Press, 1964.

[31] Krim J. Friction at the atomic scale. *Scientific American* **275**: 74–82 (1996)

[32] Leslie J. *An Experimental Enquiry into the Nature and Propagation of Heat.* Printed for J. Newman, No. 22, Poultry, T. Gillet Printer, Salisbury Square, United Kingdom, 1804.

[33] Stachowiak G W. Tribology research and enterprise in Australia. In *World Tribology Congress, New Generation Tribology for Achieving a Sustainable Society*. Japanese Society of Tribologists, 2005: 4–7.

[34] Challen J M, McLean L J, Oxley P L B. Plastic deformation in sliding contact with a hard wedge: Its relation to friction and wear. *Proc Roy Soc London Series A* **394**: 161–181 (1984)

[35] Rigney D A, Hirth J P. Plastic deformation and sliding friction of metals. *Wear* **53**: 345–370 (1979)

[36] Cocks M. Interaction of sliding metal surfaces. *Journal of Applied Physics* **33**: 2152–2161 (1962)

[37] Antler M. Processes of metal transfer and wear. *Wear* **7**: 181–204 (1964)

[38] Komvopoulos K, Saka N, Suh N P. The mechanism of friction in boundary lubrication. *Transactions ASME, Journal of Tribology* **107**: 452–463 (1985)

[39] Knox S A, Harrison C M, Britt H C, Henderson J V. Estimating prevalence of common chronic morbidities in Australia. *Med J Australia* **189**: 66–70 (2008)

[40] Access Economics. Painful realities: The economic impact of arthritis in Australia in 2007. Sydney: Arthritis Australia, 2007.

[41] Jones C, Stoffel K, Ozturk H, Stachowiak G W. The effects of surface active phospholipids on wear and lubrication of osteoarthritic sheep joints: Wear. *Tribology Letters* **16**: 291–296 (2004)

[42] Ballantine G C, Stachowiak G W. The effects of lipid depletion on osteoarthritic wear. *Wear* **253**: 385–393 (2002)

[43] Graindorge S L, Stachowiak G W. Changes occurring in the surface morphology of articular cartilage during wear. *Wear* **241**: 143–151 (2000)

[44] Wolski M, Podsiadlo P, Stachowiak G W. Directional fractal signature analysis of trabecular bone evaluation of different methods to detect early osteoarthritis in knee radiographs. *Journal of Engineering in Medicine, Proc Inst Mech Eng, Part H* **223**: 211–236 (2009)

[45] Wolski M, Podsiadlo P, Stachowiak G W. Applications of the variance orientation transform method to the multi-scale characterization of surface roughness and anisotropy. *Tribology International* **43**: 2203–2215 (2010)

[46] Wolski M, Podsiadlo P, Stachowiak G W, Lohmander L S, Englund M. Differences in trabecular bone texture between knees with and without radiographic osteoarthritis detected by directional fractal signature method. *Journal of Osteoarthritis and Cartilage* **18**: 684–690 (2010)

[47] Wolski M, Stachowiak G W, Dempsey A R, Mills P M, Cicuttini F M, Wang Y, Stoffel K K, llyod D G, Podsiadlo P. Trabecular bone texture detected by plain radiography and variance orientation transform method is different between knees with and without cartilage defects. *Journal of Orthopaedic Research* **29**: 1161–1167 (2011)

[48] Wolski M, Podsiadlo P, Stachowiak G W. Directional fractal signature analysis of self-structured surface textures. *Tribology Letters* **47**(3): 323–340 (2012)

[49] Woloszynski T, Podsiadlo P, Stachowiak G W, Kurzynski M, Lohmander L S, Englund M. Prediction of progression of radiographic knee osteoarthritis using tibial trabecular bone texture. *Arthritis & Rheumatism* **64**: 688–695 (2012)

[50] Wolski M, Podsiadlo P, Stachowiak G W. Analysis of AFM images of self-structured surface textures by directional fractal signature method. *Tribology Letters* **49**: 465–480 (2013)

[51] Podsiadlo P, Stachowiak G W. Directional multiscale analysis and optimization for surface textures. *Tribology Letters* **49**: 179–191 (2013)

[52] Stachowiak G W. Friction and wear of polymers, ceramics and composites in biomedical applications. In *Advances in Composites Tribology*, *Volume 8, Composite Materials Series.* Friedrich K ed. Elsevier, 1993: 509–557.

[53] Bhushan B, Israelachvili J N, Landman U V. Nanotribology: Friction, wear and lubrication at the atomic scale. *Nature* **374**: 607–616 (1995)

[54] Karis T E. Nanotribology of thin film magnetic recording media. In *Nanotribology, Critical Assessment and Research Needs*. Hsu S M, Ying Z C ed. Dordrecht (The Netherlands): Kluwer Academic Publishers, 2003: 291–325.

[55] Hsu S M. Nanotribology: The link to macrotribology. In *Proc. Intern. Tribology Conf., AUSTRIB '02*, Perth, Australia, 2002: 9–15.

Gwidon STACHOWIAK. He is the Head of the Tribology Laboratory at the School of Mechanical and Civil Engineering, Curtin University in Western Australia. His current work is focused on the development of methods for the characterization of multiscale 3D surface topographies, prediction of osteoarthritis in knee joints based on X-ray images and tribocorrosion. He is the editor of Tribology and Practice book series published by John Wiley and member of the editorial boards of several tribological and bio-medical journals. He is also a member of several international committees including the Executive Committee of the International Energy Agency, Research and Development of Advanced Materials for Transportation. Professor Stachowiak has published extensively and wrote/contributed to several books. He is the leading author of the books "Engineering Tribology" and "Experimental Methods in Tribology" published by Elsevier. In 2014, he was awarded Tribology Gold Medal, the World's Highest Award in Tribology in recognition of his outstanding contribution to tribology while in 2012, he was awarded the title of Doctor Honoris Causa from the Ecole Centrale de Lyon, France.

Friction **5**(3): 248–262 (2017)
https://doi.org/10.1007/s40544-017-0181-7
ISSN 2223-7690
CN 10-1237/TH

REVIEW ARTICLE

Tribology of multilayer coatings for wear reduction: A review

Mahdi KHADEM[1,2], **Oleksiy V. PENKOV**[2], **Hee-Kyung YANG**[1], **Dae-Eun KIM**[1,2,*]

[1] *Department of Mechanical Engineering, Yonsei University, Seoul 03722, Republic of Korea*

[2] *Center for Nano-Wear, Yonsei University, Seoul 03722, Republic of Korea*

Received: 11 April 2017 / Revised: 09 June 2017 / Accepted: 01 July 2017

Abstract: Friction and wear phenomena encountered in mechanical systems with moving components are directly related to efficiency, reliability and life of the system. Hence, minimizing and controlling these phenomena to achieve the desired system performance is crucial. Among the numerous strategies developed for reducing friction and wear, coatings have been successfully utilized in various engineering applications to mitigate tribological problems. One of the benefits of coatings is that they may be fabricated using a variety of materials in several different forms and structures to satisfy the requirements of the operating conditions. Among many types, coatings that are comprised of a combination of materials in the form of a multilayer have been gaining much interest due to the added degree of freedom in tailoring the coating property. In this paper, the properties and development status of multilayer coating systems for tribological applications were reviewed with the aim to gain a better understanding regarding their advantages and limitations. Specifically, focus was given to Ti-based and Cr-based coatings since Ti and Cr were identified as important elements in multilayer coating applications. Emphasis was given to materials, design concepts, mechanical properties, deposition method, and friction and wear characteristics of these types of coatings.

Keywords: multilayer coating; friction; wear; tribology

1 Introduction

Friction and wear occur in all mechanical systems with moving components that are in contact with one another. These phenomena are largely responsible for the degradation of system reliability and performance due to excessive energy consumption and progressive loss of material. In this regard, considerable efforts have been devoted to develop effective methods to minimize and control friction and wear [1–3]. One of the methods is to use materials that possess low friction and wear properties in the form of a coating on sliding components. This strategy is highly preferred because fabrication of sliding components using these materials in the bulk form is not a cost effective or practical option for industrial applications. In addition, coatings can provide unique properties and multi-functionality, and therefore, offer superior tribological properties by incorporating different materials that would otherwise not be possible when using such materials in their bulk form [4].

Coatings may be fabricated in a variety of forms and structures using different kinds of materials. Regarding the number of layers, coatings may be single layer, bilayer or multilayer (more than two layers) [5]. As for the microstructure of the coatings, it may range from a simple single homogeneous structure to more complex systems, such as alloyed, composite and gradient structures. Among the coating design concepts, multilayer coatings are particularly attractive because they provide the means to tailor the surface properties with more freedom. For instance, the ability to control residual stress, hardness to elasticity modulus ratio and adhesion to the substrate through

* Corresponding author: Dae-Eun KIM, E-mail: kimde@yonsei.ac.kr

strategic stacking of coating layers is beneficial for tribological performance improvement [6]. In this regard, the interest in multilayer coatings as an effective solution for the reduction of friction and wear has been growing rapidly.

In this paper, advancements made in the fabrication and development of multilayer coating systems for friction and wear reduction were reviewed. The aim was to provide a comprehensive overview of multilayer coatings for tribological applications and gain a better understanding of their advantages and limitations. The type of materials used for such coatings along with their design concepts, deposition method, mechanical properties, and friction and wear characteristics were investigated. Specifically, Ti-based and Cr-based coatings were emphasized since Ti and Cr were identified as elements used widely in many multilayer coating applications. Nevertheless, other types of multilayer coatings were also reviewed for comparison.

2 Materials and design

In recent years, many new materials with superior mechanical properties have been synthesized and utilized for tribological applications. These materials have been effectively incorporated in fabrication of functional coatings to reduce friction and wear. Particularly, materials used for multilayer coatings may be categorized as ceramics, metals, solid lubricants, and diamond-like carbon (DLC) [7]. Ceramics (oxides, carbides, and nitrides of transition metals) are introduced to multilayer structures to provide sufficient hardness and wear resistance due to their strong interatomic bonding. Moreover, they have excellent adhesion to metal substrates and hard alloys. A classification of hard ceramic coatings for wear protection according to their bonding characteristics is presented in Fig. 1. The downside of hard ceramic coatings is their brittleness and relatively high coefficient of friction (COF) (0.3 to 0.8) [8]. Therefore, they have limitations in tribological applications that require inherently low COF. To overcome this issue, materials with inherently low COF (below 0.1), also known as solid lubricants (e.g., MoS_2, WS_2, PbO, and graphite), are preferable to be employed as the topmost layer [9, 10]. Such coatings, however, have relatively low hardness and wear resistance. On the other hand, DLC is a unique material that offers outstanding properties, such as extreme hardness, high ductility, chemical inertness, high wear resistance and low COF (0.1 to 0.2). These properties together with optical transparency and biocompatibility make DLC an excellent candidate for a broad range of tribological applications in various industries [11–14]. The structure, composition and

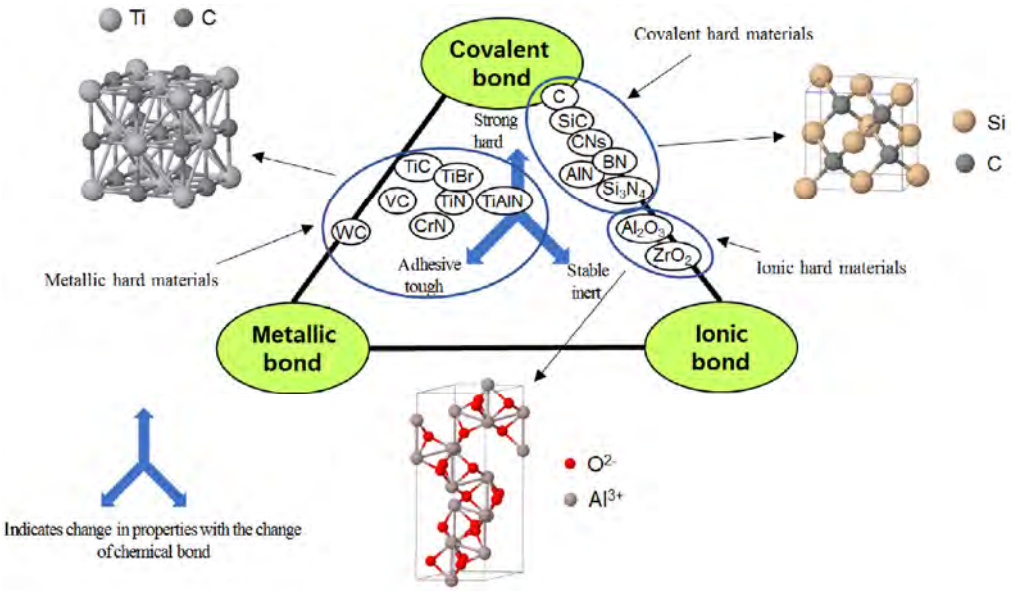

Fig. 1 Classification of different groups of hard ceramic materials on their bonding type and crystalline structure. Adopted from Ref. [6], with permission from Elsevier.

functionality of DLC coatings vary depending on the deposition method and condition. When DLC structure is sp^3-dominant, typically a higher hardness and lower can be expected. However, higher percentage of sp^3 also increases the internal stress levels that has negative effects on the coating wear resistance and limits the coating thickness. The main factors that limit the application of DLC in some cases are a high level of internal stress that limits its maximum thickness and relatively poor adhesion to metal substrates.

The coating materials discussed above certainly have merits for specific tribological applications. Nevertheless, their performance may be further enhanced by combining more than one material to produce a composite or a multilayer structure. In the material selection and design process of multilayer coatings, the basic idea is that the strength of one material should cover the weak property of the other so that superior tribological properties can be attained through the synergistic effects of these materials. For instance, a preferred multilayer coating design may be a combination of ceramics with good adhesion, solid lubricants with low COF and DLC with high hardness.

Multilayer coating design with respect to its function and structure considering the material selection of individual layers, interfacial layers and the layer structure regarding sequence and thickness allows for flexible tailoring of surface properties (e.g., hardness to elasticity modulus ratio) and performance (Fig. 2) [6]. Fundamental studies have shown that a proper ratio of hardness to elastic modulus is a major criterion that influences the abrasive wear characteristics of a coating [3, 6]. Besides hardness, high toughness should also be assured to prevent early coating failure due to crack propagation and fractures. Coatings with high hardness and toughness may be realized through combinations of metallic/metallic, metallic/covalent or metallic/ionic hard materials. Attaining high stability at the interfaces within the coating by the formation of nanocrystalline or multilayer films may help to overcome these problems since interfaces in multilayer coatings serve as sites of energy dissipation and crack deflection leading to higher overall toughness of the coating [6].

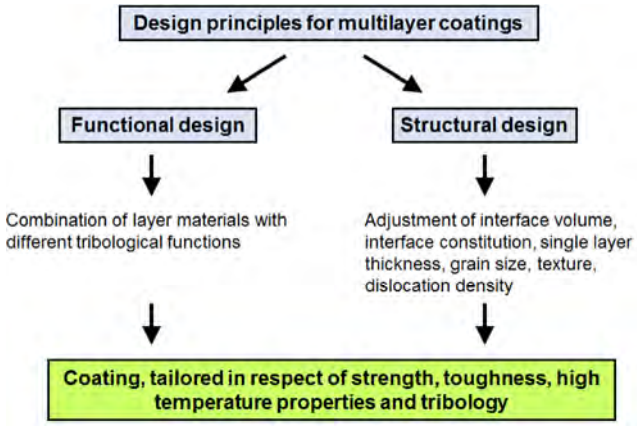

Fig. 2 Design principles of multilayer coatings. Adopted from Ref. [6], with permission from Elsevier.

When it comes to proper material selection, a variety of parameters such as hardness, elastic modulus, thermal expansion coefficient, crystal structure, stress discontinuity between layers and chemical compatibility between the coating and substrate should be considered. To optimize these parameters, one or more interlayers (also known as sublayers or adhesion layers) should be deposited on the substrate prior to deposition of the actual coating. Deposition of an interlayer significantly improves the compatibility between the substrate and coating, which in turn results in better tribological performance [15].

Studies have shown that poor compatibility, mainly regarding chemical bonding, often leads to poor adhesion between the coating and the substrate, which results in coating delamination as the coating thickness increases [16, 17]. In this regard, interlayers for adhesion improvement against the substrate are an essential component of multilayer coatings. Figure 3(a) presents a schematic of supporting layers, together with their role and functionality, in a typical multilayer coating system. The advantages derived by incorporation of the interlayer in designing multilayer coatings were demonstrated by Deng and Braun [16]. In their work, a DLC-based multilayer coating in a graded sequence was developed to optimize adhesion and ductility, which are crucial to attain good tribological performance of DLC coatings. A Ti layer was first deposited onto an AISI 420 steel substrate. Afterward, TiN, TiCN, and TiC were deposited in sequence to provide sufficient adhesion of DLC to the substrate and to

ensure smooth boundary transitions. TiN and TiC ("binary" hard materials) are hard coatings with well-known variations in stoichiometry and properties depending on the deposition parameters [18]. A quite similar strategy regarding materials and the deposition sequence was proposed by many other researchers (e.g., Fig. 3(b)) [7, 19–24]. Voevodin et al. [24] demonstrated that the drawbacks of DLC were more pronounced when applied to relatively soft substrates such as steel. They described the role of Ti and TiC layers prior to the deposition of DLC as follows: (i) formation of a load support and adhesion promoting underlayer with mechanical characteristics that vary gradually from the substrate to the DLC layer; (ii) separation of hard DLC layers with interlayers of softer material to reduce stresses and cracks; and (iii) use of crystalline interlayers that permit operation of dislocation sources for stress relaxation and deflection of cross-sectional cracks. Furthermore, by deposition of periodically stacked Ti and TiN layers, Bemporad et al. [25] overcame the problem of high internal stresses in TiN coatings responsible for limiting their maximum thickness. Considering that thickness plays a major role in tribological systems, obtaining large thickness coatings without compromising adhesion and toughness is highly desirable.

Advantages in tribological properties were also found in alloying binary components with metal/metalloid components (e.g., Ti(C,N)). Su and Kao [20] performed a wear optimization study with respect to the thickness and deposition sequence of Ti-, TiN-, and TiCN-based multilayer coatings. It was found that the coating with a total thickness of 7 μm and layer sequence of TiN/TiCN/TiN had the optimum wear resistance. However, it was found that the wear behavior was strongly dependent on the amount of alloying element [18]. Such investigations were extended to a wide variety of elements such as Cr, Zr, Al, Si, etc. [26–29]. Particularly, Cr-based coatings exhibited the potential to be a good candidate for tribological applications, and in some cases demonstrated better wear resistance than Ti-based coatings [18, 19].

3 Deposition methods

In this section, an overview of the deposition methods used for the fabrication of multilayer coatings along with their advantages and disadvantages is discussed. In the past decade, various techniques have been employed for depositing multilayer coatings. The deposition techniques that have been widely used for the fabrication of multilayer coatings may be divided into two broad categories: chemical vapor deposition (CVD) and physical vapor deposition (PVD). To determine the most suitable deposition technique for the fabrication of a multilayer coating for a given material, the effects of the deposition technique on the mechanical and tribological properties of each individual layer should be considered. Though both PVD and CVD techniques have been employed for multilayer coating deposition, the preference seems to be toward PVD techniques. In order to obtain multilayer coatings with good adhesion, mechanical and tribological properties using the CVD process, a relatively high substrate temperature is usually required (>200 ˚C). Therefore, the materials that can

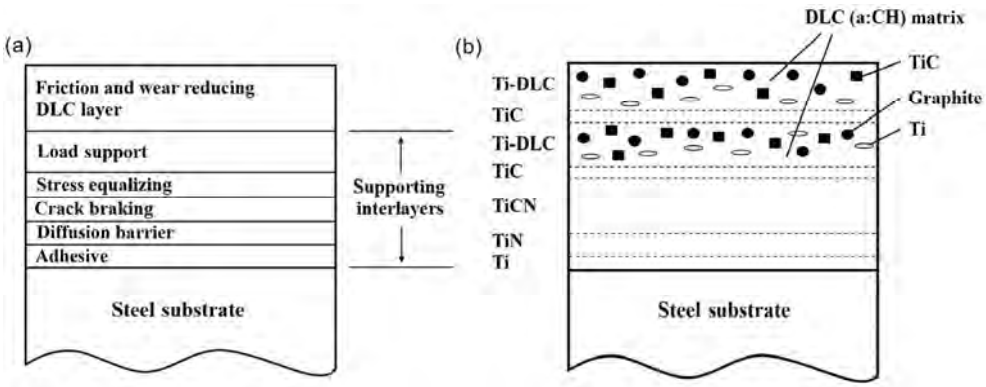

Fig. 3 (a) Schematic representation of individual layers and their functionality in a multilayer coating system. (b) Example of a functional multilayer coating developed for steel surface protection against wear. Adopted from Ref. [7], with permission from Elsevier.

be used as substrate in the CVD process are limited because their properties can be altered at elevated temperatures in some cases (e.g., polymers and some metals). There are also some studies have reported using a combination of both CVD and PVD processes to fabricate multilayer coatings [30, 31].

DLC, which is one of the most common materials used in multilayer coating systems, can be deposited using both CVD and PVD techniques. In the CVD process, methane (CH_4) gas is usually used as the carbon source that results in the incorporation of hydrogen atoms in the DLC structure during growth (known as hydrogenated DLC). Hydrogenated DLCs are rich in sp^2 hybrids with a relatively low percentage of sp^3 hybrids (less than 40%), which in turn leads to a lower hardness (lower than 20 GPa). Moreover, deposition of DLC coatings using the CVD method can result in a rough polycrystalline structure which lowers the transparency compared to that of DLCs with an amorphous structure. Therefore, DLC coatings fabricated by the CVD method are often not suitable for optical device applications [12, 32].

The drawbacks mentioned above regarding the CVD method can be overcome by using PVD-based deposition techniques. In PVD processes, the coating is deposited by condensation from a flux of neutral or ionized metal atoms in a vacuum environment [27]. Several PVD techniques can be used for deposition of hard coatings. Among them, ion plating and sputtering processes are the most common PVD processes for the deposition of DLC (or multilayers in general). Each of these PVD processes has its unique features regarding the type of evaporation of the metallic components and plasma conditions during the deposition process. In the case of ion plating, evaporation takes place by a high-energy arc that quickly moves over a spot on the metal surface to be evaporated. The plasma generated consists of highly ionized metal vapor [32]. In the case of sputtering, atoms are ejected from a target by the impact of inert gas ions or energetic neutral atoms. Ion plating generally requires a higher energy input than the PVD sputtering process. Table 1 summarizes the characteristics and parameters of PVD-based deposition techniques [27].

Ion plating-based techniques are typically used to deposit hard coatings because of the high ion energy and high ionization rate. However, the relatively large particles formed during the arc evaporation may lead to degradation of the coating properties [33]. Taking into account all the characteristics of the different PVD processes, PVD techniques based on sputtering is considered to be the suitable technique for multilayer coating fabrication [6].

Sputtering processes allow precise control of the deposition parameters. Therefore, properties of the coatings (e.g., residual stress, hardness, morphology, etc.) being deposited can be readily adjusted to obtain the optimum properties for tribological applications. Li et al. [34] studied the effect of controlling the deposition parameters on the properties of multilayer coatings. A DLC multilayer coating was produced by controlling the negative applied bias during deposition. It was shown that the residual stress significantly increased from approximately 2 to 7 GPa as the negative bias voltage increased from −70 to −200 V (Fig. 4(a)). The hardness also increased slightly from approximately 19 to 21 GPa (Fig. 4(b)). Thus, drastic variation in the residual stress and hardness could be achieved by tuning the negative bias voltage during the deposition process.

Table 1 Typical characteristics and parameters of PVD-based deposition techniques. Reprinted from Ref. [27], with permission from Elsevier.

Parameters	Processes			
	Magnetron sputtering	Anodic arc ion plating	Electron beam ion plating	Cathodic arc ion plating
Evaporation tool	Sputter effect	Electron beam	Electron beam	Thermal arc
Phase transformation	Solid-vapor	Solid-vapor	Liquid-vapor	Solid-vapor
Target geometry	Flexible	Limited	Limited	Flexible
Target ionization (%)	1–5	5–40	< 1	50–100
Additional ionization	Aimed	Unusual	Aimed	Not necessary
Inert gasses necessary	Yes	No	Variable	No
Reactive deposition	Yes	Yes	Yes	Yes

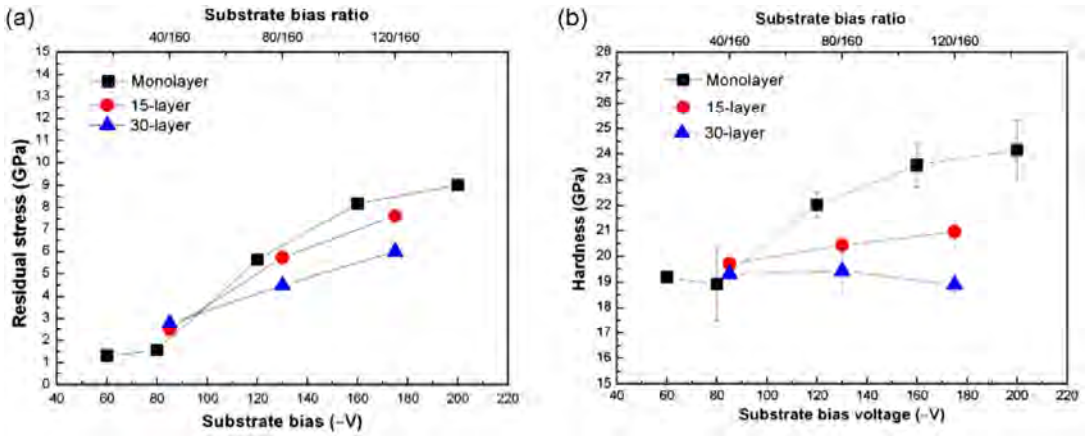

Fig. 4 (a) Residual stress and (b) hardness of coatings as a function of substrate bias and substrate bias ratio. Reprinted from Ref. [34], with permission from Elsevier.

Paulitsch et al. [35] showed that power source used for deposition can greatly influence the tribologial properties of the coatings. As given in Table 1, magnetron sputtering has a low ionization degree that often results in the formation of porous and underdense films with a high defect density if deposited at room temperature [36]. To overcome this problem, the conventional DC magnetron sputtering process was combined with high power impulse magnetron sputtering (HIPIMS) to deposit a CrN/TiN multilayer coating. HIPIMS allows a much greater metal-ion and plasma density, and thus, a higher ion to neutral sputtered species ratio due to the high-power dissipation can be delivered to the target (ionization rate above 40%) [37]. As a result, the HIPIMS process is beneficial for tailoring the morphology and structure of the coating. Experimental results demonstrated that the COF could be lowered significantly from 0.25 to 0.05 when an additional HIPIMS cathode equipped with a Cr or Ti target material was added to the process. Wang et al. [38] investigated the correlations between target power and Ar gas pressure on the characteristics W-Cu multilayer coatings. It was shown that a more dense coating could be deposited at a low Ar pressure and high power. Moreover, strong coating adhesion correlated well with dense layers and fine grain structure.

All the studies mentioned above showed that sputtering parameters significantly affect the structural, mechanical, and thus, the tribological properties of the coatings. In this regard, considering the desired material properties and target application is a major step prior to deciding the deposition method.

4 Friction and wear characteristics

The friction and wear characteristics, together with the mechanical properties of multilayer coatings fabricated using a wide range of materials were investigated. Considering the types of multilayer coatings with respect to the main element used in the coatings, the coatings were divided into three groups, namely Ti-based, Cr-based, and other materials. Ti and Cr are commonly used interlayers utilized as adhesion layers prior to deposition of the main multilayer coating on metal substrates. Ti and Cr are excellent adhesion layers because of their high binding energy that can readily form oxides, nitrides or carbides with adjacent layers. However, their effect on the performance and tribological characteristics of multilayer coatings strongly depends on their structure (e.g., polycrystalline or amorphous). Each structure can have its advantages or disadvantages, and therefore, should be decided carefully depending on the design strategy of the multilayer coating. For example, in a previous research where design of a multilayer coating with high degree of elasticity was desired, it was found that amorphous materials exhibited higher elasticity compared with their polycrystalline counterparts [3].

Despite the large number of combination of materials reported in the literature for multilayer coatings, they mostly follow a logical and established principle that

imposes a low friction and hard material as the top surface layer (e.g., DLC, WS_2, etc.). While the bottom layers should provide sufficient support in terms of adhesion, hardness, ductility and elasticity to increase the overall coating stability, the upper layer should have low friction properties to minimize the generation of frictional energy that can be used to damage the surface layer. However, even after removal of the upper layers, the multilayer coating can still maintain its anti-wear properties because periodical alternation of such materials allows effective prevention of crack deflection and propagation, which is one of the major failure modes of coatings [20, 39]. Considering these factors, a desirable multilayer structure would be a coating that provides low friction at the surface with high shear strength and adequate elasticity within the coating layers [3].

4.1 Ti-based multilayer coatings

As mentioned previously, enormous attention has been devoted to Ti and Ti-alloys as potential candidates to be used in multilayer coatings for tribological applications. In one of the earlier works, Deng and Braun [16] fabricated a multilayer system with a Ti/TiN/TiCN/TiC/DLC sequence using magnetron sputtering to improve the friction and wear properties of AISI 420 steel. A maximum hardness of 39 GPa and a minimum stable COF of ~0.25 could be achieved (counterpart: 6 mm Al_2O_3 ceramic ball; load: 100 gf). Shortly thereafter, Voevodin et al. [24] attempted a more complex multilayer structure: $(Ti/TiC/DLC/(Ti/DLC)_{\times 20})$ and $(Ti/TiC/DLC/(TiC/DLC)_{\times 20})$. The TiC/DLC combination showed a higher hardness (30 GPa) than Ti/DLC (20 GPa) and a wear rate of about 10^{-10} $mm^3/(N{\cdot}mm)$ could be obtained. The minimum COF values against sapphire and steel counterparts (10 mm; load: 10 N) were approximately 0.09 and 0.2, respectively. Ogletree and Monterio [39] demonstrated the effectiveness of DLC/TiC multilayer coating to reduce the friction of AISI 01 tool steel. The number and thickness of layers within the films were varied while the total thickness was made to be approximately constant. A minimum COF of ~0.15 was achieved (counterpart: 6.25 mm Al_2O_3 ceramic ball; load: 2 and 5 N). Su and Kao [20] performed an optimization study on multilayers with TiN/Ti/TiN and TiN/TiCN/TiN sequences. Experimental results indicated that a coating with a total thickness of 7 μm and layer sequence of TiN/TiCN/TiN exhibited good wear resistance. The TiN/Ti/TiN sequence, despite a higher hardness value, showed a lower wear resistance. A minimum COF of 0.1 in the lubrication condition was achieved (counterpart: steel ball). The potential of TiN/TiCN sequence for friction and wear reduction was further investigated by Zheng et al. [40]. A maximum hardness and minimum wear rate of 34 GPa and 1.15×10^{-9} $mm^3/(N{\cdot}mm)$, respectively, were obtained. The coating showed different COF values of 0.12 and 0.65 when slid against 3 mm Si_3N_4 ceramic ball and steel ball counterparts (load: 1 N), respectively. At elevated temperature (550 °C), Bao et al. [22] studied the tribological behavior of TiCN/TiC/TiN multilayer coatings deposited by CVD on high-speed steel substrates. The coating showed a relatively high COF (0.6) and wear rate (7.3×10^{-9} $mm^3/(N{\cdot}mm)$) at 550 °C against a 5 mm WC ceramic ball under 20 N in comparison to the COF and wear rate obtained at room temperature (0.5 and $5.3{\times}10^{-10}$ $mm^3/(N{\cdot}mm)$, respectively).

Cheng et al. [33] performed a comprehensive study on the mechanical and tribological behavior of TiN/Ti multilayer coatings. Multilayers with a fixed TiN layer thickness and different Ti layer thicknesses were deposited by using a filtered arc deposition technique. The results revealed that increasing the Ti layer thickness from 0 to 150 nm lowered the hardness (from 32 to 16 GPa) and wear resistance, significantly. A minimum wear rate and COF of ~$2{\times}10^{-9}$ $mm^3/(N{\cdot}mm)$ and ~0.6 (counterpart: 6 mm Al_2O_3 ceramic ball; load: 1 N), respectively, were achieved. By adding a DLC layer on the top and reversing the deposition sequence of TiN and Ti (Ti/TiN/DLC), Liu et al. [41] and Kot et al. [42] tried to improve the friction and wear behavior of steel substrates. A minimum wear rate of approximately 1.2×10^{-9} $mm^3/(N{\cdot}mm)$ under 5 N was obtained [42]. The multilayer coatings showed maximum hardness values of 32 GPa and 20 GPa and the minimum COF values of 0.25 and 0.15, respectively (counterparts: 4mm steel ball and 6 mm Al_2O_3 ceramic ball). Al-Bukhaiti et al. [43] assessed the effects of normal load and sliding speed on the friction and wear behavior of $[Ti/TiAlN/TiAlCN]_5$

multilayer coatings with addition of Al deposited on AISI H11 steel using magnetron sputtering. The coatings showed a maximum hardness of 20 GPa. The lowest COF and wear rate were 0.25 and ~3 × 10^{-9} $mm^3/(N·mm)$, respectively (counterpart: 6 mm Al_2O_3 ceramic ball, load: 2-10 N). Chu and Shen [44] investigated the tribological behavior of TiN/TiBN multilayer films with different bilayer thicknesses (from 1.4 to 9.7 nm) deposited on Si and AISI M42 tool steel. The mechanical and tribological properties of multilayer coatings were found to be closely related to the bilayer thickness. For the bilayer thickness of 1.8 nm, a maximum hardness of ~29.5 GPa was achieved and a minimum COF of 0.5 was obtained (counterpart: WC ceramic ball; load: 5 N). Zhang et al. [45] deposited Ti(C,N) multilayer coatings by magnetron sputtering on Si and assessed their hardness and COF with respect to the current fed through the graphite target. As the current increased from 0.3 to 1.8 A, the hardness increased initially (maximum hardness of ~45 GPa at 0.9 A) and then decreased gradually. As a result, the COF monotonically decreased down to a constant value of approximately 0.2 (counterpart: WC ceramic ball; load: 6 N). Liu et al. [46] investigated the tribological and mechanical properties of TiN/CN_x multilayer coatings deposited by magnetron sputtering. The hardness of the coatings varied from 12.5 to 31 GPa with respect to the bilayer thickness (from 4.2 to 40.3 nm). The multilayer coating with a bilayer thickness of 4.2 nm showed the highest hardness and the lowest COF and wear rate (0.12 and 7 × 10^{-11} $mm^3/(N·mm)$, respectively) against a 3 mm Si_3N_4 ball counterpart under 5 N applied load. Kumar et al. [47] fabricated and compared various TiC-metal carbide-based multilayers (ZrC, CrC, and WC) deposited on 316LN steel by magnetron sputtering. Experimental results revealed the poor crystalline nature of the TiC/CrC multilayer, which was postulated to be the reason for the relatively low hardness and wear resistance. The TiC/ZrC multilayer showed the highest hardness (~30 GPa) and the best tribological performance among the coatings with a minimum COF of 0.43 and a wear rate of 2.1 × 10^{-11} $mm^3/(N·mm)$ (counterpart: 6 mm steel ball, load: 1 N).

Multilayer coatings consisting of both Ti-based and Cr-based nitrides were also developed [35]. This study showed that the CrN/TiN multilayer coatings were effective in reducing the COF of bare steel from 0.7 to 0.35 (H–25 GPa, modulus–375 GPa) (Fig. 5(a)) by decreasing the bilayer thickness from 7.8 to 6.4 nm while keeping the CrN layer thickness constant at 3.2 nm. It should be noted that a further reduction of the COF at room temperature dry sliding condition to approximately 0.25 or 0.05 (counterpart: 6 mm Al_2O_3 ceramic ball; load: 1 N) could be obtained when Ti and Cr were deposited by an HIPIMS cathode (Fig. 5(b)).

4.2 Cr-based multilayer coatings

Numerous multilayer coatings based on Cr have also been developed. Yang and Teer [18] demonstrated

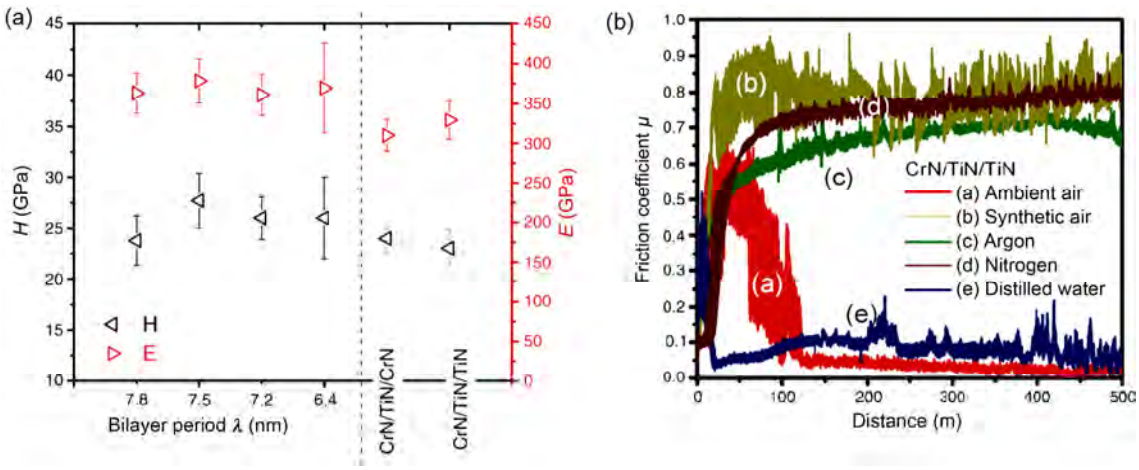

Fig. 5 (a) Hardness (*H*) and Young's modulus (*E*) of multilayer coatings with respect to bilayer thickness (right side of the dash-line: multilayers with additional CrN and TiN layer deposited by HIPIMS) and (b) COF of coatings obtained in different atmospheres. Reprinted from Ref. [35], with permission from Elsevier.

the superiority of C/Cr multilayer coated drills to those of commercial TiN coated drills. C/Cr multilayer coatings showed a wear rate of 2×10^{-11} mm^3/(N·mm), which was three times lower than that of the TiN coated drills, and a minimum COF of 0.05 was achieved (counterpart: 5 mm WC ceramic ball; load: 10–80 N). Gilewicz et al. [48, 49] used a cathodic arc evaporation method to deposit a Cr/CrCN multilayer on steel. A 0.1 μm Cr layer was used as a sublayer. The wear tests against 10 mm Al_2O_3 ceramic balls revealed that the wear resistance of the multilayer coating was lower than that of Cr or CrCN single layers. A minimum COF of ~0.4 was achieved (load: 30 N). Beliardouh et al. [50] fabricated different multilayers composed of Cr, CrN, and CrAlN on AISI 4140 steel substrates using radio frequency (RF) magnetron sputtering technique. The multilayer with the sequence of [Cr (45 nm)/CrN (106 nm)/CrAlN (150 nm)] showed the highest hardness (32 GPa) and wear resistance. A minimum COF of 0.4 against a 6 mm Al_2O_3 ceramic ball under 1 N was achieved.

Vyas et al. [51] performed a fundamental study on the frictional behavior of CrN/CN_x nano-scale multilayer coatings deposited on Si and high speed steel (HSS) by magnetron sputtering. The effects of negative substrate bias voltage and bilayer thickness on the structural and frictional properties were assessed. A maximum hardness of ~36 GPa and a minimum COF of ~0.4 at 140 V were achieved (load: 10 N). In another study performed by Bayon et al. [52], the tribo-corrosion property of Cr/CrN multilayer coatings deposited by the cathodic arc method on steel and silicon substrates was investigated. A maximum hardness of ~29 GPa and a minimum COF of ~0.3 was achieved (counterpart: 4 mm Si_3N_4 ball). A more complex system was synthesized by Shi et al. [53] by nitriding of Cr, Ti, and Al (CrN/TiN/CrN/AlN) on a Mg alloy substrate using a magnetron sputtering ion plating system at different bias voltages (ranging from –40 to –90 V). The coating deposited at –50 V showed the lowest COF of ~0.25 (counterpart: Si_3N_4 ball). Gilewicz and Warcholinski [54] improved the tribological properties of a HS6-5-2 steel substrate using a Mo_2N/CrN multilayer coating. The multilayer coating showed a hardness above 25 GPa and a lower COF and wear rate than those of the single layer CrN coating. A minimum COF and wear rate of 0.4 and 9×10^{-11} mm^3/(N·mm) (counterpart: 10 mm Al_2O_3 ball; load: 30 N) were achieved, respectively.

4.3 Other materials

A variety of materials other than Ti-based and Cr-based materials have been employed to design and fabricate multilayer coatings. As for metal/metal-based multilayer coatings, Ghosh et al. [55] deposited [Ni (4.5 nm/Cu (2, 4, and 8 nm)] multilayer coatings on a stainless steel (AISI SS 304) substrate. The multilayer coating with the minimum Cu thickness showed the lowest COF and wear rate of ~0.4 and 1.3×10^{-7} mm^3/(N·mm), respectively (counterpart: 6 mm WC ceramic ball; load: 3–11 N). Detailed investigation of the wear scar morphology, as well as wear rate measurement, revealed the significant dependence of the wear mechanism to the applied normal load. At low loads, the H/E ratio and residual stress governed the wear rate, and the principle wear mode was abrasive. At moderate loads, the role of residual stress became insignificant while wear was governed by the H/E ratio and plastic deformation. However, at higher loads, plastic deformation played a major role in dictating the wear behavior. Miki et al. [30] fabricated DLC/W-based multilayer coatings using RF CVD and magnetron sputtering on Si and studied their frictional behavior under N_2 atmosphere. A minimum COF of ~0.1 was achieved (counterpart: 6 mm steel ball; load: 1 N).

Gayathri et al. [56] performed a comprehensive study on the tribological properties of DLC in combination with various transition metals (Cr, Ag, Ti, and Ni) in the form of periodical multilayers deposited by a pulsed laser. DLC/Ni and DLC/Ti multilayer coatings showed the lowest COF of 0.1 and the highest wear resistance among the coated specimens. However, the hardness values turned out to be quite similar (9–11 GPa) for all the coated specimens. Detailed analysis revealed the formation of a tribofilm, which was believed to be responsible for the relatively low wear in the case of DLC/Ni and DLC/Ti multilayer coatings (counterpart: 6 mm steel ball; load: 1 N). Kilman et al. [31] utilized Al in hydrogenated amorphous carbon (a-C:H:Al) to fabricate a multilayer coating on AISI M2 high-speed steel. It was found that even

though the inclusion of Al lowered the mean hardness value compared to pure a-C:H coatings, the frictional behavior was improved. The COF decreased from approximately 0.2 to 0.1 when slid against a 6 mm steel ball under an applied load of 10 N.

Liu et al. [57] deposited carbon nitride (CN_x/CN_x) multilayers with sequential sp^3-rich (54% sp^3) and sp^2-rich (26% sp^3) layers on Si using magnetron sputtering technique. The multilayer coating showed a lower compressive stress (approximately 60% lower) and a higher hardness than the individual layers. A minimum COF of ~0.1 and maximum hardness of ~30 GPa could be achieved. In a more comprehensive study, a similar concept was applied to DLC multilayer coatings consisting of sp^2-rich (soft DLC) and sp^3-rich (hard DLC) phases with different thickness ratios (hard DLC/soft DLC: 2:1, 1:1, 1:2) [58]. The coatings were deposited using the filtered cathodic vacuum arc (FCVA) method on Si and Ti-6Al-4V alloy substrates. The hardness of the coatings varied from ~14 to ~24 GPa depending on the modulation ratio. It was found that the multilayer DLC coatings with different modulation ratios could effectively decrease the residual stress of monolithic hard DLC coatings (Fig. 6). The experimental results showed that the multilayer coating with 1:1 thickness ratio resulted in the best wear resistance due to a balance between hardness and residual stress.

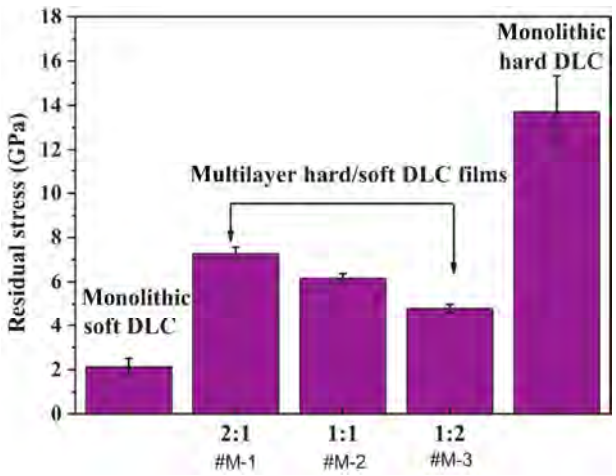

Fig. 6 Residual stress for the monolithic DLC and multilayer DLC coatings with respect to modulation ratios. (a) #M-1 (modulation ratio is 2:1), (b) #M-2 (modulation ratio is 1:1), (c) #M-3 (modulation ratio is 1:2). Reprinted from Ref. [58], with permission from Elsevier.

Bewilgua et al. [59] investigated the tribological properties of a carbon-based multilayer coating (a-C:H/a-C:H:Si:O and a-C:H/a-C:H:Si) fabricated by plasma assisted chemical vapor deposition (PACVD) using methane (CH_4), hexamethyldisiloxane (HMDSO) and tetramethylsilane (TMS) as precursors. Using this combination, a maximum hardness of approximately 23 GPa and a minimum COF of 0.1 was achieved (counterpart: steel ball). Liu et al. [60] developed a multilayer structure composed of WC and C periodic coatings fabricated by sputtering technique. A maximum hardness of ~14 GPa was achieved. The coatings were prepared with two different top layers (WC and C) and sliding tests against a steel counterpart were performed. The multilayer coating with WC top layer showed a higher COF and wear rate when compared to those of coatings with C top layer. A minimum COF of ~0.1 was achieved (load: 0.2–0.9 N). Braic et al. [61] prepared a TiSiC/NiC multilayer coating by a cathodic arc in a CH_4 atmosphere and studied the effects of bilayer thickness ranging from 2.5 to 19.8 nm on their friction and wear behavior. The best tribological characteristics were obtained for the multilayer coating with a bilayer thickness of 4.8 nm. The coatings showed hardness values ranging from 19–26 GPa and the minimum COF and wear rates were 0.16 and 2.9×10^{-7} ($mm^3/(N{\cdot}mm)$), respectively (counterpart: 6 mm sapphire ball; load: 3 N). Braic et al. [62] also investigated the structural and tribological properties of Zr/ZrCN multilayer coatings (bilayer thickness: 4.4 to 70 nm) deposited on M2 steel and Si substrates using cathodic arc technique. The coatings showed a maximum hardness of ~28 GPa. Multilayer coatings with a bilayer thickness of 13 nm exhibited a minimum COF and wear rate of 0.2 and $2{\times}10^{-9}$ $mm^3/(N{\cdot}mm)$, respectively (counterpart: 6 mm sapphire ball; load: 3 N). Ge et al. [63] employed a different strategy using VC/Ni multilayer coatings to improve the wear resistance of M2 tool steel. The coatings exhibited wear rates in the order of 10^{-9} $mm^3/(N{\cdot}mm)$, which was one order of magnitude lower than that of bare tool steel. A maximum hardness of ~18 GPa and a minimum COF of ~0.6 was achieved (counterpart: 6 mm Al_2O_3 ball; load: 1 N).

Penkov et al. [3] reported on the development of a novel functional coating that was comprised of

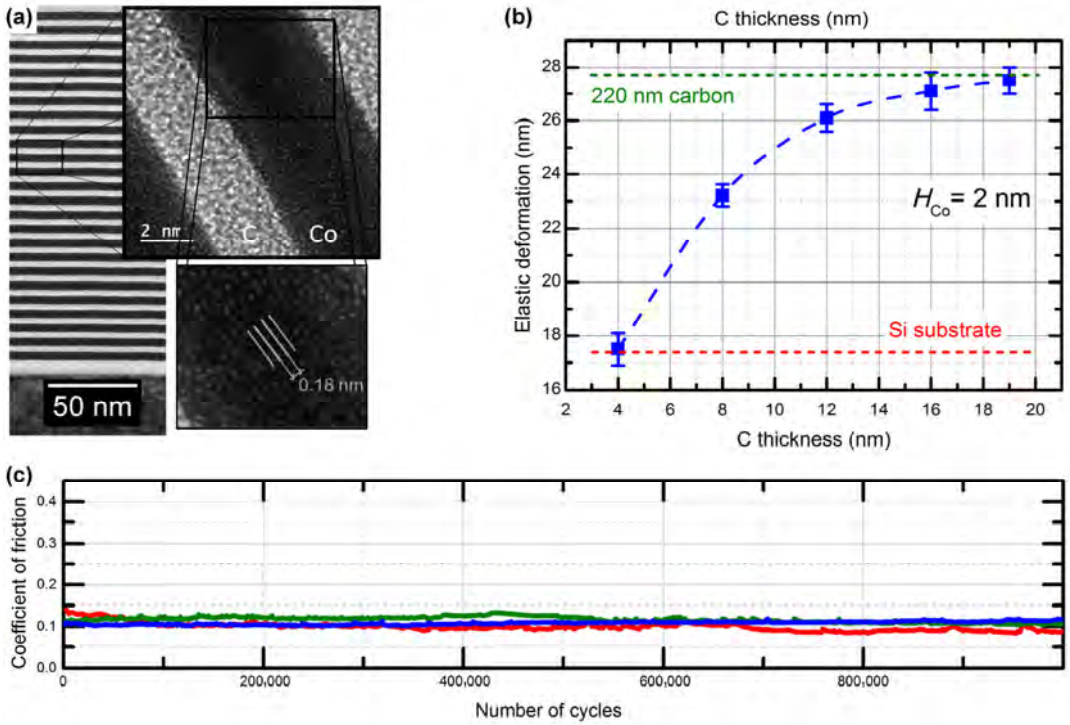

Fig. 7 (a) Cross-sectional TEM images cobalt/carbon multilayer coating. (b) Elastic deformation of the multilayer coatings as a function of the carbon thickness for a fixed cobalt thickness of 2 nm. (c) Friction coefficient as a function of the sliding distance for three repeated tests. Reprinted from Ref. [27], with permission from ACS publication.

alternating nanolayers of amorphous carbon and cobalt that exhibited extraordinarily high micro- and macro-scale wear resistance in ordinary atmospheric condition. Multilayers with various thicknesses of amorphous carbon (4, 8, 12, 16, and 19 nm) and cobalt (1.5 to 5.6 nm) were deposited to identify the optimum structure to obtain the minimum COF and wear rate (Fig. 7(a)). Co was selected as the pair material for amorphous carbon based on the following criteria: limited intermixing with carbon, formation of an amorphous structure, the ability to form a nanometer-thick continuous layer by sputtering, and a high hardness and Young's modulus [64]. A minimum wear rate of 3×10^{-13} mm^3/(N·mm) was obtained that was 8–10-fold lower than that of the lowest previously reported value (counterpart: 1 mm steel ball; load: 3 gf). Such a low wear rate could be achieved because of the unique structure of the multilayer coatings that simultaneously provided high elasticity and ultrahigh shear strength (Fig. 7(b)). The coatings showed a COF of 0.1, which remained stable for more than one million cycles (Fig. 7(c)).

As for a polymer-based multilayer coating, Ou et al. [65] successfully fabricated a polydopamine (PDA)/grapheme oxide (GO) multilayer coating on a Si substrate using a layer by layer self-assembling process. The experimental results showed that the coatings improved the frictional behavior (COF: ~0.18) significantly when compared with the bare substrate (counterpart: 3 mm steel ball; load: 0.5–1 N). Besides this work, multilayer coatings based on polymeric materials could not be found.

5 Summary

The status and properties of multilayer coating systems for tribological applications were reviewed. Special attention was given to materials, design concepts, mechanical properties, deposition method, and friction and wear characteristics of these types of coatings. Based on the extensive literature surveyed, it may be stated that multilayer coatings offer the means to tailor the surface properties of mechanical components to attain the properties in demand. The primary design

parameters for multilayer coatings are material selection, number of layers, thickness of individual layers, interlayer type and microstructures of the layers [6].

It should be noted that classification of the tribological properties of different multilayer coating systems is not straightforward due to their system and material dependencies. Friction and wear are not only dependent on the materials, but also on the deposition method and parameters together with the properties of the counter body [66]. Given the wide spectrum of materials and methods used to fabricate multilayer coatings for tribological applications, the most relevant works may be summarized as shown in Table 2.

By selecting the proper combination of materials and design strategy, multilayer coatings can be adapted to reduce friction and increase wear resistance of mechanical components in a variety of tribological applications. Because of high level of flexibility in multilayer coating systems with respect to design variables, there is still much room for further optimization of these types of coatings [67]. With further effort in identifying the effects of numerous process parameters in the fabrication and design of multilayer coatings on their tribological properties, better coating systems with superior functionality are expected to be achieved.

References

[1] Lin L, Kim D E, Kim W K, Jun S C. Friction and wear characteristics of multi-layer graphene films investigated by atomic force microscopy. *Surface and Coatings Technology* **205**: 4864–4869 (2011)

[2] Penkov O V, Kim H J, Kim D E. Tribology of grapheme: A review. *International Journal of Precision Engineering and Manufacturing (IJPEM)* **15**: 577–585 (2014)

[3] Penkov O V, Devizenko A Y, Khadem M, Zubarev E N, Kondratenko V V, Kim D E. Toward zero micro/macro-scale wear using periodic nano-layered coatings. *ACS Applied Materials and Interfaces* **7**: 18136–18144 (2015)

[4] Kot M, Major L, Lackner J, Rakowski W. Carbon based coatings with improved fracture and wear resistance. *Innovations in Biomedical Engineering* **526**: 40–48 (2016)

[5] Penkov O V, Bugayev Y A, Zhuravel I, Kondratenko V V,

Table 2 Friction and wear properties of selected multilayer coatings.

Materials/Ref.	Deposition method	Thickness (μm)	Load (N)	COF	Wear Rate ($mm^3/(N·mm)$)
$Ti/TiC/DLC/(TiC/DLC)_{\times 20}$ [24]	Magnetron sputtering	3–4	10	0.25	10^{-10}
$(TiN/TiCN)_{\times 10}$ [40]	Magnetron sputtering	~10	1	0.12	1.15×10^{-9}
TiCN/TiC/TiN [22]	CVD	5–6	20	0.5	5.3×10^{-10}
Ti/TiN/(TiN/Ti) [33]	Filtered arc	3	1	0.6	2×10^{-9}
Ti/TiN/DLC [42]	Magnetron sputtering	Variable	5	0.15	1.2×10^{-9}
$[Ti/TiAlN/TiAlCN]_{\times 5}$ [43]	Magnetron sputtering	2.8	2–10	0.25	3×10^{-9}
$(TiN/CN_x)_{\times 12–200}$ [46]	Magnetron sputtering	0.5	5	0.5	7×10^{-11}
$(TiC/ZrC)_{\times 6}$ [47]	Magnetron sputtering	2	1	0.43	2.1×10^{-11}
Carbon/Cr [18]	Magnetron sputtering	Variable	10–80	0.05	2×10^{-11}
$(Mo_2N/CrN)_{\times 6}$ [54]	Cathodic arc	~3	30	0.4	9×10^{-11}
Ni/Cu [55]	Electrodeposition	10	3–11	0.4	1.3×10^{-7}
TiSiC/NiC [61]	Cathodic arc	1.1	3	0.16	2.9×10^{-7}
Zr/ZrCN [62]	Cathodic arc	3.2	3	0.2	2×10^{-9}
VC/Ni [63]	Magnetron sputtering	1.5–2	1	0.6	10^{-9}
Co/C [3]	Magnetron sputtering	0.2	0.03	0.1	3×10^{-13}

Amanov A, Kim D E. Friction and wear characteristics of c/si bi-layer coatings deposited on silicon substrate by dc magnetron sputtering. *Tribology Letter* **48**: 123–131 (2012)

[6] Holleck H, Schier V. Multilayer PVD coatings for wear protection. *Surface and Coating Technology* **76-77**: 328–336 (1995)

[7] Voevodin A A, Schneider J M, Rebholz C, Matthews A. Multilayer composite ceramic-metal-DLC coatings for sliding wear applications. *Tribology International* **29**: 559–570 (1996)

[8] Habing K H, MeierKocker G. Possibilities of model wear testing for preselection of hard coatings for cutting tools. *Surface and Coating Technology* **62**: 428–437 (1993)

[9] Watanabe S, Noshiro S M. Tribological characteristics of WS_2/MoS_2 solid lubricating multilayer films. *Surface and Coating Technology* **183**: 347–351 (2004)

[10] Kim H J, Shin D G, Kim D E. Frictional behavior between silicon and steel coated with graphene oxide in dry sliding and water lubrication conditions. *International Journal of Precision Engineering and Manufacturing-Green Technology (IJPEM-GT)* **3**: 91–97 (2016)

[11] Penkov O V, Pukha V E, Starikova S L, Khadem M, Starikov V V, Maleev M V, Kim D E. Highly wear-resistant and biocompatible carbon nanocomposite coatings for dental implants. *Biomaterials* **102**: 130–136 (2016)

[12] Khadem M, Penkov O V, Pukha V E, Maleev M V, Kim D E. Ultra-thin nano-patterned wear-protective diamond-like carbon coatings deposited on glass using a C_{60} ion beam. *Carbon* **80**: 534–543 (2014)

[13] Fan X, Xue Q, Wang L. Carbon-based solid-liquid lubricating coatings for space applications—A review. *Friction* **3**: 191–207 (2015)

[14] Khun N W, Liu E. Tribological properties of platinum/ruthenium/nitrogen doped diamond-like carbon thin films deposited with different negative substrate biases. *Friction* **2**: 317–329 (2014)

[15] Subramanian C, Strafford K. Review of multicomponent and multilayer coatings for tribological applications. *Wear* **165**: 85–95 (1993)

[16] Deng J, Braun M. DLC multilayer coatings for wear protection. *Diamond and Related Materials* **4**: 936–943 (1995)

[17] Wiklund U, Gunnars J, Hogmark S. Influence of residual stresses on fracture and delamination of thin hard coatings. *Wear* **232**: 262–269 (1999)

[18] Yang S, Teer D. Investigation of sputtered carbon and carbon/chromium multi-layered coatings. *Surface and Coating Technology* **131**: 412–416 (2000)

[19] Su Y L, Yao S H, Leu Z L, Wei C S, Wu C T. Comparison of tribological behavior of three films-TiN, TiCN and CrN-grown by physical vapor deposition. *Wear* **213**: 165–174 (1997).

[20] Su Y, Kao W. Optimum multilayer TiN-TiCN coatings for wear resistance and actual application. *Wear* **223**: 119–130 (1998).

[21] Huang R, Chan C, Lee C H, Gong J, Lai K H, Lee S H, Li K Y, Wen L S, Sun C. Wear-resistant multilayered diamond-like carbon coating prepared by pulse biased arc ion plating. *Diamond and Related Materials* **10**: 1850–1854 (2001).

[22] Bao M. Xu H, Zhang H, Liu X, Tian L, Zeng Z, Song Y. Tribological behavior at elevated temperature of multilayer TiCN/TiC/TiN hard coatings produced by chemical vapor deposition. *Thin Solid Film* **520**: 833–836 (2011)

[23] Liu H, Jiang Y, Zhou R, Tang B. Wear behaviour and rolling contact fatigue life of Ti/TiN/DLC multilayer films fabricated on bearing steel by PIIID. *Vacuum* **86**: 848–853 (2012)

[24] Voevodin A, Walck S, Zabinski J. Architecture of multilayer nanocomposite coatings with super-hard diamond-like carbon layers for wear protection at high contact loads. *Wear* **203**–**204**: 516–527 (1997)

[25] Bemporad E, Sebastiani M, Pecchio C, De Rossi S. High thickness Ti/TiN multilayer thin coatings for wear resistant applications. *Surface and Coatings Technology* **201**: 2155–2165 (2006)

[26] Dekempeneer E, Van Acker K, Vercammen K, Meneve J, Neerinck D, Eufinger S, Pappaert W, Sercu M, Smeets J. Abrasion resistant low friction diamond-like multilayers. *Surface and Coatings Technology* **142**–**144**: 669–673 (2001)

[27] Paldey S, Deevi S. Single layer and multilayer wear resistant coatings of (Ti,Al)N: A review. *Materials Science and Engineering A* **342**: 58–79 (2003)

[28] Guan X, Wang Y, Zhang G, Jiang X, Wang L, Xue Q. Microstructures and properties of Zr/CrN multilayer coatings fabricated by multi-arc ion plating. *Tribology International* **106**: 78–87 (2017)

[29] Shugurov A R, Panin A V, Evtushenko O V, Sergeev V P, Martynyak R M. Effect of the number of layers in Zr-Y-O/Si-Al-N multilayer coatings on their mechanical properties and wear resistance. *Journal of Friction and Wear* **35**: 426–433 (2014)

[30] Miki H, Takeno T, Takagi T. Tribological properties of multilayer DLC/W-DLC films on Si. *Thin Solid Films* **516**: 5414–5418 (2008)

[31] Kilman L, Jaoul C, Colas M, Tristant P, Dublanche-Tixier C, Laborde E, Meunier F, Jarry O. Friction and wear performance of multilayered a-C:H:Al coatings. *Surface and Coatings Technology* **284**: 159–165 (2015)

[32] Robertson J. Diamond-like amorphous carbon. *Materials Science and Engineering* **37**: 129–281 (2002)

[33] Cheng Y, Browne T, Heckerman B, Bowman C, Gorokhovsky V, Meletis E I. Mechanical and tribological properties of TiN/Ti multilayer coating. *Surface Coatings Technology* 205: 146–151 (2010)

[34] Li F, Zhang S, Kong J, Zhang Y, Zhang W. Multilayer DLC coatings via alternating bias during magnetron sputtering. *Thin Solid Films* **519**: 4910–4916 (2011)

[35] Paulitsch J, Schenkel M, Schintlmeister A, Hutter H, Mayrhofer P H. Low friction CrN/TiN multilayer coatings prepared by a hybrid high power impulse magnetron sputtering/DC magnetron sputtering deposition technique. *Thin Solid Films* **518**: 5553–5557 (2010)

[36] Latteman M, Ehiasarian A P, Bohlmark J, Persson P A O, Helmersson U. Investigation of high power impulse magnetron sputtering pretreated interfaces for adhesion enhancement of hard coatings on steel. *Surface Coatings Technology* **200**: 6495–6499 (2006)

[37] Ehiasarian A P, Hovsepian P E, Hultman L, Helmerson U. Comparison of microstructure and mechanical properties of chromium nitride-based coatings deposited by high power impulse magnetron sputtering and by the combined steered cathodic arc/unbalanced magnetron technique. *Thin Solid Films* **457**: 270–277 (2004)

[38] Wang C, Brault P, Zaepffel C, Thiault J, Pineau A, Sauvage T. Deposition and structure of W–Cu multilayer coatings by magnetron sputtering. *Journal of Physics D: Applied Physics* **36**: 2709–2713 (2003)

[39] Ogletree M D, Monterio O. Wear behavior of diamond-like carbon/metal carbide multilayers. *Surface and Coatings Technology* **108**–**109**: 484–488 (1998)

[40] Zheng J, Hao J, Liu X, Liu W. Properties of TiN/TiCN multilayer films by direct current magnetron sputtering. *Journal of Physics D: Applied Physics* **45**: 095303–095312 (2012)

[41] Liu H, Jiang Y, Zhou R, Tang B. Wear behaviour and rolling contact fatigue life of Ti/TiN/DLC multilayer films fabricated on bearing steel by PIIID. *Vacuum* **86**: 848–853 (2012)

[42] Kot M, Major L, Lackner J. The tribological phenomena of a new type of TiN/a-C: H multilayer coatings. *Materials and Design* **51**: 280–286 (2013)

[43] Al-Bukhaiti M A, Al-Hatab K A, Tillmann W, Hoffmann F, Sprute T. Tribological and mechanical properties of Ti/TiAlN/TiAlCN nanoscale multilayer PVD coatings deposited on AISI H11 hot work tool steel. *Applied Surface Science* **318**: 180–190 (2014)

[44] Chu K, Shen Y. Mechanical and tribological properties of nanostructured TiN/TiBN multilayer films. *Wear* **265**: 516–524 (2008)

[45] Zhang G, Li B, Jiang B, Chen D, Yan F. Microstructure and mechanical properties of multilayer Ti(C, N) films by closed-field unbalanced magnetron sputtering ion plating. *Journal of Materials Science and Technology* **26**: 119–124 (2010)

[46] Liu D, Tu J, Gu C D, Chen R, Hong C F. Tribological and mechanical behaviors of TiN/CNx multilayer films deposited by magnetron sputtering. *Thin Solid Films* **509**: 4842–4848 (2011)

[47] Kumar D, Dinesh Kumar N, Kalaiselvam S, Radhika R, Dash S, Tyagi A K, Jayavel R. Reactive magnetron sputtered wear resistant multilayer transition metal carbide coatings: microstructure and tribo-mechanical properties. *RSC Advances* **5**: 81790–81801 (2015)

[48] Gilewicz A, Warcholinski B, Myslinski P, Szymanski W. Anti-wear multilayer coatings based on chromium nitride for wood machining tools. *Wear* **270**: 32–38 (2010)

[49] Gilewicz A, Warcholinski B. Tribological properties of CrCN/CrN multilayer coatings. *Tribology International* **80**: 34–40 (2014)

[50] Beliardouh N E, Bouzid K, Nouveau C, Tlili B, Walock M J. Tribological and electrochemical performances of Cr/CrN and Cr/CrN/CrAlN multilayer coatings deposited by RF magnetron sputtering. *Tribology International* **82**: 443–452 (2015)

[51] Vyas A, Shen Y, Zhou Z, Li K Y. Nano-structured CrN/CNx multilayer films deposited by magnetron sputtering. *Composites Science and Technology* **68**: 2922–2929 (2008).

[52] Bayon R, Igartua A, Fernandez X, Martinez R, Rodriguez R J, Garcia J A, De Frutos A, Arenas M A, Damborenea J. Corrosion-wear behaviour of PVD Cr/CrN multilayer coatings for gear applications. *Tribology International* **42**: 591–599 (2009)

[53] Shi Y, Long S, Yang S, Pan F. Deposition of nano-scaled CrTiAlN multilayer coatings with different negative bias voltage on Mg alloy by unbalanced magnetron sputtering. *Vacuum* **84**: 962–968 (2010)

[54] Gilewicz A, Warcholinski B. Deposition and characterisation of Mo_2N/CrN multilayer coatings prepared by cathodic arc evaporation. *Surface and Coatings Technology* **279**: 126–133 (2015)

[55] Ghosh S K, Limaye P K, Swain B P, Soni N L, Agrawal R G, Dusane R O, Grover A K. Tribological behaviour and residual stress of electrodeposited Ni/Cu multilayer films on stainless steel substrate. *Surface and Coatings Technology* **201**: 4609–4618 (2007)

[56] Gayathri S, Kumar N, Krishnan R, RavindranT R, Dash S,

Tyagi A K, Raj B, Sridharan M. Tribological properties of pulsed laser deposited DLC/TM (TM=Cr, Ag, Ti and Ni) multilayers. *Tribology International* **53**: 87–97 (2012)

[57] Liu D, Tu J, Zhang H, Chen R, Gu C D. Microstructure and mechanical properties of carbon nitride multilayer films deposited by DC magnetron sputtering. *Surface and Coatings Technology* **205**: 3080–3086 (2011)

[58] Xu Z, Zheng Y J, Jiang F, Leng Y X, Sun H, Huang N. The microstructure and mechanical properties of multilayer diamond-like carbon films with different modulation ratios. *Applied Surface Science* **264**: 207–212 (2013)

[59] Bewilogua K, Bialuch I, Ruske H, Weigel Kai. Preparation of a-C:H/a-C:H:Si:O and a-C:H/a-C:H:Si multilayer coatings by PACVD. *Surface and Coatings Technology* **206**: 623–629 (2011)

[60] Liu Y, Gubisch M, Hild W, Scherge M, Spiess L, Knedlik C H, Schaefer J A. Nanoscale multilayer WC/C coatings developed for nanopositioning, part II: Friction and wear. *Thin Solid Films* **488**: 140–148 (2005)

[61] Braic M, Balaceanu M, Parau A C, Dinu M. Vladescu A. Investigation of multilayered TiSiC/NiC protective coatings. *Vacuum* **120**: 60–66 (2015)

[62] Braic M, Braic V, Balaceanu M, Zoita C N, Kiss A, Vladescu A, Popescue A, Ripeanu R. Structure and properties of Zr/ZrCN coatings deposited by cathodic arc method. *Materials Chemistry and Physics* **126:** 818–825 (2011)

[63] Ge F, Zhou X, Meng F, Xue Q, Huang F. Tribological behavior of VC/Ni multilayer coatings prepared by non-reactive magnetron sputtering. *Tribology International* **99**: 140–150 (2016)

[64] Zubarev E N, Devizenko A, Penkov O V, Kondratenko V V, Sevriukov D V, Sevryukova V A, Kopylets I A. Structural and phase transformation of cobalt films grown on amorphous carbon. *Thin Solid Films* **622**: 84–88 (2017)

[65] Ou J, Liu L, Wang J, Wang F, Xue M, Li W. Fabrication and tribological investigation of a novel hydrophobic polydopamine/graphene oxide multilayer film. *Tribology Letters* **48**: 407–415 (2012)

[66] Jehn H. Multicomponent and multiphase hard coatings for tribological applications. *Surface and Coatings Technology* **131**: 433–440 (2000)

[67] Chauhan K V, Rawal S K. A Review Paper on Tribological and Mechanical Properties of Ternary Nitride based Coatings. *Procedia Technology* **14**: 430–437 (2014)

Mahdi KHADEM. He received his bachelor degree in mechanical engineering (solid design) from Qazvin International Azad University (QIAU) in 2013. After then, he joined the Center for Nano Wear (CNW) and obtained his M.S. degree from Yonsei University, in 2015. He is currently a Ph.D. student at the same center. His research interests include tribology, coating and surface design, and nanotechnology.

Dae-Eun KIM. He is currently a professor in the School of Mechanical Engineering and the Director of the Center for Nano-Wear (CNW) at Yonsei University. Prof. Kim received his B.S. degree from Tufts Univ., and M.S. and Ph.D. degrees from M.I.T. He was an assistant professor at the Ohio State University before joining Yonsei University in 1993. He served as the Editor-in-Chief of IJPEM and Senior Editor of JMST. He is also the Chair of the Technical Committee for Tribology of International Federation for the Promotion of Mechanism and Machine Science (IFToMM). His research interests are micro/nano-tribology, functional coatings, and surface modification techniques.

Friction **5**(3): 263–284 (2017)
https://doi.org/10.1007/s40544-017-0183-5
ISSN 2223-7690
CN 10-1237/TH

REVIEW ARTICLE

Influence of tribology on global energy consumption, costs and emissions

Kenneth HOLMBERG[1,*], **Ali ERDEMIR**[2]

[1] *VTT Technical Research Centre of Finland, VTT FI-02044, Finland*

[2] *Argonne National Laboratory, Argonne, IL 60439, USA*

Received: 17 May 2017 / Accepted: 06 July 2017

Abstract: Calculations of the impact of friction and wear on energy consumption, economic expenditure, and CO_2 emissions are presented on a global scale. This impact study covers the four main energy consuming sectors: transportation, manufacturing, power generation, and residential. Previously published four case studies on passenger cars, trucks and buses, paper machines and the mining industry were included in our detailed calculations as reference data in our current analyses. The following can be concluded:

– In total, ~23% (119 EJ) of the world's total energy consumption originates from tribological contacts. Of that 20% (103 EJ) is used to overcome friction and 3% (16 EJ) is used to remanufacture worn parts and spare equipment due to wear and wear-related failures.

– By taking advantage of the new surface, materials, and lubrication technologies for friction reduction and wear protection in vehicles, machinery and other equipment worldwide, energy losses due to friction and wear could potentially be reduced by 40% in the long term (15 years)and by 18% in the short term (8 years). On global scale, these savings would amount to 1.4% of the GDP annually and 8.7% of the total energy consumption in the long term.

– The largest short term energy savings are envisioned in transportation (25%) and in the power generation (20%) while the potential savings in the manufacturing and residential sectors are estimated to be ~10%. In the longer terms, the savings would be 55%, 40%, 25%, and 20%, respectively.

– Implementing advanced tribological technologies can also reduce the CO_2 emissions globally by as much as 1,460 MtCO_2 and result in 450,000 million Euros cost savings in the short term. In the longer term, the reduction can be 3,140 MtCO_2 and the cost savings 970,000 million Euros.

Fifty years ago, wear and wear-related failures were a major concern for UK industry and their mitigation was considered to be the major contributor to potential economic savings by as much as 95% in ten years by the development and deployment of new tribological solutions. The corresponding estimated savings are today still of the same orders but the calculated contribution to cost reduction is about 74% by friction reduction and to 26% from better wear protection. Overall, wear appears to be more critical than friction as it may result in catastrophic failures and operational breakdowns that can adversely impact productivity and hence cost.

Keywords: friction; wear; energy saving; emission reduction

1 Introduction

Transportation, power generation, and manufacturing are vital industrial activities in a highly developed modern society. They involve moving both people and all kinds of materials in many different forms by all types of machines and mechanical systems that have numerous moving parts and hence interacting surfaces.

* Corresponding author: Kenneth HOLMBERG, E-mail: kenneth.holmberg@vtt.fi

Smooth, reliable, and long-lasting operations of such machines are closely dependent on how well the friction and wear are controlled on their numerous interacting surfaces. The science and technology for understanding and controlling friction, wear, and lubrication of such interacting surfaces in relative motion have been named as tribology since 1966 [1].

The key motivation for establishing the new discipline of tribology was the great economic impact that wear failures had in the British industry and on the British economy in the middle of last century. At the same time, a great number of new technological solutions had been developed that could be used to reduce friction and wear but they had not yet been implemented largely. The Jost report summarised that by large scale implementation of newer and more advanced tribological technologies, 515 million UK pound could be saved annually and this would correspond to 1.36% of GNP at that time. Most importantly, this report stipulated that such savings could be achieved in a period of ten years. The British government invested 1.25 million UK pound for further development and implementation of tribology in education, research and industry, and ten years later, the savings were estimated to be 200 million UK pound annually [1–4].

The Jost report was followed by other similar studies that reported potential savings of the similar orders of magnitude in Japan (2.6% of the GNP in 1970), in Germany (0.5%, 1976), in the USA (0.79%–0.84%, 1977, 1981) and in China (2%–7%, 1986). The estimated savings show large differences probably due to differences in the level of industrialization and industrial infrastructure of each country, the year when the calculations were carried out and the method of calculations used [4–9].

There has been tremendous progress in understanding of the fundamental mechanisms of tribological phenomena and developing a myriad of new materials, surface technologies, lubricants and other types of technical solutions, such as improved design, for markedly reducing friction and improving wear protection since the time of the Jost report. Furthermore, the greater knowledge gained from worldwide tribological studies mentioned above have been implemented in higher education and industry. However, today we face new challenges in the society due to increased world population, growing demands for energy, and limitation of fossil fuel use due to environmental concerns. In fact, at these days, it has become a great importance for the sustainability of global society to curb the use of fossil fuels and hence reduce the greenhouse gas emissions [10–12].

Figure 1 shows the International Energy Agency (IEA) estimation of key technologies for reduction of CO_2 emissions in order to limit the global warming to 2 ˚C above pre-industrial levels by 2050 [13]. The largest impact (38%) is expected to come from end-use energy efficiency and in this area, tribology could contribute considerably with new technical solutions such as new materials and coatings, surface engineering (including surface treatments, modifications, and texturing), new lubricants and additives (including nanomaterials and solid lubricants); new component design with microsensors; new methodologies like biomimetics, nanotechnology and integrated computational material design [12, 14, 15]. These are all related to the concept of "green tribology" which has recently been introduced and defined as the tribological aspects of ecological balance and of environmental and biological impacts [16].

Both the world and the levels of technological achievements have changed much from the years of those earlier tribology impact reports. Still more recent studies on this topic are quite few, so there is a need for an update. Very recently Lee and Carpick [12] prepared a comprehensive report for the Department of Energy in the USA on tribological opportunities for

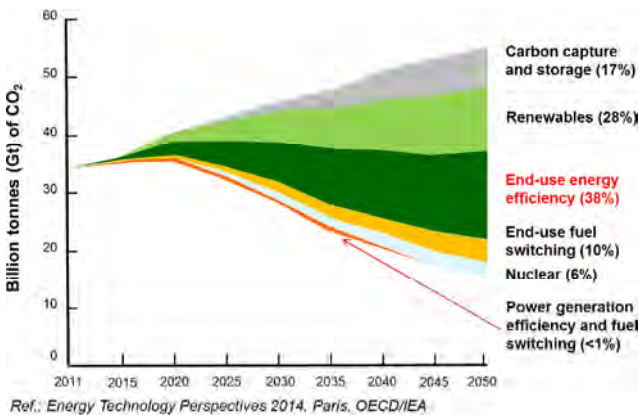

Fig. 1 Key technologies for reduction of CO_2 emissions in order to limit global warming to 2 ˚C [13].

enhancing America's energy efficiency. They identified 20 EJ (2.1% of the GNP) of energy that could be saved annually through new technologies that can be realized by targeted research initiatives in tribology. However, there is still not to our knowledge any study summarising the impact of tribology on a global level.

We have earlier calculated the impact of friction on global energy consumption in passenger cars, trucks and buses, and paper machines, and the impact of both friction and wear in the mining industry [15, 17–19]. Our intention with this work is to assess the influence of friction and wear in energy consumption, economic losses, and CO_2 emissions worldwide in the four main energy consuming sectors: transportation, industry, energy industry, and residential, and then to estimate potential savings that can be gained by putting into use of new tribological solutions that came about during the last decade or so. This is done based on the data from the four previous case studies and from other publications that we could find in the open literature.

2 Methodology

The global calculations used in this paper were carried out according to a methodology that was developed by Holmberg et al. [17] for the calculation of the impact of friction on passenger cars and in an industrial case study, i.e., paper machines mentioned earlier. The same methodology was later extended also to include the impact of friction and wear in mining [15]. The methodology is based on the combination of the analyses of several physical phenomena resulting in the consumption of energy in mechanical equipment. It includes the following analyses and calculations:

1. An estimation of the global energy consumption in targeted economic sectors.
2. Calculation of friction, wear, and energy losses in components and machinery used in such sectors.
3. Estimation of their operational effects.
4. Estimation of tribocontact-related friction and wear losses today and in the future.
5. Calculation of the global energy consumption today due to friction and wear and potential savings in the short and long runs.

Figure 2 shows the calculation methodology as used for passenger cars. First step is the estimation of annual fuel consumption found in reliable statistics divided by the number of cars worldwide which gives the energy used in one global average car. Based on statistics, a technical specification for a global average passenger car as well as global average operational conditions are defined. The components of this global average passenger car are then considered and the friction part is estimated and further broken down into microscale lubrication and contact mechanisms.

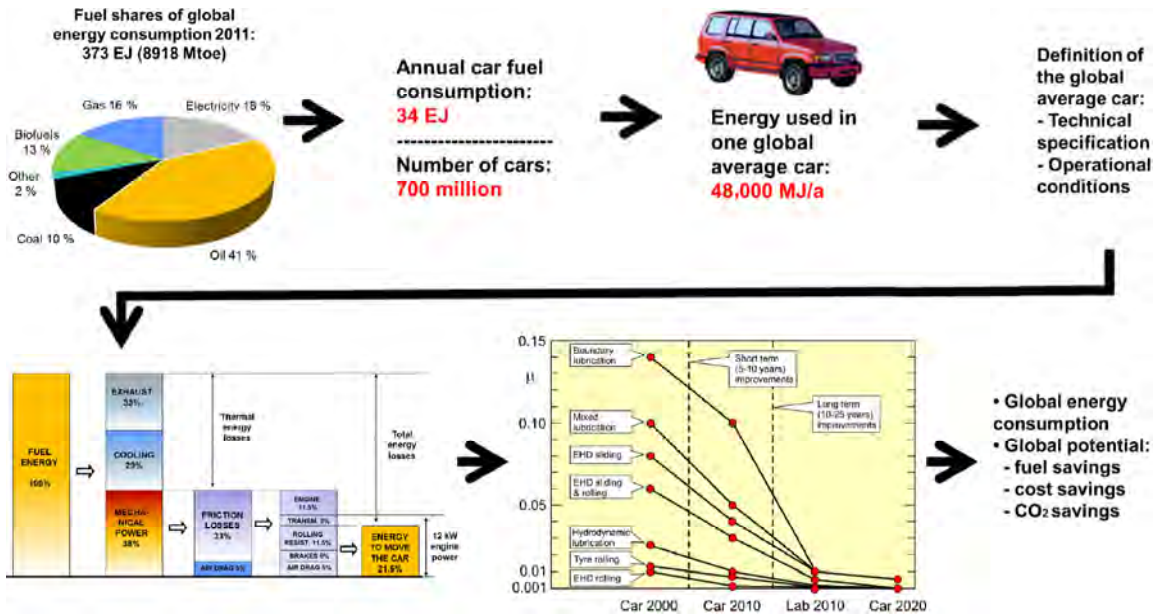

Fig. 2 Methodology for calculating global impact of friction on fuel consumption in passenger cars and potential savings [17].

The level of typical coefficients of friction in the global average car components is defined based on data from published literature. Similar levels of coefficients of friction for new cars, the lowest levels measured in laboratories so far, and estimated levels in future 2025 are estimated. This data is upscaled to global level and the global energy consumption due to friction as well as potential fuel, cost and CO_2 savings are then calculated as illustrated in Fig. 2.

The calculations were carried out on the basis of scientific publications and reports, publically available statistical data, unpublished data received directly from some operators and the authors' own experience.

3 Energy consumption worldwide

The total amount of energy generated from various energy sources like coal, oil, gas, nuclear, wind, etc., is called the total primary energy supply (TPES). The TPES for a region is the energy generated in that region + imports – exports. The global TPES was 575 EJ (13,700 Mtoe) in year 2014 and of that 167 EJ was used by the energy or power generation industry to produce electricity and heath, 12 EJ was the amount of energy lost during transfer and other losses, and the rest forms the total energy consumption, called total final consumption (TFC), as shown in Fig. 3 [20, 21].

The total consumption of energy worldwide was 396 EJ (9,425 Mtoe) in the year 2014 and it was distributed as follows [20]:

– 29% for industrial activity;

– 28% for transportation;

– 34% for domestic, including residential, services, agriculture, forestry, etc.;

– 9% for non-energy use, typically as raw materials.

4 Impact of friction and wear on energy consumption, economic losses, and emissions

From our previous case studies, we have as reference data in our calculations providing detailed information on the impact of friction from road vehicles, which account for 75% of the energy consumption in transportation sector. In the industrial sector, we have as reference data from one study focusing on how friction impacts a very advanced automated high-tech manufacturing industry, i.e., the paper production; and in another study focusing on how friction and wear impact a well-established heavy-duty but low-tech industry; the mining sector, see Fig. 3.

With regard to wear, there is detailed data only from one of the sectors we examined in the past; the mining industry, in which wear is very significant and far more important compared to other industrial sectors which do not suffer the same levels of wear. The mining study showed that of the total maintenance costs in mining, about half is due to the manufacturing of wear replacement parts and the other half originates from maintenance, down time, and labour costs [15].

In our calculations, we assume that the maintenance costs are in direct relation to the costs of wear parts and we use the data on maintenance costs in different sectors, see Fig. 4, for estimating the costs due to wear in these economic sectors [22].

In the following sections, we will estimate the energy losses due to friction and wear in the four large energy consuming sectors: namely, transportation, industry, energy industry, and residential. The industry sector represents the production and manufacturing industry while the energy industry represents the power plants for power generation and for thermal heating.

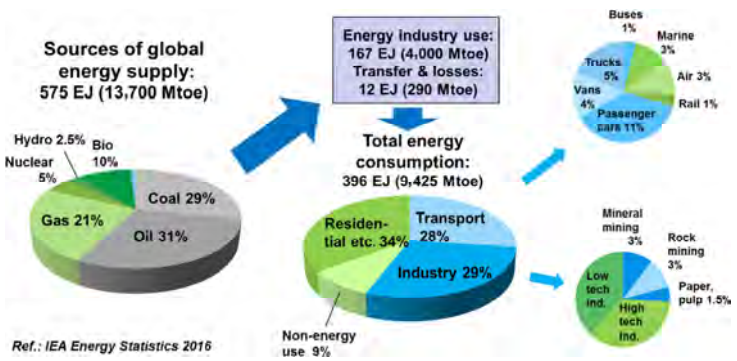

Fig. 3 Global energy supply and consumption in main economic sectors 2014. Mtoe = million tonnes of oil equivalent.

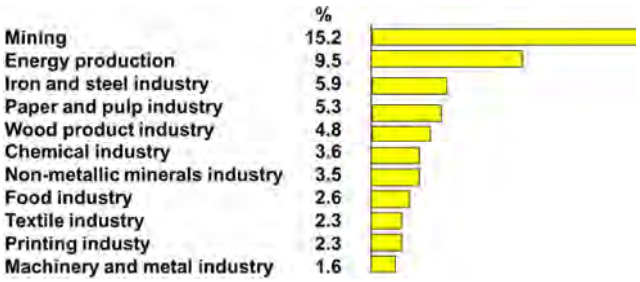

Fig. 4 Maintenance costs in industrial sectors in Finland in 1997.

4.1 Industry

The biggest industrial energy users are the chemical and petrochemical industry (30%) and the iron and steel industry (19%) that together consume half of the total energy used by all industrial sectors. Other large industrial energy users are the non-metallic minerals industry (9%, mainly cement), paper and pulp industry (6%), food and tobacco industry (5%), machinery industry (4%), and non-ferrous metals industry (4%, mainly aluminium), see Fig. 5 [13, 23].

Our previous study on paper machines showed that 32% of the electrical power used goes to overcome friction. However, the electricity used for mechanical energy is only 30% of the total energy use as 70% of the energy consumption is due to thermal energy for process heating. The energy consumed in a paper mill to overcome friction is in the range of 15%–25% [18]. In mining, on the other hand, where heavy rock materials are extracted, crashed, and transported, 40% of the energy consumption goes to overcome friction [15]. Based on this, we estimate that in industry in average, about 20% of the energy goes to overcome friction in total.

The share of energy losses due to wear in industry is calculated based on the data from mining industry [15]. In mining, the energy losses due to wear is 43% of that of friction. The wear-related energy losses include energy used for producing new parts for wear part replacement and downtime spare equipment. The cost for wear parts in mining is about the same order as the maintenance costs. We assume that also in other sectors, the cost for wear parts is proportional to the maintenance costs and we use proportion of maintenance costs of total costs for each sector presented in Fig. 4 [22]. This indicates that the cost of wear parts in industry in general is about one third of that in mining. In the case of machinery and metal industry, it is one tenth of that in mining. Thus we use for industry in total that the energy used for wear losses is 14% of that used to overcome friction.

The costs related to wear include not only the costs for wear part replacement and downtime, spare equipment, but also the costs for maintenance work which is not energy related. The costs due to wear in mining industry are 106% of the costs due to friction. We estimate the same relation between costs in the four sectors as it was for the energy losses. Thus the cost for wear in industry is 35% of the cost for friction, see Table 1.

Fig. 5 Production machines in paper, car, food, mining and steel industry.

Table 1 Comparison of energy and costs due to friction and wear for the four economic sectors.

	Energy to overcome friction as part of total energy use	Energy due to wear compared to energy loss due to friction	Costs due to wear compared to costs due to friction
Unit	%	%	%
Transportation	30	10	22
Industry	20	14	35
Energy industry	20	22	53
Residential	10	14	35
Total	20	15	37

4.2 Transportation

At present, the transportation sector includes about 1,600 million vehicles [24] used for transportation of people and freight in sea, land, and air (see Fig. 6). Road vehicles use 83EJ energy annually, which is 75% of the total energy use in transportation. The ships are the biggest energy users as calculated by the total energy use per vehicle. The average annual energy use per ship is 120,000 GJ. A road vehicle uses in average 80 GJ annually, a train 33,000 GJ, and an air plane 33,000 GJ. However, ships are the largest carriers of world freight and people by weight (73%) followed by road vehicles (15%), train (12%) and aviation (0.6%) [25, 26]. The energy intensity, defined here as the energy used to transport one tonne freight or people one kilometre, is for ships 0.3 MJ/tkm, for railway 0.6 MJ/tkm, for road vehicles 10 MJ/tkm and in aviation 35 MJ/tkm, see Table 2 [13, 25–31].

Fig. 6 Number of transportation vehicles worldwide and their global annual energy consumption and energy intensity (energy consumption per tonne weight transported and kilometre).

Road vehicles use 83 EJ annually and of that is 32% used to overcome friction [24]. There are no previous calculations available on the share of frictional energy consumption in rail, marine, and aviation. However, the share of friction in aviation is estimated to be about 10% while it is 20% in both marine and rail by considering the mechanical structures of those vehicles. Based on this, we can conclude that in transportation, with all sectors included, 30% of the energy use goes to overcome friction, see Table 1.

For the estimation of wear, data from the industrial sector is used as reference data, see section 4.1 above. The share of energy losses due to wear in transportation is estimated to be smaller than that in the industrial sector and about one fifth of that is in mining. It means that the energy loss due to wear is only 10% of the energy used to overcome friction and the cost due to wear is 22% of that due to friction. The low level of

Table 2 Key energy and energy efficiency figures in transportation.

	Number of vehicles worldwide	Global energy use	Energy use / vehicle	Part of global transport energy use	Part of global transport by weight and distance	Energy intensity
Unit		EJ/a	GJ/a	%	%	MJ/tkm
Road vehicles	$1{,}040 \times 10^6$	83	80	75	15	10
Trains	120,000	4	33,000	4	12	0.6
Ships	100,000	12	120,000	11	73	0.3
Airplanes	360,000	12	33,000	11	0.6	35
Total	$1{,}620 \times 10^6$	110		100	100	2

wear loss in transportation is explained by the very advanced materials and highly optimised lubrication technologies implemented in vehicles where part replacement or remanufacture is a much smaller issue than in many other sectors like mining.

4.3 Energy industry

The energy industry includes a large range of electricity power plants, combined heat and power plants, heat/steam plants, blast furnaces, gas works, coke ovens, oil refineries, liquefaction plants, etc. Like in the industrial sector, a great part of the energy use is thermal energy for heating. A lot of moving tribological contacts is found in power generation, such as in steam and gas turbines, hydro turbines, generators, pumps, conveyors, coal mining machines, drilling and production equipment, see Fig. 7(a) [12, 13, 20, 32].

Again detailed data on the energy consumption in mechanical equipment in the energy industry and the role of friction are hard to find in open literature. We estimate that the energy industry has a similar structure as the industrial sector where a considerable amount of the energy used is thermal energy for process heating. Based on this, we estimate that in total about 20% of the energy is used to overcome friction.

The share of energy losses and costs due to wear in energy industry is estimated to be half of that in mining. Thus the energy loss due to wear is estimated to be 22% of that due to friction and the costs due to wear are 53% of that due to friction.

4.4 Residential and services

Residential, service sector, and public buildings use a large range of energy conversion and utilization technologies. They are used in space heating and cooling/ventilation systems, in steam generation, water and heating systems, in lightning, in house-hold appliances, consumer products and in business equipment, see Fig. 7(b) [13]. The buildings have a very long life span, 40–120 years, and so has also a major part of the energy-consuming equipment, 5–20 years. A major part of the energy consumption is for space heating and cooling, and for water heating. The mechanical systems that need energy are ventilation systems, fans, pumps, etc. We estimate that 10% of the total energy use is for overcoming friction in these systems [13].

The share of energy losses due to wear in residential and services equipment is estimated to be one third of that in mining industry, being thus 14% of the energy used to overcome friction. The cost due to wear is ~35% of that due to friction.

4.5 Costs and emissions

The economic impact of friction and wear is calculated based on the costs for energy consumption to overcome friction, the costs of energy needed to manufacture wear related replacement parts and spare equipment, and cost for wear related maintenance work. A global average price of 18 € for 1 GJ energy or 1 TJ = 18 k€ is used [15].

Fig. 7 Power plant gas turbine (a) and typical residential machines (b).

The energy production and consumption is the dominating component in global greenhouse gas emissions and it forms 76% of the total emissions while agriculture, forestry and other land use form 24%, see Fig. 8.

The friction and wear related CO_2 emissions are calculated assuming that they are proportional to the energy consumption. This is a fair approximation on global scale even if there are differences in the level of emissions in the various economic sectors. The energy consumption of 1 PJ results in 0.0683 $MtCO_2$ (=36,000 $MtCO_2$/527 EJ) carbon dioxide emissions on average global level.

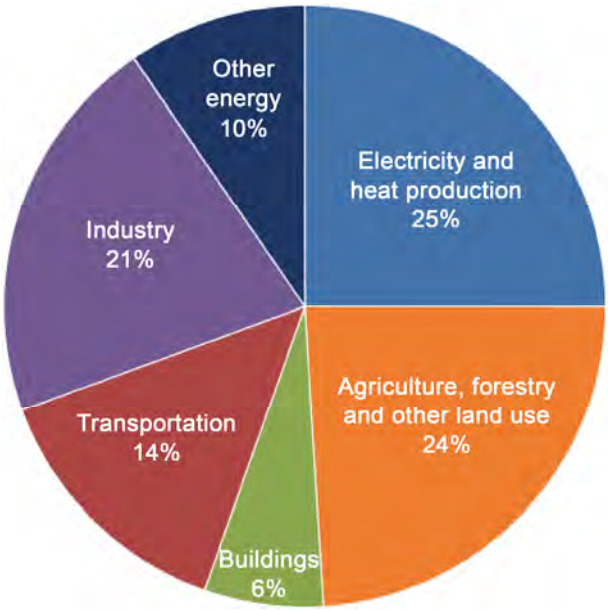

Fig. 8 Global greenhouse gas emissions by economic sector [10].

5 Impact of tribology and friction and wear reduction

5.1 Potential reduction in friction and wear

There has been a huge development in finding new tribological solutions to reduce friction and wear over the last decades [15, 17–19]. This development is illustrated in Fig. 9 where the typical friction coefficients in tribological contacts in trucks and buses in average today, in today's new commercial vehicles, lowest values measured in research laboratories today, and values predicted for future vehicles in year 2025 are shown according to contact and lubrication mechanisms.

The mechanical devices used in the four economic sectors, the level of new technological solutions implemented and operational conditions are considered. Based on that, the average friction and wear levels of today's devices are calculated and compared to the relative friction and wear reduction in today's new commercial devices, lowest levels measured in research laboratories today and levels estimated to be possible to achieve in future up to year 2030, see Table 3. These levels are named in the following as "Average 2017", "New 2017", "Laboratory 2017" and "Future 2030". The new technological solutions to achieve these reductions are presented in Section 7.

5.2 Tribological impact today and in the future

The global friction and wear losses, the economic expenditure and CO_2 emissions for each sector and in total were calculated using the data, criteria and

Table 3 Estimated relative friction and wear rate reduction trends based on data presented in Section 7 and literature [15, 17–19].

	Relative friction and wear reduction		
	From Average 2017 to New 2017	From Average 2017 to Lab 2017	From Average 2017 to Future 2030
	%	%	%
Friction reduction			
– Transport and energy industry	40	70	80
– Industry and residential	40	80	90
Wear reduction			
– Transport and energy industry	30	40	50
– Industry and residential	40	60	70

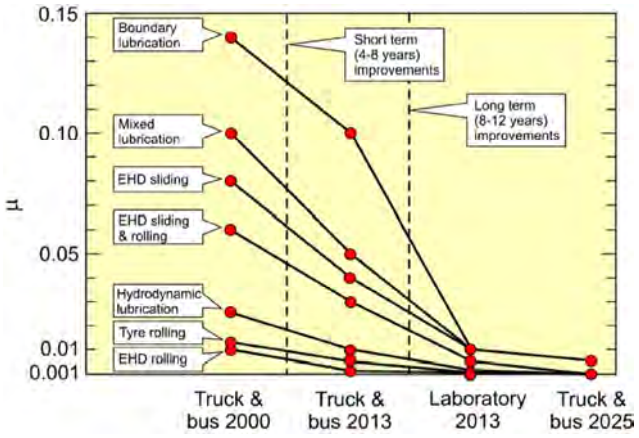

Fig. 9 Trends in the reduction of the coefficient of friction in trucks and buses for different lubrication mechanisms and for rolling friction [19].

assumptions presented above in Sections 3 and 4, and are shown in Appendix 1. The calculations show that today 103 EJ of energy is used to overcome friction worldwide and in addition, wear causes 16 EJ energy loss. The total costs of friction and wear globally are 250,000 million Euro and the total CO_2 emissions due to friction and wear are 8,120 $MtCO_2$. Corresponding cost estimates for friction and wear losses according to New 2017, Laboratory 2017 and Future 2017 are given in Appendix 1.

This is the first time to our knowledge that impact of both friction and wear has been estimated in detail on this level. Figure 10 shows a comparison of the impact of friction and wear on global level. Both with regard to energy losses and CO_2 emissions is the impact of friction six times higher than that of wear while with regard to economic impact, the friction impact is three times that of wear impact.

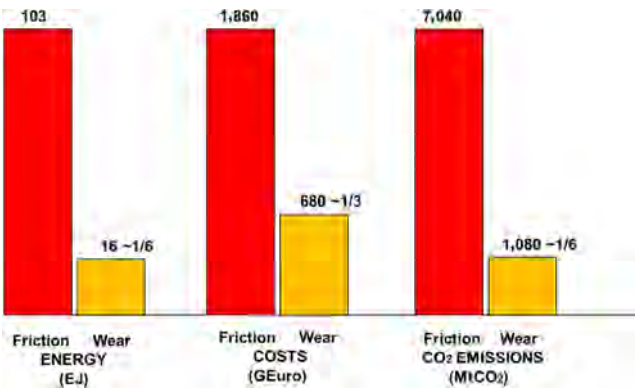

Fig. 10 Energy consumption, costs and CO_2 emissions due to friction and wear globally.

6 Potential savings by tribological advances

In the four case studies, the potential savings by implementing new tribological solutions were calculated both on the short term and on long term, as shown in Figs. 9 and 11, see also Appendix 3. The manufacturers of trucks and buses are more advanced and very quick in implementing new technologies in their products and there are big fleets with a limited number of owners so the implementation time is considered quite short. This is not the case in the mining industry with many owners with scepticisms or negative attitudes toward the deployment of new technologies. Paper machines are somewhat more advanced but due to the long lifetime of the machines, the implementation of new technologies does take time due to return on existing investment policies.

The average implementation time in all sectors was in this study estimated to be 8 years representing short term and 15 years representing long term based on considerations of the structure of the four sectors, average product lifetime and typical willingness to implement new technology in products. The savings by implementing new friction and wear solutions was calculated both on short term and on long term, see Appendix 2.

The implementation of new technology largely worldwide would save in the short term 21.5 EJ energy, 455,000 million Euro and 1,460 $MtCO_2$ emissions. In the long run, the savingscould easily amount to 46 EJ energy, 973,000 million Euro and 3,140 $MtCO_2$ emissions. The savings would be 1.39% of the GNP and 8.7% of the total global energy consumption for the time scale of 15 years.

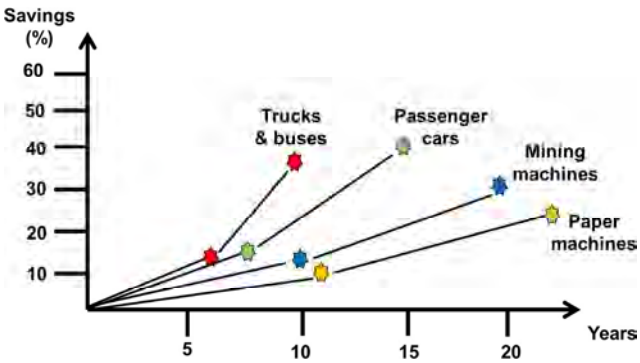

Fig. 11 Calculated potential savings over current state of the art by the introduction of advanced tribology solutions in four case studies and their time scale of implementation.

The biggest potential savings that can be achieved in the timescale of 8 years are in the transportation and energy industry sector, as shown in Fig. 12. The implementation takes longer time in the industry and residential sectors so the short term savings are not that high. The potential savings in some geographic regions are also shown in Table 4.

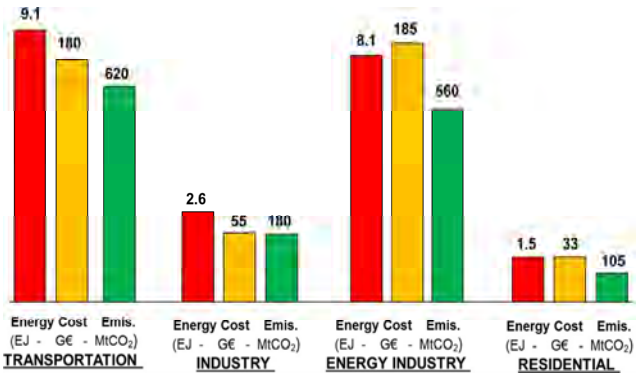

Fig. 12 Potential annual energy, cost and CO_2 emission savings globally after 8 years of intensive advanced tribology implementation.

7 Means and technologies to reduce friction and wear

In this section, we present some of the latest technological advances that can be implemented to achieve the levels of friction and wear reductions mentioned in charts and tables above. These examples mainly describe what we have named "today's best solution on the laboratory level" (Lab 2017). Some of the newest solutions for friction and wear reduction can be directly implemented or retrofitted by the users to existing machines but others may only be viable in newer or more advanced machines. Such are the changes to new type of engine lubricant, lubricant additives and tires with new materials and new design, as well as frequently replaced wear parts in other sectors. On the other hand, many of the new friction and wear reducing solutions need re-design or replacement of existing components, like the introduction of new materials, surface treatments, coatings

Table 4 Estimated potential energy and cost savings, and CO_2 emission reduction on long term (15 years) by region calculated as related to the total primary energy supply (TPES) of each region.

	TPES	Share of global TPES	Energy savings	Cost savings	CO_2 emission reduction
Unit	Mtoe	%	PJ/a	Million Euro/a	Million tonnes/a
World	13,700	100	46,000	973,000	3,140
Industrialized countries	8,220	60	27,600	583,800	1,884
Industrially developing countries	4,800	35	16,100	340,550	1,099
Agricultural countries	685	5	2,300	48,650	157
China	3,066	22.4	10,304	217,952	703
USA	2,216	16.2	7,452	157,626	509
EU-28	1,606	11.7	5,382	113,841	367
India	825	6.0	2,760	58,380	188
Russia	710	5.2	2,392	50,596	163
Japan	442	3.2	1,472	31,136	100
Brazil	303	2.2	1,012	21,406	69
Canada	280	2.0	920	19,460	63
UK	180	1.3	598	12,649	41
Finland	34	0.25	115	2,433	8

and textured components or new design solutions. This kind of improvements need to be introduced by the machine producers and will come out on the market, when the new products are launched.

New technologies for friction and wear reduction are summarised below based on more detailed descriptions in six previously published reports [12, 15, 17–19, 24] and some additional recent publications.

7.1 Lubricants

Mineral-based oil is the traditional way of lubricating sliding components and still constitutes the largest consumption by volume in the world. Synthetic-based oils are in the rise and increased in usage over the years due to their much attractive thermal and oxidative stability and longer life. Both oils provide good tribological properties as they wet and attach effectively to a steel surface, provide low shear between the sliding surfaces, and have a good load carrying capacity even under highly loaded line or point contacts. By and large, these oils still represent the largest volumes used in transportation and other industrial sectors. The load carrying property has been improved over the years by advances in viscosity index improvers, anti-wear, and anti-friction additives. Tribological research has shown that there are several ways to further improve the performance of traditional mineral oil lubrication such as:

1. Nanotechnology based anti-friction and anti-wear additives. The structure, property, and performance characteristics of the lubricant film are especially important in the very thin, elasto-hydrodynamic (EHD), and boundary lubricated (BL) contacts. The protecting fluid and boundary film thickness may be only a few micrometres and in many cases even much below one micrometre. Such contacts may be heavily loaded in certain applications by a nominal contact pressure of up to 3–4 GPa and these oils are still expected to provide low shear and good protection against wear and scuffing. As a result of concerted efforts, very low friction, even as low as a coefficient of friction of 0.005, has been measured in the presence of friction modifier additives like glycerol mono-oleate (GMO) or pure glycerol when lubricating tetragonal amorphous carbon coatings [33–35]. Nanomaterials with very promising tribological properties under investigation are carbon-based additives including nano-diamonds, onion-like carbons, carbon nanotubes, graphene, graphite as well as some inorganic fullerenes of transition metal dichalcogenides, like MoS_2 and WS_2, and copper, polymeric and boron-based nanoparticles [36–43].

2. Low viscosity oils. Our analysis has shown that viscous losses and shear in hydrodynamic contacts (HD) result in significant energy losses. If the lubricant viscosity can be further reduced while the low-friction and anti-wear functions are maintained, a very large energy saving in engines could be achieved [44, 45]. One alternative to mineral and synthetic-based hydrocarbon oils is the polyalkylene glycol (PAG)-based lubricants with lower viscosity and better environmental compatibility [46]. The use of organic friction modifiers [47], liquid crystal mesogenic fluids [48] and ionic liquids [49–52] have also provided low friction when used as additives in lubricating oils. Coefficients of friction even below 0.001 has been reported when using in a series of novel additives in such fluids [53]. Under conditions involving the uses of a mild acidic liquid and a metallic and/or ceramic material, friction coefficients of less than 0.01 have been achieved by triggering repulsive double-layer forces through the generation and adsorption of hydrogen, hydroxyl and hydronium ions on the opposing surfaces [54]. It has been suggested that by introducing artificial boundary slippage in HD journal bearings, the load carrying capacity can be considerably increased while the friction is reduced by 60% [55].

3. Vapour phase lubrication. In many lubricated tribological contacts, for example in roller bearings, the volume of the lubricant that is effective and needed for the tribological action in the contact is only a small fraction of the lubricant volume that is provided to the system. The non-active volume of the lubricant causes viscous losses. Such losses are very much reduced in vapour phase lubrication where a stream of gas transports the vaporised lubricant to the mechanical system. Vapour phase lubrication is especially beneficial in high temperature environments where liquid oil lubrication cannot operate and in microelectromechanical systems (MEMS) where the capillary effect of liquid lubrication is a problem [12, 56–60].

7.2 Materials

The materials used in tribological components have a big influence on both wear and friction. Search for new and more effective material solutions has intensified in recent decades for increased toughness, strength, hardness, all of which impact durability, and light-weightiness which also improves efficiency in vehicles. At the same time, a myriad of novel solid lubricants and their coatings has been developed to reduce wear and friction in both dry and lubricated contacts by even orders of magnitude. In particular, low-dimensional materials (such as Bucky-balls, nanotubes, nanosheets, and nano-onions of carbon- and boron-based solids as well as various transition metal dichalcogenides) have been proven to be very effective in reducing friction and wear of sliding surfaces under dry and lubricated contacts. Besides these, there have been significant strides in surface treatment and engineering fields providing very thick, hard, and slick surfaces for severe tribological applications involving abrasive, erosive, or adhesive wear. All and all, nowadays, there exist several innovative materials technologies that can improve the friction and wear properties of tribological components. Some of these advances are summarized below:

1. New materials. The erosive wear can be reduced by changing traditional cast iron to rubber coated surfaces in, e.g., pumps and pipe lines. Change from metallic component to polymers will normally reduce friction while ceramics are tribologically beneficial to use both in oil and water lubricated contacts [61]. Recently, research efforts in high-entropy alloys intensified and mainly because of their very distinct structures and compositions, they were shown to exhibit unusual physical and mechanical properties [62] as well as impressive resistance to wear and corrosion [63, 64]. Further, a new breed of non-ferrous materials (such as aluminium) named covetics consisting as much as 6 wt.% carbon has recently been developed and promises to offer much enhanced mechanical and hence tribological properties in light-weight Al alloys potentially making them suitable for sliding powertrain applications [65]. Although not new, a class of new nickel-titanium alloys, e.g., Nitinol 60 were shown to combine high hardness with superelasticity enabling unusual load-bearing capacity and other desirable tribological attributes [66]. Under boundary lubricated conditions with castor oil, such alloys were shown to exhibit friction coefficients below 0.01 [67].

2. Material treatment and surface modification. The increase of surface hardness, toughness and wear-resistance can be achieved by a variety of methods. Case carburizing, nitriding, or boronizing are classical examples that have been in use for many decades to combat friction and wear under abrasive, adhesive, and erosive conditions. More exotic methods such as shot-peening [68, 69] and friction-stir processing [70] were shown to structurally modify top surfaces at micro/nano-scales which in turn provide much improved friction and wear properties under both dry and lubricated conditions [71]. During the past decade, interest in additive manufacturing has grown exponentially for making three dimensional objects initially from polymers, but lately from metal or ceramic powders for all kinds of applications [72–74]. Tools used in additive manufacturing have become very versatile to manufacture 3D objects that can also incorporate super-hard and/or self-lubricating solids for improved friction and wear properties in numerous applications [75, 76]. The incorporation of hard and low-friction materials onto the top surfaces by various techniques including laser surfacing, particle plasma ablation, etc., can substantially increase hardness, stiffness and wear performance of the surfaces [77, 78]. The interest in cold-spray processes for friction and wear control has also intensified in recent years. They have the potential of alleviating thermal distortions and residual stress build-up which are very common with laser cladding and other similar techniques which are also used for enhanced wear resistance. They are particularly attractive for low-melting point Al and Mg alloys [79].

Traditional thermal diffusion processes, such as nitriding, carburizing, vanadizing, and boriding or boronizing are still used extensively to improve corrosion, mechanical and tribological properties of ferrous alloys. In these processes, nitrogen, carbon, or boron diffuse into the near surface regions of the workpieces and react with the metallic constituents, like Fe, and thus form thick and hard reaction layers.

Compared to quenching, such thermal diffusion processes can provide much higher resistance to corrosive, adhesive, abrasive, and erosive wear. All the thermal diffusion processes mentioned are unfortunately very slow. It may take several hours to whole day to achieve desired thicknesses or case depths. They are also energy intensive and environmentally unfriendly as they produce large volumes of CO_2 and hence expensive. Recently, an ultra-fast boriding process was developed which reduced the processing time to minutes, i.e., achieving 50 μm thick boride layer in 15 min instead of 6–8 hours with conventional pack-boriding method. It was demonstrated that such thick and hard boride layers can afford very low wear to sliding surfaces under both dry and lubricated conditions [80].

3. Thin surface coatings. Adding a thin layer (typically some few micrometres thick) of another material on the top surface can radically reduce friction and wear. This is often done in vacuum chambers by physical and chemical vapour deposition techniques (PVD and CVD). Strong materials for reducing wear both on tools and in machine components are ceramic coatings such as TiN, CrN, WC/Co, AlTiN, NiSiC, etc. Amorphous and lattice materials such as diamond like carbon (DLC) and molybdenum disulphide (MoS_2) have been especially efficient in reducing friction even down to a coefficient of friction of 0.01 and below. The thin coatings can be further improved by processing nanostructures and nanolayered coatings [14, 39, 81–84]. As a new concept, researchers have also designed smart catalytically active nano-composite layers with an ability to crack long-chain hydrocarbon molecules of base oils and turn them into diamond-like carbon tribofilms and other forms of carbon nanostructures on rubbing surfaces [41]. The resultant tribofilms were proven to be very slick and highly protective against wear and if and when worn away, they were shown to self-heal by a catalytic reaction with the lubricant.

4. Thick composite surface coatings. Thermal spraying, welded overlays, cladding and electroplating are examples of techniques used to reduce wear in heavily loaded conditions. The coating thickness is typically in the range of 0.1–50 mm. The surface is improved by the new material added which often may have a composite structure. Generally, the wear resistance of the coatings increases with their density and cohesive strength. Composite structures with carbide particles embedded into an often metallic matrix with higher elasticity and toughness provide good wear protection. A porous surface structure can be beneficial in lubricated sliding contacts as the oil pockets in pores can improve the lubrication and avoid starvation. Popular coatings to provide good wear resistance are, e.g., WC/Co, WC/Ni, WC/CoCr, CrC/NiCr, and Co-Cr-Si-Mo alloys [29, 85–89].

7.3 Component design

The design of components and the mechanical system has a great influence on both friction and wear. Tribology is a fairly new and evolving field of technology so it is still common that friction and wear aspects have been poorly considered as design criteria for mechanical systems. With proper tribological design can, e.g., the stresses in loaded contacts be reduced, lubricant access be improved, the contact space and number of contacts be reduced, lubrication mechanisms be optimised and severe wear mechanisms be avoided. Below is given only a few examples of tribological solutions for improved component design:

1. Surface texturing. The roughness and surface topography have a remarkable influence on friction and wear. Properly designed dimples, grooves and protrusions prepared on micro- or nanoscale can have a very beneficial effect. The controlled lubricant flow on microscale improves load carrying capacity and reduces friction. Laser surface texturing of piston rings has reduced fuel consumption of engines by 4% and micro-dimples produced by fine particle shot-peening has reduced friction by up to 50% [90–96].

2. Micro sensors and actuators. The engines in road transportation run in transient conditions with big changes in load and speed conditions over a broad operating range and the properties of the lubricant degrades due to time and operational effects. For this reason, the engines are typically over-designed to meet the worst possible conditions. With implementing modern micro sensors and actuators can the actual operating conditions continuously be recorded and allow for example the bearing system to be adjusted to optimise design characteristics throughout the operating range of the engine as an compensatory

strategy for mechanical wear protection. New design can allow the adjustment of the bearing area to the highest loaded region of a journal bearing. This allows modulation of bearing load capacity and its inherent friction loss [12, 97, 98].

7.4 New methodologies

The design of tribological components for optimal friction and wear performance is a very complex task if all relevant influencing variables and interactions are properly considered over scales from nano- to macro level. Traditional design includes consideration of some of the main parameters but new methodologies make it possible to perform a more accurate and comprehensive optimisation and consider a larger range of interactions and effects. Three important and rapidly evolving new methodologies are:

1. Integrated computational material engineering (ICME). Multiscale integrated material modelling and simulation based on sophisticated computer codes, finite element and other advanced modelling techniques offers a new tool for design of tribological contacts. The interactions of material behaviour, coatings and composite structures and lubricant mechanisms can be modelled over relevant scales and the performance and durability optimised with a comprehensive approach. Tribologically important but complicated features such as surface topography, thin surface films and substrate microstructures have been integrated in a 3D computer model with relevant data from nano to macro scale and used for simulation of tribological performance [99–102].

2. Nanotechnology. Tribological components have traditionally been designed on macroscale based on micro and macroscale understanding of the tribological contacts. Nanotechnology with molecular, atomic and even subatomic scale tools for material characterisation, computational modelling and even empirical testing makes it possible to investigate the basic physical and chemical contact mechanisms [103]. This information can then be used for more accurate and rigid tribological design. Besides the enhanced understanding of fundamental friction and wear mechanisms through advanced modelling and simulation approaches, many research efforts have also explored the potential usefulness of all kinds of nanomaterials for controlling friction and wear in powder and colloidal forms. Much of these studies focused on graphene and other 2D materials like h-BN, MoS_2, etc. Out of these studies, a large body of knowledge have emerged in recent years. When the cost, reliability and environmental health and safety issues have been addressed, it looks that these materials may provide great opportunities for all kinds of tribological applications [104–106].

3. Biomimetics. The nature has solved the task of controlling friction and wear in many genius ways far beyond what modern technology can offer. The hierarchical multiscale organisation and use of composite multiscale structures provides biological systems with the flexibility needed to adapt to the changing environment. The biological materials are grown without final design specifications, but by using the recipes and recursive algorithms contained in their genetic code. The remarkable properties of the biological materials can serve as source of inspiration for new technological solutions. A number of ideas for biomimetic tribological design and materials have been suggested such as the lotus effect for non-adhesive surfaces, the Gecko effect for controlled adhesion, the scorpion effect for reduced erosive wear, the shark-skin effect for suppression of turbulence, the Darkling beetle effect for water capturing, the sand fish lizard effect for moving in loose sand, dynamically tuneable surfaces for controlled liquid vs matter flow, micro-textured surfaces for controlled friction, as well as self-lubricating, self-cleaning, self-healing and de-icing biomimetic surfaces [16].

8 Discussion

8.1 Development over the last 50 years

In the Jost report [1] it was concluded that 515 million UK pounds can be saved annually after ten years of intensive and large scale implementation of new tribological technology in the UK industry. The structure of the savings is shown in Fig. 13. Much of this implementation has been done by different actions both from the government and private sector. The figure also shows the corresponding potential savings in UK today, 50 years later, calculated from

the data generated in this work. It shows that still today it would be possible achieve about the same level of savings by implementing new technology. The estimated savings in 1966 were 1.36% of GNP and today they would be 1.39% of the GNP. This can sound surprising since much technology has already been implemented over the last 50 years.

The explanation can be found when studying the structure of the savings. Fifty years ago 95% of the savings were related to wear, wear failures, breakdown and lifetime costs. The machines and equipment have over the years developed very much by new technology and they are now much more reliable, failure and breakdown is rare and maintenance costs are low. This can be seen from the figure.

It is interesting to note that fifty years ago it was estimated that 20% of the savings would come from increased lifetime but in our calculations of today that component has been considered negligible. Our understanding is that this is explained by the present situation that wear out of products is not anymore the main reason for buying a new product. Even if a car would last for 100 years, who would like to drive in the same car the whole lifetime? Even if the products still function people want to buy new products because of new design, new colours, new added functions like automation, new IT-communication possibilities and net connections, etc.

Another important observation is that the role of friction in cost savings has grown from 5% to 74%. We understand that there are two explanations for this. One is that especially over the last twenty years there have been new scientific and technological findings resulting in a breakthrough in friction reduction that could by no way have been predicted fifty years ago. In tribology textbooks written some thirty years ago it was commonly stated that the lowest coefficient of friction between two solid surfaces is 0.08 in a UHMWPE (common trademark Teflon) polymeric contact. Today superlubricity is an established field of tribology where coefficients of friction even down to 0.0001 have been reported.

The second explanation is that the role of energy consumption is much more important today. If there was high friction in some device in the old days you

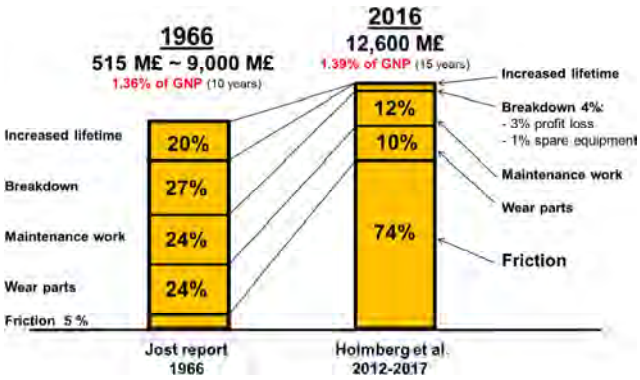

Fig. 13 Potential savings in UK 1966 and 2016 by implementing new tribology in machines and equipment, 515 million UK pounds converts to 9,000 million UK pounds of 2017 value.

just put in more power to overcome the friction. It could well be done with low energy prices. Today we need to be much more cautious with the energy consumption due to limited recourses, higher prices and greenhouse gas emissions.

The recent US report on tribological opportunities for enhancing America's energy efficiency [12] in the future presents new calculations and technologies for energy savings that are in line with this work. They identify 20 EJ (= 2.1% of the GNP) of energy that could be saved annually through technologies enabled by targeted research support in tribology. Areas where breakthroughs in tribology is needed to achieve this are low viscosity and intelligent lubricants, self-healing ultrathin tribofilms, advanced sensors and actuators for lubricant delivery modulation, nanomaterial fillers in tires, high temperature bearing lubricants, reliable wind turbine drive trains, nanoelectromechanical switches, triboelectric nanogenerators and vapour phase lubrication.

8.2 Confidence in the used method, data and sources

In the four previously published case studies on passenger cars, trucks and buses, paper machines and mining industry, we calculated in great detail the friction losses from microscale tribological contacts considering the prevailing friction and lubrication mechanisms. The wear was calculated by correlating energy costs for friction losses to costs for wear and actions due to wear failures. The accuracy of the calculations depends on the accuracy of the data that we could extract from open sources. In many cases

we have found good statistical data to use but there have also been cases of lack of reliable data that were needed. In such cases we have used estimations based on our best expert understanding. A summary of main results from the studies is in Appendix 3.

Especially for the calculations of friction and wear impact in the four economic sectors there has been little data available on the whole sector related to tribological impact. In some areas like in transportation there is very good and detailed statistical data that can be used even if data on global scale is missing. In some other areas, like in, e.g., rock mining or residential there is very little useful data available. In these areas we have studied the structure of the machinery and equipment used and correlated it to the area where we have detailed information in the four case studies.

We have all the way through the calculation process crosschecked our results with data from available sources and made corrections accordingly. Thus we are convinced that the results from the calculations are in the right order of magnitude and show the relevant trends even if the absolute values should not be considered as precise.

9 Conclusions

Calculations of the impact of friction and wear on energy consumption, economic expenditure, and CO_2 emissions are presented on a global scale. This impact study covers the four main energy consuming sectors: transportation, manufacturing, power generation, and residential. Previously published four case studies on passenger cars, trucks and buses, paper machines and the mining industry were included in our detailed calculations as reference data in our current analyses. The following can be concluded:

– In total, ~23% (119 EJ) of the world's total energy consumption originates from tribological contacts. Of that 20% (103 EJ) is used to overcome friction and 3% (16 EJ) is used to remanufacture worn parts and spare equipment due to wear and wear-related failures.

– By taking advantage of the new surface, materials, and lubrication technologies for friction reduction and wear protection in vehicles, machinery and other equipment worldwide, energy losses due to friction and wear could potentially be reduced by 40% in the long term (15 years)and by 18% in the short term (8 years). On global scale, these savings would amount to 1.4% of the GDP annually and 8.7% of the total energy consumption in the long term.

– The largest short term energy savings are envisioned in transportation (25%) and in the power generation (20%) while the potential savings in the manufacturing and residential sectors are estimated to be ~10%. In the longer terms, the savings would be 55%, 40%, 25% and 20%, respectively.

– Implementing advanced tribological technologies can also reduce the CO_2 emissions globally by as much as 1,460 $MtCO_2$ and result in 450,000 million Euros cost savings in the short term. In the longer term, the reduction can be 3,140 $MtCO_2$ and the cost savings 970,000 million Euros.

Fifty years ago, wear and wear-related failures were a major concern for UK industry and their mitigation was considered to be the major contributor to potential economic savings by as much as 95% in ten years by the development and deployment of new tribological solutions. The corresponding estimated savings are today still of the same orders but the calculated contribution to cost reduction is about 74% by friction reduction and to 26% from better wear protection. Overall, wear appears to be more critical than friction as it may result in catastrophic failures and operational breakdowns that can adversely impact productivity and hence cost.

Acknowledgements

This study has been carried out as part of the Finnish joint industrial consortium strategic research action coordinated by DIMECC Ltd within the program on Breakthrough Materials called BSA in the O'DIGS Project. We gratefully acknowledge the financial support of Tekes, the Finnish Technology Agency, the participating companies, and VTT Technical Research Centre of Finland. Additional support was provided by the U.S. Department of Energy, Basic Energy Sciences and Office of Energy Efficiency and Renewable Energy, under contract DE-AC02-06CH11357.

Appendix 1 Friction and wear impact on global energy loss, costs and emissions

Average 2017	Total	Friction				Wear				Tribology total			
Parameter	Energy	Share	Energy	Cost	Emission	Share	Energy	Cost	Emission	Share	Energy	Cost	Emission
Unit	PJ	%	PJ	MEuro	$MtCO_2$	%	PJ	MEuro	$MtCO_2$	%	PJ	MEuro	$MtCO_2$
Transportation	110000	**30**	33000	594000	2254		3300	130680	225		36300	724680	2479
Industry	116000	**20**	23200	417600	1585		3248	146160	222		26448	563760	1806
Energy industry	167000	**20**	33400	601200	2281		7348	318636	502		40748	919836	2783
Residential etc.	135000	**10**	13500	243000	922		1890	85050	129		15390	328050	1051
Total	528000		103100	1855800	7042		15786	680526	1078		118886	2536326	8120
New 2017	Total	Friction				Wear				Tribology total			
Parameter	energy	share	energy	cost	emission	share	energy	cost	emission	share	energy	cost	emission
Unit	PJ	%	PJ	MEuro	$MtCO_2$	%	PJ	MEuro	$MtCO_2$	%	PJ	MEuro	$MtCO_2$
Transportation	95817	**21**	19800	356400	1352		2317	91737	158		22117	448137	1511
Industry	105421	**13**	13920	250560	951		1949	87696	133		15869	338256	1084
Energy industry	151450	**13**	20040	360720	1369		5158	223682	352		25198	584402	1721
Residential etc.	128844	**6**	8100	145800	553		1134	51030	77		9234	196830	631
Total	481532		61860	1113480	4225		10558	454146	721		72418	1567626	4946
Laboratory 2017	Total	Friction				Wear				Tribology total			
Parameter	Energy	Share	Energy	Cost	Emission	Share	Energy	Cost	Emission	Share	Energy	Cost	Emission
Unit	PJ	%	PJ	MEuro	$MtCO_2$	%	PJ	MEuro	$MtCO_2$	%	PJ	MEuro	$MtCO_2$
Transportation	85580	**12**	9900	178200	676		1980	78408	135		11880	256608	811
Industry	95491	**5**	4640	83520	317		1299	58464	89		5939	141984	406
Energy industry	140681	**7**	10020	180360	684		4409	191182	301		14429	371542	985
Residential etc.	123066	**2**	2700	48600	184		756	34020	52		3456	82620	236
Total	444818		27260	490680	1862		8444	362074	577		35704	852754	2439
Future 2030	Total	Friction				Wear				Tribology total			
Parameter	Energy	Share	Energy	Cost	Emission	Share	Energy	Cost	Emission	Share	Energy	Cost	Emission
Unit	PJ	%	PJ	MEuro	$MtCO_2$	%	PJ	MEuro	$MtCO_2$	%	PJ	MEuro	$MtCO_2$
Transportation	81950	**8**	6600	118800	451		1650	65340	113		8250	184140	563
Industry	92846	**2**	2320	41760	158		974	43848	67		3294	85608	225
Energy industry	136606	**5**	6680	120240	456		3674	159318	251		10354	279558	707
Residential etc.	121527	**1**	1350	24300	92		567	25515	39		1917	49815	131
Total	432929		16950	305100	1158		6865	294021	469		23815	599121	1627

Appendix 2 Savings and reductions by tribology

Savings and reductions by tribology																		
Short term, 8 years	Energy losses		Energy savings				Costs		Costs savings				Emissions		Emission savings			
Parameter	Friction	Wear	Reduction	Friction	Wear	Total	Friction	Wear	Reduction	Friction	Wear	Total	Friction	Wear	Reduction	Friction	Wear	Total
Unit	PJ	PJ	%	PJ	PJ	PJ	MEuro	MEuro	%	MEuro	MEuro	MEuro	$MtCO_2$	$MtCO_2$	%	$MtCO_2$	$MtCO_2$	$MtCO_2$
Transportation	33000	3300	**25**	8250	825	9075	594000	130680	**25**	148500	32670	181170	2254	225	**25**	563	56	620
Industry	23200	3248	**10**	2320	325	2645	417600	146160	**10**	41760	14616	56376	1585	222	**10**	158	22	181
Energy industry	33400	7348	**20**	6680	1470	8150	601200	318636	**20**	120240	63727	183967	2281	502	**20**	456	100	557
Residential etc.	13500	1890	**10**	1350	189	1539	243000	85050	**10**	24300	8505	32805	922	129	**10**	92	13	105
Total	103100	15786	**18**	18600	2808	21408	1855800	680526	16	334800	119518	454318	7042	1078	16	1270	192	1462
Long term, 15 years	Energy losses		Energy savings				Costs		Costs savings				Emissions		Emission savings			
Parameter	Friction	Wear	Reduction	Friction	Wear	Total	Friction	Wear	Reduction	Friction	Wear	Total	Friction	Wear	Reduction	Friction	Wear	Total
Unit	PJ	PJ	%	PJ	PJ	PJ	MEuro	MEuro	%	MEuro	MEuro	MEuro	$MtCO_2$	$MtCO_2$	%	$MtCO_2$	$MtCO_2$	$MtCO_2$
Transportation	33000	3300	**55**	18150	1815	19965	594000	130680	**55**	326700	71874	398574	2254	225	55	1240	124	1364
Industry	23200	3248	**25**	5800	812	6612	417600	146160	**25**	104400	36540	140940	1585	222	25	396	55	452
Energy industry	33400	7348	**40**	13360	2939	16299	601200	318636	**40**	240480	127454	367934	2281	502	40	912	201	1113
Residential etc.	13500	1890	**20**	2700	378	3078	243000	85050	**20**	48600	17010	65610	922	129	20	184	26	210
Total	103100	15786	**39**	40010	5944	45954	1855800	680526	35	720180	252878	973058	7042	1078	35	2733	406	3139

Appendix 3 Summary of friction and wear savings as calculated in five studies [15, 17–19]

	Term		Savings		Economic savings		Emission reduction		Energy savings		Part of global energy	Included in calculations
	years	years	%	%	GEuro	GEuro	$MtCO_2$	$MtCO_2$	EJ	EJ	%	
Passenger cars, 2012	7.5	20	18	61	174	576	290	960	4	13.5	7.5	Friction
Trucks & buses, 2014	6	10	14	37	105	280	200	530	2.6	7.2	4.5	Friction
Paper machines, 2013	10	22.5	11	23.6	2	4.2	11	23	0.036		1	Friction
Mining industry, 2017	10	20	15	30	31	62	145	290	1	2	2.3	Friction & wear
World total 2017	8	15	15	30	410	830	2800	5700	19	39	100	Friction & wear
World energy consumption, EJ	528											
- Savings, % of world energy	4.1	8.7										
World GDP, GEuro	70,000											
– Savings, % of GDP	0.65	1.39										
World emission, $MtCO_2$	36,000											
– Savings, % of all CO_2 emiss.	4.1	8.7										

Appendix 4 Conversion factors

Energy conversions

1 kWs = 1 kJ
1 kWh = 3.6 MJ
1 Mtoe = million tonnes of oil equivalent
1 Mtoe = 41,868 TJ
1 Btu = 1,055 J
1 Quad = 1.055 EJ
1 kWh = 0.06 Euro as global average 2014
1 hour labour = 6 Euro salary cost as global average 2014
1 PJ => result in 0.0683 $MtCO_2$ emissions
1 PJ => has the price of 18 M€

Diesel fuel conversions

1 liter = 0.832 kg
1 MJ = 0.028 liter
1 liter = 35.9 MJ
1 kg = 43.1 MJ
1 kg => 3.16 kg CO_2 emission
1 liter => 2.63 kg CO_2 emission
1 liter = 0.7 Euro as global average 2014

References

[1] Jost H P (ed.). Lubrication (Tribology)–A report on the present position and industry's needs. Department of Education and Science, H. M. Stationary Office, London, UK, 1966.
[2] Jost H P. Economic impact of tribology. National Bureau of Standards special publication 423. In *Proc. 20th Meeting of the Mechanical Failures Prevention Group*. Gaithersburg, USA, 1974.
[3] Jost H P, Schoefield J. Energy saving through tribology: A techno-economic study. *Proc Instn Mech Engrs* **195**: 151–173 (1981)
[4] Jost P H. Tribology–Origin and future. *Wear* **136**:1–17(1990)
[5] JSPMI. State-of-art report on lubrication practice in Japan (in Japanese). Technical Research Institute, Japan Society for the Promotion of Machine Industry, Japan, Research Report, 1970.
[6] Research Report T76-36 Tribologie (Code BMFT-FB-T76-36). Bundesministerium fur Forschung und Technologie (Federal Ministry for Research and Technology), West Germany, 1976.
[7] ASME 1977. Strategy for energy conservation through tribology. ASME, New York, 1977
[8] ASME 1981. Strategy for energy conservation through tribology. 2nd edition, ASME, New York, 1977
[9] China 1986. An investigation on the application of tribology in China. A report by the Tribology Institution of the Chinese Mechanical Engineering Society, September 1986, Beijing, China.

[10] IPCC 2014. Climate Change 2014: Impacts, Adaptation and Vulnerability. Summary for policy makers, 5th Assessment report of the intergovernmental panel on climate change, WMO, UNEP, 2014.

[11] Wiedmann T O, Schandl H, Lenzen M, Moran D, Suh S, West J, Kanemoto K. The material footprint of nations. *PNAS* **112**: 6271–6276 (2015)

[12] Lee P M, Carpick R (eds). Tribological opportunities for enhancing America's energy efficiency. A report to the Advanced Research Projects Agency-Energy (ARPA-E) at the U.S. Department of Energy, 14.2.2017.

[13] IEA Energy Technology Persectives 2010. Scenarios & Strategies to 2050 IEA International Energy Agency, Paris, France 2010.

[14] Cha S C, Erdemir A (eds). *Coating Technology for Vehicle Applications*. Springer Verlag, Heidelberg, 2015.

[15] Holmberg K, Kivikytö-Reponen P, Härkisaari P, Valtonen K, Erdemir A. Global energy consumption due to friction and wear in the mining industry. *Tribology International* **115**:116–139 (2017)

[16] Nosonovsky M, Bhushan B. *Green Tribology – Biomimetics, Energy Conservation and Sustainability*. Springer Verlag, Berlin, Germany, 2012.

[17] Holmberg K, Andersson P, Erdemir A. Global energy consumption due to friction in passenger cars. *Tribology International* **47**: 221–234 (2012)

[18] Holmberg K, Siilasto R, Laitinen T, Andersson P, Jäsberg A. Global energy consumption due to friction in paper machines. *Tribology International* **62**: 58–77 (2013)

[19] Holmberg K, Andersson P, Nylund P O, Mäkelä K, Erdemir A. Global energy consumption due to friction in trucks and buses. *Tribology International* **78**: 94–114 (2014)

[20] IEA Key World Energy Statistics 2016. International Energy Agency, Paris, France, 2010.

[21] WEC, Global Transport Scenarios 2050. World Energy Council, London, UK, 2011.

[22] Komonen K. Maintenance key numbers–Results from 2002 year survey/Kunnossapidon tunnuslukuja-Vuotta 2002 koskevan kyselyn tuloksia (in Finnish), Finnish Maintenance Society, Helsinki, Finland, 2003.

[23] IEA Tracking Industrial Energy Efficiency and CO_2 Emissions–Energy Indicators. International Energy Agency, Paris, France, 2007.

[24] Erdemir A, Holmberg K. Energy consumption due to friction in motored vehicles and low-friction coatings to reduce it. In*Coating Technology for Vehicle Applications*. Cha S C, Erdemir A (eds). Springer Verlag, Heidelberg, 2015: 1–23.

[25] Mode of transport.Wikipedia, https://en.wikipedia.org/wiki/Mode_of_transport, 16.5.2017

[26] Rodrigue J P, Comotois C, Slack B. *The Geography of Transport Systems*. 3rd edition, Routledge, New York, USA, 2013.

[27] IEA Transport, Enenrgy and CO_2-Moving Toward Sustainability. International Energy Agency, Paris, France, 2009.

[28] RITA. Freight Transportation: Global Highlights. US Department of Transportation, Reseacrh and Innovative Technology Administration, RITA Bureau of Transport Statistics, Washington DC, USA, 2010.

[29] Davis J R (Ed.). Surface engineering for corrosion and wear resistance. ASM International, USA, 2001.

[30] EU Transport in figures–Statistical pocketbook 2015. European Union, Brussels, Belgium, 2015.

[31] Davis S C, Diegel S W, Boundy R G. *Transportation Energy Data Book*. Edition 32, Oak Ridge National Laboratory, Oak Ridge, USA, 2013.

[32] IEA World Energy Outlook 2015. International Energy Agency, Paris, France, 2015.

[33] Barros Bouchet M, Martin J M. The future of boundary lubrication by carbon coatings and environmentally friendly additives. In *Advanced Tribology*. Luo J, Meng Y, Shao T, Zhao Q (eds). Bejing, China, Tsinghua University Press & Springer, 2010: 598–599.

[34] Martin J M, Barros Bouchet M I, Sagawa T. Green tribology: Lubricant compliant superhard DLC coatings. In *Proceedings of the 4th World Tribology Conference*, Kyoto Japan, 2009.

[35] Martin J M, Barros Bouchet M I, Matta C, Zhang Q, Goddard III W A, Okuda S, Sagawa T. Gas-phase lubrication of a ta-C by glycerol and hydrogen peroxide: Experimental and computer modelling. *Journal of Physical Chemistry* **C114**: 5003–5011 (2010)

[36] Martin J M, Ohmae N. *Nanolubricants*. John Wiley & Sons Ltd., New York, USA, 2008.

[37] Kalin M, Kogovsek J, Remskar M. Mechanisms and improvements in the friction and wear behaviour using MoS_2 nanotubes as potential oil additives. *Wear* **280–281**: 36–45 (2012)

[38] Kalin M, Kogovsek J, Remskar M. Nanoparticles as novel lubricating additives in a green, physically based lubrication technology for DLC coatings. *Wear* **303**: 480–485 (2013)

[39] Xu J, Li J. New achievements in superlubricity from International Workshop on Superlubricity: Fundamental and Applications. *Friction* **3**(4): 344–351 (2015)

[40] Dai W, Kheireddin B, Gao H, Liang H. Roles of nano-particles in oil lubrication. *Tribology International* **102**: 88–98(2016)

[41] Erdemir A, Ramirez G, Eryilmaz O L, Narayanan B, Liao Y, Karmath G, Sankaranarayanan S K. Carbon-based tribofilms from lubricating oils. *Nature* **536** (7614): 67–71 (2016)

[42] Scherge M, Böttcher R, Linsler D, Kurten D. Multi-phase friction and wear reduction by copper nanoparticles. *Lubricants*

4(36):1–13 (2016)

[43] Ge X, Xia Y, Shu Z, Zhao X. Conductive grease synthesized using nanometer ATO as an additive. *Friction* **3**(1): 56–64 (2015)

[44] Tormos B, Ramirez L, Johansson J, Björling M, Larsson R. Fuel consumption and friction benefits of low viscosity engine oils for heavy duty applications. *Tribology International* **110**: 23–34 (2017)

[45] Singh S, Singh S, Sehgal A. Impact of low viscosity engine oil on performance, fuel economy and emissions of light duty diesel engine. No. 2016-01-2316. SAE Technical Paper, 2016

[46] Cuthbert J, Gangopadhyay A, Elie L, Liu Z, Mcwatt D, Hock E D, Erdemir A. Engine friction and wear performances with polyalkylene glycol engine oils. SAE Technical Paper 2016-01-2271

[47] Choo J H, Forrest A K, Spikes H A. Influence of organic friction modifier on liquid slip: A new mechanism of organic friction modifier action. *Tribology Letters* **27**: 239–244 (2007)

[48] Amann T, Kailer A. Ultralow friction of mesogenic fluid mixtures in tribological reciprocating systems. *Tribology Letters* **37**: 343–352 (2010)

[49] Qu J, Truhan J J, Dai S, Luo H, Blau P J. Ionic liquids with ammonium cations as lubricants or additives. *Tribology Letters* **22**: 207–214 (2006)

[50] Qu J, Blau P, Dai S, Luo H, Meyer III H M. Ionic liquids as novel lubricants and additives for diesel engine applications. *Tribology Letters* **35**:181–189 (2009)

[51] Qu J, Blau P, Dai S, Luo H, Meyer III H M, Truhan J J. Tribological characteristics of aluminium alloys sliding against steel lubricated by ammonium and imidazolium liquids. *Wear* **267**: 1226–1231 (2009)

[52] Zhou Y, Qu J. Ionic liquids as lubricant additives: A review. *ACS Applied Materials & Interfaces* **9**(4): 3209–3222 (2017)

[53] Li J, Zhang C, Ma L, Liu Y, Luo J. Superlubricity achieved with mixtures of acids and glycerol. *Langmuir* **29**: 271–275 (2013)

[54] Luo J, Deng M, Zhang C. Advances of Superlubricity. In *Proc. ITS-IFToMM 2017 and K-TIS 2017*, Jeju, Korea, 2017.

[55] Zhang Y. An improved hydrodynamic journal bearing with the boundary slippage. *Meccanica* **50**: 25–38 (2015)

[56] Forster N H. Rolling contact testing of vapour phase lubricants–Part III: Surface analysis. *Tribology Transactions* **42**(1): 1–9 (1999)

[57] Argibay N, Keith J H, Krick B A, Hahn D W, Bourne G R, Sawer W G. High-temperature vapour phase lubrication using carbonaceous gases. *Tribology Letters* **40**: 3–9 (2010)

[58] Greiner C, Felts J R, Dai Z, King W P, Carpick R W. Controlling nanoscale friction through the competition between capillary adsorption and thermal activated sliding. *AVS Nano* **6**(5): 4305–4313 (2012)

[59] Berman D, Krim J. Surface science, MEMS and NEMS: Progress and opportunities for surface science research performed on, or by, microdevices. *Progress in Surface Science* **88**: 171–211 (2013)

[60] Kim H J, Seo K J, Kang K H, Kim D E. Nano-lubrication: A review. *International Journal of Precision Engineering and Manufacturing* **17**(6): 829–841 (2016)

[61] Hsu S M, Shen M. Wear prediction of ceramics. *Wear* **256**: 867–878 (2004)

[62] Tsai M H, Yeh J W. High-entropy alloys: A critical review. *Materials Research Letters* **2**(3): 107–123 (2014)

[63] Buluc G, Florea I, Chelariu R, Rusu O, Carcea I. Microstructure and wear resistance of FeNiCrMnCu high entropy alloy. *Trans Tech Publications* **1143**: 3–6 (2017)

[64] Yu Y, Wang J, Li J, Yang J, KouH, Liu W. Tribological behavior of AlCoCrFeNi (Ti 0.5) high entropy alloys under oil and MACs lubrication. *Journal of Materials Science & Technology* **32**(5): 470–476 (2016)

[65] Nilufar S. Experimental investigation of structure, composition and properties of novel metal-carbon covetic materials. PhD dissertation, University of Illinois at Urbana-Champaign, USA, 2014.

[66] Della Corte C. Novel Super-Elastic Materials for Advanced Bearing Applications. In: Advances in Science and Technology, *Trans Tech Publications* **89**: 1–9 (2014)

[67] Qunfeng Z, Dong G, Martin J M. Green superlubricity of Nitinol 60 alloy against steel in presence of castor oil. Scientific Reports 6, 2016.

[68] Bagherifard S, Fernandez-Pariente I, Ghelichi R, Guagliano M. Severe shot peening to obtain nanostructured surfaces: process and properties of the treated surfaces. *Handbook of Mechanical Nanostructuring*, 299-323(2015)

[69] Unal O, Varol R, Erdogan A, Gok M S. Wear behaviour of low carbon steel after severe shot peening. *Materials Research Innovations* **17**(7): 519–523 (2013)

[70] Besharati-Givi M K, Asadi P. *Advances in Friction-stir Welding and Processing.* Elsevier, Amsterdam, the Netherlands, 2014.

[71] Seraj R A, Abdollah-Zadeh A, Hajian M, Kargar F, Soltanalizadeh R. Microstructural evolution and wear resistance of friction stir-processed AISI 52100 steel. *Metallurgical and Materials Transactions A* **47**(7): 3564–3572 (2016)

[72] Singh S, Ramakrishna S, Singh R. Material issues in additive manufacturing: A review. *Journal of Manufacturing Processes* **25**: 185–200 (2017)

[73] Frazier W E. Metal additive manufacturing: A review. *Journal of Materials Engineering and Performance* **23**(6): 1917–1928 (2014)

[74] Baig U M, Khan A A, Rajakumar D R. Wear characterization of direct steel–H20 specimens produced by additive

manufacturing techniques. In *Advances in 3D Printing & Additive Manufacturing Technologies*. Wimpenny D I, Pandey P M, Kumar L J (eds). Springer, Singapore, 2017, 121.

[75] Kasonde M, Kanyanta V. Future of superhard material design, processing and manufacturing. In *Microstructure-Property Correlations for Hard, Superhard, and Ultrahard Materials*. Kanyanta V (ed.). Springer, Singapore, 2016: 211–239.

[76] Bartolomeu F, Sampaio M, Carvalho O, Pinto E, Alves N, Gomes J R, Miranda G. Tribological behavior of Ti6Al4V cellular structures produced by Selective Laser Melting. *Journal of the Mechanical Behavior of Biomedical Materials* 2017.

[77] Sundararajan G, Joshi S V, Krishna L R. Engineered surfaces for automotive engine and power train components. *Current Opinion in Chemical Engineering* **11**: 1–6 (2016)

[78] Jacobson S, Hogmark S. Surface modifications in tribological contacts. *Wear* **266**: 370–378 (2009)

[79] Goldbaum D, Poirier D, Irissou E, Legoux J G, Moreau C. Review on Cold Spray Process and Technology US Patents. In *Modern Cold Spray*. Springer International Publishing, 2015: 403–429.

[80] Timur S, Kartal G, Eryilmaz O L, Erdemir A. U.S. Patent No. 8,951,402. Washington, DC: U.S. Patent and Trademark Office, 2015.

[81] Holmberg K, Matthews A. *Coatings Tribology–Properties, Mechanisms, Techniques and Applications in Surface Engineering. Elsevier Tribology and Interface Engineering Elsevier Series.* Amsterdam, the Netherlands: Elsevier; 2009.

[82] Berman D, Deshmukh S A, Sankaranarayanan S K R S, Erdemir A, Sumant A V. Macroscale superlubricity enabled by graphene nanoscroll formation. Science express 14 May 2015/10.1126/science.1262024.

[83] Ronkainen H, Elomaa O, Varjus S, Kilpi L, Jaatinen T, Koskinen J. The influence of carbon based coatings and surface finish on the tribological performance in high-load contacts. *Tribology International* **96**: 402–409 (2016)

[84] Yang J, Xia Y, Song H, Chen B, Zhang Z. Synthesis of the liquid-like graphene with excellent tribological properties. *Tribology International* **105**: 118–124 (2017)

[85] Davis J R (Ed.). *Handbook of Thermal Spray Technology*. TTS ASM Thermal Spray Society, ASM International, USA, 2004.

[86] Gerard B. Application of thermal spraying in the automotive industry. *Surface and Coatings Technology* **201**: 2028–2031 (2006)

[87] Lima R S, Marple B R. Thermal spray coatings engineered from nanostructural ceramic agglomerated powders for structural, thermal barrier and biomedical applications: A review. *Journal of Thermal Spray Coatings* **16**: 40–63(2007)

[88] Pawlowski L. *The Science and Engineering of Thermal Spray Coatings*. 2nd edition. John Wiley & Sons, Chichester, England, 2008.

[89] Castro R M, Cavaler L C C, Marques F M, Bristot V M, Rocha A S. Comparative of the tribological performance of hydraulic cylinders coated by the process of thermal spray HVOF and hard chrome plating. *Tribology in Industry* **36**: 79–89 (2014)

[90] Kovalchenko A, Ajayi O O, Erdemir A, Fenske G R, Etsion I. The effect of laser texturing of steel surface and speed-load parameters on lubrication regime transition from boundary to hydrodynamic. *Tribology Transactions* **47**: 299–307 (2004)

[91] Klingerman Y, Etsion I, Shinkarenko A. Improving tribological performance of piston rings by partial surface texturing. *Transactions of the ASME, Journal of Tribology* **127**: 632–638 (2005)

[92] Ryk G, Etsion I. Testing piston rings with partial laser surface texturing for friction reduction. *Wear* **261**: 792–796 (2006)

[93] Etsion I. Surface texturing. In *Handbook of Lubrication and Tribology, 2nd edition.* Totten G (ed.). CRC Taylor & Francis, London, UK, Vol 2, Chapter 53, 2012.

[94] Etsion I, Sher E. Improving fuel efficiency with laser surface textured piston rings. *Tribology International* **42**: 542–547 (2009)

[95] Ishida Y, Usami H, Hoshino Y. Effect of micro dimples on frictional properties in boundary lubrication condition. In *Proceedings of the World Tribology Congress*, Kyoto, Japan, 2009.

[96] Wang X, Yu H, Huang W. Surface texture design for different circumstances. In *Proceedings of the 1st International Brazilian Conference on Tribology*, TriboBR 2010, Rio de Janeiro, Brazil, 2010: 97–107.

[97] Canter N. Tribocatalysis: A new extreme pressure lubrication approach. *Tribology and Lubrication Technology* **72**(10): 10–11(2016)

[98] Varenberg M, Ryk G, Yakhnis A, Kligerman Y, Kondekar N, McDowell M T. Mechano-chemical surface modification with Cu_2S: Including superior lubricity. *Tribology Letters* **64**(28): 1–7 (2016)

[99] Holmberg K, Laukkanen A, Ghabchi A, Rombouts M, Turunen E, Waudby R, Suhonen T, Valtonen K, Sarlin E. Computational modelling based wear resistance analysis of thick composite coatings. *Tribology International* **72**: 13–30 (2014)

[100] Holmberg K, Laukkanen A, Turunen E, Laitinen T. Wear resistance optimisation ofcomposite coatings bycomputational microstructural modelling and simulation. *Surface and Coatings Technology* **247**: 1–13 (2014)

[101] Laukkanen A, Holmberg K, Ronkainen H, Stachowiack

G, Podsiadlo P, Wolski M, Gee M, Gachot C, Li L. Topographical orientation effects on surface stresses influencing on wear in sliding DLC contacts, Part 2: Modelling and simulations. *Wear*, in press, 2017.

[102] Schmitz GJ, Prahl U (eds). *Handbook of Software Solutions for ICME*. Wiley-VCH Verlag GmbH & Co, Weinheim, Germany, 2017.

[103] Jacobs T D, Carpick R W. Nanoscale wear as a stress-assisted chemical reaction. *Nature Nanotechnology* **8**(2): 108–112 (2013)

[104] Berman D, Erdemir A, Sumant A V. Graphene: A new emerging lubricant. *Materials Today* **17**(1): 31–42 (2014)

[105] Khare V, Pham M Q, Kumari N, Yoon H S, Kim C S, Park J I, Ahn S H. Graphene–ionic liquid based hybrid nanomaterials as novel lubricant for low friction and wear. *ACS Applied Materials & Interfaces* **5**(10): 4063–4075 (2013)

[106] Spear J C, Ewers B W, Batteas J D. 2D-nanomaterials for controlling friction and wear at interfaces. *Nano Today* **10**(3): 301–314 (2015)

Kenneth HOLMBERG. He is research professor in tribology, condition monitoring and operational reliability at the VTT Technical Research Centre of Finland. He is the author of two books on coating tribology, editor of 16 books and he has given 53 invited plenary/keynote lectures at international conferences. He has published over 200 scientific papers mainly in areas of tribology, surface engineering, lubrication, computational material modelling and simulation, operational reliability, maintenance and diagnostics. He is interim acting president of the International Tribology Council. He is leader of Model based design of tribological coating systems in IEA programme on Advanced Materials for Transportation 2012-2017. He was president of the OECD IRG Wear group 1992-2006 and chairman of the European COST 516&532 TRIBOLOGY joint research actions 1995-2008. He is chief engineer councillor at the Supreme Administrative Court of Finland and a frequently used expert in the European community and European Science Foundation research actions and programmes. He is member of the Board of Directors at the Taiho Kogyo Tribology Research Foundation (Japan), member of the Programme Committee for Materials Research at the Foundation of Strategic Research (Sweden), and a frequently used consultant for industrial contracts and R&D projects. At VTT he is presently coordinating the strategic computational materials modelling and simulation research, VTT Propertune.

Ali ERDEMIR. He is a distinguished fellow and a senior scientist at Argonne National Laboratory with international recognition and significant accomplishments in the fields of tribology, materials science, and surface engineering. He received his B.S. degree from Istanbul Technical University in 1977 and M.S. and Ph.D. degrees in materials science and engineering from the Georgia Institute of Technology in 1982 and 1986, respectively. In recognition of his pioneering research, Dr. Erdemir has received numerous coveted awards and honors, including six R&D 100 Awards, Mayo D. Hersey Award of ASME, two Al Sonntag Awards and an Edmond E. Bisson Award from the Society of Tribologists and Lubrication Engineers (STLE). He is the past president of STLE and a fellow of ASME, STLE, AVS, and ASM-International. He has authored/co-authored more than 300 research articles (260 of which are peer-reviewed) and 18 book/handbook chapters, edited three books, presented more than 160 invited/keynote/plenary talks, and holds 19 U.S. patents. His current research is directed toward nano-scale design and large-scale manufacturing of new materials, coatings, and lubricants for a broad range of applications in transportation, manufacturing, and other energy conversion and utilization systems.

Friction **5**(3): 285–307 (2017)
https://doi.org/10.1007/s40544-017-0186-2
ISSN 2223-7690
CN 10-1237/TH

REVIEW ARTICLE

Tribological behaviour of sintered iron based self-lubricating composites

Jose Daniel Biasoli DE MELLO[1,2,*], Cristiano BINDER[1], Gisele HAMMES[1], Roberto BINDER[3], Aloisio Nelmo KLEIN[1]

[1] *Laboratorio de Materiais (LabMat), Universidade Federal de Santa Catarina, Florianópolis 88.040-900, SC, Brazil*

[2] *Laboratorio de Tribologia e Materiais, Universidade Federal de Uberlândia, Uberlândia 38.400-902, MG, Brazil*

[3] *Whirlpool, Embraco Unit, Joinville 89.219-900, SC, Brazil*

Received: 09 June 2017 / Revised: 01 August 2017 / Accepted: 22 August 2017

Abstract: This work is a review of previous works, presenting and discussing the most important results obtained by an ongoing research program towards the development of innovative, low-cost, self-lubricating composites with a low friction coefficient and high mechanical strength and wear resistance. Special emphasis is given to uniaxial die pressing of solid lubricant particles mixed with matrix powders and to metal injection moulding associated with *in situ* generation of solid lubricant particles. Initially, a microstructural model/processing route (powder injection moulding followed by plasma-assisted debinding and sintering) produced a homogeneous dispersion of *in situ* generated solid lubricant particles. Micrometric nodules of graphite with diameter smaller than 20 μm were formed, constituting a nanostructured stacking of graphite foils with nanometric thickness. Micro Raman analysis indicated that the graphite nodules were composed of turbostratic 2D graphite having highly misaligned graphene planes separated by large interlamellae distance. Large interplanar distance between the graphene foils and misalignment of these foils were confirmed by transmission electron microscopy and were, probably, the origin of the outstandingly low dry friction coefficient (0.04). The effect of sintering temperature, precursor content, metallic matrix composition and surface finish is also reported. Furthermore, the influence of a double-pressing/double-sintering (DPDS) technique on the tribological performance of self-lubricating uniaxially die-pressed hBN + graphite-Fe-Si-C-Mo composite is also investigated. Moreover, the tribological behaviour of die-pressed Fe-Si-C matrix composites containing 5, 7.5 and 10 wt% solid lubricants (hBN and graphite) added during the mixing step is analysed in terms of mechanical properties and wear mechanisms. Finally, the synergy between solid lubricant particles dispersed in a metallic matrix and fluid lubricants in a cooperative mixed lubrication regime is presented.

Keywords: tribological behaviour; powder metallurgy; iron based; self-lubricating; composites; turbostratic graphite

1 Introduction

Materials developed for friction and wear mitigation are commonly known as tribomaterials. These materials must primarily have mechanical and physical properties such as strength, stiffness, fatigue life, thermal expansion, and damping, in addition to the tribological properties [1]. However, the imperative need for miniaturized, more energy-efficient mechanical systems has imposed more severe tribological contacts, increasing the operational failure for conventional designs [2]. As a consequence, the tribology of critical contacts and new contact materials is the subject of extensive research [3–5]. Moreover, these interfaces must be

* Corresponding author: Jose Daniel Biasoli DE MELLO, E-mail: d.mello@ufsc.br, ltm-demello@ufu.br

resistant to even more severe operating conditions owing to the tendency of using smaller clearances and increased speeds to achieve higher efficiency [6]. Moreover, the state of lubrication in many components is unknown and these components typically operate in the boundary and mixed lubrication regimes [7].

Hence, researchers are constantly exploring new materials and developing novel coatings. As a result, great strides have been achieved in recent years in the fabrication and diverse utilization of new tribomaterials and coatings that are capable of satisfying the multifunctional needs of more advanced mechanical systems [8].

In most common tribological applications, oils or greases are efficiently used to reduce friction and wear [9]. However, when service conditions become very severe (very high or very low temperatures, vacuum, radiation, extreme contact pressures or in very clean conditions such as foods and pharmaceuticals), oils and greases may decompose, oxidize, solidify, evaporate, or act as contaminants. In such cases, solid lubrication may be the only feasible choice for controlling friction and wear [6, 10–18]. A combination of solid and liquid lubrication is another possibility where positive synergistic effects on friction and wear may occur, particularly under mixed lubrication conditions [9].

Several inorganic materials (e.g., transition metals, graphite, hexagonal boron nitride, boric acid, etc.) can provide solid lubrication [12, 19–21]. Most of these materials, such as MoS_2, WS_2, $MoSe_2$, graphite, and hexagonal boron nitride [18, 22–25], have a lamellar crystal structure, which is responsible for their lubricious properties. However, other materials can also exhibit good lubricity despite not having a layered structure, including soft metals, polytetrafluoroethylene (PTFE), polyimide, certain oxides and rare-earth fluorides, diamond and diamond-like carbons (DLC), and fullerenes [12, 20, 21].

Possible methods for applying solid lubricants include sprinkling, rubbing, burnishing, aerosol carrier, and bonding to a surface using adhesives; however, they have been progressively substituted by advanced vacuum deposition processes. However, in all those methods, a finite film thickness limits the lubricious effect. Some self-replenishment mechanism is necessary to ensure a long-lasting lubricious effect of a solid lubricant; however, this is very challenging to achieve [10].

In addition, nanoparticles of solid lubricants (nitrates [26, 27]; fullerene-like dichalcogenides [28–30]; metallic oxides such as CuO, ZnO, ZrO_2, and TiO [31, 32]; titanium borate [33]; carbon nanotubes [34]; and graphene [35] are currently used as additives to liquid lubricants and greases to improve lubrication. However, incorporating nanoparticles into fluids and achieving good dispersion are not an easy task as the nanoparticles tend to agglomerate. To avoid such problems, some studies have shown that surface functionalization is necessary [36–38].

The production of self-lubricating composites appears to be a very encouraging solution [22, 23]. Indeed, metallic matrix self-lubricating composites have been largely used in the industry to reduce wear and friction [10]. They contain a large amount of solid lubricant particles, around 15% to 40%, which span from compounds such as MoS_2, WS_2, $MoSe_2$, NbS_2, $TaSe_2$, hBN, and MoT_{e2} to low-melting metals such as Pb, Sn, Ag, and graphite to polymers such as PTFE [22–25].

There are many manufacturing routes for producing such composites, in polymeric, metallic, or even ceramic matrices [39–41]. For particle-reinforced metallic matrix composites, the synthesis methods are generally classified into vapour deposition techniques [42], solid state processing, and liquid state processing. Copper [43], nickel [44], and ferrous alloys [45, 46] are the materials most frequently used as metallic matrices. Iron-based materials contain iron as a prime constituent and play a significant role in engineering applications owing to their low cost, ease of manufacture, high strength, toughness, ductility, and availability [1].

Powder metallurgy (PM) techniques are especially suitable for the production of such composites. PM offers low cost for large-volume production, is very versatile for producing near-net-shape components, and results in tight dimensional tolerances. Therefore, it is highly competitive and attractive in the industry. In addition, PM exhibits great suitability for tailoring the microstructure according to the property and performance requirements of a given application. In recent years, the production of iron-based sintered

tribomaterials has considerably increased at the expense of copper-based tribomaterials, owing to the lower cost and larger availability of iron powders, as well as their higher strength [47]. In the last decade, high-performance sintered iron-based self-lubricating composites were developed [1, 15, 16, 48–53] as a promising solution for combining a low friction coefficient with improved mechanical and wear resistance.

Sintered components have high porosity, which reduces the mechanical strength and load-bearing capacity when compared with fully dense materials [54, 55], but have the potential to store lubricants that can be released during use [56, 57]. In addition, trapping of wear debris from sliding interfaces may be another important task achieved by the pores [58]; however, the behaviour depends on the imposed tribological system. It has been observed that pores can be beneficial in some systems and detrimental in others [59, 60].

In this context, the production of self-lubricating composites containing small amounts of solid lubricants incorporated into a continuous matrix and having a low friction coefficient combined with high mechanical strength and wear resistance appears to be a promising solution for controlling friction and wear in modern systems and points to an engineered microstructure. In this sense, we have recently proposed [14] a new microstructural model/processing route that can produce a homogeneous dispersion of *in situ* generated, discrete, solid lubricant particles in the volume of sintered composites. The high mechanical and tribological performances of the composites are a result of the combination of matrix mechanical properties [45] and structural parameters, such as the degree of continuity of the metallic matrix, the nature, the amount [61], and the lubricant particle size and distribution [62–64] and shape, which determine the mean free path between solid lubricant particles and the active area covered by each lubricant particle. Moreover, the success of self-lubricating composites depends on the capability of the solid lubricant particles to emerge from their embedded state in the matrix and spread evenly throughout [65–67], thus forming a protective tribofilm [68], which ensures a continuous self-replenishment mechanism for solid lubricant supply [22, 23].

Roughly, powder metallurgy technologies involve all or most of the following process steps: (i) mixing of powders to create a feedstock, (ii) forming (compaction of the feedstock), (iii) sintering, and (iv) secondary operations.

Several processing parameters must be strictly controlled such as the temperature and time of sintering, compression method, techniques for the dispersion of the solid lubricant particles in the volume of the composite, etc. Sintering is the most important step in the production of the composite. The variables in sintering are the atmosphere, heating rate, temperature, dwelling time, and cooling rate. The sintering temperature should be lower than the decomposition temperature of the solid lubricant. Reactions among the matrix, alloying elements, and solid lubricant, which result in loss of solid lubricant, should also be avoided. Several techniques of compaction, such as uniaxial die pressing, extruding, rolling, 3D prototyping, isostatic pressing, cold isostatic pressing, hot isostatic pressing, split die compaction, and powder injection moulding, have to be considered, depending on the geometry and properties desired for the composite material. For the production of self-lubricating composites, the most relevant techniques are uniaxial die pressing and powder injection moulding techniques (Fig. 1).

The dominant compaction technology in terms of both tonnage quantities and number of parts produced is die pressing. Secondary operations such as machining are virtually eliminated owing to the very close tolerances of the finished parts [69]. However, depending on the configuration (single or double action), this technique yields gradients of porosity that may eventually be very high [70–72]. Typically, the production cycle comprises the following: (i) mixing of the powders (base material, alloying elements, and lubricant) to form the feedstock; (ii) filling of a die cavity with the feedstock; (iii) compaction of the powder within the die with punches to form the compact; and (iv) sintering.

Our group recently introduced [14] the use of the double-pressing/double-sintering (DPDS) technique [73] originally developed by Hoeganaes Corporation [74] as a potential option for improving the mechanical strength of self-lubricating sintered composites. The

goal of this method is to increase the density of composites by two-fold pressing.

Roughly speaking, in the metal injection moulding (MIM) process, metal powders and, eventually, precursors are pre-mixed with polymeric binders. The mixture is heated and forced under pressure into a die cavity (in a manner identical to the process used for injection moulded plastic parts) and then ejected after cooling. A subsequent debinding stage removes the polymer, and the final sintering ensures the component's required density (Fig. 1).

The debinding stage, during which the polymeric binder is removed, can greatly influence the mechanical properties of the sintered component. In our case, two steps are used for the debinding process. After the chemical debinding, subsequent plasma-assisted thermal debinding is applied. Thermal debinding, as well as sintering, is performed in a single thermal cycle (plasma-assisted debinding and sintering (PADS)) [75]. The plasma reactor, developed in Ref. [76], was specially designed for the PADS process and described in Refs. [75–77]. It allows the control of the processing temperatures and heating rates independently of the plasma parameters.

As already pointed out, the ideal microstructure of a self-lubricating composite should consist of solid lubricant particles regularly dispersed in a continuous matrix. Unfortunately, such an ideal distribution of the solid lubricant particles is not obtained simply by blending metallic and solid lubricant powders. To produce a self-lubricating sintered composite, there are basically two ways of dispersing the solid lubricant particles in the volume of the metal matrix [78, 79]:

i. mixing the solid lubricant particles with matrix powders;

ii. *in situ* generation of the solid lubricant particles during sintering by dissociation of a precursor.

In the first method, where the composite is obtained by mixing the metallic matrix powders with the solid lubricant particles, the shear stresses that occur during mixing and compacting spread the solid lubricant by shearing between the powder particles of the metal matrix. This leads to an undesirable arrangement in which the solid lubricant covers the metallic particles to a large extent [80]. The presence of these layers of insoluble solid lubricant hampers the formation of contacts between the particles during sintering. This results in a metallic matrix with a high degree of discontinuity (Fig. 2(a)) and leads to a composite material with reduced mechanical strength.

There are two possibilities to overcome these difficulties. The first one is to rearrange the solid lubricant phase in discrete agglomerates by the capillary action of a liquid phase. The second one is to produce the solid lubricant phase *in situ* during sintering by decomposition or dissociation of a precursor, giving rise to a more continuous and sound matrix (Fig. 2(b)).

Therefore, this work is a synthesis of previous works reporting the development of new, low-cost, self-lubricating composites combining a low friction coefficient with high mechanical strength and wear resistance, which are produced by both uniaxial die

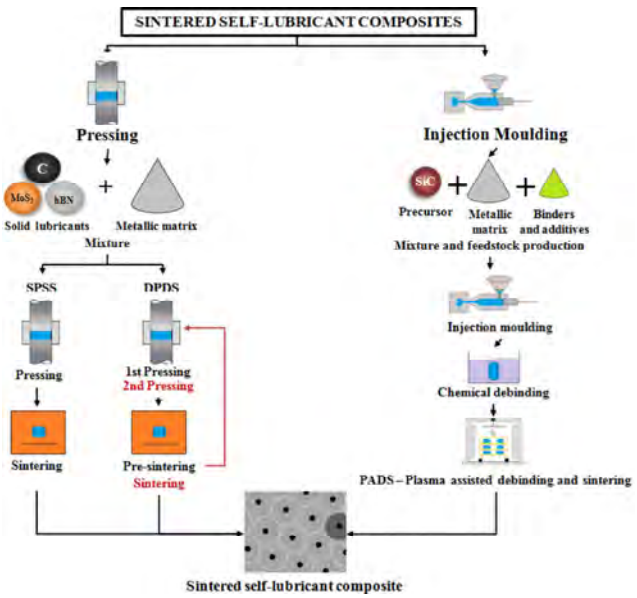

Fig. 1 Main powder metallurgy processing routes for obtaining self-lubricating composites.

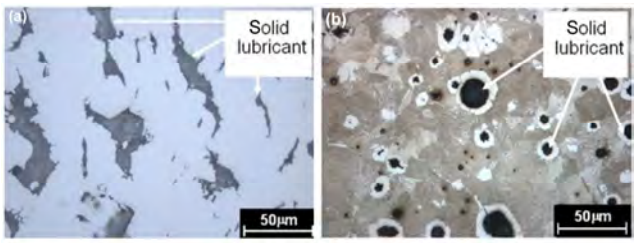

Fig. 2 Solid lubricant particle dispersion. (a) Mixing of powders prior to compaction. (b) *In situ* generation by decomposition of a precursor [81].

pressing of solid lubricant particles mixed with matrix powders and metal injection moulding associated with the *in situ* generation of solid lubricant particles.

2 Materials and methods

2.1 Metal injection moulding

As well described in previous works [2, 15, 48, 82], carbonyl iron powder was mixed with the elemental powder of the alloying elements to produce iron-based composites. Varying amounts of SiC powder (1, 2, 3, 4, and 5 wt% SiC) were also added. The feedstock for injection was prepared in a Haake Sigma mixer (180 ˚C, 70 rpm, 90 min) using 8 wt% of an organic binder system containing paraffin wax, polypropylene, stearic acid (surfactant), ethylene vinyl acetate copolymer (EVA), and amide wax. The specimens were injected (injection pressure = 100 MPa, temperature = 180 ˚C) using an Arbourg 320S injection moulding machine. The debinding was performed in two steps: a chemical debinding followed by plasma-assisted thermal debinding. A single thermal cycle was employed for both the thermal debinding and the sintering, using a so-called PADS process [75–77]. The isothermal sintering was processed at 1,100 ˚C, 1,150 ˚C, and 1,200 ˚C for 60 min.

To evaluate the influence of the matrix on the tribological behaviour, we also produced three different compositions of a 3% SiC composite (Fe-Si-C, Fe-Si-C-Ni, and Fe-Si-C-Ni-Mo). Polishing of the specimens was performed manually with a 1200-, 2400-, and 4000-grit sandpaper for 10 min and 150 rpm in a polishing machine with automatic control of the time and rotation.

2.2 Die pressing

To evaluate the synergy between the different particles of the solid lubricant, we used the conventional route of powder metallurgy. Mixtures were produced using iron as the main constituent of the matrix composite, silicon as an alloying element for stabilization of the iron alpha phase and as a hardener of the matrix, and graphite and hexagonal boron nitride as solid lubricants. The total content of the solid lubricant (5, 7.5, and 10 vol%) as well as the h-BN amount (1, 1.75 and 2.5 vol%) and graphite content was varied. The powders were homogenized in a Y-type mixer before being uniaxially pressed at 600 MPa inside a floating die using a double-action press. After the compaction, the specimens were sintered in a hybrid plasma reactor.

To study the effect of double pressing/double sintering, we added 2.5 wt% graphite + 5.0 wt% hexagonal boron nitride (h-BN) to a ferrous matrix based on a Fe-1.5Mo-1.0Si-0.8C alloy and then compacted and sintered them. As to the compaction step, three alternatives were applied: The first two routes used single-pressing/single-sintering standard die pressing, whereas the third used double pressing/double sintering [14]. The specimens produced by single pressing/single sintering were compacted at 500 and 700 MPa, respectively, and then sintered in a hybrid plasma reactor. The specimens produced by double pressing/double sintering were initially pressed at 500 MPa and then pre-sintered at 700 ˚C for 30 min. After they were cooled to room temperature, a higher pressure (700 MPa) was used in a secondary pressing step. Finally, the specimens were sintered at high temperature under conditions identical to those used for the single-pressed specimens.

Again, the processing routes are well described in previous works [14, 83].

To study the effect of solid lubrication combined with a liquid lubricant in a cooperative lubrication regime, we produced sintered composites that contain particles of the solid lubricant dispersed in a metallic matrix. The processing route is detailed in a recent publication [9], and Table 1 presents the material nominal composition.

2.3 Tribological evaluation

In all cases, the mechanical properties were evaluated

Table 1 Chemical composition of the materials used.

Alloy	Name	Elements				Lubricants	
		Fe	C (%)	Si (%)	Mo (%)	Graphite (%)	hBN (%)
Self-lubricating	C	Bal.	0.6	1	–	2.5	5
	P	Bal.	0.8	1	1.4	2.5	5
Matrix	CM	Bal.	0.6	1	–	–	–
	PM	Bal.	0.8	1	1.4	–	–

by micro-hardness and tensile tests (MPIF standard 10) [84], whereas the tribological behaviour was evaluated using two experimental routes (Fig. 3):

a. Reciprocating sliding tests were carried out at a constant normal load to obtain the friction coefficients and wear rates of the specimens and counter-bodies.
b. Incremental loading was used in reciprocating the sliding tests at regular increments of 7 N every 10 min to assess the scuffing resistance, defined as the work (N·m) until the friction coefficient first achieved values higher than 0.20, meaning the loss of the lubricity effect [85].

All tests were conducted under a constant stroke (5 mm), frequency (2 Hz), relative humidity (50%) and temperature (22 ± 4 ˚C). In all the experimental routes, a hard steel AISI 52100 ball (diameter 5 or 10 mm) fixed to a pivoted arm rested against the specimen surface.

For the lubricated tests, 3D triboscopic maps [86] allowed a better visualization of the evolution of the friction coefficient (axis z) with the position of the counter-body within each cycle (axis x, measured by an additional linear variable differential transformer sensor) and with the total number of cycles (axis y). This required the adaptation of a high-frequency acquisition system to the tribometer. A specially developed LabView® interface was used to produce the 3D maps. The use of triboscopy can help to identify localized events as well as a global evolution, and the technique is well described in Ref. [87].

The tests, detailed in a recent paper [9], were conducted under controlled relative humidity (50%) and temperature (22 ± 4 ˚C) under dry and lubricated (ISO 5 alkylbenzene linear oil + 2% ± 0.5% BTP) configurations.

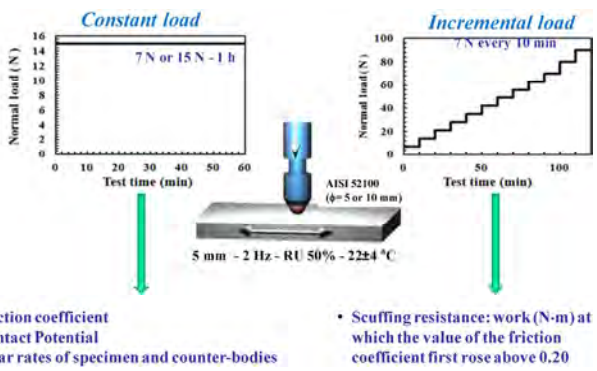

Fig. 3 Tribological characterization.

Wear scars and microstructures were studied using scanning electron microscopy with energy dispersive X-ray (SEM-EDX), transmission electron microscopy (TEM), X-ray diffraction, field emission gun scanning electron microscopy, micro Raman spectroscopy, Auger electron spectroscopy, and white light and laser interferometry. The near-surface porosity was evaluated from transversal sections at 150 μm below the surface using 50 images for each specimen and the software Analysis®.

3 Results and discussion

3.1 Metal injection moulding

The reference alloy presented a microstructure constituted of pearlite (P) and ferrite whereas the addition of SiC to the feedstock powder induced the formation of graphite nodules. Ferrite rings indicated by α surround the graphite nodules, indicated by G (Fig. 4(a)).

Thermodynamics can, in fact, predict the formation of this microstructure [68]. The parameters influencing the microstructural evolution are the amount of SiC

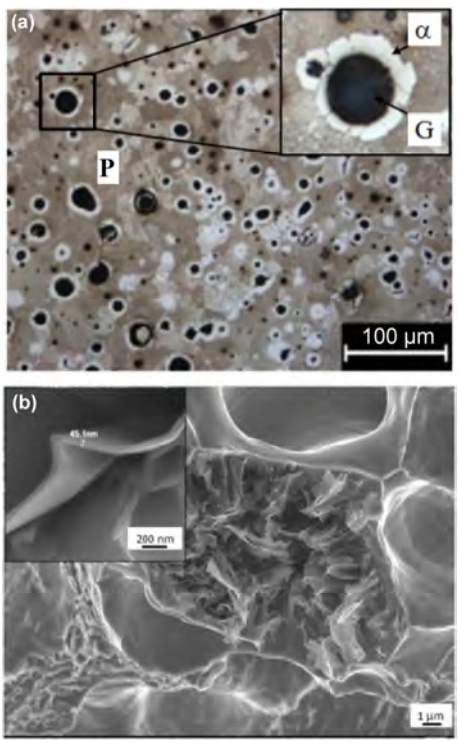

Fig. 4 Typical aspects of the microstructure. Alloy Fe + 0.6C + 4Ni. (a) General aspect, 2% SiC; (b) graphite nodule, 3% SiC.

and the sintering temperature and time [81]. This is well described in a recent paper [68]. Roughly, at the initial stage of the dissociation of the SiC particles, silicon and carbon atoms diffuse into the ferrous matrix. However, the continuous Si enrichment of the ferrous matrix leads to the stabilization of the body-centred cubic structure of the ferrous matrix (ferrite) and yields very low carbon solubility and, thus, drastically reduces the dissolution of carbon. The dissolution of silicon, in contrast, is maintained. As a consequence, ferrite rings are formed around the former SiC particles. The remaining carbon forms graphite nodules (size ≤20 μm). The detail shown in Fig. 4(b) evidences, from a cryogenically fractured surface, that the nodules are nanostructured, composed of stacking of graphite layers with a few tenths of nanometres thick.

The influence of the precursor content and of the sintering temperature on the steady-state friction coefficient under a constant normal load is synthesized in Fig. 5.

The average friction coefficient decreased as the precursor content (and, as a consequence, the number of graphite nodules) increased, independently of the sintering temperature. In general, the reduction was substantial (up to 3% SiC). For values greater than 3% SiC, the friction coefficient was almost constant.

Moreover, the sintering temperature hardly affected the friction coefficients. All composites showed considerably lower friction coefficients than the matrix alloys (graphite-free alloys).

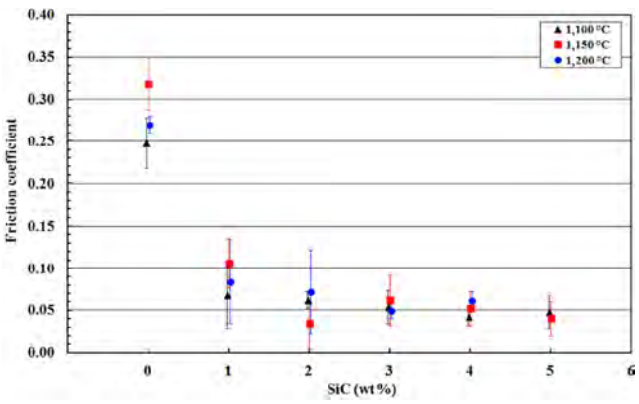

Fig. 5 Effect of silicon carbide content and sintering temperature on the steady-state friction coefficient. Constant load mode, Hertz stress 0.88 GPa. *The x* values were slightly shifted (±0.02) to the left and right for better visualization [48].

In previous papers [2, 15], we concluded that there was, unquestionably, no correlation between the friction coefficient and the mechanical properties of the composites. The outstanding tribological behaviour of these newly developed sintered composites was traced back to the occurrence of a so-called turbostratic 2D graphite, which, according to the literature, has highly misoriented graphene planes. Additionally, the interlamellae distances in 2D turbostratic graphite are much longer than those in highly oriented 3D graphite.

We supposed that graphite foils were removed from the *in situ* generated graphite nodules and remained at the interface [2]. If the reservoirs remain active (open), there will be a continuous self-replenishment of solid lubricants to the contact area and, as a consequence, the maintenance of a protective tribolayer. The small size of the powders in MIM processes makes the mean free path among graphite nodules also small. This ensures an easy "coverage" with the solid lubricant of the surface between the nodules.

To make this point clear, we tested other types of graphite under the same imposed tribological parameter; they were graphite nodules in a nodular cast iron, and the contact was flooded in graphite powder. The graphite-free alloy (0.6 wt% C steel) was also tested as a reference. Figure 6 shows the average friction coefficients (steady state) of the different materials.

The sintered steel had the highest friction coefficient. The presence of graphite (nodules in a nodular cast iron and graphite in powder) induced a strong reduction in the friction coefficient. Further reduction in the friction coefficient was observed when 3% SiC was

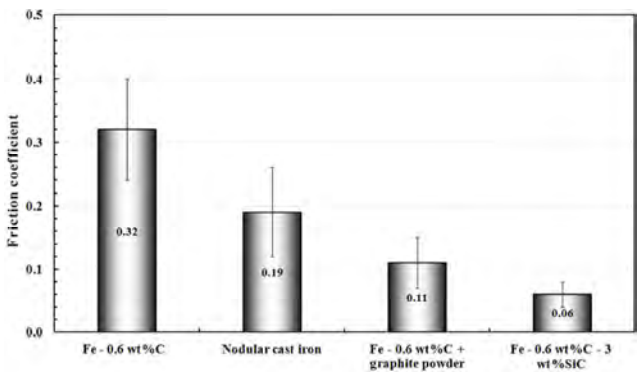

Fig. 6 Variation in the steady-state friction coefficient with the type of graphite. Constant load mode, Hertz stress 0.88 GPa [48].

added, where remarkably low friction coefficient values (0.06) were achieved.

Typical Raman spectra of the different graphite types clearly showed a G band at approximately 1,580 cm^{-1}. Graphite associated with graphite powders and nodular cast iron is characterised as a 3D graphite and is highly aligned according to the literature [48]. The spectrum of the graphite nodules produced by the SiC decomposition clearly showed a D and a D′ band (associated with crystallinity disorder). The analysis of the spectra [15, 48, 68] showed strong evidence of the presence of turbostratic 2D graphite, including widening of the bands, the ID/IG ratio, the size of the graphite crystallites and the shape of the second-order G′ band. The large interplanar distances (≥3.499 Å vs. 3.354 Å for the highly aligned 3D graphite) between the graphene foils and the misorientation of these foils were confirmed by TEM, as illustrated in Fig. 7.

The interaction between the graphene planes was strongly reduced by the large spaces between them, resulting in low shear strength. Thus, it is reasonable to suppose that, during reciprocating sliding, the graphite planes easily sheared, maintaining the contact interface highly lubricated.

On the other hand, scuffing resistance was clearly affected by the sintering temperature (Fig. 8). Significantly higher scuffing resistance (5×) was produced by low sintering temperatures. To advance this point, we used SEM to analyze cryogenically fractured samples sintered at 1,100 ℃ [2]. The analysis showed the presence of partially dissociated SiC particles within the graphite nodules (insert in Fig. 8). They probably induced a greater load-bearing capacity and the protection of the matrix/tribolayer, increasing the scuffing resistance [2].

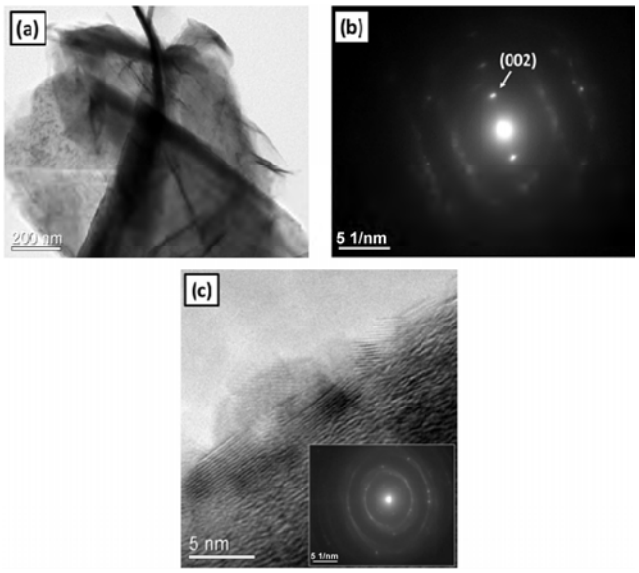

Fig. 7 Typical TEM results. (a) Bright fields of the turbostratic graphite layers. (b) SAED showing the interlamellae space. (c) HRTEM image of graphite sheets obtained from graphite nodules in the Fe + 0.6C + 3SiC specimen [68].

The addition of alloying elements to the composites produced different matrices. As already reported, the addition of SiC to the feedstock powder created graphite nodules in all three microstructures, whereas the metallic matrix varied from ferrite to martensite. Si-stabilized ferrite, with a very small fraction of pearlite, was predominant for the reference alloy (Fe + 0.6% C). The addition of nickel did not substantially change the microstructural constituents, whereas for the Ni + Mo containing alloy the metallurgical constituents changed from ferrite/pearlite to martensite [15].

The influence of metallic matrix on the steady-state friction coefficient is synthesized in Fig. 9. The reference alloy, Fe–C, had the highest mean friction coefficient (0.11). The addition of alloying elements considerably reduced the friction coefficient values (45% reduction for the Ni alloys) to as low as 0.04 (65% reduction) for the Fe–C–Ni–Mo steels [15].

The wear rates of the specimens and counter-bodies are summarized in Fig. 10. Besides presenting a different general appearance, the wear scars presented different widths. Inside the wear scars, there was clear evidence of abrasive wear, shown by the presence

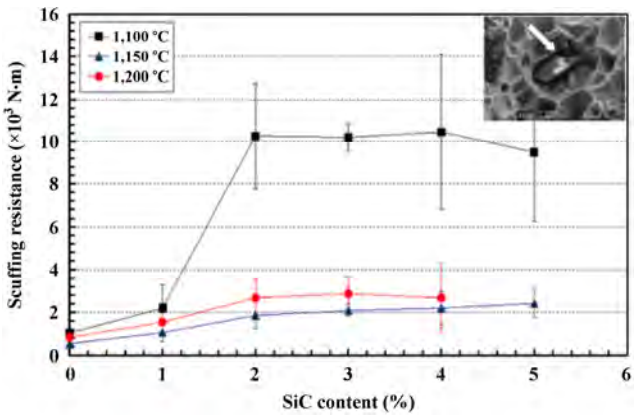

Fig. 8 Effect of SiC content and sintering temperature on the scuffing resistance. Incremental loading mode (increments of 7 N every 10 min) [2].

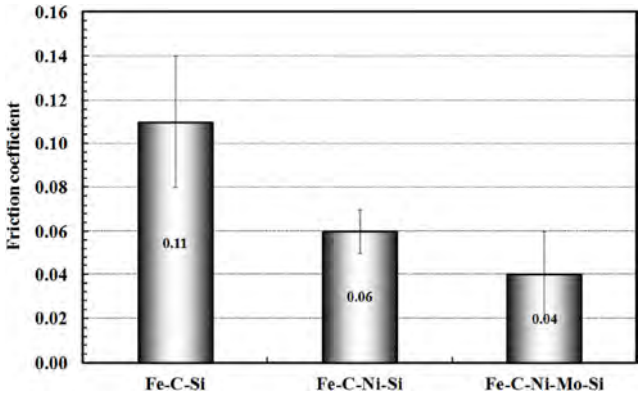

Fig. 9 Effect of metallic matrix on the friction coefficient. Constant load mode, Hertz stress 0.88 GPa [15].

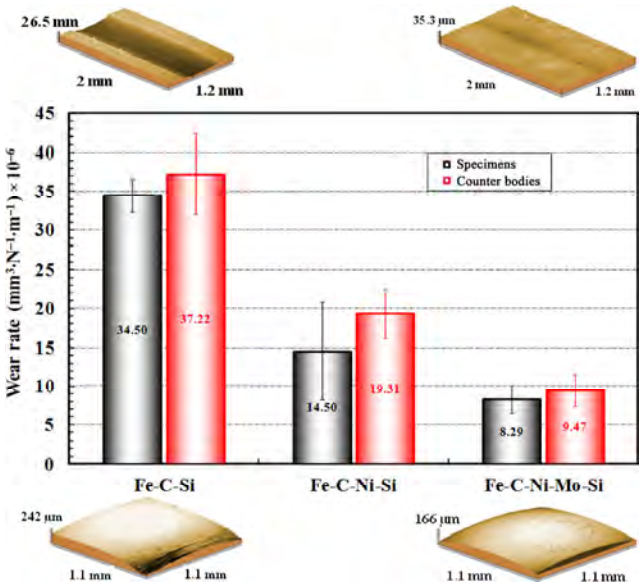

Fig. 10 Wear rates of the self-lubricating composites and AISI 52100 steel ball. Constant load mode, Hertz stress 0.88 GPa [15].

of multiple parallel scratches [15]. The intensity and number of scratches varied according to the material. The wear loss of the counter-bodies exhibited the same behaviour.

Composites containing alloying elements had the lowest wear rates. The reductions in the friction coefficient and the wear of the tribological pair could be associated with the tribofilm transfer effects from the self-lubricating composite to the counter-body and vice-versa. The existence of the protective tribolayer continually avoided metal-to-metal contact and was associated with the resistance of the metallic matrix to plastic deformation and, consequently, to the sealing of lubricant reservoirs [15].

Figures 11(a) and 11(b) presents the dominant Raman

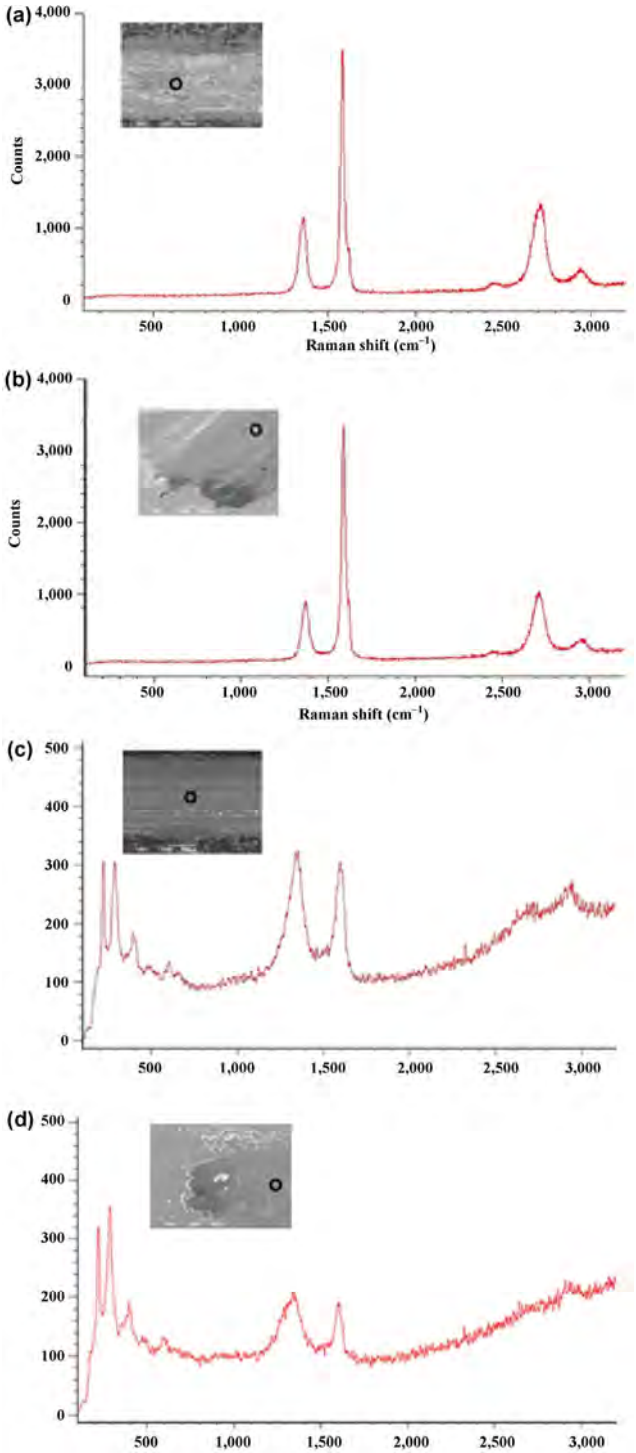

Fig. 11 Typical Raman spectra. (a) Fe-C-Ni-Mo specimen. (b) Fe-C-Ni-Mo counter-body. (c) Fe-C specimen, centre of the scar. (d) Fe-C counter-body, centre of the scar [15].

spectra found in the wear scar for the Fe-C-Ni-Mo alloy.

The spectra of the tribolayers present in the wear scars of the specimens or in the counter-bodies were

almost identical and clearly showed the beneficial presence of turbostratic 2D graphite on both sides of the tribo-pair.

On the other hand, the position in the wear scar affected the spectra found in the wear scar of the reference alloy. Close to the edges of the wear marks, spectra similar to those found in the previous case were measured, whereas those found in the centre of the scar were, to some extent, different (Figs. 11(c) and 11(d)). Aside from exhibiting lower intensities of the 2D graphite characteristic bands and a certain amount of fluorescence, the spectra also showed other smaller bands at lower frequencies. The origin of these bands was attributed to the formation of iron oxide by tribochemical reaction caused by the surrounding atmosphere. High friction coefficients provide a large amount of energy to induce tribochemical reactions. Very likely, iron oxides should induce inferior tribological performance [15].

Figure 12 shows how the surface finish affects the evolution of the friction coefficient during the test duration.

There was a pronounced transient associated with the onset of contact between the specimen and the counter-body at the beginning of the tests before a steady state was reached. The reasons for the difference in the evolution of the friction coefficient within the transient period are not yet well understood and will not be treated in the present paper. The values of the friction coefficient for each test were computed by averaging the steady-state values. The results are summarized in Fig. 13.

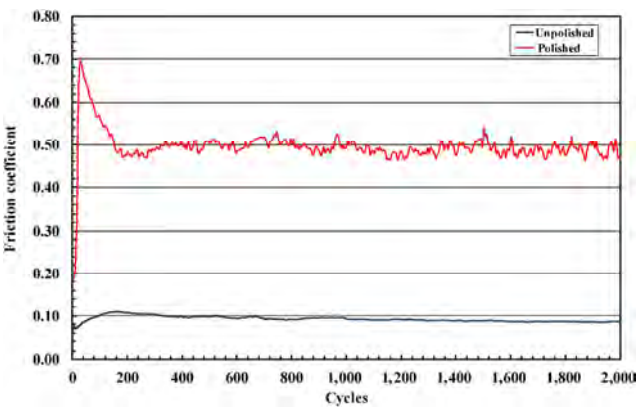

Fig. 12 Typical evolution of the friction coefficient with the number of cycles. 3% SiC, constant load mode, Hertz stress 0.88 GPa [82].

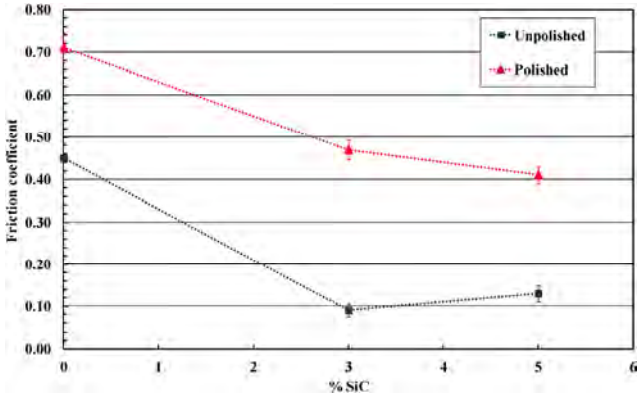

Fig. 13 Steady-state friction coefficient. Constant load mode, Hertz stress 0.88 GPa [82].

The friction coefficient was strongly influenced by the surface finish. Polished specimens exhibited significantly higher friction coefficients ($\mu \geq 0.4$), suggesting that the 2D turbostratic graphite nodules did not actively participate in the tribolayer formation. In fact, multi-elemental X-ray maps obtained by energy dispersive X-ray spectroscopy (EDS) clearly showed a large decrease in the amount of graphite nodules for the polished surface [82]. It can be concluded that, besides significantly reducing the surface roughness, polishing also affected the availability of solid lubricant reservoirs in the active sliding interface.

In addition, the friction coefficient decreased when the amount of precursor (SiC) increased for both surface finishing routes. The reference specimen (0% SiC) had a mean friction coefficient significantly higher than those of the samples containing 3% and 5% SiC.

3.2 Die pressing

Although compaction pressure had almost no influence on the microstructure of the specimens produced with the purpose of investigating the double-pressing/double-sintering (DPDS) processing route (all specimens exhibited a homogeneous dispersion of two different types of solid lubricant: graphite and hBN reservoirs), it strongly influenced their mechanical properties. A small increase (20%) in the ultimate tensile strength occurred owing to an increase in compaction pressure from 500 to 700 MPa, whereas double pressing/double sintering significantly improved the mechanical strength (50%–80%) [14].

Conversely, the effect of the production route on the friction coefficient and wear rate of both the specimens and the counter-bodies was marginal under a constant load tribological test configuration. For the single-pressing/single-sintering tests, there was a high level of dispersion of the results, which was significantly reduced when double-pressed/double-sintered specimens were tested. Finally, the wear rates of the counter-bodies were greater (4×) than those of the specimens, suggesting tribochemical effects [14].

Open reservoirs of the solid lubricant inside the wear tracks after the sliding test were a common characteristic of all the specimens investigated. Hypothetically, this effect ensured a continuous re-supply of solid lubricants to the contact, thus constantly maintaining the system in the lubricious regime (μ < 0.2). The establishment of a protective tribolayer, which contained many randomly distributed cracks, probably originated by its spalling and destruction, was another important feature in almost all of the studied wear tracks. EDS micro-analysis of the tribolayers undoubtedly revealed a strong presence of oxygen and carbon when compared with the unworn surface [14].

Peaks at approximately 1,360 and 1,590 cm^{-1} were identified in the Raman spectra of the tribolayers, as commonly found in carbonaceous materials [14]. The peak at 1,590 cm^{-1} was found for a carbon-based material that contained an sp^2-hybridised carbon. The peak at approximately 1,360 cm^{-1}, the D band, was related to a disordered carbon [88, 89]. The hexagonal boron nitride also had a Raman band close to 1,360 cm^{-1} [90, 91]. Owing to the overlapping of the h-BN and D bands, Raman analysis of the tribolayer was rather complex. Indeed, it was difficult to establish whether the peak close to 1,360 cm^{-1} was due solely to h-BN or due to a contribution of a disordered graphite that originated during sliding. Moreover, low-intensity bands at lower frequencies (100-500 cm^{-1}) were also found in the Raman spectra, possibly related to the presence of iron oxides [92]. The evolution of the contact resistance throughout the tests was another evidence of physico-chemical modifications during sliding [14].

The behaviour of all specimens in the lubricious regime (μ < 0.2) was similar, as demonstrated in Fig. 14(a). This figure depicts the typical evolutions of the friction coefficient and applied normal load with sliding distance in incremental load tests. The single-pressed/single-sintered specimens (SP-500 and SP-700) exhibited a lower and nearly equivalent scuffing resistance. On the other hand, the lubricious regime was longer for the DPDS specimen. The scuffing resistance of the composites was strongly influenced by the compaction step (Fig. 14(b)). Increasing the compaction pressure for the SPSS specimens increased substantially the scuffing resistance (43%), whereas DPDS resulted in greater improvement in the durability of the tribolayer (60% to 130%).

Additional interrupted scuffing tests helped to further elucidate the creation and deterioration of the tribolayer (Fig. 14(a)). Stop A was associated with the establishment of the tribolayer, whereas stop B was connected with the final stages, e.g., after the breakdown of the lubricious regime (μ > 0.20).

The wear tracks associated with stops A and B are illustrated in Figs. 15(a) and 15(b), respectively.

At the beginning of the process (stop A), the tribolayer, indicated by arrows, had a smooth aspect

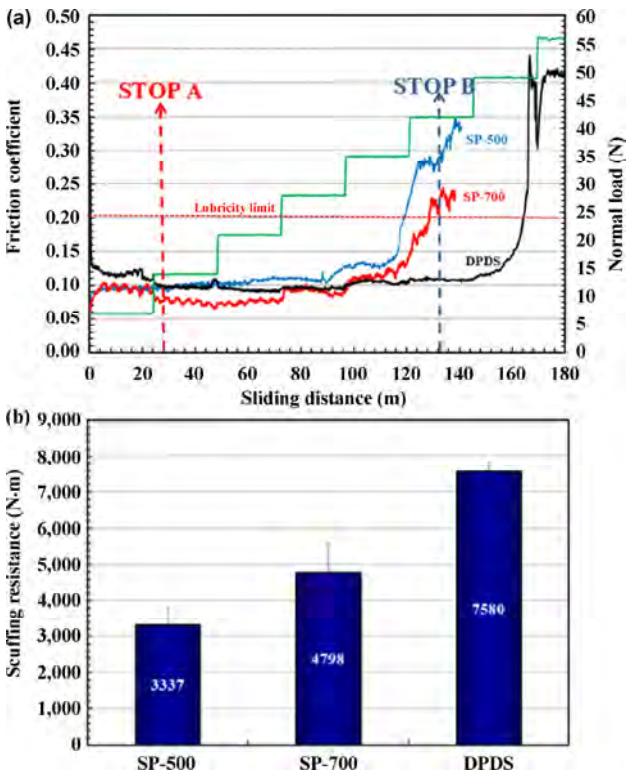

Fig. 14 Incremental normal load tests. (a) Friction coefficient and applied load's typical evolution. (b) Scuffing resistance [14].

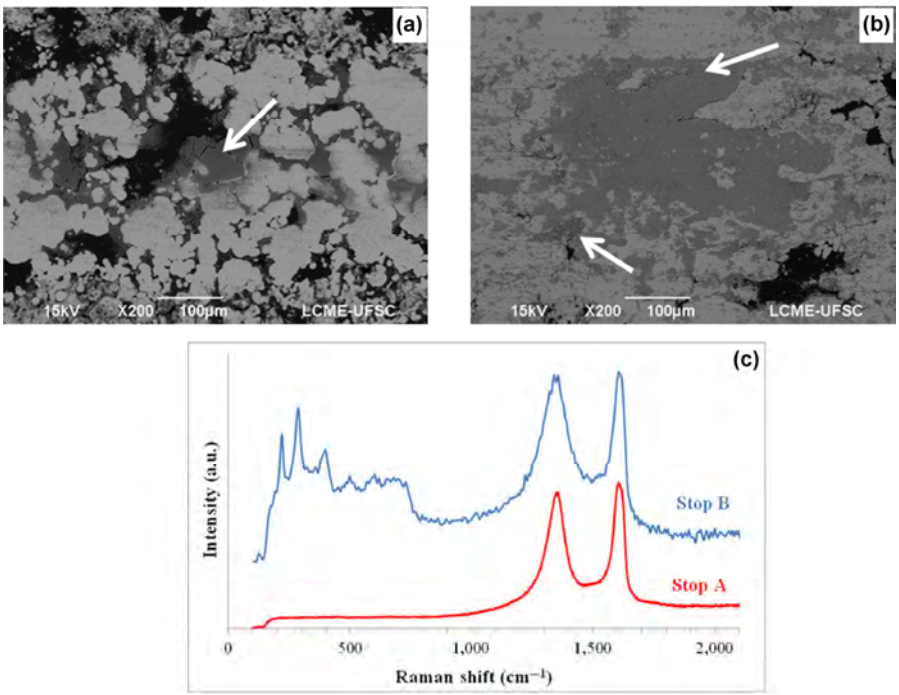

Fig. 15 Evolution of the tribolayers with the testing time. (a) BSE image, stop A. (b) BSE image, stop B. (c) Raman spectra [14].

and clearly originated in sites close to the lubricant reservoirs and then spread over the metallic matrix surface. After its collapse (stop B), the tribolayer was fragmented, with the generation of a large amount of debris (arrows). Furthermore, Raman spectroscopy (Fig. 15(c)) showed that the tribolayer was dissimilar in the two conditions. Under the conditions coupled with stop A, the spectrum only showed peaks relative to graphite, whereas the spectra for the conditions associated with stop B had, in addition, smaller bands at lower frequencies. The origin of these peaks can be attributed to the development of iron oxide by a tribochemical reaction with the surrounding atmosphere [14]. There was reasonable accordance of the peaks in the range between 225 and 650 cm^{-1} with those conventionally reported for iron oxide. The peaks at 290, 408, 497 and 607 cm^{-1} indicated the presence of hematite α-Fe_2O_3, whereas the peak at 667 cm^{-1} was assigned to magnetite Fe_3O_4 [93–95].

The near surface of the transversal sections of the specimens exhibited an evidently strong difference in porosity (inserts in Fig. 16). DPDS specimens showed porosity values around 25%–32% lower when compared to SPSS specimens. German [96] reported that mechanical strength can increase by up to 20% when porosity reduces to 2%–3%. In fact, ultimate tensile strength has shown a linear relationship with porosity [14].

The variation in scuffing resistance with porosity showed a similar relationship (Fig. 16). It seems that scuffing resistance depended on the mechanical support provided by the matrix. Increasing the compaction pressure induced a diminution in porosity, which increased the mechanical properties. Ultimately, better mechanical support was achieved, increasing markedly the durability of the protective tribolayer and, therefore,

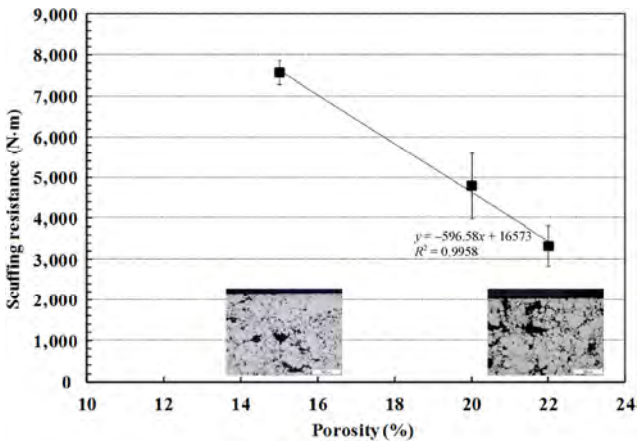

Fig. 16 Correlation between porosity and scuffing resistance.

the scuffing resistance.

The simultaneous addition of hBN and graphite induced an increase in the solid lubricant reservoirs homogeneously dispersed in the metallic matrix [83]. As expected, an increase in the solid lubricant reservoirs was observed when the total solid lubricant content increased, regardless of their solubility in the ferrous matrix. A reduction in the tensile strength was observed with an increase in the total solid lubricant content. In addition, a decrease in the ultimate tensile strength (UTS) within the three levels of the total solid lubricant was observed for increased volume percentages of hBN [83]. Solid lubricant reservoirs may be considered discontinuities in the metallic matrix and have a negative influence on the mechanical properties of sintered composites [2, 47, 61]. However, the use of graphite generates microstructural changes in which diffusion into the matrix may overcome the deleterious effect on the mechanical properties, but reduces the final amount of solid lubricant and compromises the tribological properties. Such metallurgical aspects, as the combined effect of graphite and hBN in the microstructural and tribological evolution of composites, are currently under investigation by our group. The presence of solid lubricant particles induced a complex evolution of the composite mechanical properties:

a. Strengthening of the metallic matrix due to the solubility of solid lubricants into the metallic matrix, in particular carbon diffusion from graphite, increasing the mechanical resistance.
b. Decreased mechanical resistance because of the solid lubricant particles, reducing the degree of continuity of the metallic matrix.

In the present case, it can be claimed that the reduction in continuity of the metallic matrix plays a dominant role. Typical etched composite microstructures, produced with 5 and 10 vol% of the total solid lubricant, can be observed in Fig. 17, in which the specimen containing the highest amount of solid lubricant (Fig. 17(b)) also possesses the higher amount of graphite.

All composites had an almost pearlitic matrix microstructure, with the presence of ferrite grains in the original location of pre-alloyed iron-silicon (Fe + 45 wt% Si) particles and proeutectoid cementite phases along the grain boundaries. The latter increased with the initial graphite content (Fig. 17(b)). When composites are sintered above the ferrite-austenite transformation temperature, enhanced diffusion of carbon into the matrix is likely to occur, further improving the matrix mechanical properties by solid solution and precipitation hardening mechanisms [97, 98]. Figure 18 shows the typical friction coefficient evolution with the test time of the samples produced with 5, 7.5, and 10 vol% of the total solid lubricant content. The friction coefficient of the initial lower

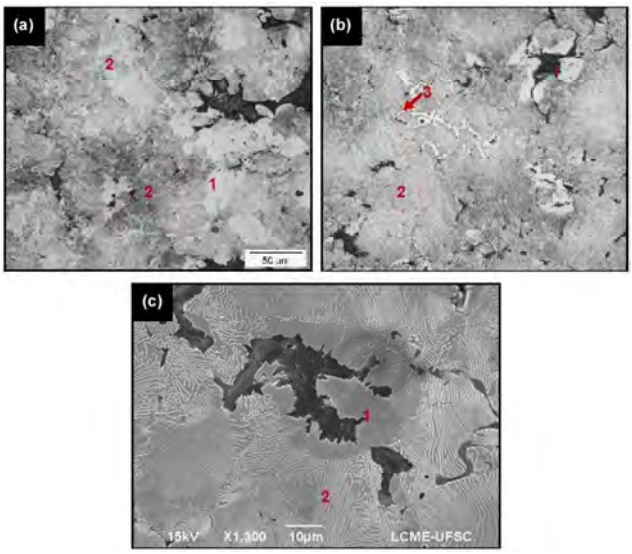

Fig. 17 Typical microstructures of the samples, containing 5 and 10 vol% of solid lubricant, presenting ferrite (1), perlite (2), and cementite (3). (a) 1 vol% hBN + 4 vol% C, (b) 1 vol% hBN + 9 vol% C, and (c) 2.5 vol% hBN + 7.5 vol% C (SEM) [83].

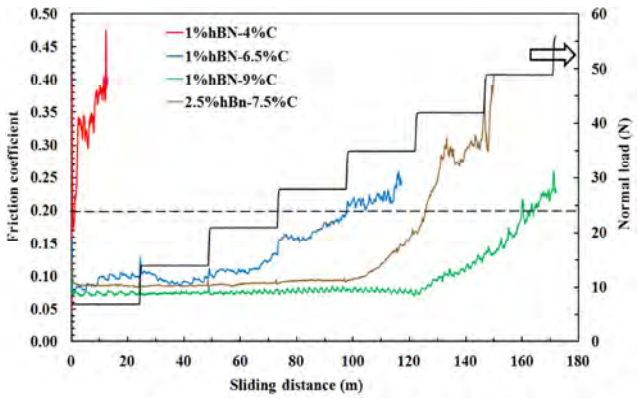

Fig. 18 Evolution of the friction coefficient with the test time, comparing the effect of the total solid lubricant amount (5, 7.5, and 10 vol%) and the effect of the hBN content (1 and 2.5 vol%). Incremental loading mode [83].

solid lubricant content sample (1 vol% hBN + 4 vol% C) sharply increased at the very beginning of the test, presenting an almost inexistent lubricious regime.

The same behaviour was exhibited by other composites containing higher percentages of hBN, but a total content solid lubricant equal to 5 vol% (1.75 vol% hBN + 3.25 vol% C and 2.5 vol% hBN + 2.5 vol% C). For higher solid lubricant contents, all the specimens behaved in a comparable manner in the lubricious regime. On the other hand, the 7.5 vol% composite presented a slightly higher friction coefficient and shorter lubricious regime, whereas the 10 vol% specimens exhibited a longer period in the lubricious regime associated with a steadier and lower friction coefficient. The samples containing 10 vol% total solid lubricant content clearly exhibited a superior performance, and the best results were obtained when combined with a lower amount of hBN, e.g., 1 vol%.

In general, as the total percentage of solid lubricant increased, a substantial rise in the scuffing resistance was noticed. However, for the three levels of total solid lubricant examined, a decrease in the scuffing resistance was observed as the hBN content increased [83].

The results of the additional scuffing resistance tests conducted and interrupted at 14 N, i.e., within the lubricious regime ($\mu < 0.2$), showed that, typically, solid lubricant reservoirs remained open inside the wear tracks [83]. This, hypothetically, ensured a continuous re-supply of solid lubricant to the contact and, as a consequence, the formation of a tribolayer, which served to continuously maintain the system in the lubricious regime ($\mu < 0.2$). It is reasonable to suppose that the wear debris from the specimens and counter-bodies was continuously comminuted, deformed and reacted with the surrounding atmosphere, forming a protective tribolayer. The tribolayer consisted of a mixture of solid lubricants possessing a lamellar structure that induced lower friction coefficients. The wear scar of the composite with a lower initial solid lubricant amount (1 vol% hBN + 6.5 vol% C) revealed a degradation of the tribolayer. For the sample 2.5 vol% hBN + 7.5 vol% C, the degradation was at an initial stage, whereas the composite with a higher initial solid lubricant amount (1 vol% hBN + 9 vol% C) showed no evidence of degradation of the tribolayer, in accordance with the scuffing resistance results [83]. The wear scars on the samples tested at a normal load of 35 N, with a friction coefficient higher than 0.2, which is beyond the lubricious regime for these conditions, showed a degradation of the tribolayer for all composites [83].

Figure 19 presents the typical Raman spectra obtained in the middle of the wear tracks of the composites, after the scuffing resistance tests were interrupted within the lubricious regime.

Typical microstructural analyses clearly showed three distinct regions, as shown in Fig. 19(a) for the 2.5 vol% hBN + 7.5 vol% C composite. The black regions (1) correspond to the solid lubricant reservoirs, where characteristic Raman peaks for both hBN and graphite can be observed, as shown in Figs. 19(b) and 19(c). The peak at approximately 1,360 cm^{-1} (Fig. 19(b)) is attributed to hBN [90, 91], whereas the presence of graphite is confirmed by the characteristic peaks in Fig. 19(c), at approximately 1,590 and 2,730 cm^{-1} [21, 89]. The grey region (2) corresponds to a mixture of the solid lubricants, as observed in Fig. 19(d), which shows the simultaneous presence of graphite and hBN characteristic bands. In this sense, it is reasonable to suppose that this represents a typical tribolayer composition. The lighter region (3) corresponds to the matrix, as shown in Fig. 19(e), in which the spectrum indicates a metallic material and the incipient presence of two small peaks related to carbon and/or hBN indicates their presence. Moreover, at low frequencies, there were low-intensity peaks that can be attributed to the formation of iron oxide by a tribo-chemical reaction with the surrounding atmosphere [94, 95].

The microstructure of the self-lubricating composites used to study the joint effect of solid lubrication in a mixed lubrication regime had two different types of solid lubricant reservoirs regularly distributed in the metallic matrix, whereas, as already indicated, the metallic matrix varied from ferrite + pearlite to martensite (Mo containing alloys) and is well described in a recent paper [9]. As expected, the Mo-rich materials (martensitic) had higher hardness. The addition of solid lubricants did not result in a significant effect on the micro-hardness [9].

Figure 20 illustrates the evolution of the friction coefficient with the sliding distance and position in the stroke under dry conditions.

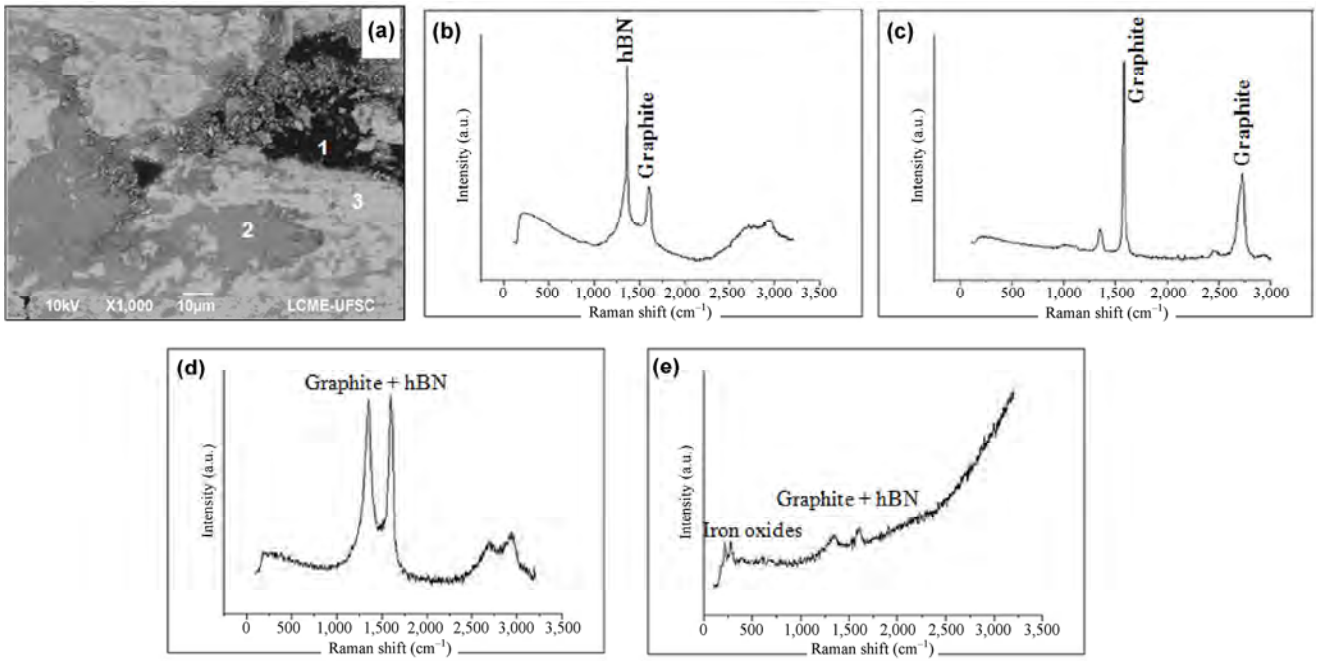

Fig. 19 (a) Typical SEM micrograph of a wear scar within the lubricious regime. Related typical Raman spectra from lubricant reservoirs (region 1, (b) and (c)), tribolayer 2 (region 2, (d)) and metallic substrate (region 3, (e)) [83].

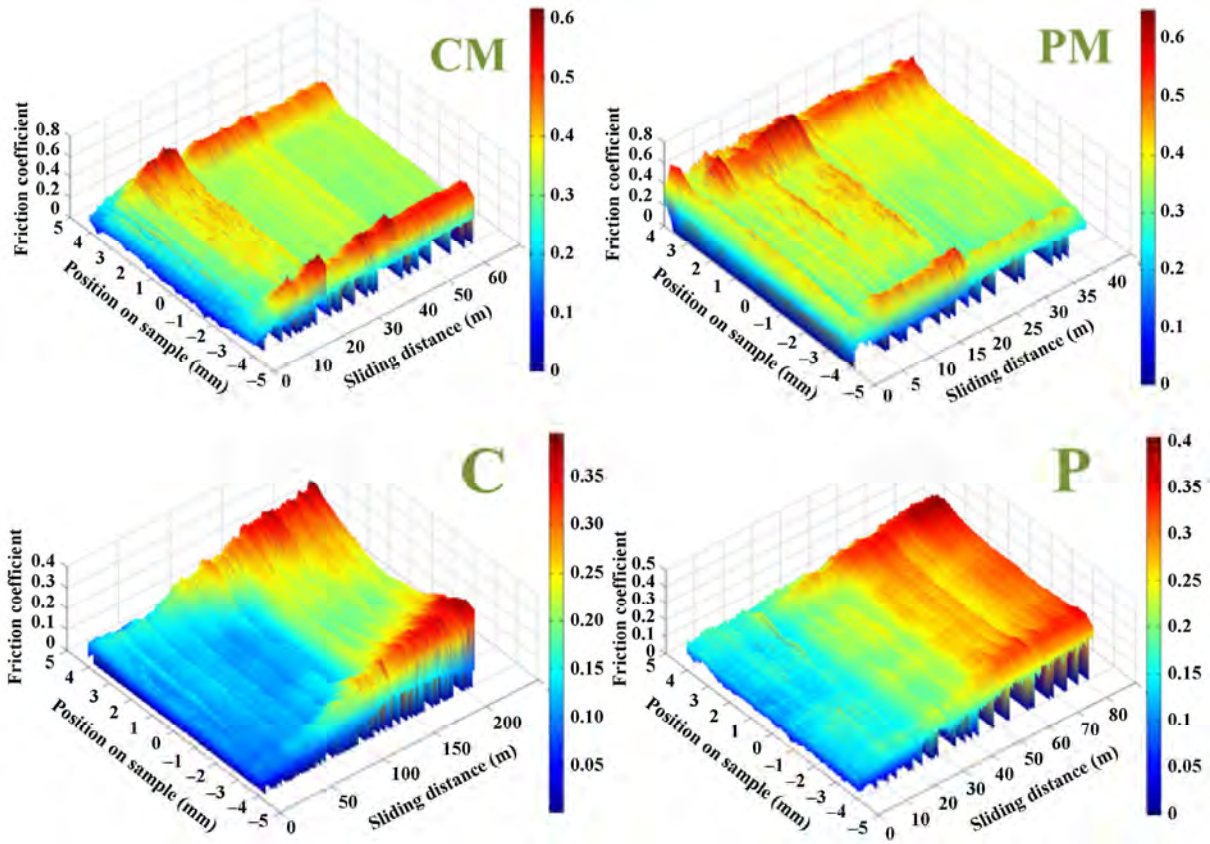

Fig. 20 Typical evolutions of the friction coefficients under dry conditions. Incremental loading mode (increments of 7 N every 10 min) [9].

For the matrix alloys (CM and PM), the friction coefficient showed a tendency to decrease with an increase in normal load. Additionally, it showed an increase at the dead centres of the movement. This difference between friction coefficients was discussed in terms of debris accumulation and change in the lubrication regime. A preponderant role was assigned to the accumulation of debris [9]. The self-lubricated composites showed a lower friction coefficient in the beginning of the test, and the friction coefficient grew continuously and gently as the test progressed (i.e., the normal force increased). For the P composite, the friction coefficient tended to increase more quickly. Additionally, for the C composite, it presented a marked tendency to increase at the dead centres of the movement.

Figure 21 shows the lubricious regime durability under dry conditions. The solid lubricant addition strongly affected the durability of the lubricious regime. The durability increased by two orders of magnitude for the martensitic samples and an impressive three orders of magnitude for the ferrite-pearlite samples. When the self-lubricating composites were compared, despite its lower hardness (composite C; HV = 171 ± 57), the ferrite-perlite matrix exhibited a lubricious regime durability (LRD) approximately one order of magnitude larger than the martensitic structure (composite P; HV = 298 ± 38).

It is reasonable to suppose that the lower hardness of the ferrite-perlite matrix led to higher wear during the lubricious regime, as confirmed by the width of the wear scars presented in Fig. 22 (red arrows) and confirmed by the wear scars profiles [9].

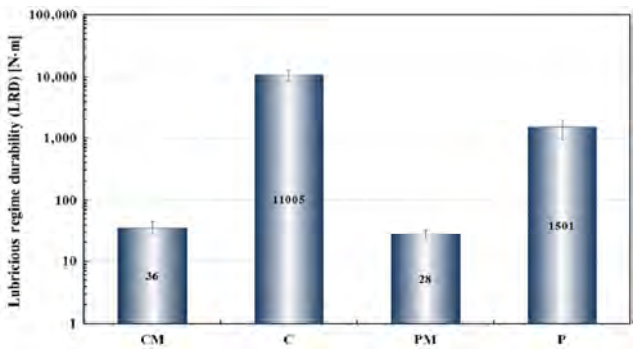

Fig. 21 Lubricious regime durability (LRD) for the dry condition. Incremental loading mode (increments of 7 N every 10 min) [9].

The figure also shows the presence of the active reservoirs of solid lubricants within the wear scars in both samples, as indicated by the green arrows. Higher wear produced a higher amount of wear debris, which, in turn, left the contact richer in solid lubricant. Indeed, the wear scar of composite C (Fig. 22(b)) exhibited a more evident and well-formed tribolayer, shown by the blue arrows, which was much less evident for the case of composite P (Fig. 22(c)). This may result in a low friction coefficient over a longer period, thus increasing the lubricious regime durability. The presence of tribolayers was even less intense for the matrix alloys, probably because of the absence of solid lubricants in the composition of the matrix alloys (Figs. 22(c) and 22(d)).

SEM-EDX analysis showed that the wear scars formed in the self-lubricating composites were quite equivalent in nature, composed mainly of iron and oxygen. Despite the differences in the prevalence of the tribolayers, they indicate the formation of iron oxide by tribochemical reactions caused by the surrounding atmosphere. The solid lubricant reservoirs were composed, as expected, of graphite and hexagonal boron nitride. In addition, the chemical composition of the tribolayers present in the matrix alloys was different from those present in the self-lubricating composites. In fact, analyses by EDX [99] showed that these tribolayers were rich in oxygen, indicating the formation of iron oxide produced by interactions with the surrounding atmosphere. They also had a small amount of chromium, probably from more severe interactions with the counter body (steel AISI 52100).

Figure 23 illustrates the evolution of the friction coefficient with the sliding distance and position in the stroke for the self-lubricated composites in all conditions.

The addition of liquid lubricant to the contact drastically changed the LRD. Indeed, the presence of the lubricant governed the phenomenon. Once again, for the ferrite-pearlite composites, friction coefficient showed a tendency to significantly increase at the dead centres.

Figure 24 compares the LRD for all conditions.

The LRD for the lubricated mode was almost equivalent for all studied materials and was approximately one order of magnitude greater than that

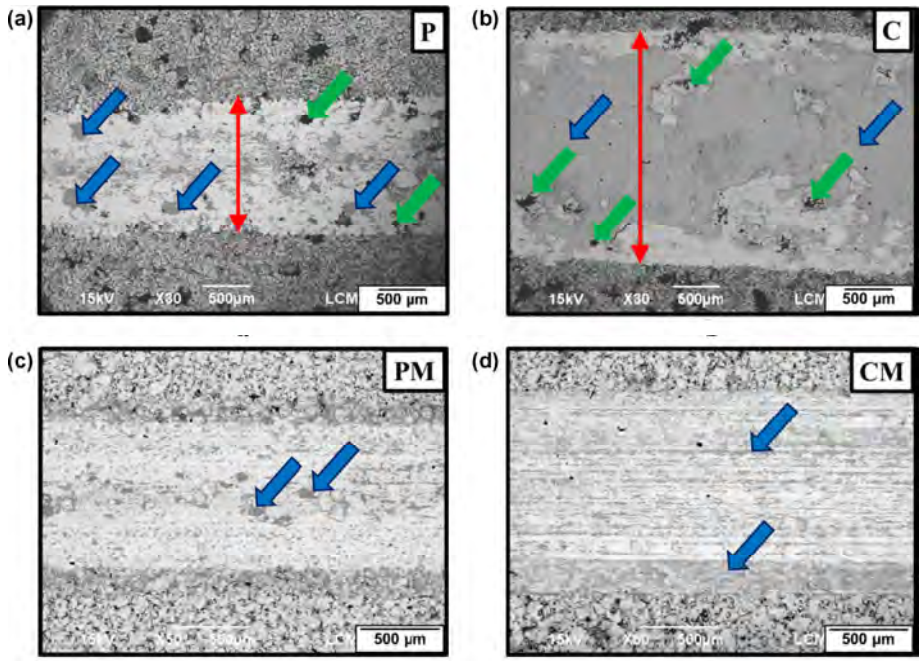

Fig. 22 Typical wear scars. (a) Composite P. (b) Composite C. (c) Alloy PM. (d) Alloy CM. Dry mode [9].

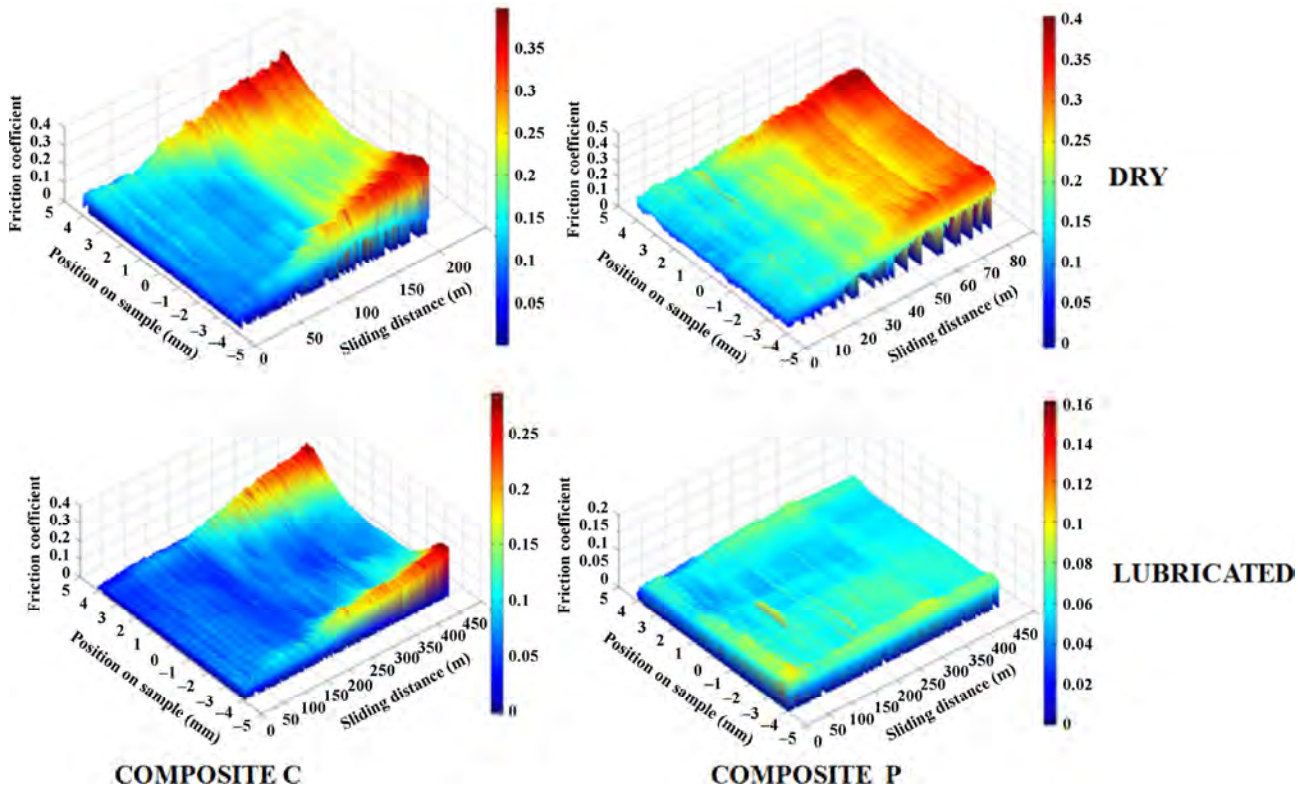

Fig. 23 Typical evolution of the friction coefficient for all conditions. Incremental loading mode (increments of 7 N every 10 min) [9].

of composite C under dry conditions, two orders of magnitude higher than that of composite P and three orders of magnitude greater than that of the CM and PM alloys.

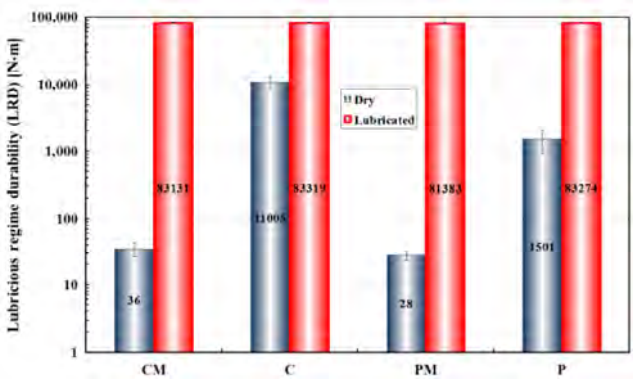

Fig. 24 Lubricious regime durability for all conditions. Incremental loading mode [9].

4 Concluding remarks

We present a synthesis of previous works, presenting and discussing the most important results produced by an ongoing research program towards the development of innovative, low-cost, self-lubricating composites with a low friction coefficient associated with high mechanical strength and wear resistance. The results clearly showed the great tailoring capability of the proposed microstructural model/processing routes applied to the development of iron-based self-lubricating composites.

Moreover, the optimized processing parameters produced, for all compaction techniques, outstanding new iron-based composites, as illustrated in Table 2.

Acknowledgments

The authors acknowledge the following Brazilian agencies for funding this research: CNPq, BNDES, Capes, Fapesc and Fapemig, as well as Whirlpool/Embraco. The helpful discussions and valuable suggestions of Prof. Henara Lillian Costa from the Federal University of Rio Grande, Brazil, are also acknowledged.

Table 2 Properties of the composites.

Property	Powder injection moulding	Uniaxial die pressing
Scuffing resistance (N·m)	8000	7580
Friction coefficient	0.04	0.10
Wear rate specimen ($mm^3 \cdot N^{-1} \cdot m^{-1} \cdot 10^{-6}$)	8.28	10.4
Wear rate counter-body ($mm^3 \cdot N^{-1} \cdot m^{-1} \cdot 10^{-6}$)	9.47	37
Ultimate tensile strength (MPa)	800	270
Elongation (%)	6.3	–

References

[1] Sharma S M, Anand A. Solid lubrication in iron based materials-A Review. *Tribology in Industry* **38**(3): 318–331 (2016)

[2] De Mello J D B, Binder C, Binder R, Klein A N. Effect of precursor content and sintering temperature on the scuffing resistance of sintered self lubricating steel. *Wear* **271**: 1862–1867 (2011)

[3] Cannaday M L, Polycarpou A A. Tribology of unfilled and filled polymeric surfaces in refrigerant environment for compressor application. *Tribology Letters* **19**: 249–262 (2005)

[4] Demas N G, Polycarpou A A. Tribological investigation of cast iron air-conditioning compressor surfaces in CO_2 refrigerant. *Tribology Letters* **22**: 271–278 (2006)

[5] Lee Y Z, Oh S D. Friction and wear of the rotary compressor vane–roller surfaces for several sliding conditions. *Wear* **255**: 1168–1173 (2003)

[6] Solzak T A, Polycarpou A A. Tribology of WC/C coatings for use in oil-less piston-type compressors. *Surface & Coatings Technology* **201**: 4260–4265 (2006)

[7] Pergande S R, Polycarpou A A, Conry T F. Nanomechanical properties of aluminum 390-T6 rough surfaces undergoing tribological testing. *Journal of Tribology—Transactions of the ASME* **126**: 573–582 (2004)

[8] Bhushan B (Ed.) *Modern Tribology Handbook II*. New York (USA): CRC Press, 2001.

[9] Oliveira Jr M M, Hammes G, Binder C, Klein A N, de Mello J D B. Solid lubrication in fluid film lubrication. *Lubrication Science*, Accepted (2017)

[10] Erdemir A. Solid lubricants and self-lubricating films. In *Modern Tribology Handbook*. Bhushan B Ed. New York

(USA): CRC Press, 2001.

[11] Myoshi K. Solid lubricants and coatings for extreme environments: State of the art survey. NASA/TM -214668, Ohio, USA, 2007.

[12] Sliney H E. Solid lubricant materials for high temperatures: A review. *Tribology International* **15**: 293–302 (1982)

[13] De Mello J D B, Binder R, Demas N G, Polycarpou A A. Effect of the actual environment present in hermetic compressors on the tribological behaviour of a Si-rich multifunctional DLC coating. *Wear* **267**: 907–915 (2009)

[14] Hammes G, Schroeder R, Binder C, Klein A N, de Mello J D B. Effect of double pressing/double sintering on the sliding wear of self-lubricating sintered composites. *Tribology International* **70**: 119–127 (2014)

[15] de Mello J D B, Binder C, Hammes G, Klein A N. Effect of the metallic matrix on the sliding wear of plasma assisted debinded and sintered MIM self-lubricating steel. *Wear* **301**: 648–655 (2013)

[16] Scharf T W, Prasad S V. Solid lubricants: A review. *Journal of Materials Science* **48**(2): 511–531 (2013)

[17] Katz A, Redlich M, Rapoport L, Wagner H D, Tenne R. Self lubricating coatings containing fullerene-like WS_2 nanoparticles for orthodontic wires and other possible medical application. *Tribology Letters* **21**(2): 135–139 (2006)

[18] Donnet C, Erdemir A. Solid lubricant coatings: Recent developments and future trends. *Tribology Letters* **17**(3): 389–397 (2004)

[19] Lancaster J K. Solid lubricants. In *CRC Handbook of Lubrication: Theory and Practice of Tribology Vol. II Theory and Design*. Booser E R (Ed.). CRC Press, Boca Raton, FL, USA, 1984: 269–290.

[20] Lansdown A R. *Molybdenum Disulphide Lubrication. Tribology Series 35*. Dowson D (Ed.). Elsevier, Amsterdam, 1999.

[21] Brookes C A, Brookes E J. Diamond on perspective. A review of mechanical properties of natural diamond. *Diamond Rel Mater* **1**: 13–17 (1991)

[22] Donnet C, Erdemir A. Historical developments and new trends in tribological and solid lubricant coatings. *Surf Coat Technol* **180–181**: 76–84 (2004)

[23] Erdemir A. Review of engineered tribological interfaces for improved boundary lubrication. *Tribol Int* **38**: 249–256 (2005)

[24] Pauleau Y, Thièry F. Deposition and characterization of nanostructured metal/carbon composite films. *Surf Coat Tech* **180**–**181**: 313–322 (2004)

[25] Xiong D. Lubrication behavior of Ni-Cr-based alloys containing MoS_2 at high temperature. *Wear* **251**: 1094–1099 (2001)

[26] Kimura Y, Wakabayashi T, Okada K, Wada T, Nishikawa H. Boron nitride as a lubricant additive. *Wear* **232**: 199–206 (1999).

[27] Mosleh M, Atnafu N D, Belk J H, Nobles O M. Modification of sheet metal forming fluids with dispersed nanoparticles for improved lubrication. *Wear* **267(**5–8): 1220–1225 (2009)

[28] Rapoport L, Feldman Y, Homyonfer M, Cohen H, Sloan J, Hutchison J L, Tenne R. Inorganic fullerene-like material as additives to lubricants: structure-function relationship. *Wear* **225–229***:* 975–982 (1999)

[29] Joly-Pottuz L, Dassenoy F, Belin M, Vacher B, Martin J M, Fleischer N. Ultralow-friction and wear properties of IF-WS2 under boundary lubrication. *Tribology Letters* **18**(4): 477–485 (2005)

[30] Tontini G, Semione G D, Bernardi L C, Binder R, de Mello J D B, Drago V. Synthesis of nanostructured flower-like MoS_2 and its friction properties as additive in lubricating oils. *Industrial Lubrication and Tribology* **68**(6): 658–664 (2016)

[31] Hernández Battez A, González R, Viesca J L, Fernández J E, Díaz Fernández J M, Machado A, Chou R, Riba J. CuO ZrO_2 and ZnO nanoparticles as antiwear additive in oil lubricants. *Wear* **265**(3–4): 422–428 (2008)

[32] Wu Y Y, Tsui W C, Liu T C. Experimental analysis of tribological properties of lubricating oils with nanoparticle additives. *Wear* **262**(7–8): 819–825 (2007)

[33] Hu Z S, Dong J X. Study on antiwear and reducing friction additive of nanometer titanium borate. *Wear* **216**(1): 87–91 (1998)

[34] Pacheco F G, Oliveira Jr M M, Santos A P, Costa H L, de Mello J D B, Furtado C A. Tribological evaluation of carbon nanotubes as additives in palm biolubricants. Submitted to *Lubricants* (2017)

[35] Eswaraiah V, Sankaranarayanan V, Ramaprabhu S. Graphene-based engine oil nanofluids for tribological applications. *ACS Applied Materials Interfaces* **3**(11): 4221–4227 (2011)

[36] Fan X, Wang L. High-performance lubricant additives based on modified graphene oxide by ionic liquids. *Journal of Colloid and Interface Science* **452**: 98–108 (2015)

[37] Choudhary S, Mungse H P, Khatri O P. Dispersion of alkylated graphene in organic solvents and its potential for lubrication applications. *Journal of Materials Chemistry* **22**(39): 21032 (2012)

[38] Zhang W**,** Zhou M, Zhu H, Tian Y, Wang K, Wei J, Ji F, Li X, Li Z, Zhang P, Wu D. Tribological properties of oleic acid-modified graphene as lubricant oil additives. J*ournal of Physics D: Applied Physics* **44(**20): 205303 (2011)

[39] Burri D L, Sawyer W G. A low friction and ultra-low wear

rate PEEK/PTFE composite. *Wear* **261**: 410–418 (2006)

[40] Ouyang J H. Microstructure and tribological properties of $ZrO_2(Y_2O_3)$ matrix composites doped with different solid lubricants from room temperature to 800 ºC. *Wear* **267**: 1353–1360 (2009)

[41] Chen B, Bi Q, Yang J, Xia Y, Hao J. Tribological properties of solid lubricants (graphite h-BN) for Cu-based P/M friction composites. *Tribol Int* **41**: 1145–1152 (2008)

[42] Moghadam A D, Omrani E, Menezes P L, Rohatgi P K. Mechanical and tribological properties of self-lubricating metal matrix nanocomposites reinforced by carbon nanotubes (CNTs) and graphene: A review. *Composites Part B Engineering* **77**: 402–420 (2015)

[43] Tsuya Y, Shimura H, Umeda K. A study of the properties of copper and copper-tin base self-lubricating composites. *Wear* **22**: 143–162 (1972)

[44] Liu E R, Wang W, Gao Y, Jia J. Tribological properties of Ni-based self-lubricating composites with addition of silver and molybdenum disulfide. *Tribology International* **57**: 235–241 (2013)

[45] Binder C, Hammes G, Schroeder R M, Klein A N, de Mello J D B, Binder R. Fine tuned steels point the way to focused future. *Metal Powder Report* **65**: 29–37 (2010)

[46] Mahathanabodee S, Palathai T, Raadnui S, Tongsri R, Sombatsompop N. Effects of hexagonal boron nitride and sintering temperature on mechanical and tribological properties of SS316L/h-BN composites. *Materials & Design* **46**: 588–597 (2013)

[47] Teisanu C, Gheorghe S. Development of New PM Iron-Based Materials for Self-Lubricating Bearings. *Advances in Tribology* **2011**: 248037 (2011)

[48] Campos K R, Kapsa P, Binder C, Klein A N, de Mello J D B. Tribological Evaluation of Self-lubricating Sintered Steels. *Wear* **332**: 932–940 (2015)

[49] Schroeder R, Klein A N, Binder C, de Mello J D B. Internal lubricant as an alternative to coating steels. *Met Powder Rep* **65**(7): 24–31 (2010)

[50] Ünlü B S. Tribological and Mechanical Properties of PM Journal Bearings. *Powder Metal* **54**(3): 338–342 (2011)

[51] Merie V V, Candea V C, Popa C O. The influence of nickel content on the properties of fe-based friction composite materials. *Metal Int* **16**(4): 93–96 (2011)

[52] Yilmaz S S, Ünlü B S, Varol R. Effect of boronizing and shot peening in ferrous based FeCu–graphite powder metallurgy material on wear microstructure and mechanical properties. *Mater Des* **31**(9): 4496–4501 (2010)

[53] Dhanasekaran S, Gnanamoorthy R. Microstructure strength and tribological behavior of Fe–C–Cu–Ni sintered steels prepared with MoS_2 addition. *J Mater Sci* **42**(12): 4659–4666 (2007)

[54] De Mello J D B, Binder R, Klein A N, Hutchings I M. Effect of compaction pressure and powder grade on microstructure and hardness of steam oxidised sintered iron. *Powder Metall* **441**: 53–61 (2001)

[55] De Mello J D B, Hutchings I M. Effect of processing parameters on the surface durability of steam-oxidized sintered iron. *Wear* **250**: 435–448 (2001)

[56] Lim S C, Brunton H. The unlubricated wear of iron. *Wear* **113**: 371–382 (1986)

[57] Simchi A, Danninger H. Effects of porosity on delamination wear behaviour of sintered plain iron. *Powder Metallurgy* **47**: 73–80 (2004)

[58] Ahn H S, Kim J Y, Lim D S. Tribological behaviour of plasma-sprayed zirconia. *Wear* **203**: 77–87 (1997)

[59] Chen Q, Li D Y, Cook B. Is porosity always detrimental to the wear resistance of materials?—A computational study on the effect of porosity on erosive wear of TiC/Cu composites. *Wear* **267**(5–8): 1153–1159 (2009)

[60] Dubrujeaud B, Vardavoulias M, Jeandin M. The role of porosity in the dry sliding wear of a sintered ferrous alloy. *Wear* **174(**1–2): 155–161 (1994)

[61] Huang C, Du L, Zhang W. Effects of solid lubricant content on the microstructure and properties of $NiCr/Cr_3C_2$–BaF_2·CaF_2 composite coatings. *Journal of Alloys and Compounds* **479**: 777–784 (2009)

[62] Zhu S, Bi Q, Yang J, Liu W, Xue Q. Effect of particle size on tribological behaviour of Ni_3Al matrix high temperature self-lubricating composites. *Tribology International* **44**: 1800–1809 (2011)

[63] Reeves C J, Menezes P L, Lovell M R, Jen T C. The influence of surface roughness and particulate size on the tribological performance of bio-based multi-functional hybrid lubricants. *Tribology International* **88**: 40–55 (2015)

[64] Zhang D, Lin P, Dong G, Zen Q. Mechanical and tribological properties of self-lubricating laminated composites with flexible design. *Materials & Design* **50**: 830–838 (2013)

[65] Xu Z, Zhang Q, Huang X, Liu R, Zhai W, Yang K, Zhu Q. An approximate model for the migration of solid lubricant on metal matrix self-lubricant composites. *Tribology International* **93**: 104–114 (2016)

[66] Alexeyev N, Jahanmir S. Mechanics of friction in self lubricating composite materials I: Mechanics of second phase deformation and motion. *Wear* **166**: 41–48 (1993)

[67] Alexeyev N, Jahanmir S. Mechanics of friction in self lubricating composite materials II: Deformation of the interfacial film. *Wear* **166**: 49–54 (1993)

[68] Binder C, Bendo T, Hammes G, Neves G O, Binder R, de Mello J D B, Klein A N. Structure and properties of *in situ*-generated two-dimensional turbostratic graphite nodules. *Carbon*, Accepted (2017)

[69] Metal Powder Industries Federation. *Conventional Powdered Metal Component.* Princeton (USA): PM Design Center, 2012.

[70] Tamura S, Aizawa T, Mitzuno T, Kihara J. Steel powder compaction analysis. *International Journal of Powder Metallurgy* **34**: 50–59 (1998)

[71] Al-Qureshi H A, Galiotto A, Klein A N. On the mechanics of cold die compaction for powder metallurgy. *Journal of Materials Processing Technology* **166**: 135–143 (2005)

[72] Pavanati H C, Maliska A M, Klein A N, Muzart J L R. Comparative study of porosity and pores morphology of unalloyed iron sintered in furnace and plasma reactor. *Materials Research* **10**(1): 87–93 (2007).

[73] Milligan D, Engstrom U, Lingenfelter J, Dizdar S, Nyberg I. Materials properties of heat treated double pressed/sintered P/M steels in comparison to warm compacted/sinter hardened materials. *SAE Technical Paper* 2003-01-0338 (2003)

[74] James W B, Causton R J, Fulmer J J. Optimized double press-double sinter powder metallurgy method. US Patent 5080712, 1992.

[75] Machado R, Ristow Jr W, Klein A N, Muzart J L R, Fredel M C, Wendhausen P A P, Fusão D, Alba P R, da Silva N F O, Mendes L A. Industrial Plasma reactor for plasma assisted thermal debinding of powder injection molded parts. US Patent US7718919B2 PCT (WO 2006012718) and INPI (PI-0403536-4), 2010.

[76] Wendhausen P A P, Fusao D, Klein A N, Muzart J L R, Ristow Jr W, Machado R. Plasma assisted debinding and sintering: process and equipment. In *Proceeding of the Powder Metallurgy World Congress & Exhibition EURO PM2004*, 2004: 37–142.

[77] Klein A N, Muzart J L R, Souza A R, Fredel M C, Wendhausen P A P. Process for removal of binders from parts produced by powder injection moulding. US patent US 6579493 B1, 2003.

[78] Klein A N, Binder C, Hammes G, de Mello J D B, Ristow W, Binder R. Self lubricating sintered steels with high mechanical resistance obtained via *in situ* formation of solid lubricant particles during sintering. In *Proceedings of EURO PM2009*, 2009: 191–196.

[79] Binder R, Klein A N, Binder C, Hammes G, Parucker M L, Ristow Jr W. Composição metalúrgica de materiais particulados produto sinterizado autolubrificante e processo de obtenção de produtos sinterizados autolubrificantes. Patent application PI 0803956-9 INPI, Brazil, 2008.

[80] Binder R, Binder C, Ristow Jr W, Klein A N. Composition of particulate materials for forming self-lubricating products in sintered steels product in self- lubricating sintered steel and process for obtaining self-lubricating products in sintered steel. PI0805606-Brazil; US 20110286873A1-USA; International Number: WO 2010/069020 A2-Europe; CN102497948A-China; JP 2012-512320-Japan; 10-2011-0110179-South Korea; SG 172168 A1-Singapore TW 201034773 A1-Taiwan, 2008.

[81] Binder C. Desenvolvimento de novos tipos de aços sinterizados autolubrificantes a seco com elevada resistência mecânica aliada a baixo coeficiente de atrito via moldagem de pós por injeção. (In Portuguese). Ph. D Thesis. Florianópolis (Brazil) Federal University of Santa Catarina, 2009.

[82] Campos K R, Kapsa P, Binder C, Klein A N, de Mello J D B. Influence of surface finishing on the tribological behaviour of self-lubricating iron based composites. *Tribology Transactions*, Accepted (2017)

[83] Hammes G, Mucelin K J, Gonçalves P C, Binder C, Binder R, Janssen R, Klein A N, de Mello J D B. Effect of hexagonal boron nitride and graphite on mechanical and scuffing resistance of self lubricating iron based composite. Wear **376**–**377**: 1084–1090 (2017)

[84] Metal Powder Industries Federation. Standard test methods for metal powders and powder metallurgy products. 2012: 37–42.

[85] de Mello J D B, Binder R. A methodology to determine surface durability in multifunctional coatings applied to soft substrates. *Tribology international* 3**9**: 769–773 (2006)

[86] dos Santos M B, Costa H L, de Mello J D B. Potentiality of triboscopy to monitor friction and wear. *Wear* **332**–**333**: 1134–1144 (2015)

[87] Fontaine J, Bein M, Le Mogne T, Grill A. How to restore superlow friction of DLC: The healing effect of hydrogen gas. *Tribology International* **37**: 869–877 (2004)

[88] Ferrari A C, Robertson J. Resonant Raman spectroscopy of disordered amorphous and diamond like carbon. *Phys Rev B* **64**: 075414 (2001)

[89] Robertson J. Diamond-like amorphous carbon. *Mater Sci Eng* **R37**: 129–281 (2002)

[90] Zhang W J, Chong Y M, Bello I, Lee S T. Nucleation growth and characterization of cubic boron nitride (cBN) films. *J Phys D Appl Phys* **40**: 6159–6174 (2007)

[91] Arenal R, Ferrari A C, Reich S, Wirtz L, Mevellec J-Y, Lefrant S, Rubio A, Loiseau A. Raman spectroscopy of single-wall boron nitride nanotubes. *Nano Lett* **6**(8): 1812–1816 (2006)

[92] de Faria D L A, Venâncio S S, de Oliveira M T. Raman microspectroscopy of some iron oxides and oxyhydroxides.

J Raman Spectrosc **28**: 873–878 (1997)

[93] Oh S J, Cook D C, Townsend H E. Characterization of iron oxides commonly formed as corrosion product on steel. *Hyperfine Interactions* **112**: 59–65 (1998)

[94] Crockett R M, Derendinger M P, Hug P L, Roos S. Wear and electrical resistance on diesel lubricated surfaces undergoing reciprocating sliding. *Tribology Letters* **16**: 187–194 (2004)

[95] Ouyang M, Hiraoka H. Structure and magnetic properties of iron oxide films deposited by excimer laser ablation of a metal-containing polymer Materials. *Research Bulletin* **32**: 1099–1107 (1997)

[96] German R M. *Powder Metallurgy And Particulate Materials Processing. 1st ed*. Princeton New Jersey Metal Powder Industries Federation, 2005.

[97] Hammes G, Gonçalves P, Binder C, Furlan K P, Klein A N. Fe-hBN Composites produced by double pressing and double sintering. *Mater Sci Forum* **802**: 311–316 (2014)

[98] Smith W F. *Structure and Properties of Engineering Alloys*. New York (USA): Mc Graw-Hill, 1993.

[99] Oliveira Jr M M. Lubrificação sólida em meio fluído. (In Portuguese). M. Sc. Dissertation. Universidade Federal de Uberlândia Uberlândia Brazil, 2013.

José Daniel Biasoli DE MELLO. He is an emeritus professor in the College of Mechanical Engineering at the Federal University of Uberlândia, Brazil and a visiting professor at the Federal University of Santa Catarina, Florianópolis, Brazil. He is also a senior researcher (level 1) of the National Research Council (CNPq), Brazil. He received his B.S. degree in mechanical engineering from the Federal University of Uberlândia. In 1983, he received his Doc. Ing. degree in metallurgy from the Institut National Polytechnique de Grenoble, Grenoble, France. He acted as Professeur Associé in the École Nationale Supérieure de Mécanique et Microtechniques, Besançon, France (1990). In 1998–1999, he worked as a visiting scholar at the Department of Materials Science and Metallurgy, University of Cambridge, UK. In 2007 he worked as a Fulbright visiting professor at the University of Illinois at Urbana-Champaign, USA. He is a member of the editorial board of several journals including ***Friction***. Professor De Mello has published more than 300 full papers in proceedings of national and internationals conferences, congresses and journals. Professor De Mello's current researches are abrasion-corrosion, surface durability of solid lubricants, and tribological behaviour of sintered material.

Cristiano BINDER. He received the bachelor degree in chemical engineering from the Federal University of Santa Catarina (2004), the master degree in materials science and engineering from the Federal University of Santa Catarina (2006) and the PhD degree in materials science and engineering from the Federal University of Santa Catarina (2009). He is currently a professor at the Federal University of Santa Catarina. He has experience in the field of materials engineering, focusing on plasma materials processing, powder metallurgy, and surface engineering. He authored/ co-authored 42 research papers and holds 15 patents.

Gisele HAMMES. She received her bachelor degree in materials engineering from the Federal University of Santa Catarina (2004), and her MS and PhD degrees in materials science and engineering from the Federal University of Santa Catarina in 2006 and 2011, respectively. She is currently a postdoctoral researcher at Materials Laboratory at this university, working with self-lubricating materials, soft magnetic materials, and surface engineering. She has published 18 papers and holds 4 patents.

Roberto BINDER. He received the degree in mechanical engineering from the Federal University of Santa Catarina (1993) and the master degree in materials science and engineering from the Federal University of Santa Catarina (1996). He is currently a senior researcher at the Brazilian Compressors Company (EMBRACO), where he has been working since 1998. He is a corporate specialist in engineering and materials science, acting as coordinator of research projects in partnerships with universities and research institutes, activities that aim to overcome the state of the art materials solutions for refrigeration compressors. He has experience in powder metallurgy and surface treatments, working mainly on the following topics: iron and sintered steel, solid lubricants, plasma nitriding, DLC coatings, tribology, and materials characterization techniques.

Aloisio Nelmo KLEIN. He received his B.S. degree in physics (1976) and his master degree in materials engineering (1979) from Federal University of Rio Grande do Sul (Brazil) and his PhD. degree from University of Karlsruhe (Germany) in 1983. He is a full professor at the Mechanical Engineering Department, Federal University of Santa Catarina where he works since 1983. Professor Klein has published more than 340 full papers in proceedings of national and internationals conferences, congresses, and journals. He also holds 123 national and international patents. He is the head of the Laboratory of Materials (LabMat/UFSC) since 1984. He led the creation of the postgraduate course in materials science and engineering (master's and doctorate) at UFSC (1994) and the creation of the undergraduate course in Materials Engineering UFSC (1997 to 1999).

Friction **5**(3): 308–325 (2017)
https://doi.org/10.1007/s40544-017-0177-3
ISSN 2223-7690
CN 10-1237/TH
RESEARCH ARTICLE

Strength of adhesive contacts: Influence of contact geometry and material gradients

Valentin L. POPOV[1,2,*], **Roman POHRT**[1], **Qiang LI**[1]

[1] *Institute of Mechanics, Technische Universität Berlin, Berlin 10623, Germany*

[2] *National Research Tomsk Polytechnic University, Tomsk 634050, Russia*

Received: 01 April 2017 / Revised: 07 June 2017 / Accepted: 19 June 2017

Abstract: The strength of an adhesive contact between two bodies can strongly depend on the macroscopic and microscopic shape of the surfaces. In the past, the influence of roughness has been investigated thoroughly. However, even in the presence of perfectly smooth surfaces, geometry can come into play in form of the macroscopic shape of the contacting region. Here we present numerical and experimental results for contacts of rigid punches with flat but oddly shaped face contacting a soft, adhesive counterpart. When it is carefully pulled off, we find that in contrast to circular shapes, detachment occurs not instantaneously but detachment fronts start at pointed corners and travel inwards, until the final configuration is reached which for macroscopically isotropic shapes is almost circular. For elongated indenters, the final shape resembles the original one with rounded corners. We describe the influence of the shape of the stamp both experimentally and numerically.

Numerical simulations are performed using a new formulation of the boundary element method for simulation of adhesive contacts suggested by Pohrt and Popov. It is based on a local, mesh dependent detachment criterion which is derived from the Griffith principle of balance of released elastic energy and the work of adhesion. The validation of the suggested method is made both by comparison with known analytical solutions and with experiments. The method is applied for simulating the detachment of flat-ended indenters with square, triangle or rectangular shape of cross-section as well as shapes with various kinds of faults and to "brushes". The method is extended for describing power-law gradient media.

Keywords: adhesion; boundary element method (BEM); flat-ended indenters, gradient media

1 Introduction

"Adhesion" is a term which is used for describing different phenomena depending on the branch of science and technology [1]. In the present paper we understand under "adhesion" the relatively weak, so-called van der Waals interaction which acts between any electrically neutral bodies [2, 3]. These forces cause "sticking together" of two solids when they are brought into a contact. In everyday life, adhesive forces can be easily seen in a contact of a very soft elastic material (an elastomer or a jelly) and a smooth solid body. It appears also in a contact of two solids divided by a soft layer as in various types of "stickers" and sticking plasters which are widely used in domestic, industrial and medical applications [4]. Adhesion is used by many groups of living organisms as a mechanism allowing them to attach to various kinds of surfaces [5]. The most famous example of an extremely effective adhesion device is gecko feet which inspired numerous studies of adhesion in the last decade [6]. Adhesion plays an important role in cell mechanics and proliferation [7]. Adhesion is of high technological interest as it is the basis for huge industries of adhesive bonding or reversible "sticking". However, it can also be an annoying and disturbing

* Corresponding author: Valentin L. POPOV, E-mail: v.popov@tu-berlin.de

factor, e.g., preventing a rapid opening of elastomer valves.

Even when the van der Waals forces are much weaker than covalent interactions, the adhesive stress is high enough (on the order of magnitude of 10 GPa [8]) to provide high strength adhesive bonding in all the cases when it is possible to create an intimate contact on the atomic scale. As stated by Kendall [9], "solids are expected to adhere; the question is to explain why they do not, rather than why they do!" The reason for the obvious weakness of macroscopic adhesion in everyday-life is in most cases either a stress concentration on the boundary of a contact, a crack or the roughness of surfaces that hinders the intimate contact of the two bodies. The influence of roughness was in focus of adhesion studies over many years. Now it is well understood under which conditions the roughness can "kill" the adhesion [10, 11] and when it can even enhance it [12].

However, not only roughness defines the adhesive contact. Even in the presence of perfectly smooth surfaces, geometry can come into play in form of the macroscopic shape of the contacting region. Think for instance of medical plasters which have sharp rectangular shape. It is commonplace experience that they tend to detach at their corners first. With rounded edges instead, they hold a lot better, so their sticking capability depends on the contour. This influence of the macroscopic shape of the contact area remained till now out of focus of the research of adhesion. In the present paper we will report an experimental and numerical study on a related model problem. We will consider rigid cylindrical indenters with flat but oddly shaped face in contact with a soft, adhesive counterpart (as schematically shown in Fig. 1). Despite the apparent simplicity of the system, it shows non-trivial and very puzzling behavior!

In mathematical sense, an adhesive contact is equivalent to a crack. In their paper from 1971 [13] —maybe the most famous paper on the theory of adhesive contacts—Johnson, Kendall and Roberts wrote: "the approach followed in this analysis, is similar to that used by Griffith in his criterion for the propagation of a brittle crack." They realized that the adhesive contact is nothing but an "inverted crack"

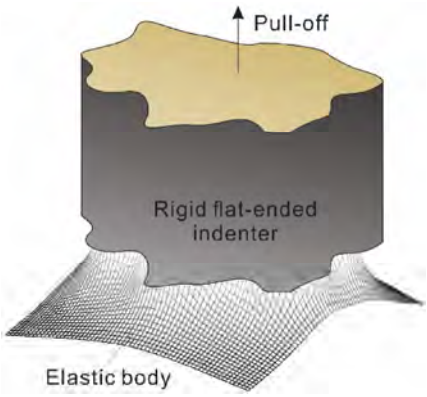

Fig. 1 We consider adhesive contacts of rigid indenters with flat but oddly shaped face with elastic half-space.

and repeated the Griffith analysis for this particular geometrical configuration. In the early 1970s, models in fracture mechanics were already well developed. Because these could be transferred, the theory of adhesion advanced rapidly [14]. Almost at the same time, Cruse, Rizzo and Brebbia introduced the method they called boundary element method (BEM) [15]. However, early formulations of BEM [16, 17] suffered from the problem of inverting the fully populated matrices. Only after algorithms based on fast Fourier transformation were introduced, the BEM became an efficient method. The incorporation of the Griffith criterion in these modern implementations of BEM was first done in 2015 by Pohrt and Popov [18]. The same idea was independently proposed in 2016 by Hulikal et al. [19]. Recently, Rey et al. [20] suggested an alternative approach to the adhesive BEM, which is based on the minimization of the total energy. In the following sections we use the adhesive BEM as described in Ref. [18] for the simulation of adhesion in contacts with various macroscopic shapes and compare with experimental data. We start in Section 2 with general considerations of the adhesion of rigid flat-ended indenters and introduce notions and definitions used later in the paper. We then describe in Section 3 how the Griffith' approach is implemented in the modern boundary element programs for numerical simulation of adhesive contacts in the case of homogeneous media. In the same section, the validation of the method through comparison with known analytical solutions is presented. Sections 4 to 9 are devoted to numerical analysis of the detachment of flat-ended

stamps of various shape of cross-section. Section 10 describes experiments with adhesive contacts of flat-ended indenters. In Section 11, the generalization of the adhesive BEM to graded materials is presented followed by conclusions in section 12.

2 General theoretical considerations

2.1 Flat-ended cylinder with circular cross-section

In the present paper we consider adhesive contacts between variously shaped bodies, but the main attention is paid to "flat ended stamps". Here we introduce some notations which will be needed for discussion in subsequent sections. We start our discussion with recapitulation of the classical problem of adhesion of a flat-ended cylinder with circular cross-section solved by Kendall in 1971 [21]. Let us consider an adhesive contact between a rigid body with plane surface and an elastic half-space in a state with a contact radius a and the indentation depth d. The differential stiffness of a contact with the radius a is equal to

$$k = 2E^* a \tag{1}$$

where $E^* = E/(1-\nu^2)$ is the reduced modulus of elasticity, E is the Young's modulus and ν the Poisson ratio [8]. The elastic energy stored in the medium is equal to $U_{\text{el}} = (1/2)kd^2 = E^* ad^2$ and the adhesion energy $U_{\text{ad}} = -\gamma_{12}\pi a^2$, where γ_{12} is the work of adhesion per unit area. Thus, the total energy of the system is equal to

$$U_{\text{tot}} = U_{\text{el}} + U_{\text{ad}} = E^* ad^2 - \gamma_{12}\pi a^2 \tag{2}$$

At a given d, this function has a maximum at

$$a_{\text{c}} = \frac{E^* d^2}{2\pi\gamma_{12}} \tag{3}$$

This maximum is the only equilibrium state and it is non-stable. If the initial value of a exceeds the critical value defined by Eq. (3), the contact spreads to the infinity (or, if the plane is finite, to the maximum possible radius). For any initial a smaller a_{c}, it shrinks to zero, and the bodies lose the contact. For a cylindrical indenter with finite radius a, Eq. (3) gives the relation between the radius and the critical value of d in the moment of detachment: $a = E^* d_c^2/(2\pi\gamma_{12})$, whence

$$d_c = -\sqrt{\frac{2\pi\gamma_{12}a}{E^*}} \tag{4}$$

where we take the negative solution, as only in this case detachment is (geometrically) possible. The normal force in this critical state is

$$F_{\text{N}} = kd_{\text{c}} = -2E^* a\sqrt{\frac{2\pi\gamma_{12}a}{E^*}} = -\sqrt{8\pi E^*\gamma_{12}a^3} \tag{5}$$

The corresponding "force of adhesion" F_{A} is just the absolute value of this force:

$$F_A = \sqrt{8\pi E^*\gamma_{12}a^3} \tag{6}$$

which reproduces the solution of Kendall [21].

It is interesting to note that in the moment of detachment the elastic energy $U_{\text{el,c}}$ is equal to

$$U_{\text{el,c}} = 2\pi a^2\gamma_{12} \tag{7}$$

while the energy which is needed in order to create the surface area πa^2 should be only

$$\Delta U_{\text{ad}} = \pi a^2\gamma_{12} \tag{8}$$

Thus, half of the external work used for detaching the punch is not for creating the surface, but will eventually dissipate in elastic waves emitted into the elastic body.

2.2 Flat-ended cylinder with arbitrary cross-section

The above analysis can be easily generalized for adhesion of flat-ended indenters whose cross-sections are not a circle but are compact and have no sharp corners (as, e.g., a square or a triangle with rounded corners or similar). In such cases, the contact stiffness is given approximately by

$$k = \beta\cdot 2E^*\sqrt{\frac{A}{\pi}} \tag{9}$$

where A is the cross section area of the indenter and β is a numerical factor on the order of unity. As shown numerically in Ref. [22], for a square cross-section $\beta = 1.021$. For any shape with rounded corners,

this coefficient is even smaller. Thus, with an accuracy of about 2% we can use the Eq. (9) with $\beta = 1$. In this approximation, Eq. (2) takes the form

$$U_{\text{tot}} \approx E^* \sqrt{\frac{A}{\pi}} d^2 - \gamma_{12} A \tag{10}$$

It has one single maximum at

$$A_{\text{c}} \approx \frac{1}{\pi}\left(\frac{E^* d^2}{2\gamma_{12}}\right)^2 \tag{11}$$

At the given cross-section area A, this equation determines the critical approach d_{c}:

$$A \approx \frac{1}{\pi}\left(\frac{E^* d_{\text{c}}^2}{2\gamma_{12}}\right)^2 \tag{12}$$

It is easy to see that Eqs. (4) and (5) remain valid if the "effective radius" $\sqrt{A/\pi}$ is used instead of a. Thus, the estimations of the adhesive force and critical indentation depth are given by the equations

$$F_{\text{A,upper}} = \sqrt{8\pi E^* \gamma_{12} \left(\sqrt{A/\pi}\right)^3} \tag{13}$$

and

$$d_{\text{c,upper}} = -\sqrt{\frac{2\pi\gamma_{12}\sqrt{A/\pi}}{E^*}} \tag{14}$$

We have used index "upper" as the above values give the upper bound of the adhesive stress and distance. All stamps with a "near-circle" cross-section will detach similar to a cylindrical punch: Detachment occurs (almost) at once, at latest when the cross-section area and the approach satisfy Eq. (11). This however, is not valid for more complicated shapes. We will see that for complicated shapes the detachment generally occurs not instantaneously.

At this point let us introduce some notations which we will use in the further analysis. For characterizing a particular shape we will use the so-called "Holm-radius" $a_{\text{H}} = a_{\text{H}}(\{A\})$ [23]. Note that $a_{\text{H}}(\{A\})$ is not a function of the contact area but a functional of the complete contour of the contact, which is stressed by using curly brackets $\{\cdot\}$. The Holm-radius represents the radius of an equivalent circle having the same contact stiffness as the original shape. For a circle $a_{\text{H}} = \sqrt{A/\pi}$ is just the radius of the indenter. In general case

$$a_{\text{H}}(\{A\}) \geq \sqrt{A/\pi} \tag{15}$$

Using the notion of the Holm-radius, Eq. (2) can be rewritten as

$$U_{\text{tot}} = E^* a_{\text{H}}(\{A\}) d^2 - \gamma_{12} A \tag{16}$$

while the normal force is defined as

$$F = 2a_{\text{H}}(\{A\}) E^* d \tag{17}$$

Formally, the stability conditions for a particular contact configuration can be found by solving the variational problem of minimizing the energy functional (16). The explicit analytical form of the functional $a_{\text{H}}(\{A\})$ is not known. Therefore, we will conduct further studies using numerical methods.

However, it is possible to give analytically the upper and lower bounds of the interval in which the main part of the detachment process occurs. As we have seen, within an accuracy of a few percent, the detachment process must start at the distance d_{c} satisfying the condition (12) at the latest. According to the simple estimation, the detachment should occur at once. Equation (13) gives the upper bound for the force of adhesion. However, due to the non-circle form, there exist a possibility that the detached region will spread in a non-circular fashion so that the first term in Eq. (16) dominates the second one. The possibility of this adjustment will be completely exhausted as soon as the contact configuration reaches the incircle of the cross-section, whose radius we denote as a_{incircle}. After achieving this configuration, no equilibrium is possible as this circle has definitely under-critical area. The corresponding normal force in this state represents the lower bound of the adhesion force possible for the given cross-section:

$$F_{\text{A,lower}} = \sqrt{8\pi E^* \gamma_{12} a_{\text{incircle}}^3} \tag{18}$$

In this state, the approach is given by

$$d_{\text{c,lower}} = -\sqrt{\frac{2\pi\gamma_{12} a_{\text{incircle}}}{E^*}} \tag{19}$$

3 Numerical simulation of adhesion

The Griffith' approach to cracks [24] played a prominent role in materials science. His idea was to consider the balance of elastic energy which is released due to a small change in the position of the crack tip and the work of adhesion which is needed to create new free surfaces—instead of a much more complicated stress analysis. The energy-based approach is especially favorable in the case of cracks and adhesive contacts as it allows avoiding the handling of stress singularities at the crack tip. In the preceding section we already used the Griffith energy balance approach to derive Kendall's result for a circular cylinder. Below we discuss briefly the main idea of the Griffith' energy based approach implemented in the boundary element method (BEM) [18].

Let us consider the simplest discretization of the contacting surfaces consisting of square elements with the side length Δ as shown in Fig. 2. The complete procedure of BEM for non-adhesive contact is described, e.g., in Refs. [25, 26]. In each calculation iteration of the BEM, the stress and displacement of each particular discretization element are determined and it is decided if the element should still remain in contact. For non-adhesive contacts this is the case as long as the pressure remains positive. In an adhesive contact, pressures may become negative and thus a more elaborated rule of detachment is needed. In Ref. [18], Pohrt and Popov suggested to make the decision about detachment of a single element based on the Griffith' energy criterion: the element will detach if the energy released by its detaching exceeds the work of adhesion. Following that, we can obtain a stress criterion.

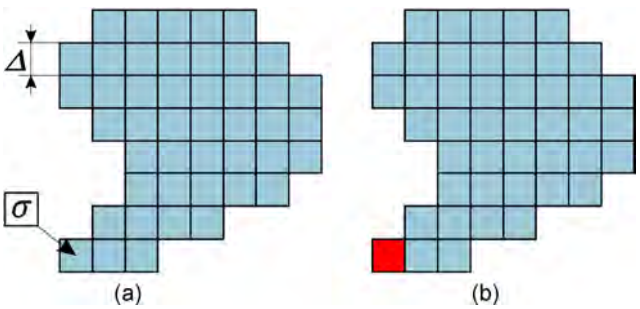

Fig. 2 In each calculation step, stress in each particular discretization element is determined. If the stress σ in a given element at the boundary of the contact area exceeds the critical value (22), it is "detached" and the stress in this element is set zero.

The drop of normal stress results in a decrease of the elastic energy [18] (see also Ref. [8], 2nd edition, Chapter 19):

$$\Delta U_{\mathrm{el}}(\tau) = \kappa \frac{\sigma^2}{E^*} \Delta^3 \tag{20}$$

with

$$\kappa = \frac{2}{3\pi}\left(1 - \sqrt{2} + \frac{3}{2}\log\left(\frac{\sqrt{2}+1}{\sqrt{2}-1}\right)\right) \approx 0.473201 \tag{21}$$

The element is in the state of indifferent equilibrium if the change of elastic energy is equal to the work of adhesion needed for creating the free surface with the area Δ^2, $\Delta U_{\mathrm{adh}} = \gamma_{12}\Delta^2$, or with Eq. (20), $\kappa\sigma^2\Delta^3/E^* = \gamma_{12}\Delta^2$, where γ_{12} is the work of adhesion per unit area. For the critical detachment stress we obtain

$$\sigma_{\mathrm{c}} = \sqrt{\frac{E^*\gamma_{12}}{0.473201\cdot\Delta}} \tag{22}$$

This is a *local*, *mesh-dependent* detachment criterion. It is local in the sense that the critical stress does not depend on the stress in any other parts of the contact. Mesh dependent means that the detachment criterion explicitly depends on the mesh-size. If the tensile stress in one of the elements at the boundary of the contact area is σ and this element will detach, then the stress decreases from σ to zero (the element is shown red in Fig. 2(b)).

The algorithm for a pull-off simulation of adhesive contact is the following. The indenter is initially pressed into the elastic half space to some depth without consideration of adhesion, which results in a surface displacement and some contact area. Now the indenter is pulled off in incremental steps. In each step, the contact area is first considered unchanged, and the stress corresponding to the change of surface deformation is calculated in all points of the calculation grid in the contact area as well as displacements outside the contact area. For this sake, the procedure of non-adhesive BEM described in Ref. [25] is used. Then the stress criterion is checked: all elements whose tensile stress exceeds the criterion are separated from the contact, and a new contact area is obtained.

With this new contact area the stress distribution is recalculated. The procedure is repeated until the stresses in all elements are below the detachment condition. Finally, the normal force can be calculated by integrating the pressure, and the simulation continues to the next pull-off step.

The above adhesive BEM formulation was validated by comparison with known exact analytical solutions as, e.g., flat cylindrical punch [19], parabolic bodies [13] or cone [27], and also passed usual tests of independence of mesh size and orientation of the discretization network [28]. Results of test simulations are illustrated in Fig. 3.

The presented set of simulation results confirms that:

(a) The numerical method reproduces with high precision the known analytical solutions.

(b) Neither the macroscopic force-approach dependence nor the contact configuration does depend on the mesh size.

(c) The simulation results do not depend on the grid orientation.

(d) The square numerical grid has no influence on the axial symmetry of the simulated problem: The simulated contact areas remain exactly circular in spite of the different symmetry of the simulation grid.

Other classes of exact or "asymptotically exact" solved problems are the two-dimensional or "quasi-two-dimensional" problems (as, e.g., a contact of a torus with an elastic half-space). These analytic solutions were also used for testing the above adhesive BEM (see details see in Ref. [29].)

4 Arbitrary contact shapes: Numerical simulation

In Section 4, we use the above adhesive BEM [18] for simulation of contacts of flat-ended stamps having

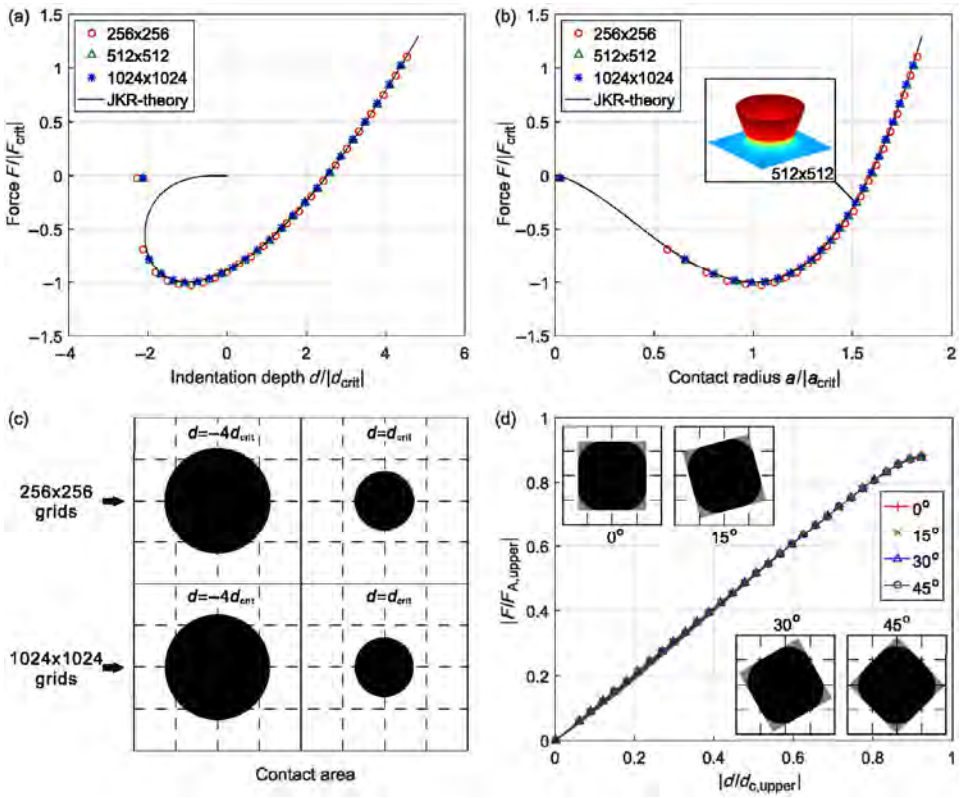

Fig. 3 Comparison of a BEM simulation of the adhesive contact between a parabolic indenter and elastic half-space (JKR-problem) and the analytical solution with (a) force-vs-approach and (b) force-vs-contact-radius relations for three different mesh sizes. (c) Contact areas at four selected approaches illustrating the ideally circular form of contact. (d) Adhesive contact of a square punch in different orientations with 512×512 grid points (dashed lines indicate the orientation of meshing grids), illustrating that neither the contact form not the force-approach-relations do depend on the grid orientation.

non-circle cross-section shape. We simulate the flat adhesive contact for a series of compact shapes. With controlled pull-off-distance d we found the contact area A and the corresponding elastic force as a function of d. Of course, the complete stress and displacement fields are the necessary "byproducts" of the simulation.

4.1 Convex cross-sections

Let us start with simply-connected shapes such as that of a square or triangle. In this case, a rough picture of the detachment process is given by the approximation described in Section 2.2: With increasing distance between the bodies, the force should first increase linearly up to the critical value (14) and then drop abruptly to zero. In reality we expect not an abrupt but a "rapid" decrease.

Numerically calculated force-distance dependencies are presented in Fig. 4. The force and the distance are here normalized by the critical values of the "upper bound" (13) and (14). The quality of the approximation and the deviations can thus be immediately seen. Numerical results confirm the general picture predicted by the simple approximation: the force increases almost linearly and then drops to zero. While for circular cylinders it drops at once, other forms show some prior decrease in the force. The maximum force of adhesion comes very close to the predicted one (the maxima of all curves approach the value "1" in dimensionless units).

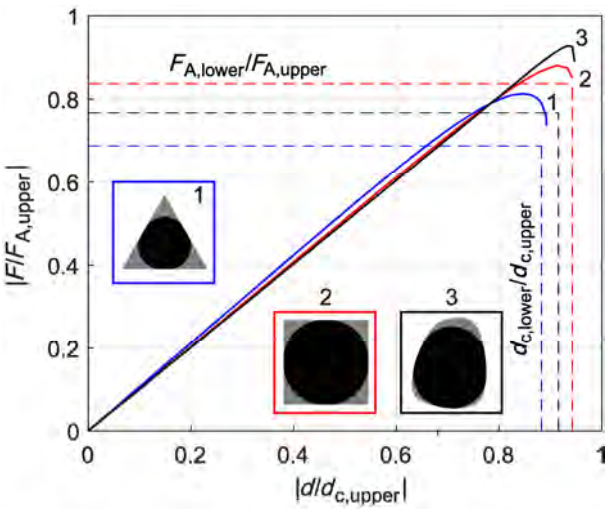

Fig. 4 Force-distance dependencies for simply connected convex profiles: triangle, square, an "arbitrary" shape. The very rough picture in this case is similar to that of a circular cylinder: the normal force first increases linearly with the distance between bodies and then drops sharply. However, the transition from the linear increase to the complete detachment now takes some (small) interval of detachment distances. The state corresponding to the incircle of the corresponding shape is shown with dashed lines.

4.2 Concave cross-sections with outstanding sharp parts

From Fig. 4 one can already see that the deviations from abrupt detachment become larger with the increase of the deviation of the shape from a circle. They become even more pronounced in the case when the indenter shape has sharp outstanding parts like the star shown in Fig. 5. In this case, partial detachment starts early at sharp ends and propagates inwards. After achieving the maximum, the force starts decreasing with further increase of the distance between the bodies. The last stable configuration is very close to

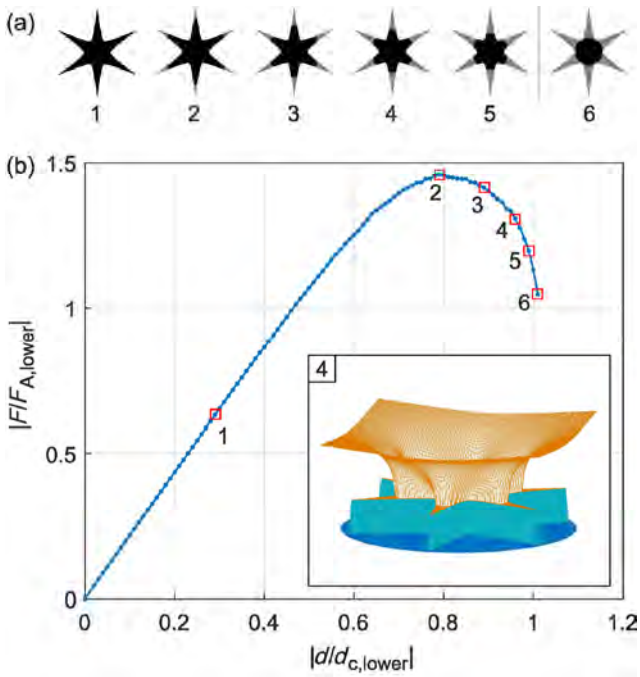

Fig. 5 Detachment process of a flat-ended indenter with the cross-section in form of a "star". (a) A series of contact configurations: grey color shows the initial shape of the indenter and black color the remaining contact area. The detachment starts at the pointed ends of the star and spreads inwards up to a state which is close to the incircle of the shape. (b) Dependence of the absolute value of the normal force on the approach. The force is normalized to the low bound value (18) and the approach to the corresponding value (19). Subplot of (b): Three-dimensional "snap-shot" of the surface of the elastic half-space at a moment of partial detachment.

the incircle of the shape (see Fig. 5(a)). In the subplot Fig. 5(b), the dependence of the normal force on the distance is shown. Note that in this plot the force and the distance are normalized to the values corresponding to the incircle (normalization differs from that used in Fig. 4). The last stable state approaches the value "1" both for the force and distance which in normalized units corresponds to the incircle.

4.3 General discussion of detachment of arbitrary macroscopically isotropic shapes

Let us discuss the detachment of arbitrary complicated shapes, like those shown in Fig. 6. While at the present time a formal formulation of the stages of detachment process is not available, the general rules can be formulated at least qualitatively:

1. The detachment process tends to start at the points having the largest distance from the center of the profile and at the sharp corners.

2. While the outer parts may already be completely detached, the remaining part, which is still adhering, will provide some resistance until aproaches the incircle of the shape.

3. Small heterogeneities such as holes and other small defects have no pronounced influence on the process of detachment. In particular, the detachment rarely starts from the inner discontinuities of the shape.

This last point is interesting with respect to the problem of influence of defects and damages on the general strength of an adhesive contact. In the next section, we study this question in more detail.

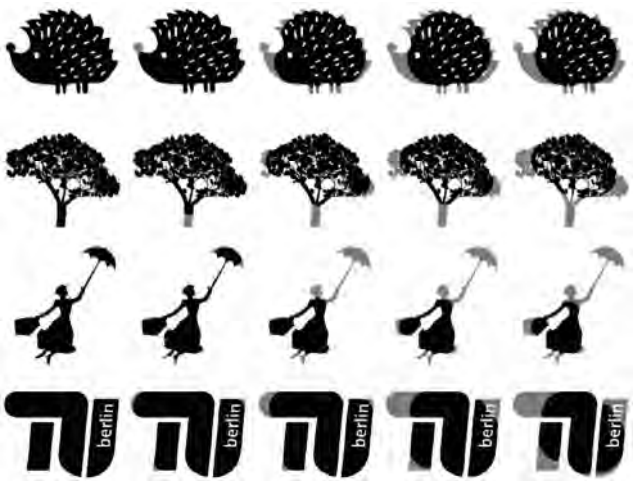

Fig. 6 Decreasing contact areas during the detachment process for a series of flat-ended indenters.

5 Influence of internal discontinuities of the contact shape

Small discontinuities at the face of the flat-ended indenter apparently have no essential influence on the adhesive strength. This is related to the fact that the strength of the contact is determined by the interplay of elastic energy (determined mostly by the stiffness of the contact) and the work of adhesion, which is proportional to the contact area. Small discontinuities do not influence the overall stiffness of the contact, and their influence on the contact area is proportional to the area of the discontinuity. This property can be seen in the curves depicted in Fig. 7.

One can easily see that the V-shaped damage has practically no influence on the overall behavior. Even in the direct vicinity of the damage line there are almost no distinctions in the way that region is detached. One can suggest the following very rough estimation of the influence of damage on the adhesive strength. Assuming that the damage does not change the stiffness (which is governed by the outer bounds of A) and the damage changes the contact area in proportion $A_{\text{real}} = \xi A$, where ξ is the filling factor of the damage,

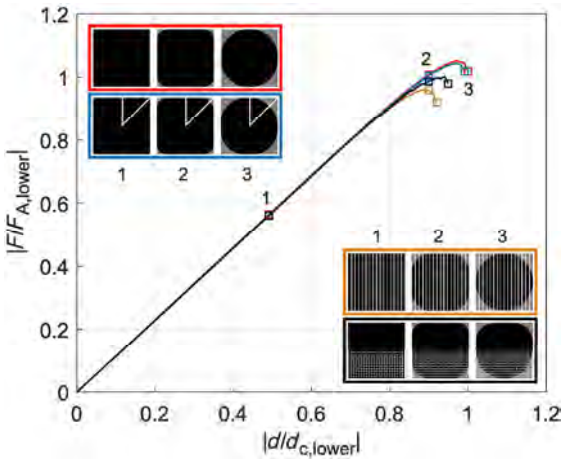

Fig. 7 Contact configurations and force-distance dependencies for a series of squares containing different kinds of faults. The plain square indenter is given as a reference. It is compared with the same square having discontinuities in form of a "V", a series of vertically oriented line-discontinuities as well as line discontinuities filling only the half of the square.

we can rewrite Eq. (10) in the form

$$U_{\text{tot}} \approx E^* \sqrt{\frac{A}{\pi}} d^2 - \gamma_{12} \xi A \tag{23}$$

which differs from Eq. (10) only by replacing the work of adhesion γ_{12} by the effective work of adhesion $\xi\gamma_{12}$. Equation (13) for the upper limit of the adhesive force will be changed to give

$$F_{\text{A,upper}} = \sqrt{8\pi E^* \xi \gamma_{12} \left(\sqrt{A/\pi}\right)^3} \tag{24}$$

Thus, the force of adhesion will be roughly proportional to the square root of the filling factor ξ.

6 Adhesion of brushes

An interesting and important case are brush-like structures: A series of cylindrical, flat-ended columns distributed in some limited area. The discussion of brushes is interesting in particular in the context of contact splitting which is often believed to enhance adhesion. We will show that in our model problem, the splitting alone never enhances adhesion.

Here we present qualitative results for square bruhes. The results were obtained for regular, random and mixed brushes with columns of various shape and distribution (see Fig. 8(a)). While the details of the contact shapes and force-distance dependencies may slightly depend on the particular brush, their general properties are very robust: the sequence of the contact shapes detaching is always similar to that of a continuous square (Fig. 8(b)), and the force-distance dependencies almost collapse to a single linear dependence of the force of adhesion and on the square root of the filling parameter ξ as defined in the Section 5. This master curve shows that the concept of effective surface energy introduced in Section 5 is reasonably applicable.

7 Profiles with nearly constant normal force

The fact that for complicated shapes the normal force can both increase and decrease with detachment distance, puts the question if it is possible to design a shape providing a particular desired behavior, e.g., a constant normal force independent on distance.

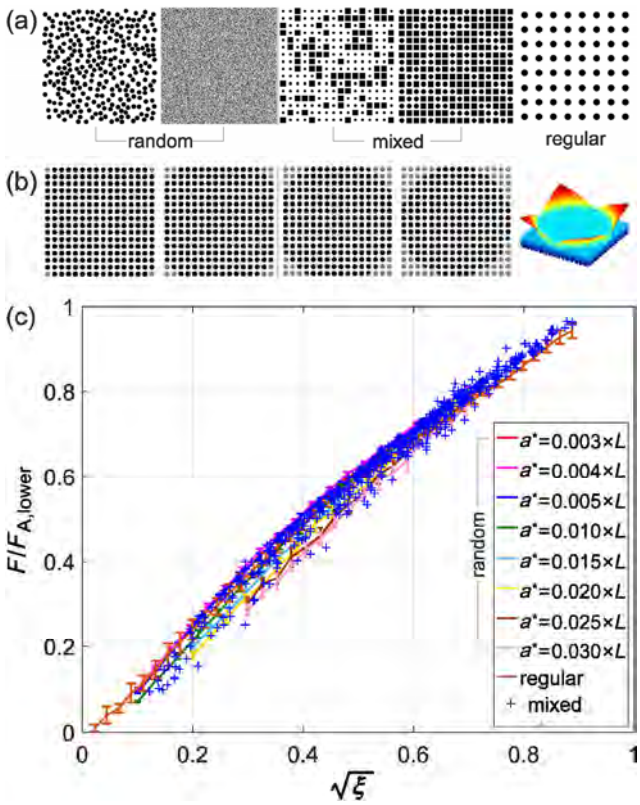

Fig. 8 (a) Shapes and distributions of spikes in a square brush studied here. (b) Consecutive stages of the contact configuration for increasing detachment distance and particular shape of the surface of the elastic counterpart at one of the displayed stages. (c) Simulation points for various brushes and sizes of spikes: All points collapse approximately to a single master curve which is approximately a linear function of the square root of the filling factor ξ. It is given approximately for all cases by Eq. (24). a^* is the radius of the spikes and L is the side length of square. The force is normalized to the value $F_{\text{A,low}}$, corresponding to the radius a_{incircle} of the complete square.

The existence of profiles with a constant normal force can also be deduced from the example of brushes. Let us consider an indenter which filling parameter ξ is a function of the radius r. Assuming that the discontinuities of the shape do not influence the stiffness, we can write the total energy as

$$U_{\text{tot}} \approx E^* a d^2 - \gamma_{12} \int_0^a 2\pi r \xi(r)\,\mathrm{d}r \tag{25}$$

The equilibrium state is determined from the requirement of the minimum of the total energy:

$$\frac{\partial U_{\text{tot}}}{\partial a} \approx E^* d^2 - \gamma_{12} 2\pi a \xi(a) = 0 \tag{26}$$

The relation between d and a is thus given by

$$d = \sqrt{\frac{\gamma_{12} 2\pi a \xi(a)}{E^*}} \tag{27}$$

The normal force in this state is given by

$$F_N = 2E^* ad = \sqrt{8\gamma_{12} E^* \pi a^3 \xi(a)} \tag{28}$$

It is independent of a if $a^3\xi(a) = \text{const}$ or

$$\xi(a) = \text{const}/a^3 \tag{29}$$

Any structure showing in some interval of a this dependence of the filling parameter on the radius should provide an approximately constant adhesive force. For example, one can realize such structure by designing a star with rays having in some interval the thickness which is inversely proportional to the second power of radius. In Fig. 9, we present a spiral which was designed to show this dependence in the outer arms.

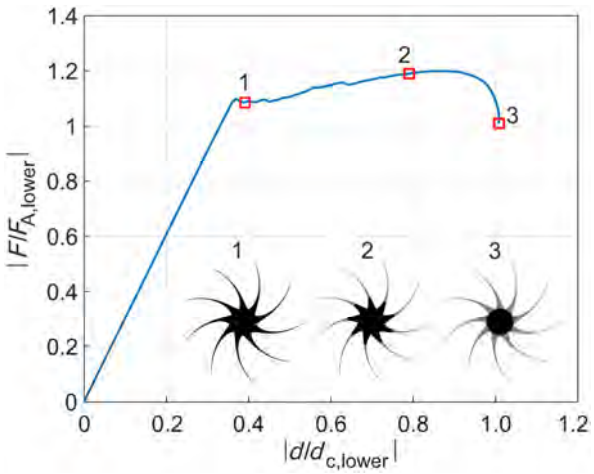

Fig. 9 Detachment process of a flat-ended indenter with the cross-section in form of a "star" having "rays" which satisfy Eq. (29). In this case, a constant pulling force is predicted in the whole range where this dependence is valid.

8 The role of filling parameter

Simulating the detachment of various indenter shapes has revealed a simple rough picture behind it, which we would like to discuss briefly at this point. If the dimensions of the shape are not clearly dominated by one of the in-plane-orientations (as the most shapes considered in this paper) then the detachment can be qualitatively understood in terms of the average filling parameter ξ. During the detachment process the remaining contact area contracts inwards and can be assigned an effective radius radius a. The stiffness of this contact area is almost independent from the structure of faults in the shape and can be approximated by the contact stiffness of the complete circle with the same radius: for homogeneous media, $k = 2E^* a$. On the other hand, the change in adhesive energy is determined by the product of the change of the contact area and the filling factor ξ. The approximate total energy is thus generally given by Eq. (25). The equilibrium radius a is given by requiring that the energy acquires a minimum: Eq. (26). However, this equilibrium condition can only be realized if the equilibrium is stable, thus, additionally the condition $\partial^2 U_{tot}/\partial^2 a > 0$ must be satisfied. From Eq. (26), it follows

$$\frac{\mathrm{d}}{\mathrm{d}a}(a\xi(a)) < 0, \quad \text{stability condition} \tag{30}$$

The radius of the last stable configuration is thus determined by the condition

$$\frac{\mathrm{d}}{\mathrm{d}a}(a\xi(a)) = 0, \quad \text{last stable state} \tag{31}$$

Thus, if the average filling factor at the given radius a is decreasing with the increase of radius faster than $1/a$, there is stable shrinking of the adhesive contact. The critical configuration is determined by the condition that the filling factor is decreasing approximately as $1/a$.

9 Detachment of elongated shapes

The rule that the last stable configuration approaches the incircle of the cross-section is not always applicable especially when the incircle is not defined uniquely. This can be easily illustrated on the example of a flat-ended stamp in form of a stretched rectangle (Fig. 10). As in the case of square shape, detachment starts at the sharp corners. However, we found the last stable configuration to correspond to the state when the detachments of two corners merge together forming a sort of "partial incircle" of the shape. Further increase of distance leads to an abrupt detachment (see Fig. 10(a)).

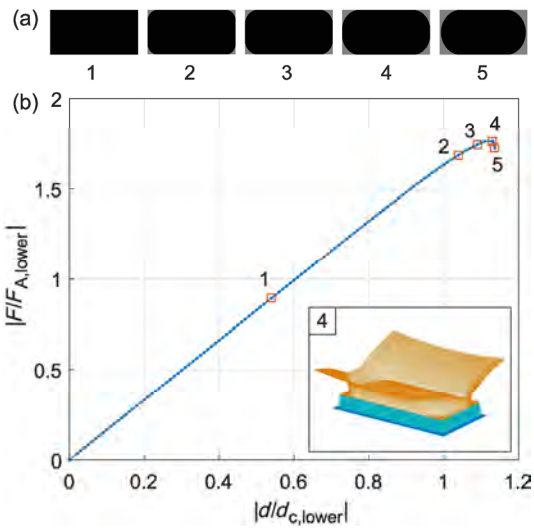

Fig. 10 Detachment of a stamp with a rectangular cross-section: (a) Consecutive shapes of the remaining contact area; the last one shown configuration corresponds to the last state of stable equilibrium. (b) The force-distance dependence. The complete detachment occurs in a configuration which strongly differs from the largest incircle of the rectangle.

It is interesting to note that this behavior can still be understood qualitatively within the above described concept of "damage filling factor". Let us consider the extreme case of a very long rectangular stamp as shown in Fig. 11. If the half width of the remaining adhering area is a, then the contact stiffness will scale approximately linearly with a (up to a logarithmic factor). On the other hand, as the thickness of the rectangle is constant, the "filling factor" will be approximately inversely proportional to the radius a. Thus, for the rectangle, the stability condition (30) is never satisfied. As a matter of fact, the rectangular shape represents a degenerate case when all configurations correspond to the critical state. Therefore, even a small slope of the shape leads to to the possibility of a stable propagation of the detachment front as illustrated in Fig. 11.

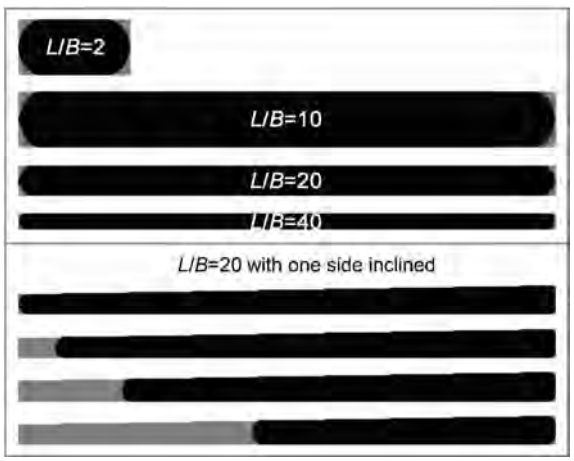

Fig. 11 Detachment of flat-ended stamps with rectangular cross-sections having various aspect ratios L/B. We show only the final stable states. Independently from the aspect ratio, the final state corresponds to almost complete rectangle with rounded-up corners. When the shape has an inclination, a continuous detachment becomes possible.

10 Complicated contact shapes: Comparison of simulation and experiment

In addition to our numerical studies, we conducted experiments with a series of compact flat indenter shapes. We did this to further validate our numerical method and to see whether the principal features of the detachment behavior could be reproduced. The experiments were conducted using a setup as depicted in Fig. 12. The rigid indenter consisted of a laser-cut acrylic glass with flat face. It was brought into contact with transparent gelatin with illumination from the sides. The acrylic glass was lifted with a precision linear stage attached to a strain gage sensor recording the adhesive force. The actual contact region was recorded from underneath using a digital camera.

In the distance-force-dependencies we find experimentally that the general features match those of the simulations. First we observe that the adhesive force always starts to rise linearly with the lifting height. In a second phase, detachment becomes visible and we observe a weaker rise of F with d. When the lifting is stopped and reversed, we find that the contact configuration reassumes the shape corresponding to the same height from the lifting phase. Thus, we deal with reversible adhesion. Finally the contact is lost completely and relatively fast. It then consists of a quickly shrinking circle. As in the simulations, the last stable configuration can be roughly approximated by the largest circle to fit inside the initial shape.

Figure 13 presents a comparison of the detachment process from experiment and simulations. The consecutive shapes of the remaining adhesive contact zones are very similar to the simulation results for all experiments which we carried out. The differences

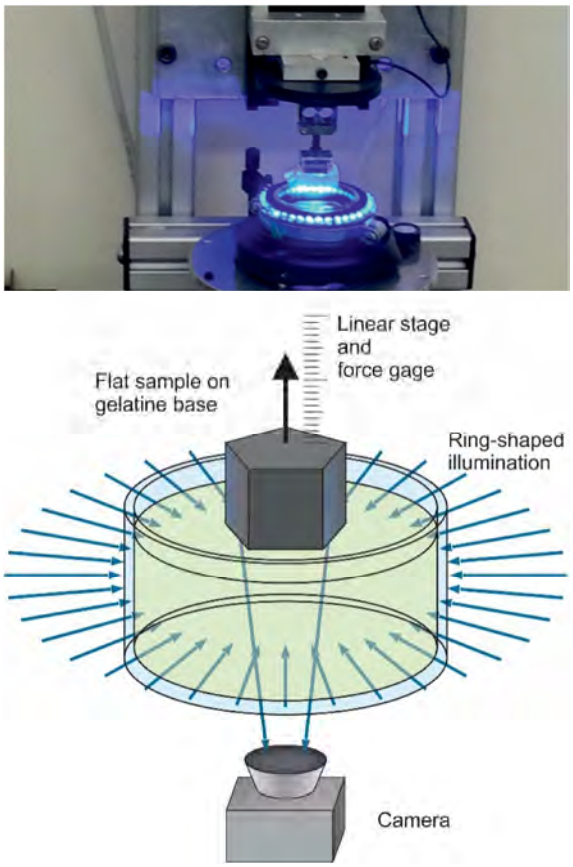

Fig. 12 Schematic display of the experimental setup. A flat but oddly shaped sample of acrylic glass is placed on a gelatin base and slowly pulled off. The contact between both can be observed by a camera through the gelatin. For increased visibility of the edges, the contact zone is illuminated in a circular fashion.

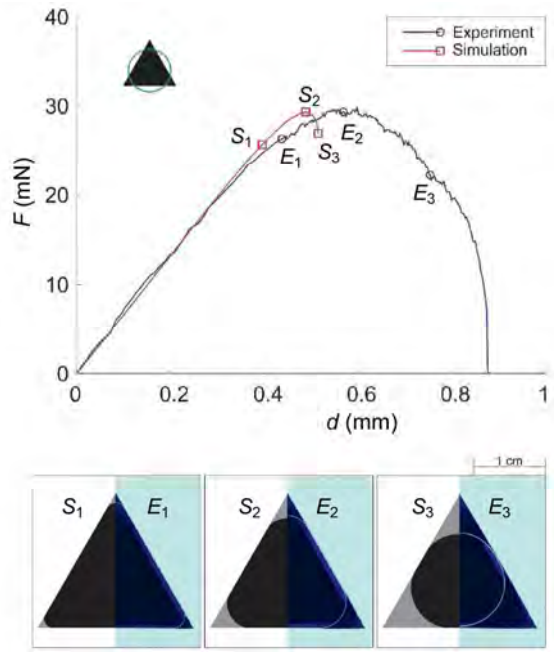

Fig. 13 Dependency of the attracting force on the pull-off distance for a triangular shape. The blue curve represents experimental data, while the red curve is obtained by simulation. The simulation results were fitted to the experimental data by assuming $E^* = 6.02$ kPa and $\gamma_{12} = 0.062$ N·m^{-1}. Highlighted points (S_1, S_2, S_3, E_1, E_2, E_3) refer to Fig. 13 (below). The green circle in the shape representation depicts the equivalent Holm-radius of the triangular shape. In the lower part, the real contact area for selected pull-off-states is shown. All three pictures show numerical results on the left hand side, where the initial shape is gray, and remaining contact area is black. The right hand sides show photographic images of the contact. The edge of the contact zone can be seen as a bright line.

in the force-displacement relations are stronger: The plateau region, where most of the detachment happens, is larger in experiments than it is in simulations (see for instance the positions of the point S_1, S_2 and S_3 and the corresponding experimental points E_1, E_2 and E_3 in Fig. 13). This discrepancy may be related to the viscoelasticity of the highly deformable gelatin which we used in experiments. We noticed that changes of pull-off speed were directly altering the measured normal force when performed during the partial detachment phase. This hints to some time-depend response of the material and can explain the discrepancy with respect to d. Discrepancies between theory and experiment may also be due to the half-space approximation used in theoretical consideration. In the experiment, the finite size of the gelatin samples necessarily introduces deviations from the half-space assumption.

In spite of the differences in the force-distance dependencies, we consider the practically exact coincidence of the shapes of the consecutive contact forms as important experimental validation to the adhesive BEM formulation used in simulations.

Note that the presented experiments indicate that for the used gelatin the "stress criterion" of detachment as defined in Ref. [30] should be applied, not the "deformation criterion". According to the stress criterion, the same configurations of the adhesive contact are achieved at the same forces, not at the same distances.

The shapes shown in Figs. 13–15 are representative for the general behavior of the cases we investigated. First we observe F to rise strictly linearly with d. In this phase, the contact area remains intact without any detachment and the ratio is equal to the contact stiffness of the initial shape. This is to be expected

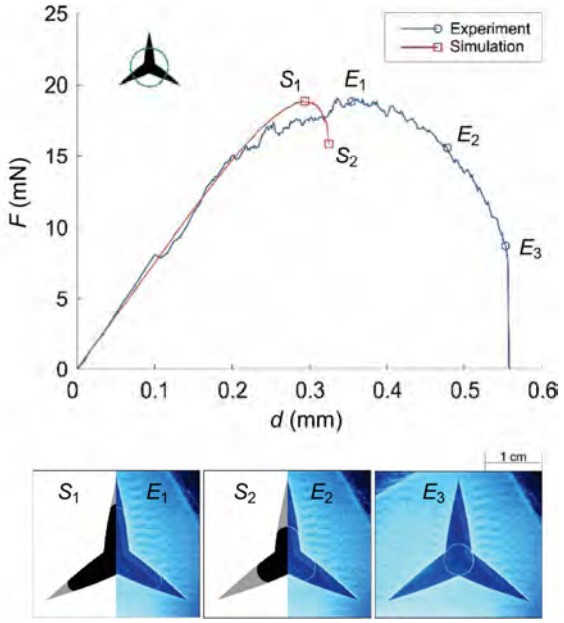

Fig. 14 Dependency of the attracting force on the pull-off distance for a star shape. The blue curve represents experimental data, while the red curve is obtained by simulation. The simulation results were fitted to the experimental data by assuming $E^* = 7.60$ kPa and $\gamma_{12} = 0.060$ N·m^{-1}. Highlighted points (S_1, S_2, E_1, E_2, E_3) refer to the lower part where real contact area for selected pull-off-states are shown. For the third photograph of the experiment, no equivalent stable solution in the numerical simulation was reached.

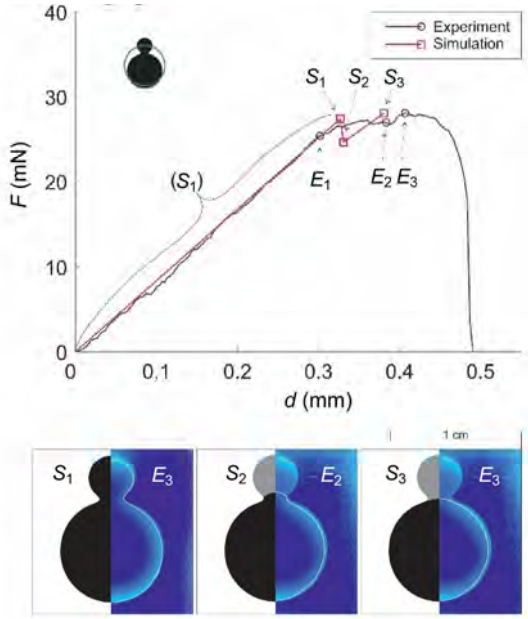

Fig. 15 Dependency of the attracting force on the pull-off distance for a shape composed of two circles. The blue curve represents experimental data, while the red curve is obtained by simulation. The simulation results were fitted to the experimental data by assuming $E^* = 9.28$ kPa and $\gamma_{12} = 0.030$ N·m^{-1}. Highlighted points (S_1, S_2, S_3, E_1, E_2, E_3) refer to the lower part where the real contact area for selected pull-off-states is shown. The green circle in the shape representation depicts the equivalent Holm-radius of the shape. In the photographs of the experiment (E_1, E_2, E_3), the actual edge of the contact has been retraced with a semi-transparent white line for better visibility.

from the linear elasticity. We then observe a transition to a second phase, where detachment starts at sharp corners or outstanding parts of the shape or border segments with high curvature and then moves inwards. In the $\bar{F} - \bar{d}$ -curve, this goes along with a decline of the slope. After the bodies have lost contact at the sharp corners and outstanding parts, the region evolves in such a way, that the minimum radius of curvature is increased with increasing height. For various shapes, the force decreases after having reached a local maximum.

All simulations and experiments reached a point when the remaining contact collapses abruptly. The last stable contact region resembles the incircle of the initial contact zone. The run of the curve between phase 2 and the final detachment can have different characteristics. In the case of the triangular and star shape, we find a local maximum in the force. For a circle (not shown), the intermediate phase vanishes and the end of phase 1 coincides with the maximum force and the onset of final detachment. For more complicated shapes, the force can achieve several maxima and have several jumps corresponding to partial instabilities.

The shape shown in Fig. 15 was designed to cause a discontinuity in the adhesive force when the smaller circle detaches and we obtain two local maxima in the $\bar{F} - \bar{d}$ -curve. The reason for this is the constriction in the shape. According to the discussion in Section 8, a stable shrinking of the contact area is only possible if the filling factor ξ is increasing fast enough with decreasing the radius. In the case of shapes with constriction, we have the opposite case when the filling factor decreases with decreasing the radius. Thus, the propagation of the contact will be instable and there will be a jump to the next state when the condition of continuous shrinking, Eq. (30), is satisfied again.

Note however, that there are some differences between experiment and theory: In the simulation, the detachment of the upper part from S_1 to S_2 is abrupt. While the experiment also shows the feature of

non-monotonous dependency of force as a function of distance, the dependency has no abrupt stages. The reason could be again the viscoelasticity of the gelatin.

Also note that in the experimental state E_3 shown in Fig. 15, the boundary line of the adhesive zone does not match exactly the contour of the stamp. This may indicate that the assumption of infinitely short action range of adhesive forces lying behind the JKR-type of adhesion is not completely applicable to gelatin. Small detachment at the boundary is an effect which can be expected in the case of finite action range of the adhesion forces [31].

11 Adhesion of graded media

In the previous sections, we studied the adhesive contact of flat punches that were placed in contact with a linear elastic medium. We shall now consider the adhesive problem when the elastic body is characterized by a depth-dependent modulus of elasticity. This so-called functionally graded materials (FGM) became increasingly popular since 1990s. The gradually varying composition and structure of FGM result in the continuous changes in properties of materials, thus providing new mechanical properties which cannot be achieved with homogeneous materials [31, 32]. Living species have "discovered" FGM millions of years ago. Gradient media can be found in many biological structures as skin, bones or bamboo trees [33].

In the present section we only consider materials whose elastic coefficient is a function of the normal coordinate $E = E(z)$. This dependence can be either stepwise (as, e.g., in layered or coated materials) or continuous (FGM). For simplicity, we confine ourselves to the model case of materials with a power-law dependency of the elastic modulus on depth:

$$E(z) = E_0\left(\frac{z}{c_0}\right)^k, \quad -1 < k < 1 \tag{32}$$

where E_0 is a characteristic elastic modulus and c_0 is a characteristic length. We additionally assume that the Poisson ratio of the graded medium is constant and equal to

$$\nu = \frac{1}{2+k} \tag{33}$$

which guarantees decoupling of the normal and tangential contact problems [34].

For the graded medium defined by Eqs. (32) and (33), the contact stiffness for indentation with a rigid cylinder having the radius a is given by Refs. [34, 35]

$$k(a) = \frac{4(2+k)\cos(k\pi/2)}{(3+k)}\frac{E_0}{c_0^k}a^{1+k} \tag{34}$$

For the total energy $\frac{1}{2}k(a)d^2 - \gamma_{12}\pi a^2$, we thus have

$$U_{\text{tot}} = \frac{2(2+k)\cos(k\pi/2)}{(3+k)}\frac{E_0}{c_0^k}a^{1+k}d^2 - \gamma_{12}\pi a^2 \tag{35}$$

For $k < 1$, the total energy has only one maximum at the critical radius a_{c} determined by the condition

$$\begin{aligned}&\frac{\partial U_{\text{tot}}}{\partial a} = \frac{2(2+k)(1+k)\cos(k\pi/2)}{(3+k)}\frac{E_0}{c_0^k}a^k d^2 - \gamma_{12}2\pi a\\ &\frac{\partial U_{\text{tot}}}{\partial a}(a = a_c) = 0\end{aligned} \tag{36}$$

As in the case of homogeneous media discussed in Section 2, the contact either shrinks to zero or expands to infinity depending on whether the initial radius was smaller or larger than a_{c}. For a finite indenter, Eq. (36) determines the relation between the critical detachment distance and the radius of the indenter:

$$\frac{2(2+k)(1+k)\cos(k\pi/2)}{(3+k)}\frac{E_0}{c_0^k}a^k d_{\text{c}}^2 = \gamma_{12}2\pi a \tag{37}$$

For the critical distance we get

$$d_{\text{c}} = \left(\frac{2\pi(3+k)\gamma_{12}c_0^k}{2(2+k)(1+k)\cos(k\pi/2)E_0 a^{k-1}}\right)^{1/2} \tag{38}$$

and for the adhesion force $F_{\text{A}} = k(a)d_{\text{c}}$,

$$F_{\text{A}} = \sqrt{\lambda(k)8\pi E_0\gamma_{12}\frac{a^{3+k}}{c_0^k}} \tag{39}$$

with

$$\lambda(k) = \frac{2(2+k)\cos(k\pi/2)}{(3+k)(1+k)} \tag{40}$$

For damaged surfaces with the average filling factor $\xi(a)$, the adhesion force is estimated similarly to the

procedure described by Eqs. (25)–(28) and is roughly equal to

$$F_{\mathrm{A}} \approx \sqrt{\lambda(k) 8\pi E_0 \xi(a) \gamma_{12} \frac{a^{3+k}}{c_0^k}} \tag{41}$$

A numerical procedure for the simulation of graded materials can be formulated using the same idea of balancing elastic energy and surface energy as described in Section 3. A detailed analysis carried out in Ref. [28] shows that now the detachment criterion (22) has to be replaced by

$$\sigma_{\mathrm{c}} = \sqrt{\Psi(k,\nu) \frac{E_0 \gamma_{12}}{c_0^k \Delta^{1-k}}} \tag{42}$$

where $\Psi(k,\nu)$ is a factor depending on the power k and the Poisson ratio ν, which was found numerically in Ref. [28]. An example of the detachment of a flat-ended indenter having the shape of a star calculated with BEM using the detachment criterion (42) is shown in Fig. 16.

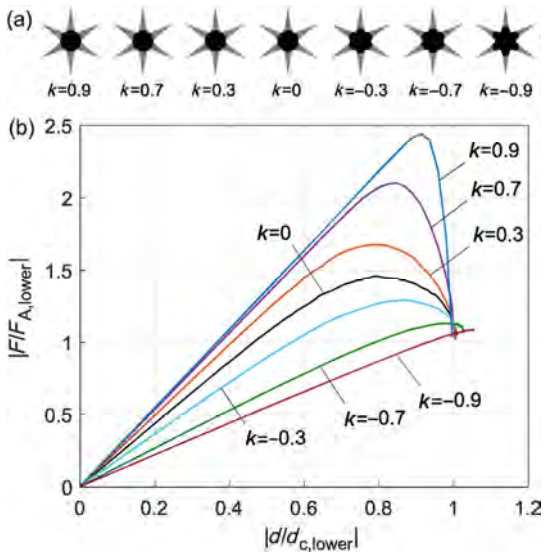

Fig. 16 Detachment of a flat-ended stamp with cross-section in form of a star from gradient media with various power k. (a) The last stable configuration for different $-1 < k < 1$. (b) The force-displacement dependencies show that the media with positive power k develop a much more pronounced pre-detachment leading to a maximum of force, while the media with large negative powers tend to a "brittle" detachment almost without pre-detachment. In the limiting case $k = -1$ the force-displacement dependence degenerates into a linear dependency up to the point where the contact suddenly is lost.

For all media with $0 < k < 1$, the detachment starts at the sharp ends on the outside and ends up at the incircle of the star. The larger the power of the medium (thus the softer it is at the immediate surface) the larger is the maximum force and the work of fracture after achieving the maximum force (fracture toughness) contact. Media with negative power $-1 < k < 0$ show a different behavior. Now the last stable state is reached earlier than the incircle of the shape would suggest. For the limiting case $k = -1$ the last configuration is almost the non-disturbed initial shape. Correspondingly, the deviation from the force-displacement linearity decreases with increasing absolute value of k and the fracture toughness decreases rapidly. Thus, the soft surface facilitates both the magnitude of the adhesion force and the work of adhesion between maximum force and complete collapse of the contact.

12 Discussion and conclusion

As expected from our theoretical considerations, the adhesive contact of flat bodies within the assumptions of JKR theory can clearly depend on the macroscopic shape of the contact zone. Our results show that adhesion is not only governed by small-scale roughness properties of the surfaces but depends strongly on the bulk shape of the initial adhesive zone. During pull-off, the detachment starts at the exposed outer parts of the shape such as tentacles or sharp corners, then the contact zone shrinks, approaching a final state after which the detachment occurs in an instable way. In the final state, the remaining contact has a shape with circularly rounded corners. In the course of detachment, one or multiple maxima can occur. These phenomena can be observed both in experiment and simulation. In direct comparison however, the experiments develop more slowly near the instabilities.

While the macroscopic shape of the stamp has essential influence on the adhesive strength, small inner discontinuities do not. Their influence can be characterized relatively well with a filling parameter quantifying the fraction of the continuous part of the cross-section relatively to the nominal area. In particular, the detachment of square brushes occurs almost in the same way as of the corresponding full square. For determining the adhesive force, only the

work of adhesion has to be multiplied with the filling factor of the shape.

Special attention has to be paid, when the filling factor depends on the distance from the center of the contact zone. This dependence will then be the parameter determining both the character of detachment and the size and shape of the final state before sudden loss of contact.

We anticipate our work to inspire a broader view on adhesion problems, differentiating small-scale roughness effects from the macro-shape. For instance, one could design adhesive bonds that show distinct partial detachment below their maximum strength, giving an early warning of critical failure.

Acknowledgement

Authors acknowledge the assistance of C. Jahnke in conduction of experiments and very useful discussions of adhesion with gradient media with M. Heß and E. Willert. This work has been conducted under partial financial support from DFG (Grant number PO 810/22-1).

Contributions of authors: R. Pohrt built the experimental setup and processed the experimental data. R. Pohrt and Q. Li executed the numerical simulations. Theoretical analysis was carried our primarily by V. L. Popov. All authors contributed equally to the writing of the manuscript.

References

[1] Lee L H (Ed.). *Fundamentals of Adhesion*. New York: Springer Science & Business Media, 1991

[2] Dzyaloshinskii I E, Lifshitz E M, Pitaevskii L P. General Theory of van der Waals' Forces. *Soviet Physics Uspekhi* **4**: 153–176 (1961)

[3] Landau L D, Lifshitz E M. *Statistical Physics, Pt. 2, (Volume 9 of the Course of Theoretical Physics).* Oxford: Pergamon Press, 1980

[4] Afferrante L, Carbone G. The ultratough peeling of elastic tapes from viscoelastic substrates. *Journal of the Mechanics and Physics of Solids* **96**: 223–234 (2016)

[5] Popov V L, Filippov A E, Gorb S N. Biological microstructures with high adhesion and friction. Numerical approach. *Physics-Uspekhi* **59**(9): 829–845 (2016)

[6] Autumn K, Liang Y A, Tonia Hsieh S, Zesch W, Chan W P, Kenny T W, Fearing R, Full R J. Adhesive force of a single gecko foot-hair. *Nature* **405**: 681–685 (2000)

[7] Köster S, Janshoff A. Editorial–Special issue on mechanobiology. *Biochimica et Biophysica Acta (BBA) - Molecular Cell Research* **1853**(11, Part B): 2975–2976 (2015)

[8] Popov V L. *Contact Mechanics and Friction─Physical Principles and Applications*. Berlin: Springer-Verlag Berlin Heidelberg, 2010

[9] Kendall K. *Molecular Adhesion and Its Applications*. New York (US): Springer Science & Business Media, 2001

[10] Luan B, Robbins M O. The breakdown of continuum models for mechanical contacts. *Nature* **435**(7044): 929–932 (2005)

[11] Ciavarella M. On Pastewka and Robbins' criterion for macroscopic adhesion of rough surfaces. *Journal of Tribology* **139**(3): 031404 (2017)

[12] Guduru P R. Detachment of a rigid solid from an elastic wavy surface: theory. *Journal of the Mechanics and Physics of Solids* **55**(3): 445–472 (2007)

[13] Johnson K L, Kendall K, Roberts A D. Surface energy and the contact of elastic solids. *Proc. R. Soc. London A* **324**: 301–313 (1971)

[14] Maugis D. Adhesion of spheres: The JKR-DMT transition using a Dugdale model. *Journal of Colloid and Interface Science* **150**(1): 243–269 (1992)

[15] Cheng A H-D, Cheng D T. Heritage and early history of the boundary element method. *Engineering Analysis with Boundary Elements* **29**: 268–302 (2005)

[16] Cruse T A. *Boundary Element Analysis in Computational Fracture Mechanics*. Kluwer, Dordrecht, 1988

[17] Blandford G E, Ingraffea A R, Liggett J A. Two-dimensional stress intensity factor computations using the boundary element method. *International Journal for Numerical Methods in Engineering* **17**(3): 387–404 (1974)

[18] Pohrt R, Popov V L. Adhesive contact simulation of elastic solids using local mesh-dependent detachment criterion in Boundary Elements Method. *Facta Universitatis, Series: Mechanical Engineering* **13**(1): 3–10 (2015)

[19] Hulikal S, Bhattacharya K, Lapusta N. A threshold-force

model for adhesion and mode I fracture. arXiv:1606.03166.

[20] Rey V, Anciaux G, Molinari J-F. Normal adhesive contact on rough surfaces: efficient algorithm for FFT-based BEM resolution. *Comput Mech*, DOI: 10.1007/s00466-017-1392-5 (2017)

[21] Kendall K. The adhesion and surface energy of elastic solids. *Journal of Physics D: Applied Physics* **4**(8): 1186 (1971)

[22] Li Q, Popov V L. Indentation of flat-ended and tapered indenters with polygonal cross-section. *Facta Universitatis Series: Mechanial Engineeering* **14**(3): 241–249 (2016)

[23] Holm R, Holm E. *Electric Contacts Handbook*. Berlin: Springer-Verlag, 1958

[24] Griffith A A. The phenomena of rupture and flow in solids. *Philosophical Transactions of the Royal Society of London, A* **221**: 163–198 (1921)

[25] Pohrt R, Li Q. Complete boundary element formulation for normal and tangential contact problems. *Physical Mesomechanics* **17**(4): 334–340 (2014)

[26] Putignano C, Afferrante L, Carbone G, Demelio G. A new efficient numerical method for contact mechanics of rough surfaces. *International Journal of Solids and Structures* **49**(2): 338–343 (2012)

[27] Maugis D, Barquins M. Adhesive contact of a conical punch on an elastic half-space. *Le Journal de Physique Lettres* **42**(5): 95–97 (1981)

[28] Li Q, Popov V L. Boundary element method for normal non-adhesive and adhesive contacts of power-law graded elastic materials. *arXiv:1612.08395* (2016)

[29] Argatov I I, Li Q, Pohrt R, Popov V L. Johnson-Kendall-Roberts Adhesive Contact for a Toroidal Indenter. *Proceedings of the Royal Society of London, Series A* **472**(2191): (2016)

[30] Popov V L. Basic ideas and applications of the method of reduction of dimensionality in contact mechanics. *Physical Mesomechanics* **15**: 254–263 (2012)

[31] Maugis D. Adhesion of spheres: The JKR-DMT transition using a Dugdale model. *Journal of Colloid and Interface Science* **150**(1): 243–269 (1992)

[32] Suresh S. Graded materials for resistance to contact deformation and damage. *Science* **292**: 2447–2451 (2001)

[33] Jha D K, Kant T, Singh R K. A critical review of recent research on functionally graded plates. *Composite Structures* **96**: 833–849 (2013)

[34] Hess M, Popov V L. Method of dimensionality reduction in contact mechanics and friction: A user's handbook. II Power-law graded materials. *Facta Universitatis, Series: Mechanical Engineering* **14**(3): 251–268 (2016)

[35] Heß M. A simple method for solving adhesive and non-adhesive axisymmetric contact problems of elastically graded materials. *International Journal of Engineering Science* **104:** 20–33 (2016)

Valentin L. POPOV. He is full professor at the Berlin University of Technology. He studied physics and obtained his doctorate in 1985 from the Moscow State Lomonosov University. 1985–1998 he worked at the Institute of Strength Physics and Materials Science of the Russian Academy of Sciences and was a guest professor in the field of theoretical physics at the University of Paderborn (Germany) from 1999 to 2002. Since 2002 he is the head of the Department of System Dynamics and the Physics of Friction at the Berlin University of Technology. He has published over 300 papers in leading international journals and is the author of the book "Contact Mechanics and Friction: Physical principles and applications" which appeared in three editions in German, English, Chinese, and Russian. He is the member of editorial boards of many international journals and is organizer of more than 20 international conferences and workshops over diverse tribological themes. Prof. Popov is Honorary Professor of the Tomsk Polytechnic University, of the East China University of Science and Technology, and of the Changchun University of Science and Technology and Distinguished Guest Professor of the Tsinghua University. His areas of interest include tribology, nanotribology, tribology at low temperatures, biotribology, the influence of friction through ultrasound, numerical simulation of contact and friction, research regarding earthquakes, as well as topics related to materials science such as the mechanics of elastoplastic media with microstructures, strength of metals and alloys, and shape memory alloys.

Roman POHRT. He is independent researcher at the Berlin University of Technology. He studied physical engineering science with special focus on simulation and optimization of discrete and continuous problems. Since he joined the group of Prof. V. Popov in 2010, he has been conducting experimental and numerical research on a variety of tribology related industry problems. In his PhD thesis R. Pohrt focussed on linking scales in the elastic contact of fractal rough surfaces, for which he was awarded by the German Tribological Society in 2013. R. Pohrt has authored a series of influential papers on different tribological problems, applying and extending state-of-the-art numerical methods. His areas of interest include contact mechanics, rail-wheel-interaction of trains, manufacturing technology, and lubrication and more generally the influence of surface topography on tribological phenomena.

Qiang LI. He is a postdoctoral researcher at the Berlin University of Technology. He studied mechanical engineering in East China University of Science and Technology. He obtained his doctorate at the Berlin University of Technology in 2014 and now works as a scientific researcher at the Department of System Dynamics and the Physics of Friction headed by Prof. V. L. Popov. He has published over 20 papers in international journals including Physical Review Letters. His scientific interests include tribology, elastomer friction, hydrodynamic lubricated contact, numerical simulation of frictional behaviors, and fast numerical method based on boundary element method.

Friction **5**(3): 326–338 (2017)
https://doi.org/10.1007/s40544-017-0178-2
ISSN 2223-7690
CN 10-1237/TH

RESEARCH ARTICLE

A comparison of stick and slip contact conditions for a coated sphere compressed by a rigid flat

Shai RONEN, Roman GOLTSBERG*, Izhak ETSION

Department of Mechanical Engineering, Technion, Haifa 32000, Israel

Received: 28 April 2017 / Revised: 09 June 2017 / Accepted: 19 June 2017

Abstract: A finite element analysis is used to study the elastic-plastic contact of a coated sphere compressed by a rigid flat under the stick contact condition. This was done for a wide range of hard coating material properties and coating thicknesses. A comparison with the slip contact condition is presented in terms of the critical contact parameters (at yield inception) and plasticity evolution. Empirical expressions are provided for critical interferences of the first and second yield inceptions, in the coating and on the substrate side of the interface, respectively. An expression is also provided for the dimensionless coating thickness for optimal resistance to plasticity under the stick contact condition. Additionally, the relations between different contact parameters in the elastic-plastic regime are presented. In general, it was found that the contact condition has a negligible effect on the contact parameters, except for phenomena occurring close to the contact area.

Keywords: contact mechanics; coatings; stick; elastic-plastic

1 Introduction

In many engineering applications, mechanical components are in contact and slide relative to each other. Coatings are commonly used in these cases to improve tribological performance, for instance, the enhancement of electrical and thermal conductivity and reduction of friction and wear. These improvements can be seen in a variety of applications, including the automotive [1], electronics [2–5], optical storage disk [6], and cutting tool industries [7]. Despite the wide usage of coatings in many industries, the selection of coating thickness and mechanical properties is still done mainly by trial and error, which wastes funds and time. Optimization of coating properties for specific applications, based on a scientific theory, is still lacking.

The real surfaces of mechanical components are rough and can be modeled as clusters of asperities. The interaction between such rough surfaces occurs at the summits of their contacting asperities [8, 9]. Hence, in order to gain a good understanding of such interactions, it is necessary to first study the contact mechanics of a single asperity. This may then be extended to a contact model for a rough surface with a statistical distribution of asperities. There are two approaches to study the contact mechanics of a single asperity, namely flattening and indentation [10]. Most of the theoretical studies on spherical coated contacts that have been published so far focus on the indentation of coated flat substrates by an uncoated spherical indenter [11–17]. This approach is mainly used to characterize the mechanical properties of coatings. However, in order to investigate the optimum tribological performance, flattening, rather than indentation, is the better choice. This is because when tangential loading is applied, indentation is associated with high abrasive friction and wear that results from plowing, compared to the mild adhesive friction and wear of flattening.

Historically, the contact of a single uncoated spherical

* Corresponding author: Roman GOLTSBERG, E-mail: goltsberg.roman@gmail.com

Nomenclature

A	contact area
a	contact radius
C_v	$1.234+1.256\nu$
E	Young's modulus
L	load in stick
P	load in slip
R	radius of the spherical substrate (inner radius of the coating)
r	radial distance from the center of contact interface
t	coating thickness
Y	yield strength
z	vertical distance from the center of contact interface
δ	interference in stick
ν	Poisson's ratio
ε_y	yield strain Y/E
σ_{eq}	equivalent von Mises stress
ω	interference in slip

Subscripts

c	critical value
c1	first critical value
c2	second critical value
c_co	critical value of solid sphere made of the coating material
c_su	critical value of solid sphere made of the substrate material
co	coating
p	corresponds to peak value
st	stick contact condition
su	substrate

asperity was studied by Hertz in 1882 (see, e.g., Ref. [18]). Hertz assumed frictionless (slip) contact of perfectly elastic solids and provided relations between different contact parameters, such as contact load, contact area, and interference. Kogut and Etsion [19] extended Hertz's study for a homogeneous frictionless spherical contact into the elastic-plastic regime, using a finite element method (FEM). By properly normalizing the contact parameters, simple empirical relations were achieved. Goodman [20] was probably the first to address the elastic spherical contact problem under the stick contact condition, and present an analytical solution. Goodman assumed a Hertzian distribution of contact pressure and introduced a tangential stress distribution over the contact area to account for the stick contact condition. A more accurate analysis of indentation under the stick condition was published by Spence [21], who numerically solved the shear stresses and pressure distribution over the contact area and calculated the total compressive load. It follows from the results obtained by Spence, that for small values of Poisson's ratio the influence of the shear stresses on the contact area is significant. Brizmer et al. [22] studied, using FEM, the effect of the contact conditions and material properties on the elasticity terminus of a spherical contact under stick and slip contact conditions. It was found that for small values of the Poisson's ratio, the behavior for stick is much different than that for slip, which was attributed in Ref. [22] to the high tangential stresses at the contact interface in the former case. The critical values (at yield inception) of interference and load for the stick condition are lower than the corresponding values for the slip condition, and the location of yield inception is closer to the contact area for the stick condition. At higher values of Poisson's ratio, the tangential stresses under the stick contact condition are lower and the critical values for stick and for slip become comparable. Brizmer et al. [23] extended the study in Ref. [22] into the elastic-plastic regime. The results, presented in Refs. [19, 23], were experimentally verified by Overcharenko et al. [24].

Goltsberg et al. [25] investigated the plastic yield inception of a coated sphere pressed by a rigid flat under the slip contact condition. An optimum value of the coating thickness for the best resistance to the onset of plasticity was found, and a potential weakening effect at very small coating thicknesses was detected.

Similar behavior was found for indentation of a coated flat by a rigid sphere in Ref. [26]. The existence of the weakening effect was experimentally verified by Huang et al. [27]. This weakening effect was extensively studied and characterized in Ref. [28]. Further studies by Goltsberg and Etsion [29, 30] provided universal relations for various contact parameters in the elastic regime of a coated spherical contact. Sun et al. [31] used FEM to analyze the plastic deformation of a coated spherical contact for the indentation approach. They presented results for relatively thin coatings, where yielding first occurred on the substrate side of the substrate/coating interface followed by a second yielding on the coating side of the interface at higher indentation depth. In Refs. [32, 33], it was found for some specific cases of indentation that the first yield inception occurred within the coating. In these cases, increasing the indentation depth beyond the first yield caused a second yield inception on the substrate side of the interface. All these studies [31–33] examined a limited number of mechanical and geometrical properties of the coating and the substrate materials. Chen et al. [34] investigated the elastic-plastic contact of a coated sphere compressed by a rigid flat under the slip contact condition. This was done for relatively thick coating thicknesses, where the first onset of plasticity occurred in the coating and the second on the substrate side of the interface. Empirical expressions were provided for the critical interferences of the first and second yield inceptions as functions of the coating thickness and material properties. It was shown that a combination of a thick coating and small moduli ratio E_{co}/E_{su} is beneficial for protecting against substrate yielding.

As can be seen from the above literature review, the flattening of a coated spherical contact has been modeled so far only under the slip contact condition. Hence, the main goal of the present study is to investigate the coated spherical contact under the stick contact condition for a wide range of coating and substrate material properties. The stick contact condition is necessary to study the combined, normal, and tangential loading, which is essential for future research on the effect that coating properties have on friction and wear.

2 Theoretical background

Figure 1 schematically presents a coated sphere system before loading (Fig. 1(a)) and, in contact, after loading (Fig. 1 (b)) by a rigid flat. It consists of a solid spherical substrate of radius R, which is covered by a coating layer of thickness t. The application of a load, P, results in a corresponding interference, ω, of the rigid flat, and the formation of a contact area with radius a, owing to the deformation of the coated sphere. When the coating material is identical to the substrate material, Fig. 1 merely describes a homogeneous uncoated case.

Brief descriptions of a homogeneous spherical contact model under the stick contact condition and a coated sphere under the slip contact condition are provided in the following sections.

2.1 Yield inception of a homogeneous sphere under the stick contact condition [22]

The critical interference δ_c and critical load L_c at yield inception under the stick contact condition were given

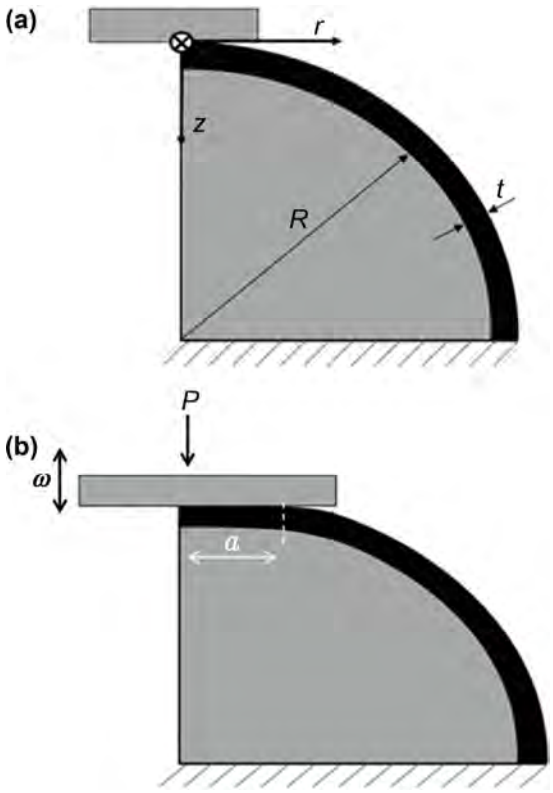

Fig. 1 Schematic of a coated deformable sphere pressed by a rigid flat, before loading (a) and in contact after loading (b) (taken from Ref. [30]).

by Brizmer et al. [22] in the following form:

$$\frac{\delta_c}{\omega_c} = 6.82\nu - 7.83\left(\nu^2 + 0.0586\right) \quad (1)$$

$$\frac{L_c}{P_c} = 8.88\nu - 10.13\left(\nu^2 + 0.089\right) \quad (2)$$

where ω_c and P_c are the corresponding critical parameters under perfect slip are given by

$$\omega_c = \left[C_v \frac{\pi\left(1-\nu^2\right)}{2}\left(\frac{Y}{E}\right)\right]^2 R \quad (3)$$

$$P_c = \frac{\pi^3 Y}{6} C_v^{\ 3}\left[R\left(1-\nu^2\right)\left(\frac{Y}{E}\right)\right]^2 \quad (4)$$

It was found that for ductile materials ($0.2<\nu<0.5$), the yield inception always occurs at a single point on the axis of symmetry. As can be seen in Fig. 2, for small values of ν, the critical interference and the critical load in the stick contact condition are considerably smaller than their corresponding parameters in the slip contact condition. This is because of high tangential stresses at the contact interface under stick. For increasing values of the Poisson's ratio, the tangential stresses, under the stick contact condition, decrease and the critical parameters become comparable to those in slip.

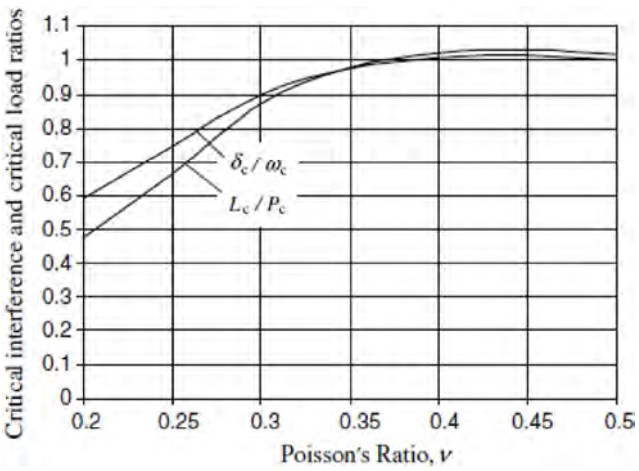

Fig. 2 The ratios of the critical interference, δ_c/ω_c, and critical load, L_c/P_c, for yield inception of ductile materials in full stick over perfect slip [22].

2.2 Coated sphere under the slip contact condition [25, 34]

Figure 3, taken from Ref. [25], presents the dimensionless critical load P_c/P_{c_co} of a coated sphere as a function of the dimensionless coating thickness t/R, for different P_{c_co}/P_{c_su} ratios. P_{c_co} and P_{c_su} are the critical loads at yield inception for a homogeneous sphere made of the coating and substrate materials, respectively [25]. As can be seen, the highest resistance to the onset of plasticity for each curve is associated with a certain value of the dimensionless coating thickness. This coating thickness depends on material properties, and it was given in Ref. [25] in the form

$$\left(\frac{t}{R}\right)_p = 2.824\left(\frac{E_{su}}{Y_{su}}\right)^{-1.014}\left(\frac{P_{c\_co}}{P_{c\_su}}\right)^{0.536} \quad (5)$$

where

$$\frac{P_{c\_co}}{P_{c\_su}} = \left(\frac{C_{v\_co}}{C_{v\_su}}\right)^3 \frac{\left(1-\nu_{co}^2\right)}{\left(1-\nu_{su}^2\right)}\left(\frac{Y_{co}}{Y_{su}}\right)^3\left(\frac{E_{su}}{E_{co}}\right)^2 \quad (6)$$

When the substrate and coating material have the same Poisson's ratio, Eq. (5) can also be written as (provided in Ref. [34])

$$\left(\frac{t}{R}\right)_p = 2.824\left(\frac{E_{co}}{E_{su}}\right)^{0.536}\left(\frac{E_{co}}{Y_{co}}\right)^{-1.608}\left(\frac{E_{su}}{Y_{su}}\right)^{0.594} \quad (7)$$

It should be noted here that both Eqs. (5) and (7) were obtained for a relatively small range of E_{co}/E_{su} values, between 1 and 4.5.

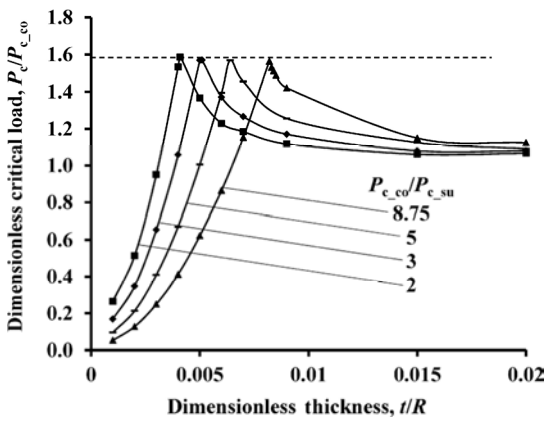

Fig. 3 Dimensionless critical load as a function of the dimensionless thickness t/R, for different values of critical loads ratios [25].

It was found that for very thin coatings, where t/R is much smaller than $(t/R)_p$, yielding initiates within the substrate (location 1 in Fig. 4). When t/R is higher, but still lower than $(t/R)_p$, yield inception occurs on the substrate side of the interface (location 2 in Fig. 4). When t/R is higher than $(t/R)_p$, the yield inception occurs slightly below the contact area within the coating (location 3 in Fig. 4). Although the analysis in Ref. [25] was performed mainly for $\nu = 0.32$, it was indicated that for a coated sphere under the slip contact condition, the effect of varying the Poisson's ratio is negligible (less than 10%).

Chen et al. [34] showed that for $t/R > (t/R)_p$, as the interference increases above that corresponding to the first yield in the coating, ω_{c1}, a second yield occurs in the substrate at a second critical interference, ω_{c2}. The empirical expressions for these two critical interferences were given in Ref. [34] as follows:

$$\frac{\omega_{c1}}{\omega_{c\_co}} = 1 + 3.78\left(\frac{t}{R}\right)^{-1.29}\left(\frac{E_{co}}{E_{su}} - 1\right)^{0.811}\left(\frac{E_{co}}{Y_{co}}\right)^{-1.3} \quad (8)$$

$$\frac{\omega_{c2}}{\omega_{c\_co}} = 0.25\left(\frac{t}{R}\right)^{1.34}\left(\frac{E_{co}}{E_{su}}\right)^{-0.14}\left(\frac{E_{co}}{Y_{co}}\right)^{2}\left(\frac{E_{su}}{Y_{su}}\right)^{-0.66} \quad (9)$$

3 The finite element model

The commercial FE package ANSYS 14.0 was used to solve the contact problem using an axisymmetric 2D model, as presented in Fig. 5. The nodes on the bottom

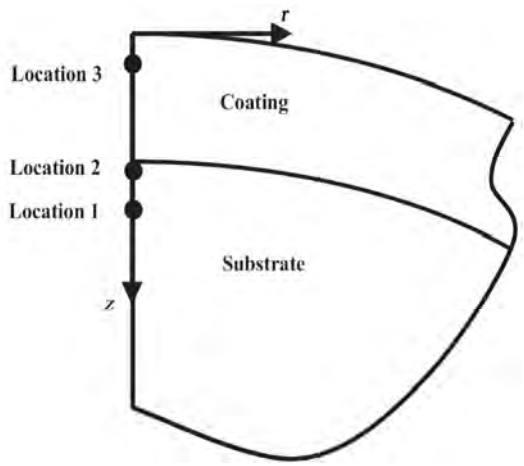

Fig. 4 Typical locations of yield inception in a coated sphere compressed by a rigid flat [25].

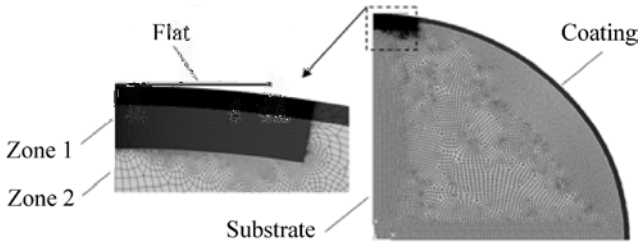

Fig. 5 The finite element mesh of a coated sphere.

of the system were constrained in both the axial and radial direction. To simulate the rigidity of the flat, its Young's modulus was chosen to be seven orders of magnitude higher than that of the coating and the substrate. An eight-node axisymmetric quadrilateral solid element (PLANE183) was used for the coating, substrate, and flat. A three-node contact element (CONTA175) was used on the outer surface of the coating, and a target element (TARGE169) was used at the bottom of the rigid flat. The mesh of the coated sphere was divided into two different mesh density zones (see Fig. 5). Zone 1, with a uniform fine density mesh, contains the part of the coated system where plasticity evolves in both the coating and the substrate. In this zone, the typical length of the elements for any radius R was in the order of $0.001R$. The width of zone 1 was chosen to be 15 times the width of the contact radius for the case of the Hertz solution. Zone 2 had a gradually coarser mesh with increasing distance from zone 1. The total number of nodes in zones 1 and 2 was about 50,000.

The following main assumptions are adopted for the model [34]:

1. The coating is perfectly bonded to the substrate.
2. The coating and substrate materials are homogenous.
3. The coating and substrate are free of residual stresses.
4. The Poisson's ratio for the coating and substrate materials are constant and equal, i.e., $\nu_{co} = \nu_{su} = 0.32$.

The only different assumption compared to that in Ref. [34] is that a stick contact condition prevails between the coating and the rigid flat.

The substrate and coating materials were defined as elastic-plastic with linear isotropic hardening and a tangent modulus of 2% of their respective Young's modulus, similarly to the definition in Ref. [34]. This hardening enables to compare the results of this paper

to those published for the slip contact condition in Ref. [34]. As was stated in Ref. [23], 2% isotropic hardening is the upper limit of many practical materials; it improves convergence, compared to an elastic perfectly plastic material model, with a small effect on the results (of less than 2.5%).

The input parameter for the analysis was the displacement of the rigid flat in the axial direction, and all the corresponding results were obtained as output.

The convergence was tested by refining the mesh size until further refinement had negligible effect on the results. The accuracy of the finite element model was tested by comparison with the Hertz solution [18] for a homogenous sphere (identical coating and substrate materials) under the slip contact condition. The difference in the results was less than 1%.

4 Results and discussion

The following typical input parameters were used for the numerical simulations: the radius of the spherical substrate varied in the range $2 \le R \le 12$ mm and the dimensionless coating thickness t/R was varied in the range $0.002 \le t/R \le 0.05$. The Young's moduli of the substrate and the coating materials varied in the range $200 \le E_{su} \le 600$ GPa and $400 \le E_{co} \le 2{,}000$ GPa. The yield stresses of the substrate and the coating materials varied in the range $140 \le Y_{su} \le 1000$ MPa and $285 \le Y_{co} \le 3{,}300$ MPa. The Poisson's ratios ν of the substrate and the coating were maintained equal and varied in the range $0.2 < \nu < 0.45$. This was done to cover a wide range of mechanical properties ratios, as follows: $2 \le E_{co}/E_{su} \le 10$, which defines the mismatch between the coating and the substrate Young's modulus; $0.0007 \le Y_{su}/E_{su} \le 0.0017$, which defines the substrate yield strain ε_{y_su}; and $0.0007 \le Y_{co}/E_{co} \le 0.0017$, which defines the coating yield strain ε_{y_co}.

In the following sections, the results obtained under the stick contact condition are discussed in comparison with the case of the slip contact condition, indicated as "slip" in all the figures.

4.1 Yield inception

Figure 6 presents the typical results for the dimensionless critical load L_c/P_{c_co} versus the dimensionless coating thickness, for various values of the Poisson's ratio. The case indicated as "slip" presents the critical load P_c/P_{c_co} under the slip contact condition [25]. As can be seen, the general behavior under both stick and slip is similar, showing a maximum resistance to yield inception at a certain peak dimensionless thickness $(t/R)_p$. It was found that under stick, like under slip, for coating thicknesses below $(t/R)_p$, the first yield inception always occurs in the substrate. As can be seen in Fig. 6, the effect of ν on L_c for such thicknesses is negligible. However, the peak values of L_c/P_{c_co} and their corresponding $(t/R)_p$ increase with increasing Poisson's ratios. Also, for $t/R \ge (t/R)_p$, where yield inception occurs in the coating, the critical load L_c/P_{c_co} at any given t/R is higher for a larger Poisson's ratio. A similar behavior was also shown in Ref. [22] for a homogeneous sphere under the stick contact condition, where a larger Poisson's ratio results in lower tangential stresses in the contact area and a lower equivalent von Mises stress. For large coating thicknesses, the critical load approaches asymptotically the critical load in the case of a homogenous sphere made of the coating material. This case was analyzed in Ref. [22], and indeed Eq. (2) exactly fits the results shown in Fig. 6 for large t/R values (see also L_c/P_c in Fig. 2).

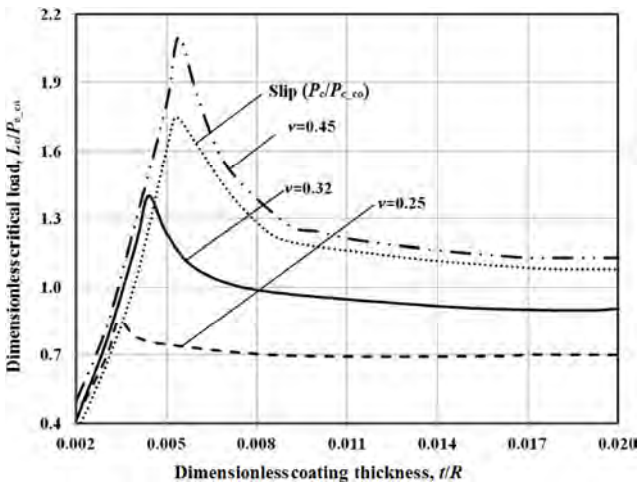

Fig. 6 Dimensionless critical load L_c/P_{c_co} vs. dimensionless thickness t/R ($E_{co}/E_{su} = 4$, $\varepsilon_{y\_su} = \varepsilon_{y\_co} = 0.001$).

Figure 7 presents a comparison between the dimensionless von Mises stress σ_{eq}/Y along the axis of symmetry for stick and slip contact conditions at equal critical loads, which can be obtained at the intersection of the slip curve with any of the stick curves in Fig. 6. The results in Fig. 7 are for the case of $\nu = 0.32$,

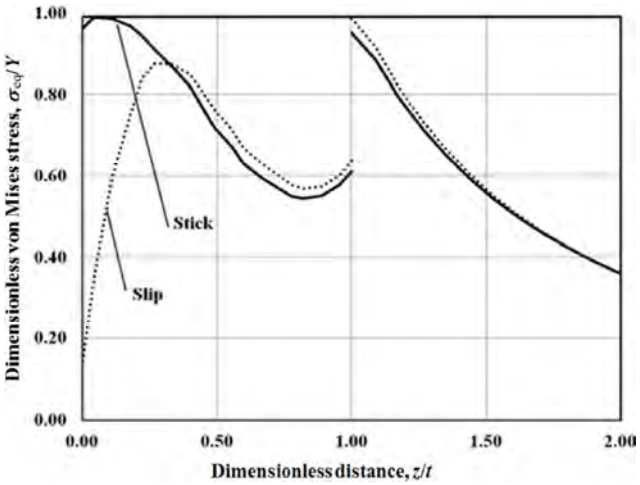

Fig. 7 Dimensionless von Mises equivalent stress along the axis of symmetry (t/R = 0.0045, E_{co}/E_{su} = 4, ε_{y_su} = ε_{y_co} = 0.001, δ/R = ω/R = 1 × 10^{-5} and ν = 0.32).

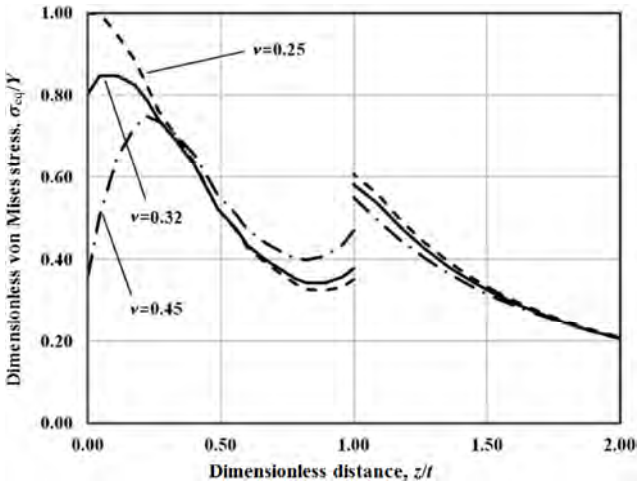

Fig. 8 Dimensionless von Mises equivalent stress along the axis of symmetry (t/R = 0.0045, E_{co}/E_{su} = 4, ε_{y_su} = ε_{y_co} = 0.001, δ/R = 6.5 × 10^{-6}).

t/R = 0.0045, and δ/R = ω/R = 1 × 10^{-5}. It should be noted here that this intersection occurs at t/R>$(t/R)_p$ for the stick case but at t/R<$(t/R)_p$ for the slip case. Hence, according to Ref. [25], the location of yield inception for the slip case is within the substrate. In Fig. 7, the results are presented against the dimensionless distance z/t, measured along the axis of symmetry from the center of the contact area. The coating/substrate interface is located at z/t = 1, and the normalization of σ_{eq} is done using the corresponding yield stress of the relevant material. As can be seen from the figure that the difference between the two contact conditions is apparent only close to the contact area, where the stress level under the stick contact condition is much higher than that under the slip contact condition. For the slip case, the yield inception (σ_{eq}/Y = 1) occurs at the substrate side of the interface, while for the stick case it occurs within the coating, slightly below the contact area.

Figure 8 presents the typical results for the effect of the Poisson's ratio under the stick contact condition, on σ_{eq}/Y along the axis of symmetry, for the same coating thickness t/R = 0.0045 as in Fig. 7, but at a fixed dimensionless interference δ/R = ω/R = 6.5 × 10^{-6} (different loads). For that interference, the case with ν = 0.25 reached the critical load while the other cases did not. Here again, like in Fig. 7, the difference between the various cases is apparent close to the contact area. The equivalent von Mises stress in this region increases with decreasing Poisson's ratio, and at the same time its peak value occurs closer to the contact area, similar to the findings for a homogeneous sphere [22]. A higher peak value of σ_{eq}/Y at a given interference indicates a smaller resistance to yield inception. This explains the increase in peak values of L_c/P_{c_co} with increasing Poisson's ratios, shown in Fig. 6.

By curve fitting the numerical results of $(t/R)_{p\_st}$ as a function of ε_{y_su}, ε_{y_co}, E_{co}/E_{su}, and Poisson's ratio over the entire range of the input parameters, the following empirical relation was obtained:

$$\left(\frac{t}{R}\right)_{p\_st} = 3.95\nu^{0.724}\left(\frac{E_{co}}{E_{su}}\right)^{0.39}\left(\varepsilon_{y\_co}\right)^{1.41}\left(\varepsilon_{y\_su}\right)^{-0.45} \quad (13)$$

The (R^2) goodness-of-fit for Eq. (13) was higher than 0.98. A comparison between Eq. (13) under the stick contact condition and Eq. (7) under the slip contact condition shows similarity in the structure, except for the dependence on Poisson's ratio under the stick contact condition.

Further investigation of the elastic-plastic regime under the stick contact condition was limited to dimensionless thicknesses t/R>$(t/R)_{p\_st}$ in order to ensure that the first yield inception will occur within the coating. This excludes unfavorable instances of possible failure owing to coating delamination or the weakening effect caused by yield inception at the coating/substrate interface or within the substrate.

Normalizing the first critical interference δ_{c1} (for cases with first yield inception within the coating) by the critical interference ω_{c_co} of a homogeneous sphere made of the coating material (as was done in Ref. [34]), and curve fitting the numerical results, the following empirical dimensionless expression was obtained:

$$\frac{\delta_{c1}}{\omega_{c\_co}} = [6.82\nu - 7.83(\nu^2 + 0.0586)] \left[1 + 0.007\left(\frac{E_{co}}{E_{su}} - 1\right)^{0.646} \left(\varepsilon_{y\_co}\right)^{0.244} \left(\frac{t}{R}\right)^{-1.21}\right] \quad (14)$$

The (R^2) goodness-of-fit for Eq. (14) was higher than 0.93. The first bracket of the equation presents the equation dependence of Poisson's ratio, while the second bracket presents the equation dependence of the geometrical and other material properties. In the first set of brackets, the dependence on the Poisson's ratio is identical to that for a homogeneous sphere (E_{co}/E_{su} = 1) under the stick contact condition (Eq. (1)). In the second set of brackets, it can be seen that when selecting the mechanical properties of a homogeneous sphere, the expression degenerates to 1 and Eq. (1) is obtained. Likewise, for large t/R, where the coated sphere behaves like a homogeneous sphere made from the coating material, the second set of brackets also degenerates to 1, and Eq. (1) is obtained again. Eq. (14) is independent of ε_{y_su}. This is because the substrate is still elastic in this regime and the only parameter influencing the substrate is E_{su}.

When the interference increases above that corresponding to the first yield in the coating, δ_{c1}, a second yield inception occurs in the substrate at a second critical interference δ_{c2} (similar to the behavior under the slip contact condition [34]). The empirical expressions obtained from the best fit of the numerical results for the interference, contact load, and contact area at the second yield inception are as follows:

$$\frac{\delta_{c2}}{\omega_{c\_co}} = \left(\frac{t}{R}\right)^{1.17} \left(\frac{E_{co}}{E_{su}} - 1\right)^{-0.09} \left(\varepsilon_{y\_co}\right)^{-1.93} \left(\varepsilon_{y\_su}\right)^{0.89} \quad (15)$$

$$\frac{L_{c2}}{P_{c\_co}} = \left(\frac{t}{R}\right)^{1.8} \left(\frac{E_{co}}{E_{su}} - 1\right)^{-0.27} \left(\varepsilon_{y\_co}\right)^{-2.3} \left(\varepsilon_{y\_su}\right)^{0.78} \quad (16)$$

$$\frac{A_{c2\_st}}{A_{c\_co}} = \left(\frac{t}{R}\right)^{1.6} \left(\frac{E_{co}}{E_{su}} - 1\right)^{-0.2} \left(\varepsilon_{y\_co}\right)^{-2} \left(\varepsilon_{y\_su}\right)^{0.7} \quad (17)$$

The (R^2) goodness-of-fit for Eqs. (15), (16), and (17) was higher than 0.97, 0.95, and 0.99, respectively. As can be seen from the equations, the second critical parameters are independent of the Poisson's ratio (had less than 5% influence for the entire range of the Poison's ratios), and for a homogeneous sphere (E_{co}/E_{su} = 1) a second yield inception is unattainable (second yield parameters approach infinity). Simulations that were conducted under the slip contact condition, for the same mechanical parameters, showed very similar results for the second critical parameters. Hence, it can be concluded that for the entire range of input parameters in this study the effect of the contact condition on the second critical parameters is negligible.

4.2 Plasticity evolution

To better understand why the stick contact condition only affects the first yield inception in the coating and has a negligible effect on the second yield inception in the substrate, the plasticity boundaries under stick were compared to those under the slip contact condition for several special interferences, which are described in Ref. [34]. These special cases are: (1) the elastic core in the coating under the contact area completely disappears and a second yielding occurs on the substrate side of the interface; (2) reappearance of the elastic core under the contact area owing to increased plasticity in the substrate; (3) first appearance of a second elastic core in the coating; and (4) merging of the first and second elastic cores in the coating.

Figures 9 and 10 present the evolution of the plastic zones for a thick coating t/R = 0.05 and two extreme cases of low and high mismatch of the coating and substrate moduli of elasticity, respectively. Each figure presents equal dimensional interferences in slip and stick, $\omega = \delta$. However, the dimensionless interferences ω/ω_{c1} and δ/δ_{c1} are different because $\omega_{c1} \neq \delta_{c1}$ (see Eqs. (8) and (14)). The solid and dashed lines in these figures represent the plastic boundaries for the stick and slip contact conditions, respectively. Hence, the zones within these boundaries are plastically deformed, while those outside are still elastic. As the finite element

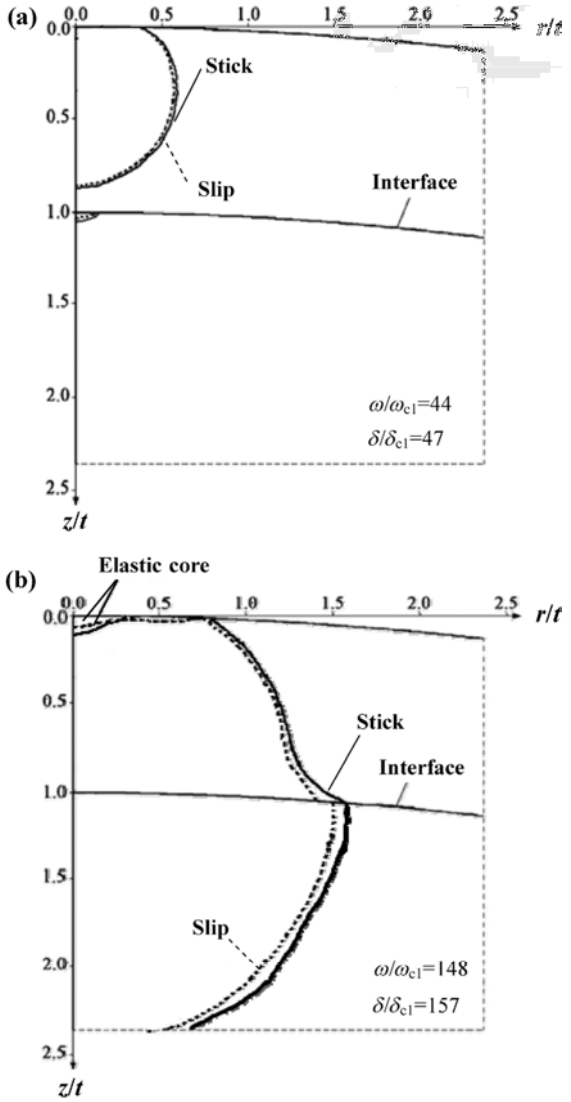

Fig. 9 Evolution of the plastic zones in the coated sphere (ν = 0.32, t/R = 0.05, ε_{y_su} = ε_{y_co}=0.001 and E_{co}/E_{su} = 2). (a) ω/ω_{c1} = 44 and δ/δ_{c1} = 47 and (b) ω/ω_{c1} = 148 and δ/δ_{c1} = 157.

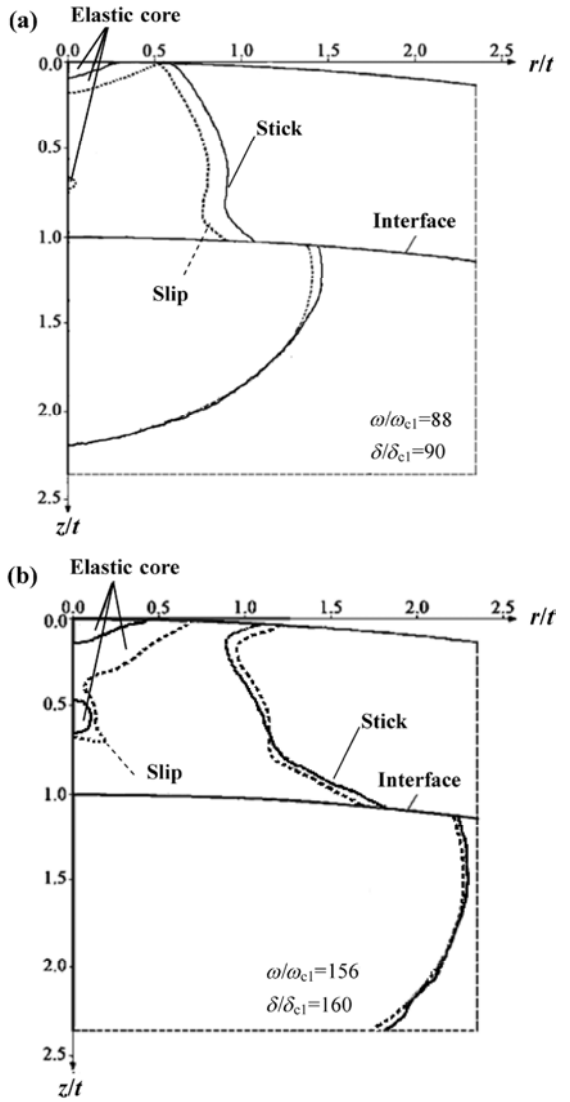

Fig. 10 Evolution of the plastic zones in the coated sphere (ν = 0.32, t/R = 0.05, ε_{y_su} = ε_{y_co} = 0.001 and E_{co}/E_{su} = 10). (a) ω/ω_{c1} = 88 and δ/δ_{c1} = 90 and (b) ω/ω_{c1} = 156 and δ/δ_{c1} = 160.

is axisymmetric, only half of the model is shown, and both axes are normalized using the coating thickness. In both cases, the Poisson's ratio is ν = 0.32. Figures 9(a) and 9(b) present the two special cases (1) and (2) above, respectively. In Fig. 9(a), the plastic zones in the coating at ω/ω_{c1} = 44 and δ/δ_{c1} = 47 are almost identical for stick and slip. However, the evolution history (not shown in the figure) is very different. For slip, an elastic core was present under the contact area for lower interference, which vanished at ω/ω_{c1} = 44. This elastic core did not appear in stick. Moreover, as shown in Fig. 9(a), the second yield inception in the substrate occurs simultaneously at ω/ω_{c1} = 44 and δ/δ_{c1} = 47 for slip and stick, respectively. In Fig. 9(b), at ω/ω_{c1} = 148 in slip and δ/δ_{c1} = 157 in stick, the plastic zones in the coating and substrate for slip and stick also look similar. The main difference between the two cases is, once again, the elastic core in the coating under the contact area. In slip, this elastic core, which vanished at ω/ω_{c1} = 44, reappears under the entire contact area at ω/ω_{c1} = 148. In stick, at δ/δ_{c1} = 157, the elastic core just appears for the first time. Figures 10(a) and 10(b) present, respectively, the two other special cases, (3) and (4), indicated above. Here again, the plastic zones in the substrate are almost identical for slip and stick and the main difference is in the elastic

cores within the coating. In Fig. 10(a), at $\omega/\omega_{c1} = 88$ and $\delta/\delta_{c1} = 90$, a second elastic core in the coating appears only in slip, and the first elastic core in stick is smaller than that in slip. In Fig. 10(b), at $\omega/\omega_{c1} = 156$ and $\delta/\delta_{c1} = 160$, the two elastic cores in slip have merged while these in stick are still separated. A similar behavior to that shown in Figs. 9 and 10 was also observed when comparing the conditions of slip and stick for the case of thinner coating with $t/R = 0.016$.

As can be seen, the contact condition has a significant effect on the plasticity evolution mainly within the coating close to the contact interface. The main difference that was observed is the behavior of the elastic cores for both contact conditions. This difference may be attributed to the additional tangential stresses at the contact area in stick.

4.3 Contact load and contact area

Figures 11 and 12 present typical dimensional results for the contact load L and contact area A_{st}, respectively, versus the interference δ. The individual effects of E_{co}/E_{su} and t/R are shown separately in parts (a) and (b), respectively. In each case the presented results are terminated at $\delta = \delta_{c2}$ (see Eq. (15)). As can be seen, different moduli ratios or coating thicknesses result in different load-interference and area-interference curves. In Fig. 11, it can be seen that at any given interference, increasing the moduli ratio or the coating thickness increases the contact load. Figure 12 shows that the contact area is almost linearly related to the interference. At any given interference, increasing the moduli ratio or decreasing the coating thickness decreases the contact area. This is similar to the results shown in Refs. [29, 30] for the slip contact condition in the elastic regime [29]. For large interferences ($\delta > \delta_{c1}$), varying the Poisson's ratio in the range $0.25 < \nu < 0.45$ had negligible effect (less than 8%) on the results of the contact load and contact area. Normalizing the numerical results of the contact load, L, contact area, A_{st}, and the interference, δ, by their corresponding numerical second critical values L_{c2}, A_{c2_st}, and δ_{c2}, consolidated the different curves (various coating thicknesses t/R and various E_{co}/E_{su} ratios) in Figs. 11 and 12 into single curves, as can be seen in Fig. 13. The empirical relations for the dimensionless numerical

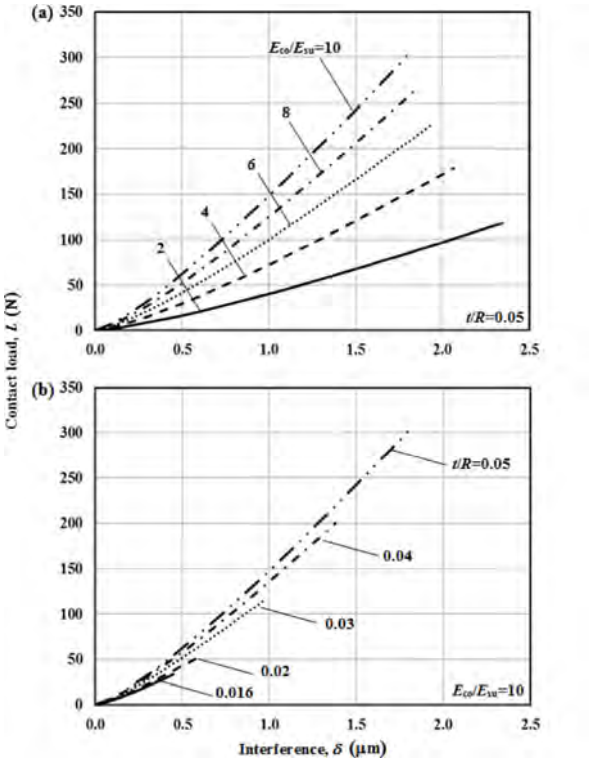

Fig. 11 Typical results for the contact load L vs. the interference δ ($\varepsilon_{y\_su} = \varepsilon_{y\_co} = 0.001$, $\nu = 0.32$): (a) $t/R = 0.05$ and (b) $E_{co}/E_{su} = 10$.

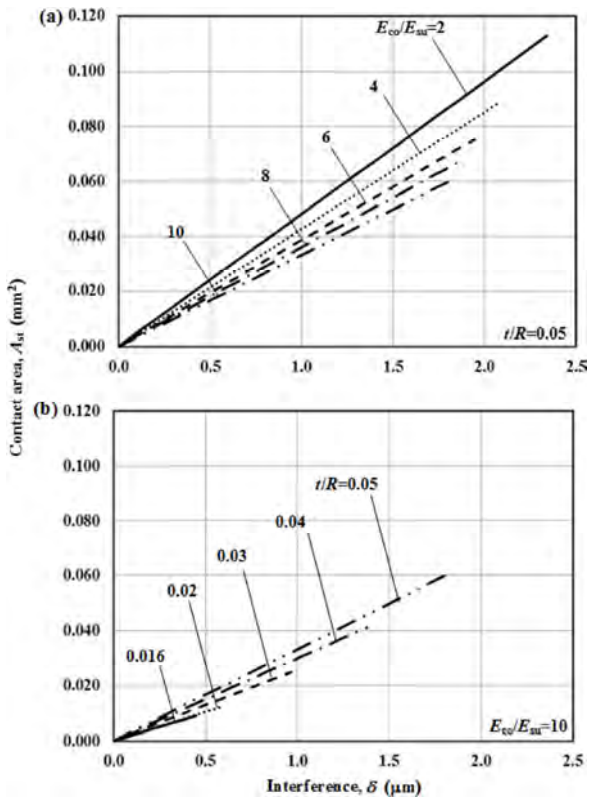

Fig. 12 Typical results for the contact area A_{st} vs. the interference δ ($\varepsilon_{y\_su} = \varepsilon_{y\_co} = 0.001$, $\nu = 0.32$): (a) $t/R = 0.05$ and (b) $E_{co}/E_{su} = 10$.

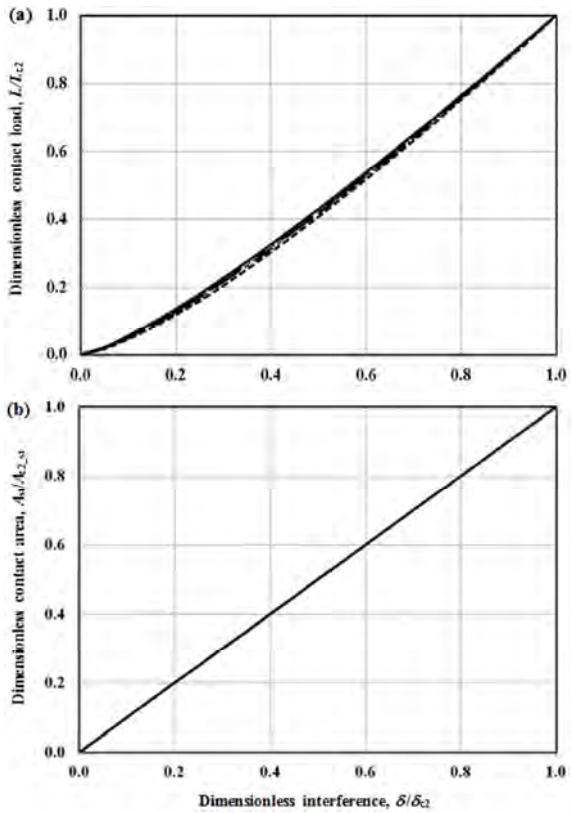

Fig. 13 (a) Dimensionless contact load L/L_{c2} and (b) dimensionless contact area A_{st}/A_{c2_st} vs. the dimensionless interference δ/δ_{c2} for all the cases shown in Figs. 11 and 12.

results in the elastic-plastic regime for the range $\delta_{c1} < \delta \le \delta_{c2}$ are

$$\frac{L}{L_{c2}} = \left(\frac{\delta}{\delta_{c2}}\right)^{1.25} \tag{19}$$

$$\frac{A_{st}}{A_{c2\_st}} = \frac{\delta}{\delta_{c2}} \tag{20}$$

The (R^2) goodness-of-fit for Eqs. (19) and (20) was better than 0.99. Simulations under the slip contact condition showed very similar results, indicating that the effect of contact condition on the contact parameters in the investigated elastic-plastic regime is negligible.

5 Conclusion

FEM was used to investigate the elastic-plastic contact of a coated sphere with a hard coating, compressed by a rigid flat under the stick contact condition. The effect of mechanical and geometrical properties on the contact parameters such as interference, load, and contact area was studied and compared with the corresponding results under the slip contact condition.

It was found that the general behavior of the onset of plasticity under stick and slip is similar, showing a maximum resistance to yield inception at a certain peak dimensionless thickness $(t/R)_p$. The effect of the contact condition on the dimensionless contact parameters in the elastic-plastic regime, up to the second critical interference δ_{c2}, is negligible except for the first critical interference δ_{c1} for coating thicknesses above $(t/R)_p$, when the first yield inception occurs within the coating slightly below the contact area. This is due to the additional tangential stresses at the contact area in stick.

The plasticity evolution under stick was studied and compared with that under the slip contact condition. The effect of the contact condition on the plastic zone boundaries is negligible, except for the evolution of elastic cores within the coating. This, too, may be attributed to the additional tangential stresses at the contact area in stick, which affect the stress level only within the coating close to the contact area.

The main purpose of studying the coated spherical contact under the stick condition is the ability to add a tangential loading, which cannot be supported under slip. Hence, this study is the first step towards developing a coated spherical contact under combined normal and tangential loading, which can be helpful in future research, to model the effect of coating properties on friction and wear. Substantial work is still needed in the future to consider additional parameters, and remove some of the simplified assumptions in the present analysis.

Acknowledgment

This paper is part of IEA AMT IA technical activities.

References

[1] Treutler C P O. Industrial use of plasma-deposited coatings for components of automotive fuel injection systems. *Surface and Coatings Technology* **200:** 1969–1975 (2005)

[2] Scharf T W, Prasad S V, Dugger M T, Kotula P G, Goeke R S, Grubbs R K. Growth, structure, and tribological behavior of atomic layer-deposited tungsten disulphide solid lubricant coatings with applications to MEMS. *Acta Materialia* **54:** 4731–4743 (2006)

[3] Law H H, Holden C A, Sapjeta J, Crane G R, Nakahara S. Electrical contact phenomena of nickel electrodeposits with sharp micro-asperities. *Transactions on Components Hybrids and Manufacturing Technology* **14**: 585–591 (1991)

[4] Neubauer E, Korb G, Eisenmenger-Sittner C, Bangert H, Chotikaprakhan S, Dietzel D, Mansanares A M, Bein B K. The influence of mechanical adhesion of copper coatings on carbon surfaces on the interfacial thermal contact resistance. *Thin Solid Films* **433**: 160–165 (2003)

[5] Clarke D R. Materials selection guidelines for low thermal conductivity thermal barrier coatings. *Surface and Coatings Technology* **163**: 67–74 (2003)

[6] Piazza F, Grambole D, Schneider D, Casiraghi C, Ferrari A C, Robertson J. Protective diamond-like carbon coatings for future optical storage disks. *Diamond and Related Materials* **14**: 994–999 (2005)

[7] Schintlmeister W, Wallgram W, Kanz J, Gigl K. Cutting tool materials coated by chemical vapor deposition. *Wear* **100**: 153–169 (1984)

[8] Greenwood J, Williamson J. Contact of nominally flat surfaces. *The Royal Society (London)* **295**: 300–319 (1966)

[9] Chang W, Etsion I, Bogy D B. An elastic-plastic model for the contact of rough surfaces. *ASME Journal of Tribology* **109**: 257–263 (1987)

[10] Jackson R L, Kogut L. A comparison of flattening and indentation approaches for contact mechanics modeling of single asperity contacts. *Tribology Transactions* **128**: 209–212 (2006)

[11] Komvopoulos K. Finite element analysis of a layered elastic solid in normal contact with a rigid surface. *ASME Journal of Tribology* **110**: 477–485 (1988)

[12] Kral E, Komvopoulos K, Bogy D. Finite element analysis of repeated indentation of an elastic-plastic layered medium by a rigid sphere, Part II: Subsurface results. *Journal of Applied Mechanics* **62**: 29–42 (1995)

[13] Ronkainen H, Koskinen J, Varjus S, Holmberg K. Load-carrying capacity evaluation of coating/substrate systems for hydrogen-free and hydrogenated diamond-like carbon films. *Tribology Letters* **6**: 63–73 (1999)

[14] Ye N, Komvopoulos K. Indentation analysis of elastic-plastic homogeneous and layered media: criteria for determining the real material hardness. *ASME Journal of Tribology* **125**: 685–691 (2003)

[15] Botelho T D S, Progri R, Inglebert G, Robbe-Valloire F. Analytical and experimental elastoplastic spherical indentations of a layered half-space. *Mechanics of Materials* **40**: 771–779 (2008)

[16] Ahmadi S R, Shakeri M, Sadough A. Stress analysis in thin coatings and substrate subjected to point contact loading (mechanics of scratch test). *Journal of Materials Processing Technology* **205**: 89–98 (2008)

[17] Kulchytsky-Zhyhailo R, Rogowski G. Stresses in hard coating due to a rigid spherical indenter on a layered elastic half-space. *Tribology International* **43**: 1592–1601 (2010)

[18] Johnson K L. *Contact Mechanics 1st ed.* Cambridge: Cambridge University Press, 1985.

[19] Kogut L, Etsion I. Elastic-plastic contact analysis of a sphere and a rigid flat. *Journal of Applied Mechanics* **69**: 657–662 (2002)

[20] Goodman L E. Contact stress analysis of normally loaded rough spheres. *Journal of Applied Mechanics* **29**: 515–522 (1962)

[21] Spence D A. The Hertz contact problem with finite friction. *Journal of Elasticity* **5**(3–4): 297–319 (1975)

[22] Brizmer V, Kligerman Y, Etsion I. The effect of contact conditions and material properties on the elasticity terminus of a spherical contact. *International Journal of Solids and Structures* **43:** 5736–5749 (2006)

[23] Brizmer V, Zait Y, Kligerman Y, Etsion I. The effect of contact conditions and material properties on elastic-plastic spherical contact. *Journal of Mechanics of Material and Structures* **1**(5): 865–879 (2006)

[24] Overcharenko A, Hlperin G, Verberne G, Etsion I. *In situ* investigation of the contact area in elastic-plastic spherical contact during loading-unloading. *Tribology Letters* **25**(2): 153–160 (2007)

[25] Goltsberg R, Etsion I, Davidi G. The onset of plastic yielding in a coated sphere compressed by a rigid flat. *Wear* **271**: 2968–2977 (2011)

[26] Song W, Li L, Ovcharenko A, Jia D, Etsion I, Talke F E. Plastic yield inception of an indented coated flat and comparison with a flattened coated sphere. *Tribology International* **52**: 61–67 (2012)

[27] Huang X, Kasem H, Shang H F, Shao T M, Etsion I. Experimental study of a potential weakening effect in spheres with thin hard coatings. *Wear* **296**: 590–597 (2012)
[28] Goltsberg R, Etsion I. A model for the weakening effect of very thin hard coatings. *Wear* **308**: 10–16 (2013)
[29] Goltsberg R, Etsion I. A universal model for the load–displacement relation in an elastic coated spherical contact. *Wear* **322**: 126–132 (2015)
[30] Goltsberg R, Etsion I. Contact area and maximum equivalent stress in elastic spherical contact with hard coating. *Tribology International* **93**: 289–296 (2016)
[31] Sun Y, Bloyce A, Bell T. Finite element analysis of plastic deformation of various TiN coating/substrate systems under normal contact with a rigid sphere. *Thin Solid Films* **271**: 122–131 (1995)
[32] Kral E, Komvopoulos K, Bogy D. Finite element analysis of repeated indentation of an elastic-plastic layered medium by a rigid sphere, Part II: Subsurface results. *Journal of Applied Mechanics* **62**: 29–42 (1995)
[33] Yoo Y-H, Lee W, Shin H. Spherical nano-indentation of a hard thin film/soft substrate layered system: II. Evolution of stress and strain fields. *Modeling and Simulation in Materials Science and Engineering* **12**: 69–78 (2004)
[34] Chen Z, Goltsberg R, Etsion I. Plasticity evolution in a coated sphere compressed by a rigid flat. *Tribology International* **98**: 116–124 (2016)

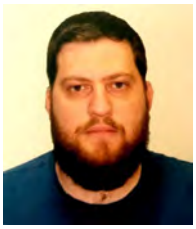

Shai RONEN. He received his bachelor degree in mechanical engineering in 2010 from Technion-Israel Institute of Technology. Recently he had obtained his master degree in design and manufacturing management from the same institute.

Roman GOLTSBERG. He received his bachelor degree in mechanical engineering in 2010 from Technion-Israel Institute of Technology. In 2015 he had obtained his Ph.D. degree in mechanical engineering from the same institute. His research interests include contact mechanics of coatings and hydrodynamic bearings.

Izhak ETSION. He received his PhD degree in 1974 from Technion-Israel Institute of Technology. Since then he was a faculty at the Department of Mechanical Engineering where he is currently a Professor Emeritus. His research interests are in hydrodynamic lubrication, surface texturing, contact mechanics, nano-tribology and bio-tribology. Etsion has published over 200 papers on various aspects of tribology and holds 15 patents. He is the founder of Surface Technologies Ltd. that developed the laser surface texturing (LST) technology for friction and wear reduction. His honors include Fellow of the ASME (1999), Fellow of the STLE (2001), the STLE 2005 International Award and the ASME 2016 Mayo D. Hersey Award.

Friction **5**(3): 339–350 (2017)
https://doi.org/10.1007/s40544-017-0179-1
ISSN 2223-7690
CN 10-1237/TH

RESEARCH ARTICLE

Combined effect of surface microgeometry and adhesion in normal and sliding contacts of elastic bodies

Irina GORYACHEVA*, Yulia MAKHOVSKAYA

Institute for Problems in Mechanics of the Russian Academy of Sciences, Pr. Vernadskogo 101-1, Moscow 119526, Russia

Received: 28 April 2017 / Revised: 06 June 2017 / Accepted: 19 June 2017

Abstract: In this study, models are proposed to analyze the combined effect of surface microgeometry and adhesion on the load–distance dependence and energy dissipation in an approach–separation cycle, as well as on the formation and rupture of adhesive bridges during friction. The models are based on the Maugis–Dugdale approximation in normal and frictional (sliding and rolling) contacts of elastic bodies with regular surface relief. For the normal adhesive contact of surfaces with regular relief, an analytical solution, which takes into account the mutual effect of asperities, is presented. The contribution of adhesive hysteresis into the sliding and rolling friction forces is calculated for various values of nominal pressure, parameters of microgeometry, and adhesion.

Keywords: adhesion; roughness; discrete contact; rolling friction; sliding friction

1 Introduction

Adhesive interactions play a very important role in surface friction, particularly at micro and nanoscale levels [1, 2]. It was established experimentally and theoretically that at these scale levels, the contact characteristics and friction forces depend on the mechanical properties of the interacting bodies, their surface energy, and surface microgeometry.

Theoretical models that have been developed to analyze the adhesion during contact of deformable bodies differ in constitutive equations for solids, models of adhesive interaction, and description of the geometry of contacting surfaces. The commonly used models of adhesive interaction include the classical JKR [3] and DMT [4] theories, Maugis–Dugdale model [5], exact form of the Lennard–Jones potential [6] as well as its approximations by various analytical functions [7], double-Hertz approximation [8], and piecewise-constant approximation [9]. The geometry of interacting surfaces can be described as a set of asperities of determined configuration, or it can be modeled by statistical or fractal approaches. All these models and approaches being combined in the formulation of a contact problem have generated a large number of theoretical works, each having a specific limit and applicability area.

The normal adhesive contact between rough elastic bodies was first studied by Johnson [10] and Fuller and Tabor [11], who employed exponential and Gaussian distributions of heights of asperities, respectively, and the JKR model of adhesion. It was shown that large diversity of heights of asperities leads to low adhesion between the surfaces, because high asperities coming into contact can cause elastic forces of repulsion between the surfaces. The DMT model of adhesion was generalized for the case of a rough surface with a specified distribution of heights in Ref. [12]. The method suggested by Fuller and Tabor [11] was applied in Ref. [13] to describe a rough contact with the use of the Maugis–Dugdale model. The adhesion of rough elastic bodies with arbitrary nominal geometry at macrolevel was modeled in Ref. [14] by applying a statistical description of roughness at microlevel and the JKR and DMT models of adhesion. The models of adhesive contact developed by Rumpf [15] and Rabinovich et al. [16] consider rigid rough surfaces

* Corresponding author: Irina GORYACHEVA, E-mail: goryache@ipmnet.ru

having hemispherical asperities, whose centers lie on the surfaces (small asperities superimposed on large asperities), and both models use the Derjaguin approximation for adhesive interaction [17] (see the discussion on Derjaguin approximation in Ref. [18]).

There were several studies that considered normal contact between rough surfaces with adhesion by using a fractal approach. Following are several examples. A contact problem between self-affine fractal surfaces was studied using a method of dimensionality reduction in Ref. [19]. The fractal approach was also employed in Ref. [20] for studying adhesive contact between rough surfaces. An approach similar to fractal surface roughness description was used by Persson and Tossati with the JKR [21, 22] and DMT [23] models of adhesion. A model for adhesion between self-affine rough surfaces based on the JKR theory was suggested by Ciavarella [24] for a contact close to saturation. A numerical simulation of adhesion for self-affine rough surfaces was carried out in Ref. [25]. The results of this simulation and the applicability area of the DMT approximation in rough adhesive contacts were discussed in Refs. [26, 27]. A simplified model for adhesion between elastic rough solids with Gaussian multiple scales of roughness was suggested in Ref. [28]. The limitations of the fractal approach to describe the roughness of real surfaces were discussed by Borodich et al. [29, 30].

To analyze the effect of the shape of asperities and their mutual arrangement, it is necessary to consider contact problems for surfaces with regular relief. Periodic formulations of contact problems often allow a closed-form solution, which takes into account the mutual effect of contact spots through the elastic body. Two-dimensional contact problems for a rough surface with periodic relief and an elastic half-plane were solved [31–33] for various models of adhesion. For a 3D case, the adhesive contact between a periodic system of asperities and elastic half-space was modeled in Ref. [34] by using the Maugis–Dugdale approximation and by considering the shape of asperities and mutual effect of contact spots.

According to the classical approach [35], the sliding friction force is the sum of two components: mechanical component and adhesive component. The adhesive component is assumed to be equal to the force required for plastic shear to occur on the microcontacts. This approach to modeling the adhesion component of the friction force was developed in Refs. [36–38]. However, it is known that adhesion can contribute to the friction force even in the absence of plastic deformation, e.g., at very small loads. To model the adhesion friction force in this case, an approach is developed by considering the adhesion contact as opening and closing cracks [39]. It was established experimentally that the value of the friction force between two solids correlates with the value of adhesion hysteresis in an approach–separation cycle of these solids [40–42]. Models relating adhesion friction force to adhesion hysteresis were suggested for a cylinder [43] and a periodic rough surface [44] sliding on an elastic body. Adhesion hysteresis was taken into account as the difference in the surface energy before and after the moving contact zone. Another approach was suggested by Heise and Popov [45], who calculated the sliding friction force between two rough surfaces as a result of adhesion hysteresis in the approach–separation cycle for asperities. They used the JKR model of adhesion and random distribution of heights of asperities. In Ref. [46], the adhesion component of the sliding friction force was modeled by calculating the energy dissipation in the formation and rupture of the adhesive contacts between asperities of rough surfaces in sliding. In this model, rough surfaces had regular relief and the Maugis–Dugdale model of adhesion was used, making it possible to apply the solution in a wide range of geometric and adhesive characteristics.

Adhesive interactions also contribute into the rolling resistance [1]. The adhesive component of the rolling resistance was calculated in Ref. [1] based on the assumption that each approach and separation of molecules is accompanied by an energy loss. In Ref. [47], the rolling resistance was accounted for by the attraction of separating parts of the surfaces owing to the opposite electrical charges arising between them. The adhesive component of the rolling resistance was calculated in Ref. [48] based on the energy dissipation mechanism in the approaching and separation of asperities of contacting surfaces in the process of rolling.

The present study focuses on the analysis of the effect of adhesive interaction modeled by the Maugis–Dugdale approximation in normal and frictional (sliding

and rolling) contacts of elastic bodies with regular surface relief. The combined effect of adhesion and surface microgeometry on the load–distance dependence and energy dissipation in the approach–separation cycle, as well as on the formation and rupture of adhesive bridges during friction is analyzed. For the normal adhesive contact of surfaces with regular relief, an analytical solution that takes into account the mutual effect of asperities is presented.

2 Normal contact of a rough surface with elastic half-space in the presence of adhesion

2.1 Model of adhesion

The adhesive force per unit area $p_a(z)$ is approximated by a piecewise constant function known as the Maugis–Dugdale model [5]:

$$p_a(z)=\begin{cases}-p_0, & 0<z\le h_0\\ 0, & z>h_0\end{cases} \tag{1}$$

In this case, the work of adhesion w is defined by

$$w=\int_0^\infty p_a(z)\,\mathrm{d}z=p_0h_0 \tag{2}$$

For a spherical punch in contact with an elastic half-space, the model of adhesion as defined by Eqs. (1)–(2), provides a closed-form solution [5]. Unlike the classical models of adhesion, i.e., the JKR [3] and DMT [4] models, the Maugis–Dugdale model is applicable to solids of arbitrary stiffness in a wide range of adhesion parameters.

2.2 Problem formulation

We consider the interaction of two solids with nominally flat surfaces (Fig. 1). Solid 1 is rigid and is covered with rigid hemispherical asperities of equal radius R, while solid 2 is an elastic half-space with a smooth surface. We assume that the asperities are in the nodes of a hexagonal lattice with a lattice spacing l. The origin of the local cylindrical system of coordinates (r, z, ϕ) coincides with the point at which an asperity touches the undeformed half-space. The z-axis is directed into the half-space. In this system of coordinates, the shape of each asperity is described by the function $f(r)=r^2/(2R)$.

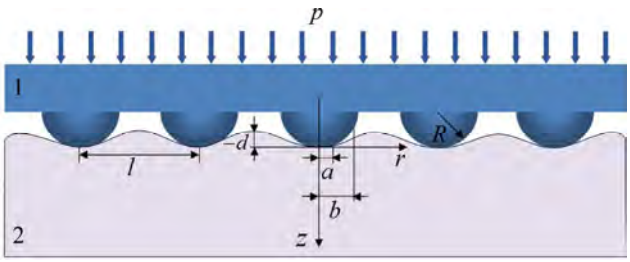

Fig. 1 Contact scheme between a rigid rough surface and an elastic half-space in the presence of adhesion.

Solid 1 is acted upon by a uniform nominal pressure p. The distributions of pressure and elastic displacement of the boundary of the half-space are assumed to be axisymmetric near each asperity. The gap between the contacting surfaces near an asperity can be represented as

$$h(r)=f(r)-f(a)+u(r)-u(a) \tag{3}$$

where $u(r)$ is the elastic displacement of the boundary of the half-space in the z direction, and a is the radius of the contact spot.

To take into account the adhesive attraction between the surfaces, we use the Maugis–Dugdale model defined by Eqs. (1)–(2) and assume that a negative pressure $(-p_0)$ is applied to the elastic half-space in the ring-shaped region $a\le r\le b$ around each asperity. From Eq. (2), we obtain the relation for the gap at $r=b$:

$$h(b)=\frac{w}{p_0} \tag{4}$$

The values of the work of adhesion w and adhesive pressure p_0 are assumed to be known.

The problem is solved by the method of localization [49]. In accordance to this method, to determine the stress–strain state near a contact spot, one should replace the effect of the remaining contact spots by the action of an averaged pressure in the region $r\ge R_{\mathrm{eff}}$. The solution to this problem was established in Ref. [34] for a system of asperities, whose shape is described by the power-law function of an even degree. We will use the results obtained in Ref. [34] for the case of asperities of hemispherical shape.

If the surfaces are in contact, the following relations

for the nominal pressure p and distance d between the surfaces are valid:

$$p=\frac{\pi}{\sqrt{3}l^2}\frac{4E^*a^3/(3R)-2p_0b^2\left(\arccos(a/b)+a\sqrt{1-\left(a/b\right)^2}\Big/b\right)}{\arccos(a/R_{\text{eff}})+a\sqrt{1-\left(a/R_{\text{eff}}\right)^2}\Big/R_{\text{eff}}} \tag{5}$$

$$d=-\frac{a^2}{R}+\frac{2p_0b}{E^*}\sqrt{1-\left(\frac{a}{b}\right)^2}+\frac{2pR_{\text{eff}}}{E^*}\sqrt{1-\left(\frac{a}{R_{\text{eff}}}\right)^2} \tag{6}$$

The contact radius a and the external radius of the region of adhesion b are related by the equation that follows from Eqs. (3)–(4) and has the form

$$h(b)=\left(\frac{b^2}{2R}-d\right)\frac{2}{\pi}\arccos\frac{a}{b}+\frac{a^2}{\pi R}\sqrt{\left(\frac{b}{a}\right)^2-1}-\frac{4p_0}{\pi E^*}(b-a)-\frac{4pR_{\text{eff}}}{\pi E^*}\left[E\left(\frac{b}{R_{\text{eff}}}\right)-E\left(\arcsin\frac{a}{b},\frac{b}{R_{\text{eff}}}\right)\right]=\frac{w}{p_0} \tag{7}$$

where $E(x), E(\theta,x)$ are complete and incomplete elliptic integrals of the second kind, respectively. In Eqs. (5)–(7), we use the notation $E^*=E/(1-\nu^2)$, where E and ν are the Young's modulus and Poisson's ratio of the elastic half-space, respectively, and $R_{\text{eff}}=l(\sqrt{3}/(2\pi))^{1/2}$.

If the surfaces are not in contact and they interact only by adhesive forces, the nominal pressure and distance are defined by

$$p=-\frac{2\pi p_0b^2}{\sqrt{3}l^2},\quad d=-\frac{b^2}{2R}+\frac{4}{\pi E^*}p_0b\left[1-\frac{b}{R_{\text{eff}}}E\left(\frac{b}{R_{\text{eff}}}\right)\right]+\frac{w}{p_0} \tag{8}$$

The solution specified by Eqs. (5)–(8) is applicable for $l > b$.

If q is the normal force acting on each asperity, then from the geometry of the problem it follows that

$$p=\frac{2q}{\sqrt{3}l^2} \tag{9}$$

From Eqs. (5)–(7), by taking into account Eq. (9) and setting $l\to\infty$, we obtain the solution to the contact problem for an individual hemispherical asperity of radius R acted upon by a normal load q and an elastic half-space:

$$q=\frac{4E^*}{3}\frac{a^3}{R}-2p_0b^2\left(\arccos\frac{a}{b}+\frac{a}{b}\sqrt{1-\left(\frac{a}{b}\right)^2}\right),\quad d=-\frac{a^2}{R}+\frac{2p_0b}{E^*}\sqrt{1-\left(\frac{a}{b}\right)^2} \tag{10}$$

$$\left(\frac{b^2}{2R}-d\right)\frac{2}{\pi}\arccos\frac{a}{b}+\frac{a^2}{\pi R}\sqrt{\left(\frac{b}{a}\right)^2-1}-\frac{4p_0}{\pi E^*}(b-a)=\frac{w}{p_0} \tag{11}$$

Eqs. (9)–(10) coincide with the solution obtained by Maugis [5].

For the case where an individual asperity interacts with the elastic half-space without contact, from Eqs. (8) and (9) for $l\to\infty$ we have

$$q=-\pi b^2p_0,\quad d=-\frac{b^2}{2R}+\frac{4}{\pi E^*}p_0b+\frac{w}{p_0} \tag{12}$$

2.3 Parametrization

For convenience in the calculation and analysis of results, we use the following parametrization by introducing a dimensionless nominal pressure p^* and dimensionless distance between the surfaces d^* in accordance with the following relations:

$$p^*=\frac{l^2}{\sqrt{3}\pi w\ R}p,\quad d^*=\frac{4}{3}\left(\frac{E^{*2}}{\pi^2w^2R}\right)^{1/3}d \tag{13}$$

The solution to the problem depends on the following two dimensionless parameters:

$$\lambda=p_0\left(\frac{9R}{2\pi wE^{*2}}\right)^{1/3} \tag{14}$$

$$L=l\left(\frac{\sqrt{3}}{2\pi}\right)^{1/2}\left(\frac{E^*}{\pi wR^2}\right)^{1/3} \tag{15}$$

A parameter similar to λ was first used in Ref. [5]; this parameter specifies the characteristics of adhesive

interaction of elastic spheres. The adhesion parameter λ is related to the parameter μ_T introduced by Tabor [50] as

$$\lambda = \frac{16}{9^{2/3}3^{1/2}(2\pi)^{1/3}}\mu_T \approx 1.1\mu_T \quad (16)$$

The parameter L characterizes the mutual effect of the asperities. For large values of L, the mutual effect is insignificant.

2.4 Results of calculations

For the calculations, we use Eqs. (5)–(8) with the parametrization given by Eqs. (13)–(15), which allow us to prescribe the values of the parameters λ and L. These are used to calculate the dimensionless distance d^* between the interacting surfaces for various values of the dimensionless nominal pressure p^*. The results obtained are shown in Fig. 2.

The results are presented in the domain of negative values of the nominal pressure, because in this domain, the effect of the adhesive forces is very significant. The results indicate that the adhesion parameter λ significantly affects the dependence of the nominal pressure on the distance. An increase in the parameter λ leads to a considerable increase in the values of negative nominal pressures at which the surfaces can be in contact. A decrease in the parameter L, which characterizes the distance between asperities, leads to an increase in the pull-off pressure (maximum absolute value of the negative pressure at which the contact exists) and a shift of this value to the direction of smaller distances between the interacting bodies. Thus, surfaces with asperities located closer to each other can sustain higher values of negative pressure in contact.

In an adhesive contact of elastic bodies, the work required to separate contacting surfaces from each other is in general, higher than the work done in approaching the surfaces from infinity to the initial distance. Thus, hysteresis takes place in the approach–separation cycle. This follows from the ambiguity of the curves of the nominal pressure vs distance, which can be observed for sufficiently large values of the adhesion parameter λ. When the surfaces move away from each other, the contact breaks at point A with a jump to point B. When the surfaces approach each other, a jump in contact occurs from C to D. The difference between the values of the work in the approach and separation of the surfaces is equal to the dashed area in Fig. 2; it can be calculated in accordance with the relation

$$\Delta w = \int_{ABCD} p(d)\,\mathrm{d}d \quad (17)$$

Graphs of the dimensionless energy dissipation in the approach–separation cycle vs the adhesion parameter λ are shown in Fig. 3. The energy dissipation per unit area is calculated in dimensionless form:

$$\Delta w^* = \Delta w \frac{4l^2}{3\sqrt{3}}\left(\frac{E^{*2}}{\pi^5 w^5 R^4}\right)^{1/3}.$$

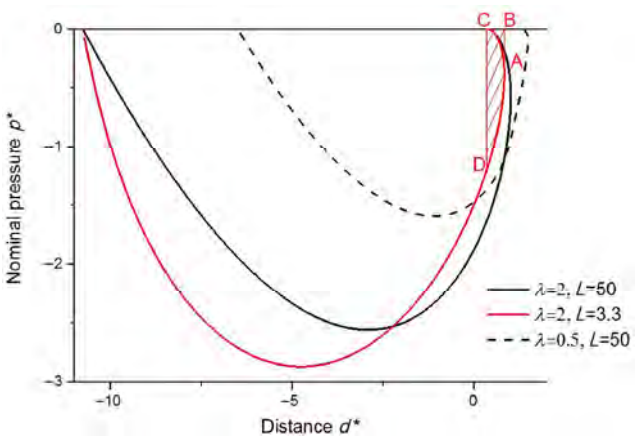

Fig. 2 Dimensionless nominal pressure vs distance in normal approach and separation of rough surfaces.

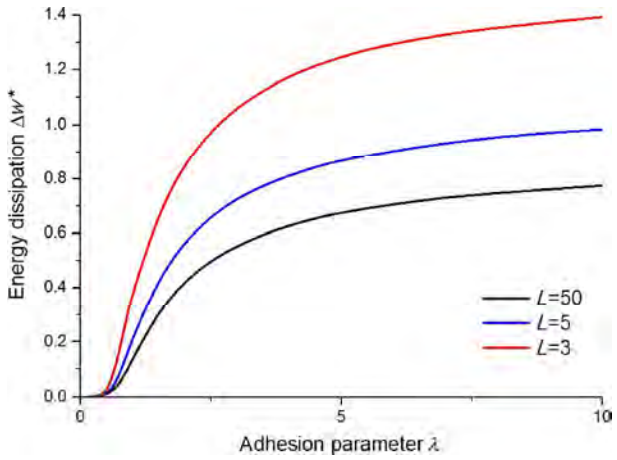

Fig. 3 Energy dissipation per unit area in the approach–separation cycle of rough surfaces.

The results indicate that the energy dissipation tends to approach zero as $\lambda \to 0$ and to a constant value as $\lambda \to \infty$. An increase in the contact density leads to an increase in the energy dissipation per unit area of the interacting surfaces.

Note that for two single elastic asperities, the analysis of the energy dissipation in an approach–separation cycle vs adhesion parameter was first carried out in Ref. [51] based on an analytical representation of the contact problem solution for the Maugis–Dugdale model of adhesion and power-law shapes of asperities. In Ref. [52], the effect of the Tabor parameter on the hysteretic loss was numerically studied for two elastic spheres interacting with the Lennard–Jones potential. The results of both these studies indicate that for smooth bodies, the dependence of the energy dissipation on the adhesion parameter is similar to that presented in Fig. 3 for a rough solid.

The obtained calculation results of the energy dissipation in the approach–separation cycle can be used to estimate the contribution of adhesion in the friction force in sliding and rolling contacts of rough surfaces.

3 Adhesion in sliding of rough surfaces

Consider the mutual sliding of two rough surfaces of regular shape. It is assumed that the upper and lower surfaces have the same period of roughness l (Fig. 4). Let surface 1 covered with asperities of radius R_1 be at rest, while surface 2, covered with asperities of radius R_2, moves in the tangential direction along the x-axis, with the vertical distance between the surfaces δ (along the z-axis) being constant. Each pair of asperities does not interact with each other initially; then, they come into contact and experience mutual sliding until the contact breaks.

To calculate the contribution of adhesive hysteretic losses into the total friction force, we assume that

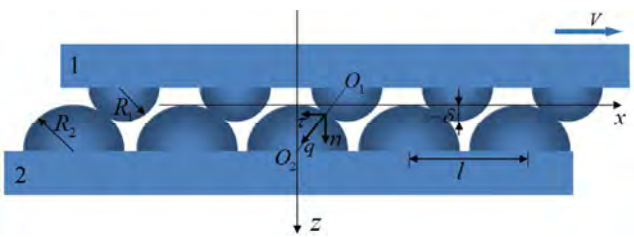

Fig. 4 Sliding scheme of two regular rough surfaces.

there is no shear stress within each contact spot. It should be also mentioned that here and in subsequent sections, the interaction of each pair of asperities is modeled separately; thus, the mutual effect of asperities is not taken into account similar to what was done in Section 2.

Because the asperities have spherical shapes, the force of interaction between them acts along the line O_1O_2 passing through the centers of the spheres. The tangential stresses are assumed to be zero; hence, the contact problem for two asperities is axisymmetric with respect to the line O_1O_2 at each instant of time. The force of interaction q as a function of the distance between two asperities d is defined by Eqs. (10) and (11) for the case involving contact between asperities and by Eq. (12) for the case with no contact. The force q can be divided into normal n and tangential τ components:

$$n = \frac{q(R_1 + R_2 + \delta)}{\sqrt{(R_1 + R_2 + \delta)^2 + x^2}}, \quad \tau = \frac{qx}{\sqrt{(R_1 + R_2 + \delta)^2 + x^2}} \tag{18}$$

where x is the tangential displacement of surface 1 with respect to surface 2.

Graphs of the dimensionless normal $n/(\pi R^* w)$ and tangential $\tau/(\pi R^* w)$ forces acting on an asperity of surface 1 during sliding along the x-axis are shown in Fig. 5. The results are obtained for the following values of the parameters characterizing the elastic and adhesive properties of the surfaces: $w/(p_0 R^*) = 0.1$ and $p_0/E^* = 0.5$. Here, R^* and E^* are the reduced radius of the asperities and elastic modulus, respectively:

$$\frac{1}{R^*} = \frac{1}{R_1} + \frac{1}{R_2}, \quad \frac{1}{E^*} = \frac{1-\nu_1}{E_1} + \frac{1-\nu_2}{E_2}.$$

The ratio of the reduced radius of the asperities to the distance between them is taken as $R^*/l = 0.3$. The curves shown in Figs. 5(a) and 5(b) correspond to the dimensionless vertical distance between the surfaces $\delta/R^* = -0.1$ and $-\delta/R^* = -0.3$, respectively. The results indicate that in the process of sliding, the tangential force τ changes its sign from positive (acting in the direction of sliding) to negative (acting in the direction opposite to sliding). Based on the obtained relations from Eqs. (10)–(12) and (18), we calculate the

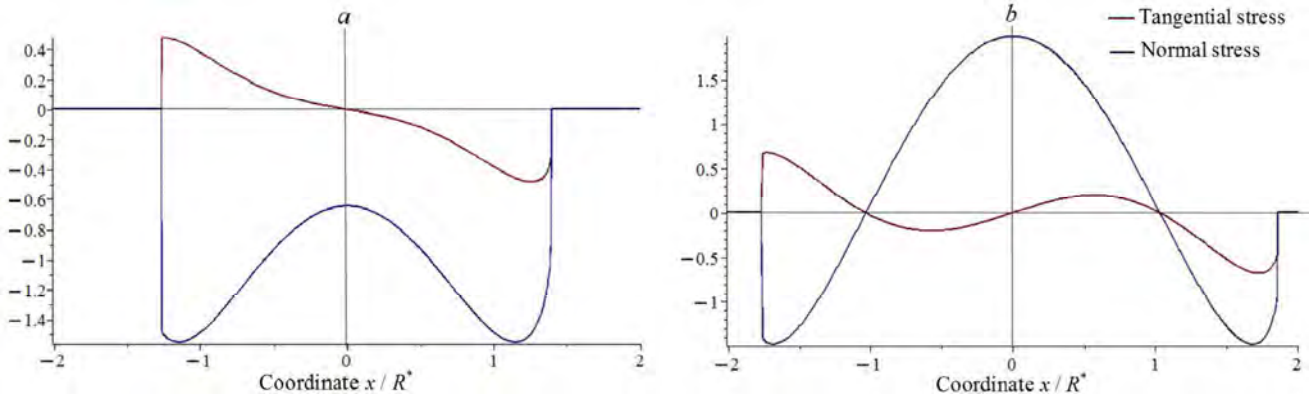

Fig. 5 Normal and tangential forces between two asperities in the sliding of two rough surfaces.

average normal and tangential forces acting on a unit area of surface 1 from surface 2:

$$T = \frac{1}{l}\int_{-l/2}^{l/2} \tau(s)\mathrm{d}s\,, \quad P = \frac{1}{l}\int_{-l/2}^{l/2} n(s)\mathrm{d}s.$$

The mean tangential force T is not equal to zero because of the energy dissipation occurring in the approach–separation cycle of asperities. This force, which is associated with the energy losses in the formation and breaking of adhesive bonds, can be called the adhesive component of the friction force. The coefficient of friction is defined by the relation

$$\mu = \frac{T}{P}.$$

Graphs of the coefficient of friction μ vs the dimensionless nominal pressure $P/(\pi E^* l^2)$ are shown in Fig. 6 for various values of the dimensionless reduced radius of asperities R^*/l for $w/(p_0 R^*) = 0.1$ and $p_0 / E^* = 1$. It is observed that the coefficient of friction increases with decreasing nominal pressure, and it attains considerably high values at very small pressures. This behavior is a characteristic of the adhesive component of the friction force. An increase in the radius of the surface asperities leads to an increase in the coefficient of friction.

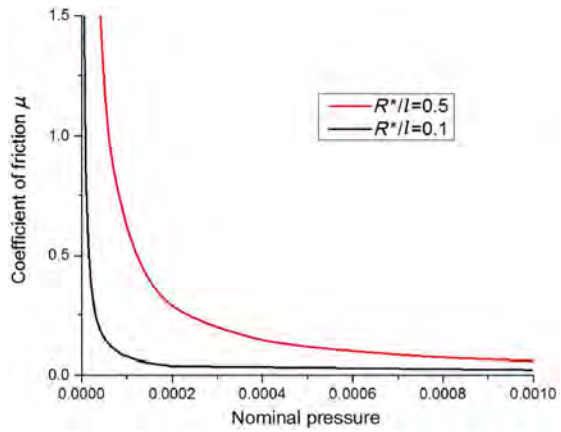

Fig. 6 Coefficient of friction vs nominal pressure.

4 Adhesive resistance to rolling of rough bodies

Consider a rigid rough cylinder of radius R rolling on the boundary of an elastic half-space (Fig. 7). The cylinder is acted upon by a normal force P and is rolling with an angular velocity ω. The surface of the cylinder is covered with a periodic system of rigid asperities located in the nodes of the rectangular lattice with spacing l. The height distribution of the asperities is described by the function $\phi(t)$. All asperities have the same radius R_0.

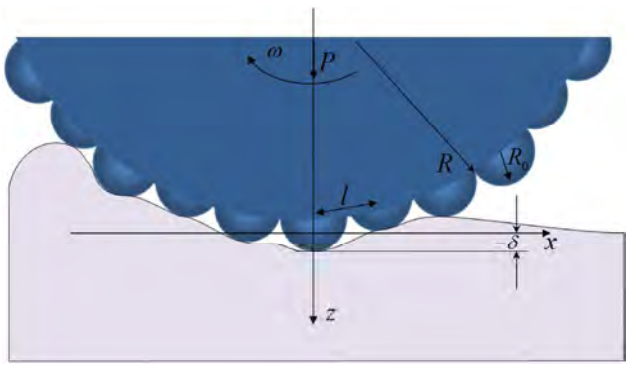

Fig. 7 Rolling scheme of a rough cylinder on an elastic half-space.

The problem is considered in the moving system of coordinates, whose *z*-axis passes through the axis of the cylinder and is directed in the half-space. Meanwhile, the *x*-axis coincides with the undeformed surface of the elastic half-space and is directed in the direction of motion of the cylinder. The value of the gap between the surfaces of the rough cylinder and the elastic half-space is defined by the expression

$$h(x,y) = u(x,y) + f(x,y) + \delta,$$

where $u(x,y)$ is the elastic displacement of the surface of the half-space in the *z* direction, $f(x,y)$ is a function describing the shape of the surface of the rough cylinder, and δ is the normal distance between the cylinder and the half-space.

The cylinder and the half-space are in contact over the areas of real contact A_i, in which the condition of contact is satisfied:

$$h(x,y) = 0, \quad (x,y) \in A_i.$$

The tangential stresses on the real areas of contact are assumed to be zero. The surfaces of the cylinder and half-space are attracted to each other owing to adhesion. The adhesion attraction takes place in the areas B_i, which are either ring-shaped surrounding the real contact areas A_i, or circular for asperities that are not in contact with the half-space. The dependence of the adhesive force on the gap between the surfaces is described by the piecewise constant function defined by Eq. (1). Thus, the adhesive pressure $p_a(x,y)$ on the surface of the elastic half-space is defined by

$$p_a(x,y) = \begin{cases} -p_0, & h(x,y) \le h_0 \\ 0, & h(x,y) > h_0 \end{cases}, \quad (x,y) \in B_i.$$

The work of adhesion is defined by Eq. (2).

During rolling, each *i*-th asperity approaches the surface of the elastic half-space beginning from a distance δ_∞, at which surfaces do not attract, to a minimum distance δ_0^i, which occurs in the point of maximum loading of the nominal contact area. Afterward, the asperity moves away from the surface of the half-space up to the distance δ_∞. It was shown in Section 2 that in the approach–separation cycle of an asperity and the elastic half-space, energy dissipation occurs (dashed region in Fig. 2). For an asperity that passes through the contact zone in the rolling of a rough cylinder, the energy dissipation is calculated as

$$\Delta w = \int_{\delta^{\text{app}}}^{\delta^{\text{sep}}} \left[q_i^{\text{app}}(\delta) - q_i^{\text{sep}}(\delta) \right] \mathrm{d}\delta \tag{19}$$

where $q_i^{\text{app}}(\delta)$ is the force–distance dependence in the approach (branch BCD in Fig. 2) and $q_i^{\text{sep}}(\delta)$ is the force–distance dependence in the separation (branch DAB in Fig. 2). The energy dissipation as defined by Eq. (19) differs from zero under the condition that the minimum distance between the surfaces is smaller than the distance at which they come into contact (point *C* in Fig. 2). This value is denoted as δ^{app}.

As the cylinder makes a full revolution, the energy dissipation will be equal to $\Delta w N_1$, where N_1 is the number of asperities for which the minimum distance to the half-space for a full revolution of the cylinder is smaller than δ^{app}. It is assumed that this energy loss is equal to the work of the moment of rolling resistance per one revolution $2\pi M$. Then, the moment of rolling resistance can be expressed as

$$M = \frac{\Delta w N_1}{2\pi}.$$

For a model of a rough cylinder having *N* asperities of the same height in the cross-section, the number N_1 is defined by the following stepwise function:

$$N_1 = \begin{cases} N, & c \ge c^{\text{app}} \\ 0, & c < c^{\text{app}} \end{cases}.$$

We can also consider a case where the asperities have a statistical distribution of heights:

$$N_1 = N \int_{-\infty}^{c} \varphi(t)\mathrm{d}t.$$

where $\varphi(t)$ is the density of distribution, for example, according to the Gauss law:

$$\varphi(t) = \frac{1}{\sqrt{2\pi}\sigma} \mathrm{e}^{-\frac{1}{2}\frac{t^2}{\sigma^2}}.$$

The graphs of the dimensionless moment of rolling resistance $\frac{M}{E^* R^3}$ vs the dimensionless distance bet-

ween the cylinder and the half-space are shown in Fig. 8 for the one-level roughness model (curve 1) and Gaussian distribution of heights of asperities (curve 2). The results are obtained for $\frac{w}{p_0 R_0} = 0.1$, $\frac{p_0}{E^*} = 0.1$, $\frac{R_0}{R} = 0.01$, and $N = 10,000$; the mean square deviation for the case of a Gaussianian height distribution is $\frac{\sigma}{R} = 0.01$. The results indicate that as the distance between the surfaces decreases (the indentation of the cylinder into the half-space increases), the rolling resistance increases sharply in the case of one-level roughness and smoothly in the case of height distribution. At large indentations of the cylinder into the elastic half-space, the rolling resistance tends to approach a constant value that depends on the geometrical characteristics of the cylinder, elastic properties of the half-space, and characteristics of adhesion.

The results obtained indicate also that the moment of rolling resistance $\frac{M}{E^* R^3}$ increases as the work of adhesion w increases. This is illustrated by the graphs shown in Fig. 9, which are obtained for $\frac{p_0}{E^*} = 0.1$, $N = 10,000$, and various radii of curvature of asperities $\frac{R_0}{R} = 0.01$ (curve 1) and $\frac{R_0}{R} = 0.012$ (curve 2) for the case of asperities of the same height and when the distance between the cylinder and the half-space is smaller than δ^{app}. It is evident that the moment of rolling resistance tends to approach a constant value as the work of adhesion increases, which is the result

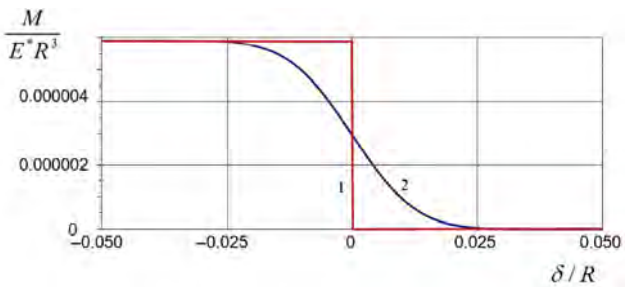

Fig. 8 Moment of rolling resistance vs dimensionless distance between a cylinder and elastic half-space.

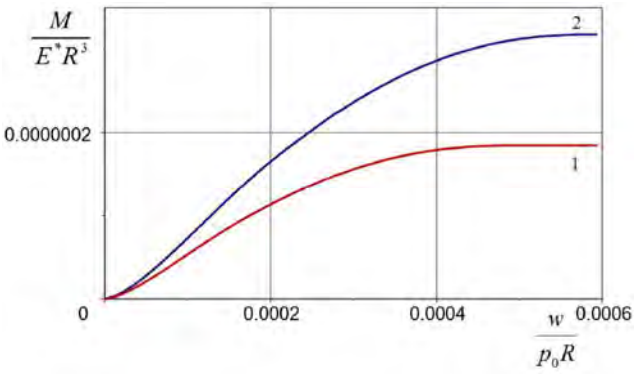

Fig. 9 Moment of rolling resistance vs dimensionless work of adhesion.

of using the simplified Maugis–Dugdale model as defined by Eq. (1), to describe the adhesive interaction of the surfaces instead of the full Lennard–Jones form. It also follows from the results that the adhesive losses of energy and hence, the rolling resistance, are higher for asperities with larger radius R_0.

5 Conclusion

In this study, an approach is developed to investigate the combined effect of the parameters of adhesive interaction and surface microgeometry on the contact characteristics and energy dissipation in an approach–separation cycle of elastic bodies with regular surface relief, as well as in their mutual sliding and rolling.

The load–distance dependence and the energy dissipation in the approach–separation cycle are calculated for two elastic bodies, one of which is covered with a periodic system of asperities of spherical shape, by taking into account the forces of both elastic compression and adhesive attraction between the surfaces. The mutual effect of microcontacts was taken into account, making it possible to establish the dependence of the characteristics in question on the shape and density of the asperities and the parameters of adhesion.

A method is developed to calculate the adhesive component of the friction force in the conditions of mutual sliding and rolling of elastic bodies with regular surface microgeometry. The method is based on the determination of the energy dissipation in the

approach–separation cycle of asperities. Based on the model calculations performed, the dependencies of the coefficient of friction on the nominal pressure are established for various values of the parameters of roughness and adhesion.

The results obtained can be applied for controlling the microgeometric parameters of dry surfaces to attain the required frictional characteristics on specified regimes of interaction.

Acknowledgment

This work was carried out under the financial support of the Russian Science Foundation (grant No. 14-29-00198). The authors are also grateful for the discussion within the framework of the CARBTRIB International network supported by the Leverhulme Trust.

References

[1] Tomlinson J A. A molecular theory of friction. *Philos Mag* **46**: 905–939 (1929)

[2] Derjaguin B. Molekulartheorie der äußeren Reibung. *Z Phys* **88**: 661–164 (1934)

[3] Johnson K L, Kendall K, Roberts A D. Surface energy and the contact of elastic solids. *Proc Roy Soc Lond* A **324**: 301–313 (1971)

[4] Derjaguin B V, Muller V M, Toporov Y P. Effect of contact deformations on the adhesion of particles. *J Colloi. Interface Sci* **53**(2): 314–326 (1975)

[5] Maugis D. Adhesion of spheres: The JKR-DMT transition using a Dugdale model. *J Colloid Interface Sci* **150**: 243–269 (1992)

[6] Greenwood J A. Adhesion of elastic spheres. *Proc Roy Soc Lond A* **453**: 1277–1297 (1997)

[7] Barthel E. On the description of the adhesive contact of spheres with arbitrary interaction potentials. *J Colloid Interface Sci* **200**: 7–18 (1998)

[8] Greenwood J A, Johnson K L. An alternative to the Maugis model of adhesion between elastic spheres. *J Phys D-Appl Phys* **31**(22): 3279–3290 (1998)

[9] Goryacheva I G, Makhovskaya Y Y. An approach to solving the problems on interaction between elastic bodies in the presence of adhesion. *Dokl Phys* **49**(9): 534–538 (2004)

[10] Johnson K L. Non-Hertzian contact of elastic bodies. In *The Mechanics of the Contact Between Deformable Bodies*. Pater D E, Kalker J J, Eds. Delft University Press, 1975: 26–40.

[11] Fuller K N G, Tabor D. The effect of surface roughness on the adhesion of elastic solids. *Proc Roy Soc London A* **345**: 327–342 (1975)

[12] Maugis D. *Contact, Adhesion and Rupture of Elastic Solids*. Berlin: Springer-Verlag, 2000.

[13] Morrow C, Lovell M, Ning X. A JKR-DMT transition solution for adhesive rough surface contact. *J Phys D* **36**: 534–540 (2003)

[14] Galanov B A. Models of adhesive contact between rough elastic bodies. *Int J Mech Sci* **53**: 968–977 (2011)

[15] Rumpf H. *Particle Technology*. London: Chapman & Hall, 1990.

[16] Rabinovich Y I, Adler J J, Ata A, Singh R K, Moudgil B M. Adhesion between nano-scale rough surfaces: I. Role of asperity geometry. *Journal of Colloid and Interface Science* **232:** 10–16 (2000)

[17] Derjaguin B. Untersuchungen uber die Reibung und Adhasion, IV. Theorie des Anhaftens kleiner Teilchen. *Kolloid Zeitschrift* **69:** 155–164 (1934)

[18] Borodich F M. The Hertz-type and adhesive contact problems for depth-sensing indentation. *Advances in Applied Mechanics* **47**: 225–366 (2014)

[19] Popov V L, Filippov A E. Adhesive properties of contacts between elastic bodies with randomly rough self-affine surfaces: A simulation with the method of reduction of dimensionality. *Phys Mesomech* **15**(5): 324–329 (2012)

[20] Sahoo P, Chowdhury S K R. A fractal analysis of adhesion at the contact between rough solids. *Proc. Instn. Mech. Engrs.* **210**: 269–279 (1996)

[21] Persson B N J, Tossati E. The effect of surface roughness on the adhesion of elastic solids. *J Chem Phys* **115**: 5597–5610 (2001)

[22] Persson B N J. Adhesion between elastic bodies with randomly rough surfaces. *Phys Rev Lett* **89**: 245502-1-245502-4 (2002)

[23] Persson B N, Scaraggi M. Theory of adhesion: Role of surface roughness. *J Chem Phys* **141**(12): 124701 (2014)

[24] Ciavarella M. Adhesive rough contacts near complete contact. *International Journal of Mechanical Sciences* **104**: 104–111 (2015)

[25] Pastewka L, Robbins M O. Contact between rough surfaces and a criterion for macroscopic adhesion. *Proceedings of the National Academy of Sciences* **111**(9): 3298–3303 (2014)

[26] Ciavarella M. On Pastewka and Robbins' criterion for macroscopic adhesion of rough surfaces. *Journal of Tribology* **139**(3): 031404 (2017)

[27] Ciavarella M. On the use of DMT approximations in adhesive contacts, with remarks on random rough contacts. *Tribology International* **114**: 445–449 (2017)

[28] Ciavarella M. A very simple estimate of adhesion of hard solids with rough surfaces based on a bearing area model. *Meccanica*, DOI 10.1007/s11012-017-0701-6 (2017)

[29] Borodich F M. Fractal contact mechanics. In: *Encyclopedia of Tribology*. Wang Q J, Chung Y-W (Eds.). Springer, 2013: 1249–1258.

[30] Borodich F M, Pepelyshev A, Savencu O. Statistical approaches to description of rough engineering surfaces at nano and microscales. *Tribology International* **103**: 197–207 (2016)

[31] Hui C Y, Lin Y Y, Baney J M, Kramer E J. The mechanics of contact and adhesion of periodically rough surfaces. *J Polym Sci B* **39**: 1195–1214 (2001)

[32] Adams G G. Adhesion at the wavy contact interface between two elastic bodies. *ASME J Appl Mech* **71**(6): 851–856 (2004)

[33] Chumak K. Adhesive contact between solids with periodically grooved surfaces. *Int J Solids Struct* **78**: 70–76 (2016)

[34] Makhovskaya Y Y. Discrete contact of elastic bodies in the presence of adhesion. *Mech Solids* **38**(2): 39–48 (2003)

[35] Bowden F P, Tabor D. *Friction and Lubrication of Solids*. Oxford (UK): Oxford University Press, 1950.

[36] Chowdhury S K, Roy Ghosh P. Adhesion and adhesional friction at the contact between solids. *Wear* **174**: 9–19 (1994)

[37] Kogut L, Etsion I. Static friction model for elastic-plastic contacting rough surfaces. *J Tribol-T ASME* **126**: 34–40 (2004)

[38] Sahoo P, Mitra A, Saha K. Elastic-plastic adhesive contact of rough surfaces using n-Point asperity model. *J Phys D: Appl Phys* **42**: 1–13 (2009)

[39] Johnson K L. Adhesion and friction between a smooth elastic spherical asperity and a plane surface. *Proc R Soc. Lond A* **453**: 163–179 (1997)

[40] Chaudhury M K, Owen M J. Adhesion hysteresis and friction. *Langmuir* **9**(1): 29–31 (1993)

[41] Szoszkiewicz R, Bhushan B, Huey B D, Kulik A J, Gremaud G. Correlations between adhesion hysteresis and friction at molecular scales. *The Journal of Chemical Physics* **122**(14) (2005)

[42] Yoshizawa H, Chen Y-L, Israelachvili J. Fundamental mechanisms of interfacial friction. 1. Relation between adhesion and friction. *J Physical Chemistry* **97**(16): 4128–4140 (1993)

[43] Barquins M. Adherence, friction and contact geometry of a rigid cylinder rolling on the flat and smooth surface of an elastic body. *J Nat Rub Rs* **5**(3): 199–210 (1990)

[44] Carbone G, Mangialardi L. Adhesion and friction of an elastic half-space in contact with a slightly wavy rigid surface. *Journal of the Mechanics and Physics of Solids* **52**(6): 1267–1287 (2004)

[45] Heise R, Popov V L. Adhesive contribution to the coefficient of friction between rough surfaces. *Tribology Letters* **39**(3): 247–250 (2010)

[46] Goryacheva I, Makhovskaya Y. A model of the adhesive component of the sliding friction force. *Wear* **270**: 628–633 (2011)

[47] Derjaguin B V, Krotova N A, Smilga V P. *Adhesion of Solids*. London: Consultants Bureau, 1978.

[48] Goryacheva I G, Makhovskaya Y Y. Adhesive resistance in the rolling of elastic bodies. *J Appl Math Mech* **71**(4): 485–493 (2007)

[49] Goryacheva I G. *Contact Mechanics in Tribology*. Dordreht: Kluwer Academic Publishers, 1997.

[50] Tabor D. Surface forces and surface interactions. *J Colloids Interface Sci* **58**(2): 2–13 (1977)

[51] Goryacheva I G, Makhovskaya Y Y. Adhesive interaction of elastic bodies. *Journal of Applied Mathematics and Mechanics* **65**(2): 273–282 (2001)

[52] Ciavarella M, Greenwood J A, Barber J R. Effect of Tabor parameter on hysteresis losses during adhesive contact. *Journal of the Mechanics and Physics of Solids* **98**: 236–244 (2017)

Irina GORYACHEVA. She received her Ph.D. degree in Moscow State University in 1974 and her D. Sci degree in Institute for Problems in Mechanics of the Russian Academy of Sciences in 1988. She is the full member of the Russian Academy of Sciences since 2003. Her current position is a professor of the Moscow State University and Moscow Institute of Physics and Technology, head of the Tribology Laboratory at Institute for Problems in Mechanics. Her research interests cover a broad range of problems in contact mechanics and tribology.

Yulia MAKHOVSKAYA. She received her Ph.D. degree in Institute for Problems in Mechanics of the Russian Academy of Sciences in 2001. Her current position is a senior researcher in the Tribology Laboratory at Institute for Problems in Mechanics. Her research interests lie in modeling the interaction of elastic and viscoelastic bodies taking into account adhesion.

Friction **5**(3): 351–360 (2017)
https://doi.org/10.1007/s40544-017-0185-3
ISSN 2223-7690
CN 10-1237/TH

RESEARCH ARTICLE

Design and application of friction pair surface modification coating for remanufacturing

Haidou WANG[1,*], Guozheng MA[1,*], Binshi XU[1], Qingsong YONG[1,2], Pengfei HE[1]

[1] *National Key Lab for Remanufacturing, Academy of Armored Forces Engineering, Beijing 100072, China*

[2] *China Aerodynamics Research and Development Center, Mianyang 621000, China*

Received: 12 June 2017 / Accepted: 11 August 2017

Abstract: Friction, wear, and contact fatigue are the main causes of energy loss, material waste, and equipment failure. The aim of remanufacturing is to repair and modify the damaged equipment surface, and the surface coating is the major material that allows the remanufactured parts to be used in a new round of operation. Thus, the design and preparation of surface coatings are very important to repair, strengthen, or modify the friction pairs, in order to ensure long-term operation of the remanufactured parts. Recently, a lot of research on designing and preparing friction pair surface modification coatings has been conducted by the National Key Laboratory for Remanufacturing (NKLR). The research conducted achieved the following goals: the mechanism of micro/nano multilayer surface modification coatings with long-term efficacy life was revealed, and the corresponding design considerations and preparation methods of nanocrystalline micro tribological coatings were innovatively developed. A series of new "two-step" processes to prepare sulfide solid lubricating coatings were developed. The competitive failure mechanism of the surface coating in simultaneous wear and fatigue conditions was revealed, and some composite coatings with dual properties of wear resistance and fatigue resistance were prepared. Based on the stress distribution of friction surface contact areas and the piezoelectric effect, a failure warning intelligent coating is designed and developed. These coatings have been successfully applied to critical friction components, such as the spindle of large centrifugal compressors, engine cylinder piston components, and driver gear pairs.

Keywords: remanufacturing; surface coating; solid lubrication; contact fatigue; intelligent sensing coating

1 Introduction

Friction and wear of relatively moving components cannot be avoided. Significant economic loss and energy waste can be caused by wear [1]. Remanufacturing practices also show that wear is considered as a major damage form of workblanks for remanufacturing (old equipment or parts). Additionally, it has been reported that many remanufactured parts failed due to oversized components, surface cracking, or plastic deformation caused by friction, wear, and contact fatigue in their new round of service. China's independent innovative remanufacturing engineering has developed surface coating techniques that are capable of not only repairing the surface damage to recover the original shape and size of parts, but also using the newest surface treatment processes and applying high performance materials to the remanufactured part surface, in order to achieve excellent tribological properties [2].

Recently, the equipment remanufacturing practice has paid considerable attention to the tribology issue related to key kinematic pairs. The National Key Lab for Remanufacturing (NKLR) adopts the structure-function integrated approach to design and deposit surface modifying coatings on friction pair surfaces. This approach facilitates monitoring and improvement

* Corresponding author: Haidou WANG, E-mail: wanghaidou@tsinghua.org.cn; Guozheng MA, E-mail: magz0929@163.com

of the performance of the friction pair surfaces in terms of their self-lubrication, wear resistant, anti-fatigue, and friction pair service conditions. Based on the related theory of tribology, material, and surface science, the theoretic and technical problems of structural design, preparation technology, and performance evaluation of the coatings are conquered by restraining the thermodynamic condition and controlling the dynamic process of the coating forming process. Currently, the developed coatings have been successfully applied to modify the surface performance of moving parts and to remanufacture key heavy vehicle components, engineering machinery, and other kinds of industrial equipment.

2 Design, preparation, and application of friction pair surface performance modification coatings

2.1 Design, preparation, and application of solid lubrication coatings

Having been conducting the relative studies for more than ten years, our laboratory comprehensively applies various surface technologies such as vacuum infiltration, magnetron sputtering, thermal spraying, sol-gel, etc. Most of the common problems (low adhesive strength, complex producing process, low content of lubricant phase, and short lifespan) of traditional solid lubrication coatings were addressed by combining the structure, technology, and function of the applied coatings. Furthermore, using these technologies facilitates the deposition of solid lubrication coatings with a wide range of thicknesses onto a variety of friction surfaces. This enables us to examine the tribological behavior and performance evolution mechanism of solid lubrication coatings, and significantly promotes the operating performance, service life, and reliability of the moving parts under extremely harsh operating and weather conditions [3].

2.1.1 *Composite nano-multilayer lubrication film of transition metal sulfide prepared by plating-penetrating*

The key friction pairs of diesel engine in heavy vehicles, i.e., cylinder/piston, crankshaft/connecting rod, valve components, etc., chronically operate under high temperature, speed, and contact stress conditions. Further, the surface accuracy and dimension tolerance requirements of the friction pairs are very strict. Serious accidents, starting difficulty, and power failure may occur if the main components of the engine suffer serious damage like scuffing, adhesion, and fatigue spalling [4]. Reliable lubrication is important to address the above friction failure problems. However, the traditional lubrication methods (oil/grease) are not sufficient to satisfy the lubrication demand for heavy equipment operating with high intensity for a long time under severe conditions.

To address this issue, a composite multilayer solid lubrication coating with a bimetal matrix and multiphase lubricants is designed and deposited through composite surface engineering technologies, such as a combination of physical vapor deposition and low temperature ion sulfurizing technologies [5]. First, nanoscale multilayer metal films (Fe/Mo, Fe/W, W/Mo, etc.) are alternately deposited by dual-target magnetron sputtering technology. Subsequently, various lubricating phases (FeS/MoS_2, FeS/WS_2, WS_2/MoS_2, etc.) are generated in multilayer films using low temperature ion sulfurizing technology. Thus, the composite multilayer solid lubrication coating with transition metals (Fe, Mo, W, etc.) as the matrix combined with diverse lubricants (FeS, MoS_2, WS_2) was formed accordingly [6]. Figure 1 shows the surface topography and the element distribution with depth of FeS/MoS_2 multilayer films.

The effect of precursor metal film structure on the following sulfurizing process, and the "sputtering etching" effect of ion bombardment on the film surface during sulfurizing have been studied. Based on the thermodynamics conditions analysis, such as the diffusion law and reaction temperature, it is found that the precursor film made of transition metallic elements (Fe, Mo, W, etc.) must form metal-sulfides during the following sulfurizing process, and S in the film can only exist in the form of an intermetallic compound. The reaction kinetics factors, which can promote the generation of sulfides, and the reaction of transition metal film (Mo, W, etc.) with S have been summarized. Moreover, the effects of the structure and mechanical properties of the Fe/Mo, Mo/W multilayer films, and mono-metal films with different thicknesses on the follow-up sulfurizing process and tribology

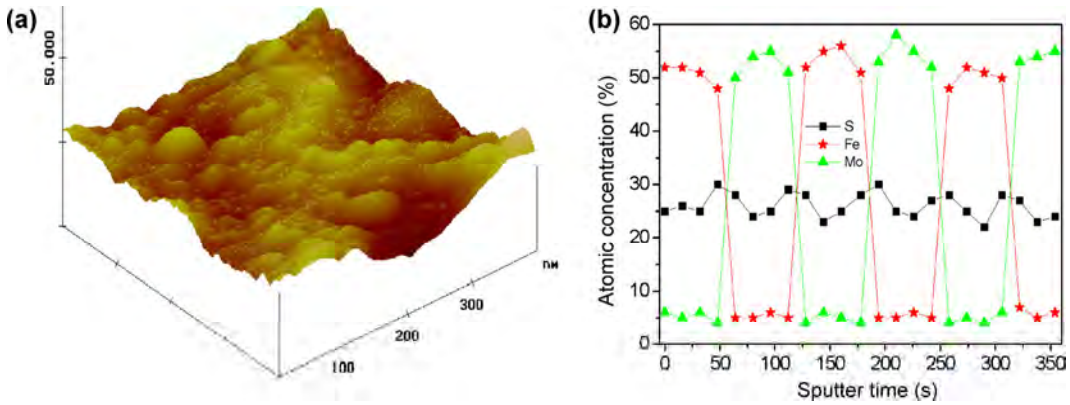

Fig. 1 Surface morphology of FeS/MoS_2 nano multilayer film (a) and the element distribution with surface coating of FeS/MoS_2 multilayer films (b) [6].

behavior of the films have been studied. The effects of the microstructure properties, i.e., ultra-fine grain, multiple interface, and high stress, on the performance of antifriction, wear-resistance, and anti-scratch characteristics of the multilayer films (such as FeS/MoS_2 and WS_2/MoS_2), have also been analyzed [7, 8].

The distinct advantages of this solid lubricating coating are that the assemble mode of the sublayers can be adjusted based on the material of the substrate, which contributes to the best matchup of material properties between the substrate and coating. The high-density layer boundary inside the coating can form an ideal channel for the diffusion of S during sulfurizing. Additionally, the nanoscale multilayer structure can attain stress adjustment between film-to-substrate interface and layer-to-layer. There are more than two kinds of lubricating phases inside the coating. Further, the abundant S at the boundary of the layers can react with the matrix metal under the influence of friction high-temperature, and generate new lubricating phase. Thus, this kind of solid lubricating coating exhibits distinct advantages, such as high bond strength, high content of lubricants, strong bearing capacity, and long service life. Such properties are suitable for applications that involve surface modification of key precise friction pairs, which operate under harsh conditions including high temperature, high speed, and high stress conditions.

The above technologies have been applied to repair and strengthen the main components of diesel engine, such as the cylinder, crankshaft, connecting rod, and camshaft. After depositing the FeS/MoS_2 solid lubricating film on the key friction pairs, the reliability and performance of the engine has been significantly improved, its smoke level has been reduced by about 40%, the output power has been increased by 2%–5%, the fuel consumption has been reduced by 5%, and the active time of the repaired heavy vehicle has been doubled. These technologies have also been applied for modifying the surface of forming equipment, such as closure rails of precision machine tools, bending molds of hydraulic plate bender, hobbing cutters, and hydraulic rubber cutters. The results show that the rails wear-resistance and the performance accuracy of machine tools both have been obviously improved, the service life of the bending molds subject to high load and intense temperature has been doubled, the sticky rate of hot forging mould has been reduced to 80% and the lifetime of this mold has been doubled, the lifetime of cutters has been extended 50%, the anti-abrasion property of hobbings has been significantly improved, and the lifetime of cutters has been trebled.

2.1.2 *A series of "two-step" process for preparation of iron-based sulfide lubricant coatings*

In the past decades, a series of "two-step" preparation technologies for iron-based sulfide lubricant coatings have been developed. The hardness, fatigue strength, and wear resistance of friction pair surfaces can be greatly improved through preprocesses such as nitriding, carbonitriding, shot blasting, supersonic fine particles bombarding, etc. Then, a self-lubricating surface that is rich in sulfide lubricants can be generated *in-situ* using sulfurizing technology. This special

composite surface has a soft outside layer of low shear strength and good lubricating performance, and a hard subsurface with high strength and toughness and high load-carrying capacity, which can achieve a synergetic effect to improve durability and lubrication properties. As shown in Fig. 2, the nitrided-sulphurized surface layer, which is formed by the two-step composite chemical heat treatment of "carbonitriding/nitriding and ion sulfurizing" has much better abrasive-resistance and load-carrying capacity compared to the traditional nitriding layer. Moreover, it has more durative and stable antifriction property compared to the direct sulphurized surface layer. Thus, the combination of the two technologies conduced multiple improvements in the surface tribological properties [9]. This technology has already been applied to the tribological modification of large compressor rotating shafts and main rotors of rubber mixing machine.

An innovative ion sulphurizing process assisted by surface mechanical treating has been studied in-depth. The steel surface was pretreated using shot blasting and supersonic fine particles bombarding, respectively. This can form martensite phase transformation hardening layer, high density interface layer, and high surface activity nanocrystalline layer on the workpiece surface of sulfurizing, which also increased the substrate hardness and sulfurizing layer thickness (as shown in Fig. 3) [10]. Thus, the antifriction and wear resistance

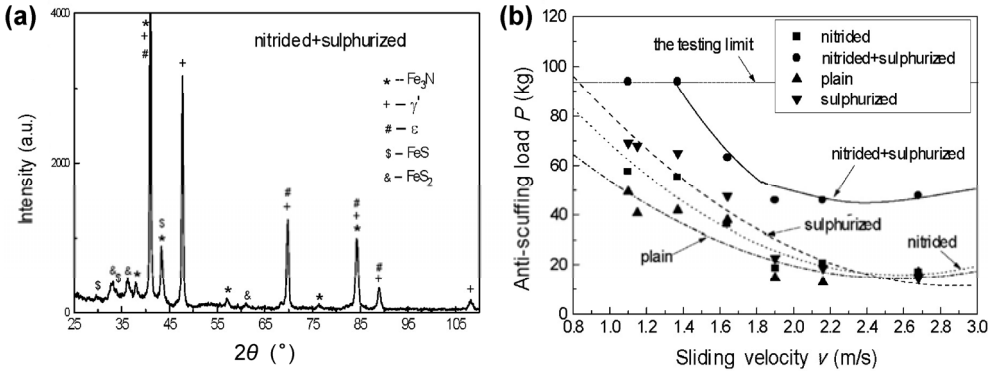

Fig. 2 Phase structure diagram of nitriding+sulfurizing surface (a) and *P*-*V* diagram under oil lubrication condition (b) [9].

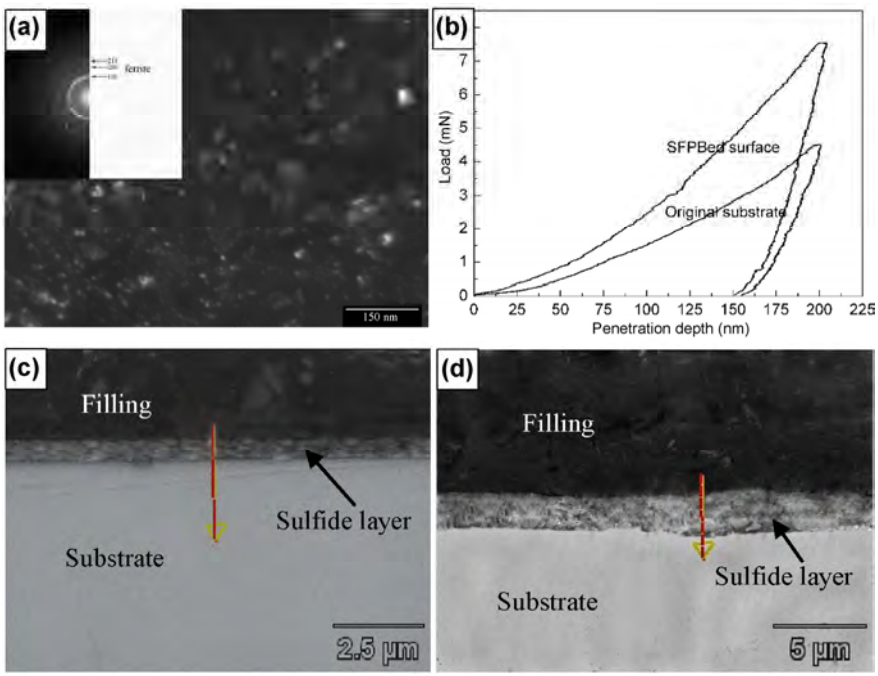

Fig. 3 Morphology (a) and hardness (b) of surface nanocrystalline layer on 1Cr18Ni9Ti steel obtainedby supersonic fine particles bombarding; comparison of sulphurized layer without (c) and with (d) pretreatment.

properties of the sulfurizing film were remarkably improved.

The conventional plasma sulphurizing technology is mainly used for the surface modification of iron-based bulk materials. Considering that the thermal spraying technology has no special material constraints for both coating and substrate, a two-step combination technology of "spraying iron-based coating and ion sulfurizing" has been developed, which successfully deposited sulfide films on the surface of all kinds of non-ferrous metal materials. A solid lubricating coating which is rich in FeS lubricant and micropores for oil storage has been formed by spraying iron-based coatings with a porous structure (FeCrBSi, 3Cr13, etc.) on the surface of key friction pairs, and subsequent sulfurizing [11]. The porous structure not only provides micro-channels for the diffusion of S atoms during the sulfurizing process and promotes the synthesis of high density solid lubricating phase, but also has the essential properties of oil storage and wear debris gathering. The solid lubricating phase can adapt to work conditions in which traditional lubricants cannot effectively work, such as dense sand, high temperature, and arctic conditions. Moreover, in the severe conditions that involve heavy load, high impact, and dry friction, oil stored in the micropores will enter the friction interface to form an oil film, which effectively improves the lubricating conditions. This technology has been successfully applied to the cylinder components of heavy vehicles and engineering machinery, while also being used in surface modification to improve the running mechanism of crawler equipments. Real heavy vehicle testing has proved that composite solid lubricating coatings represented by 3Cr13/FeS coating can minimize abrasive wear and scuffing of cylinders operating in dry conditions. It can double the lifetime of cylinder body, and reduce the engine failure rate by 20%. The oil-storage function of the composite coating successfully solved the starting up difficulty in armored engineering vehicles operating under starved-oil and severe cold conditions, and improved the success rate of one-time startup to 85% under the extremely cold temperatures of –35 ℃. This series of composite coatings have also been applied to the surface tribology properties modification of the moving parts of crawler equipments, which doubled the lifetime of their vulnerable parts, such as creeper treads, dowels, and driving wheels.

2.1.3 *Preparation of inorganic solid lubricant coatings by other surface technologies*

The brush plating technology has many advantages as it involves using simple devices and flexible processes to obtain fast plating rate and high bond strength that can be used in wide range of applications [12]. Recently, a lot of research on brush plating of soft metal self-lubricating coatings (Ag, Sn, Zn, In, etc.) has been carried out by NKLR. Specifically, the Ni/In composite plating exhibits well adaption in vacuum space environment, in which it can rapidly form stable transfer film on the friction pair surface, resulting in relatively excellent resistance to adhesive-wear and good antifriction performance, as shown in Fig. 4.

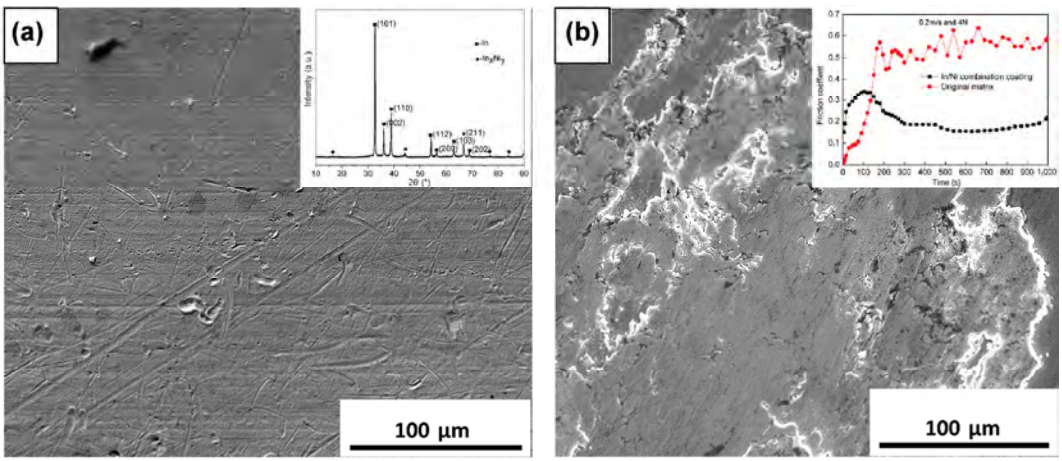

Fig. 4 Microstructure and tribological properties of Ni/In composite coating (a) coating and (b) wear spot.

Furthermore, the n-Al_2O_3/Ni functional layer is introduced, which exhibits good load-bearing and wear resistance properties under the Ni/In coating, and thus an n-Al_2O_3/Ni/In composite multilayer coating is formed. The multifunctional space tribology experiment system is used to test the friction and wear properties of this coating under four kinds of environmental conditions, including atmosphere, vacuum, atomic oxygen erosion, and ultraviolet radiation, as shown in Fig. 5. It is found that the n-Al_2O_3/Ni/In composite coating is composed of granular asperities of approximately 2 μm diameter. In addition, the coating is flat and smooth at the macro level, without relatively high porosity, nodule and local coarse structure, and exhibits good antifriction properties in all of the above-mentioned environmental conditions.

Further, the Zn/FeS and Zn/graphite coatings were deposited using "sol-gel" technology, and the effect of the content and wettability of the lubricant particles on the bond strength and tribological properties of the coatings were analyzed. Additionally, an iron-based solid lubricating coating was prepared with FeS and FeS_2 powder by plasma spraying technology and high-speed flame spraying technology, respectively. The melting, decomposition, oxidation, and regeneration phenomena of the spraying powder during spraying of the iron-based multiphase composite coating were studied. A Ni/MoS_2 composite coating was also deposited by plasma spraying technology, and the effects of its microstructure, cohesive strength, and bond strength on wear-resistance and anti-scuffing properties of the coating were analyzed.

2.2 Design, preparation, and application of wear-resistance & anti-fatigue integration coating

Wear and contact fatigue are considered as the most important damage mechanisms of key friction pair components. The focus of the existing surface strengthening modification technologies is often limited to improving the wear resistance of components [13]. Particularly, the coating has contrary and uniform characters of high-free-energy and multiple interfaces, so its wear resistance and anti-fatigue properties show a competitive rule of interplay and interaction. Thus, the forming method and evaluation technique of wear-resistant and fatigue-resistant integrative coatings were studied in-depth, and the service life and reliability of the key friction components of the equipments were improved.

2.2.1 *High quality forming of wear-resistant and anti-fatigue integrative coatings deposited by plasma spraying*

The plasma sprayed coatings have exhibited excellent wear resistance properties in moving parts. However, the deposition process of the coating that determines its microstructure involves a lot of interfaces. This induces coating invalidation that co-affected by wear and fatigue under the practical service condition. The key to improve the wear resistance and fatigue resistance properties of the plasma sprayed coatings synchronously is to enhance the bond strength and cohesion strength of the coatings. After long-term study, a series of methods are proposed to extend the

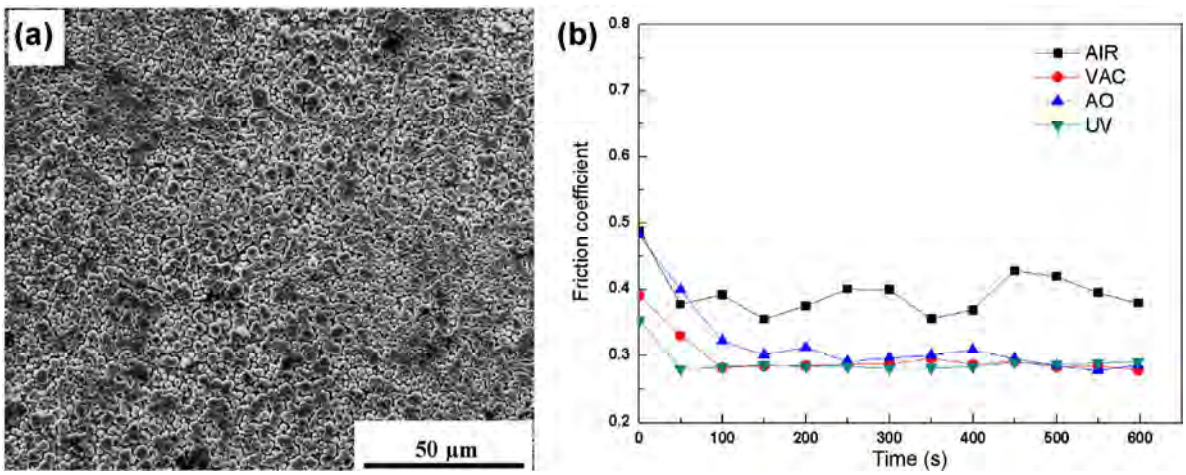

Fig. 5 Surface morphology (a) and friction coefficient under space environment (b) of n-Al_2O_3/Ni/In.

contact fatigue lifetime of plasma sprayed coatings. The proposed methods are summarized as follows: (1) the coating forming parameters can be optimized and the cohesion strength of the coating can be greatly enhanced by the state monitoring of spraying particles and the temperature field of the plasma beam; (2) the micro interlock bond strength of the interface can be improved by using the laser micromachining technology to make the coating/substrate interface textured; (3) the cohesion strength and bond strength of the coating can be considerably increased by using post-processing technologies such as re-melting and hot isostatic pressing, to eliminate the micro-defects in the coating and interface, and to release the stress adequately. In this way, the high quality forming of metal-based coatings (Fe-based and Ni-based), cermet coatings (NiCr-Cr_2C_3 and WC-Co), and composite ceramic coatings (Al_2O_3-TiO_2 and Cr_2O_3-Al_2O_3) are achieved (as shown in Fig. 6 that illustrates the micro-morphology of plasma spraying Al_2O_3/40 wt% TiO_2 (AT40) coating) and successfully applied to various equipment components [14, 15].

The NiCr-Cr_2C_3 cermet coating is successfully used for modifying the surface of wheel ball bearings of certain overloaded vehicles turret rotation mechanism. The wear-resistant and anti-fatigue performance of the components after strengthening has been significantly enhanced, and their service life has been tripled. The NiCr-Cr_2C_3 coating and Al_2O_3-TiO_2 composite ceramic coating are also widely applied to modify the performance of key friction pairs of oil and gas drilling equipments. After spraying the NiCr-Cr_2C_3 hard coating on the cemented carbide wear plate, its hardness and wear resistance are greatly increased. The practical drilling application shows that the cemented carbide wear plate strengthened by the above technology can effectively eliminate the wear failure of the centering guide, and significantly extend its service life. Meanwhile, the Al_2O_3-TiO_2 composite ceramic coating can improve the wear resistance and corrosion resistance of the oil drill pipe and screw to a great extent, and extend its service life by 1.5 times. The Fe-based self-fluxing alloy coating greatly enhances the wear resistant and anti-fatigue performance of the key friction pairs of industrial equipments, such as the roller of rolling machine, compressor vane, and tools used in rubber molding. Both the service life and product quality of the equipment have been considerably improved.

2.2.2 *Wear-resistant and fatigue-resistant integrative coatings deposited by brush plating and its engineering application*

In terms of brush plating wear resistant/anti-fatigue coatings, the NKLR successfully developed a series of nanocomposite brush plating solutions and corresponding plating processes, such as n-Al_2O_3/Ni, n-ZrO_2/Ni, n-(Al_2O_3-ZrO_2)/Ni, n-(Al_2O_3-SiC)/Ni, n-(Al_2O_3-CNTs)/Ni, etc., which are used to remanufacture and repair heavy vehicle running gear parts, aeroengine compressor blades, automotive engine components, and machine parts [16]. In particular, the Ni-Co-based nanocomposite (n-Al_2O_3/Ni-Co) rotary brush plating technology, which has been successfully developed recently, can replace the hard chromium coating, and

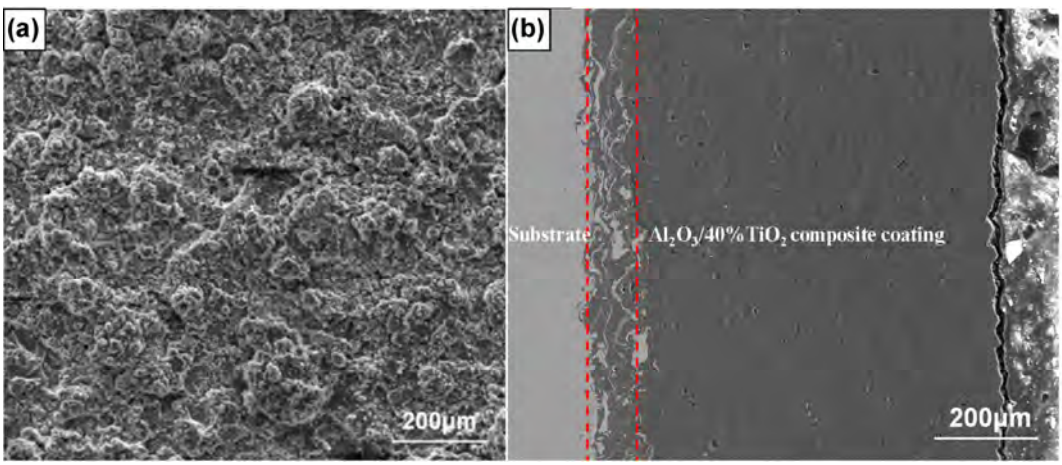

Fig. 6 Surface (a) and cross-sectional (b) morphology of AT40 coating deposited by plasma spraying [15].

can be used for the remanufacturing of gun barrels, hydraulic parts of aircraft landing gear, hydraulic cylinders, and piston rods. This technology can not only realize high quality repair of local and large area damages in chromium-plated parts at a lower cost, but also can eliminate the risk of environmental pollution by the traditional chrome-plating that contains Cr^{6+} solution. Brush plating by n-Al_2O_3/Ni-Co composite coating was successfully used to repair serious local gouge in hydraulic rods. Further, the wear resistance of the composite coating is significantly higher than that of hard chromium plating. Although friction coefficient of the composite coating is equivalent to that of the hard chromium plating, its tribological properties are more stable during long-term operations [16].

2.3 Intelligent sensing coating with the function of in situ condition monitoring for friction moving components

The continuous accumulation of micro-damage in the key friction pairs in service can cause serious sudden accidents. Thus, it is necessary to monitor the surface condition of equipment components in order to recognize any damage instantly. However, the existing monitoring technologies that rely on embedding or attaching sensors to the monitored components have some disadvantages, for example: in some cases it is difficult to approach the contact interface to place the sensor. The sensor itself can be easily damaged during equipment operation, the surface integrity may be affected by external sensors, or the bond strength of the attached sensor is weak, and it is difficult to securely fix it to complex shaped surfaces.

To tackle the above issues, we developed an intelligent sensing coating, which integrates the friction modification and condition monitoring of friction pairs based on the force-electric mapping relation of piezoelectric materials. Figure 7 shows the structure of the intelligent sensing coating and its layers from outside to inside are surface work layer, piezoelectric sensor layer, transitional insulating layer, respectively: (1) the surface work layer, which is composed of alloy material (FeCrBSi, NiCrBSi), is used to resist wear and fatigue, and also acts as an electrode for the sensor layer; (2) the piezoelectric sensor layer, which consists of piezoelectric ceramic material (PZT, $BaTiO_3$), is used to recognize any change in the stress state of the surface work layer when damage occurs [17] to be converted into current signals and transferred through the piezoelectric effect; (3) the transitional insulating layer is composed of an intermetallic compound and ceramic (NiAl-Al_2O_3), which not only improves the bond strength between the coating and substrate but also prevents the charge loss. In general, the new type of intelligent sensing coating can electronically monitor the degree of damage and stress state of the part surface in real time, and overcome the past limitation of relying on the post analysis monitoring technology such as change of libration, torque and friction coefficient, or variation in oil composition [18].

The abovementioned intelligent sensing coating has successfully passed the evaluation carried out in a tank engine bench test. The performed test proved that the coating can maintain low friction for a long time under high temperature and high stress conditions, and can predict most (about 80%) fatigue peeling and heavy wear. This research can provide pivotal technical

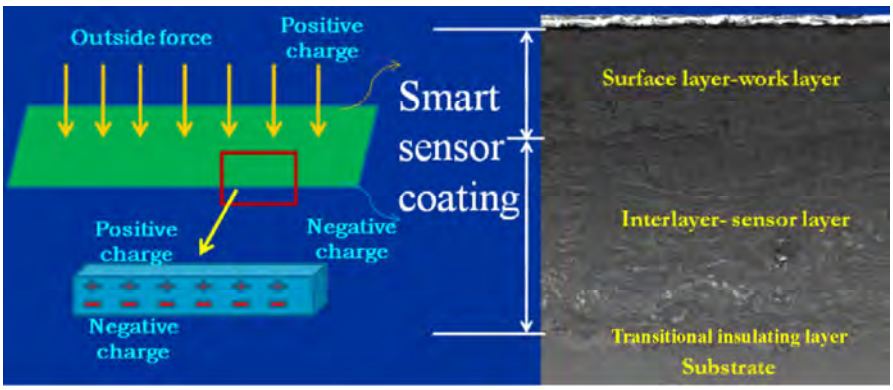

Fig. 7 Schematic diagram and Microstructure of PZT intelligent sensing composite coating.

support for developing intelligent friction pairs. The intelligent sensor coating technology has also been broadly applied to relevant tribology testers. The technology facilitated achieving a dynamic warning for fatigue/wear failure and accurate calculation of the coating's remaining service life, and thus promoted the development of intelligent testers with high resolution, efficiency, and automation.

3 Conclusion

Friction, wear, and contact fatigue are the main causes of energy consumption, material waste, and equipment damage. Thus, developing an appropriate method to reduce wear, alleviate fatigue, extend service life, and improve operational reliability is a major technical challenge to guarantee long-term service life of friction moving components. Based on the surface science theory and structure-function integration design approach, the latest achievement in surface engineering technology was comprehensively applied to design surface modification coatings that can endow the functions of solid lubrication, anti-fatigue, wear resistance, and automatic sensing to the surface of key friction pair. The relevant basic-research findings are reviewed to complement and enhance the basic tribology theory. In addition, it is found that the design, deposition, and evaluation technology of the developed friction pair surface modification coatings can significantly improve the working performance properties, extend the service life, and allow real-time monitoring of the service condition of the equipment key moving components. Further, the technologies discussed in this study have been successfully applied to remanufacture, strengthen, and repair key moving components of heavy equipment engines, machining and forming tools, oil, and gas drilling equipment, etc. In general, these technologies can provide theoretical and technical support for surface modification, strengthening, and remanufacturing of key friction pairs.

Acknowledgements

The authors are grateful for the financial support by NSFC (Nos. 51675531 and 51535011) and NSF of Beijing (No. 3172038), and the Tribology Science Fund of State Key Laboratory of Tribology (No. SKLTKF16A05).

References

[1] Xie Y B, Zhang S W. *Progress and Development Stratagem of Tribology Science And Engineering.* (in Chinese). Beijing: Higher Education Press, 2009.

[2] Xu B S. *Equipment Remanufacturing Engineering.* (in Chinese). Beijing: National Defense Industry Press, 2013.

[3] Erdemir A. Review of engineered tribological interfaces for improved boundary lubrication. *Tribology International* **38**: 249–256 (2005)

[4] Wong W V, Tung C S. Overview of automotive engine friction and reduction trends-Effects of surface, material, and lubricant-additive technologies. *Friction* **4**(1): 1–28 (2016)

[5] Watanabe S, Noshiro J, Miyake S. Friction properties of WS_2/MoS_2 multilayer films under vacuum environment. *Surface & Coatings Technology* **188**–**189**: 644–648 (2004)

[6] Wang H D, Xu B S, Liu J J, Zhuang D M. Characterization and anti-friction on the solid lubrication MoS_2 film prepared by chemical reaction technique. *Science & Technology of Advanced Materials* **6**(5): 535–539 (2005)

[7] Xu G Z, Zhu M H, Liu J J, Zhou Z R, Liang H. The effect of pre-treatment of substrate on fretting tribological behavior of MoS_2 coatings. *Wear* **255**(1–6): 246–252 (2003)

[8] Zhu L N, Wang C B, Wang H D, Xu B S, Zhuang D M, Liu J J, Li G L. Tribological properties of WS_2 composite film prepared by a two-step method. *Vacuum* **85**(1): 16–21 (2010)

[9] Zhang N. Investigations of the microstructure, tribological behaviors and mechanisms of sulphide layer produced by low temperature ion sulphurization. (in Chinese). Dissertation of Tsinghua University, 2000.

[10] Tong W P, Han Z, Wang L M, Lu J, Lu K. Low-temperature nitriding of 38CrMoAl steel with a nanostructured surface layer induced by surface mechanical attrition treatment. *Surface & Coatings Technology* **202**: 4957–4963 (2008)

[11] Kang J J, Wang C B, Wang H D, Xu B S, Liu J J, Li G L. Characterization and tribological properties of composite 3Cr13/FeS layer. *Surface & Coatings Technology* **203**(4): 1927–1932 (2009)

[12] Xu B S, Wang H D, Dong S Y, Jiang B, Tu W Y. Electrodepositing nickel silica nano-composites coatings. *Electrochemistry Communications* **7**(6): 572–575 (2005)

[13] Ahmed R, Hadfield M. Failure modes of plasma sprayed WC–15% Co coated rolling elements. *Wear* **230**: 39–55 (1999)

[14] Fujii M, Yoshida A, Ma J, Shigemura S, Tani K. Rolling contact fatigue of alumina ceramics sprayed on steel roller under pure rolling contact condition. *Tribology International* **39**: 856–862 (2006)

[15] Kang J J, Xu B S, Wang H D, Wang C B. Influence of contact stress on rolling contact fatigue of composite ceramic coatings plasma sprayed on a steel roller. *Tribology International* **73**: 47–56 (2014)

[16] Gudmand-Høyer L, Bach A, Nielsen G T, Morgen P. Tribological properties of automotive disc brakes with solid lubricants. *Wear* **232**: 168–175 (1999)

[17] Ctibor P, Sedlacek J, Pala Z. Structure and properties of plasma sprayed $BaTiO_3$ coatings after thermal posttreatment. *Ceramics International* **41**(6): 7453–7460 (2015)

[18] Sheng C, Fatih D. $BaTiO_3$-$SrTiO_3$ layered dielectrics for energy storage. *Materials Letters* **65**: 978–981 (2011)

Haidou WANG. He received his Ph.D degree in Department of Mechanical Engineering from Tsinghua University in 2003. He joined the National Key Laboratory for Remanufacturing at Academy of Armored Forces from then on. He is a professor and the deputy director of the laboratory. His current research areas cover the surface engineering, remanufacturing and tribology, especially in service life evaluation of surface coatings and solid film lubrication.

Guozheng MA. He received his M.S. and Ph.D degrees in National Key Laboratory for Remanufacturing at Academy of Armored Forces, China, in 2010 and 2014, respectively. And then, he joined the National Key Laboratory for Remanufacturing. His research interests include surface engineering, remanufacturing and tribology.